AFRPL-TR-75-44

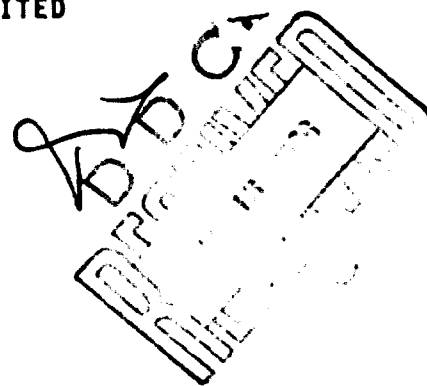# EXTERNAL CATALYST BREAKUP PHENOMENA

INTERIM REPORT

EXXON RESEARCH AND ENGINEERING CO.
GOVERNMENT RESEARCH LABORATORY
LINDEN, NEW JERSEY 07036

AUTHORS: W. F. TAYLOR, EXXON RESEARCH 7 ENG. CO.
           W. T. WEBBER, MCDONNELL DOUGLAS ASTRONAUTICS

SEPTEMBER   I 9 7 5

AIR FORCE ROCKET PROPULSION LABORATORY
DIRECTOR OF SCIENCE AND TECHNOLOGY
AIR FORCE SYSTEMS COMMAND
EDWARDS, CALIFORNIA 93523

FOREWORD

This report was submitted by Exxon Research & Engineering Company, Government Research Laboratory, Linden, New Jersey 07036, under contract F04611-74-C-0032, jc order No. 305811TM with the Air Force Rocket Propulsion Laboratory, Edwards, CA 93523.

This report has been reviewed by the Information Office/DOZ and is releasable to the National Technical Information Service (NTIS). At NTIS it will be available to the general public, including foreign nations.

This report is unclassified and suitable for public release.

STEVEN G. WAX, Lt., USAF
Project Engineer

FORREST FORBES, GS-14, Chief
Propellant Section

FOR THE COMMANDER

CHARLES E. STEBER, LtCol., USAF
Chief, Liquid Rocket Division

NOTICES

A

REPORT DOCUMENTATION PAGE

READ INSTRUCTIONS
BEFORE COMPLETING FORM

1. REPORT NUMBER	2. GOVT ACCESSION NO	3. RECIPIENT'S CATALOG NUMBER
AFRPL-TR-75-44		

4. TITLE (and Subtitle)

EXTERNAL CATALYST BREAKUP PHENOMENA

5. TYPE OF REPORT & PERIOD COVERED

Interim Technical Rept.
June 74 to Apr 75

6. PERFORMING ORG. REPORT NUMBER

7. AUTHOR(s)

W. F. Taylor, Exxon Research & Eng. Co.
W. T. Webber, McDonnell Douglas Astronautics

8. CONTRACT OR GRANT NUMBER(s)

F04611-74-C-0032

9. PERFORMING ORGANIZATION NAME AND ADDRESS

Exxon Research and Engineering Company
Government Research Laboratory
Linden, New Jersey 07036

10. PROGRAM ELEMENT, PROJECT, TASK
AREA & WORK UNIT NUMBERS

11. CONTROLLING OFFICE NAME AND ADDRESS

Air Force Rocket Propulsion Laboratory
Edwards, California 93523

12. REPORT DATE

September 1975

13. NUMBER OF PAGES

264

14. MONITORING AGENCY NAME & ADDRESS(if different from Controlling Office)

15. SECURITY CLASS. (of this report)

Unclassified

15a. DECLASSIFICATION/DOWNGRADING
SCHEDULE

16. DISTRIBUTION STATEMENT (of this Report)

APPROVED FOR PUBLIC RELEASE DISTRIBUTION UNLIMITED

17. DISTRIBUTION STATEMENT (of the abstract entered in Block 20, if different from Report)

18. SUPPLEMENTARY NOTES

19. KEY WORDS (Continue on reverse side if necessary and identify by block number)

Catalyst
Hydrazine
Monopropellant
Hydrazine Catalyst Engine
Catalyst Breakup

20. ABSTRACT (Continue on reverse side if necessary and identify by block number)

The overall objective of the work in this program is to investigate the
external breakup mechanisms of Shell 405 catalyst so as to establish an
understanding of the phenomenon which can aid in extending catalyst life
in use in monopropellant hydrazine thrusters. The program involves the
joint efforts of Exxon Research and Engineering Company, McDonnell Douglas
Astronautics Company and TRW Inc. The program involves both experimental
and analytical studies of potential catalyst breakup mechanisms.

391338

A number of different mechanisms were identified for study following a review of the literature and other available information. To date fourteen specific mechanisms from the general areas of fluid dynamic erosion, pressure crushing, differential thermal expansion, particle movement, thermal shock and pore pressure gradients have been screened. Major breakup mechanisms or factors identified to date include particle to particle crushing as a result of various static pressure crushing forces, build-up of pressure within the catalyst pore as a result of imbibed liquid hydrazine, the fact that a voided thruster bed has sufficient gas velocity for particle movement, and loss of catalyst physical properties such as crush strength with use. Other significant mechanisms or factors identified include fluid dynamic erosion from a pulsed liquid stream and from particulates in hydrazine and thermal shock during liquid quench cooldown. Five mechanisms or factors were judged not to be significant. Although the program is not completed, the results to date were examined for thruster design implications.

SUMMARY AND CONCLUSIONS

The overall objective of the work in the program is to investigate the external breakup mechanisms of Shell 405 catalyst so as to establish an understanding of the phenomenon which can aid in extending catalyst life in use in monopropellant hydrazine thrusters. The External Catalyst Breakup Phenomena program involves the joint efforts of Exxon Research and Engineering Company (prime contractor) and McDonnell Douglas Astronautics Company and the Systems Group of TRW, Inc. A study of Internal Catalyst Breakup Phenomena is being carried out separately by United Technologies Research Center under a different contract (FO4611-74-C-0031). The overall effort is coordinated by the Air Force with the assistance of a Scientific Advisory Board. The program involves both experimental and analytical studies of potential external catalyst breakup mechanisms. This interim report describes work conducted during the period of June 1974 to April 1975.

A number of different mechanisms were identified for study following a review of the literature and other available information. To date fourteen specific mechanisms from the general areas of fluid dynamic erosion, pressure crushing, differential thermal expansion, particle movement, thermal shock and pore pressure gradients have been screened. Major mechanisms or factors important to catalyst breakup identified to date include:

- Particle to particle crushing as a result of various static pressure forces.

- A voided thruster bed has sufficient gas velocity for particle movement.

- Corroboration of the deleterious effect of the buildup of pressure within the pores as a result of imbibed liquid hydrazine.

- Loss of catalyst physical properties such as crush strength after thruster exposure.

- Erosion by a pulsed liquid stream at high velocity.

- Thermal shock from liquid quench cooldown.

- Erosion resulting from solid particles present in the hydrazine.

Five mechanisms or factors were judged not to be significant as follows:

- Fluid dynamic erosion by a pure gas.

- Fluid dynamic erosion by liquid drops in a gas.

- Pore pressure gradients during rapid pressurization or depressurization (in the absence of liquid).

- Transient effects per se in bed pressure buildup.

- Thermal shock from heating a particle with hot combustion gases.

- 1 -

Although the program has not yet been completed, the results
to date point to a number of variables or factors involved in thruster
operation where operating envelopes possibly could be developed to enhance
catalyst life.

- Gas fluid dynamic erosion per se is not a mechanism of cat-
  alyst breakup, nor can gas velocities be reduced to the
  point where incipient particle movement will not occur in
  a voided bed. However, higher gas velocities result in
  greater static pressure crushing forces on the bottom of
  the bed. In addition, since abrasion by solid particles
  flowing in a gas is strongly dependent on particle velocity,
  higher gas velocities increase the danger from solid particle
  abrasion if the catalyst starts to breakup from another
  mechanism.

- Reduction of the particulate level in the hydrazine used
  below the current spec level could provide an added margin
  of safety regarding possible abrasion losses from solid
  particles flowing in the gas.

- Liquid hydrazine in contact with catalyst particles generates
  a number of potentially deleterious situations. The impact
  of a pulsed, liquid stream can erode the particles. Data
  indicates that this can be controlled to a great extent by
  reducing the liquid velocity. During a cold start contact
  with hydrazine leading to liquid wetting can lead to very
  high internal pressures as a result of the imbibed liquid
  decomposing in-situ to give product gases. A number of
  approaches in this respect could be pursued.

  - Increasing the headspace area above the bed to prevaporize
    the hydrazine as much as possible.

  - Raising the catalyst bed temperature. Although at this time
    the effect of temperature on internal pressure has not
    been defined, qualitatively, higher temperatures should
    reduce liquid penetration and ultimately result in a film
    binding condition which will prevent any actual liquid from
    contacting the catalyst.

  - Smaller catalyst particles should allow easier relief of
    internal pressures. However, other mechanisms are influenced
    by catalyst particle size so that tradeoffs will probably
    be involved in optimizing the catalyst particle size.

Similarly , thermal shock from liquid hydrazine is potentially deleterious, and means to minimize this possibility could include steps such as reducing the catalyst particle size so as to reduce the Biot number or adjusting conditions including catalyst particle temperature to insure that a low heat transfer rate film boiling condition will be present rather than a high heat transfer rate nucleate boiling condition.

● Factors generating pressure forces which could result in particle to particle crushing must be carefully examined.

- Bed preloads would appear to be deleterious

- The possible additive effect of various pressure forces must be avoided. Analytical results indicate that the pressure forces from flowing gases are established very rapidly (in milliseconds) compared with cold start thermal expansion compression effects (max $\triangle V/V$ compression occurs at approximately 0.5 sec after start. Any relaxation of preload forces would presumably occur even later during the dilation portion of the thermal expansion cycle. Thus it would appear possible during the initial cold start that preload forces, the flowing gas $\triangle P$ forces, and the differential thermal expansion compression forces would all occur simultaneously and result in a total force which is additive in a complex manner. This interaction could seriously overstress a bed.

- Pressure crushing forces from differential thermal expansion effects must be carefully considered, such as the possibility that a dilated bed during firing will completely or partially repack itself. The strong effect of bed loading on the magnitude of both the initial compression and final dilation, suggest benefits from reducing this variable.

- Isolating the catalyst particles from one another so as to avoid high particle to particle stresses may have merit.

- Particles from a partially degraded bed could be trapped in the interstices of the lower bed and thus raise the pressure drop across the bed, resulting in further bed compression losses.

- Although the transients per se involved in pressure shocks are not deleterious, the magnitude of this force must be given serious consideration

- The effect of the thr .ter environment on the loss of
  individual catalyst particle crush strength and other
  critical properties must be considered. For example thermal
  cycling fatigue may degrade crush strength leading ultimately
  to bed failure.

- Means to reduce the relatively large scatter in individual
  particle crush strength would eliminate a significant
  fraction of weak particles present in even a fresh catalyst
  bed, and thus have merit. In addition, loss in average
  particle crushing strength and increase in scatter following
  thruster exposure sharply incre..ses the percent of very weak
  particles. Thus this prob'em may b. intensified w'th thruster
  aging.

During the period covered in this report the Task I Phenomenological
Survey studies have been completed and the majority of the Task III analytical
supporting analyses have been completed. In the remaining portion of the
program the planned Task II testing will be carried out along with the
remaining analytical supporting analyses. Experimental work is planned to
continue the study of static pressure crushing and to investigate abrasion
effects in a voided bed. Studies of "pop" shock dynamic pressure crushing,
fatigue effects in cyclic hot gas thermal shock and liquid quench thermal
shock and interactions or synergisms are planned. Catalyst testing work with
used catalyst samples will be conducted in an attempt to determine the effect
of thruster exposure on the ability of Shell 405 to maintain its physical
properties such as crush strength. Analytical studies will include both
parametric studies of existing programs and further development of the
structures analysis programs.

The modeling studies have again pointed out, in general, the need
for the best possible values for Shell 405 material properties. In addition,
these analytical studies identified a particular need for the Poisson ratio,
tensile failure strength and multiaxis compressive failure strength.

- 4 -

PREFACE

This Interim Technical Report describes work carried out under Contract No. F04611-74-C-0032 during the period from the start of the program in June 1974 to April 1975. It was principally written by Dr. W. F. Taylor, Program Manager, Exxon Research and Engineering Company (ER&E) and Mr. W. T. Webber, McDonnell Douglas Astronautics Company (MDAC). The program was administered by Dr. D. Grafstein (ER&E). Contributions were made by the following individuals:

Dr. M. Boudart, Stanford University

Dr. W. D. English, MDAC

Mr. A. R. Carabranr, ER&E

Dr. D. P. H. Hasselman, Lehigh University

Mr. R. J. Hoffman, MDAC

Dr. J. D. Kuenzly, TRW

Mr. M. Lieberman, ER&E

Dr. E. M. Magee, ER&E

Mr. D. D. Quan, MDAC

Mr. R. L. Sackheim, TRW

Mr. S. A. Schechter, MDAC

The project monitor on this program is 1st Lieutenant Steven G. Wax, AFRPL.

TABLE OF CONTENTS

TABLE OF CONTENTS (Cont'd)

LIST OF FIGURES

LIST OF FIGURES (Cont'd)

LIST OF FIGURES (Cont'd)

LIST OF TABLES

1. INTRODUCTION

Monopropellant hydrazine is widely regarded as the established standard for unmanned spacecraft auxiliary propulsion systems. To date, there are over 30 United States flight programs that use hydrazine propulsion systems with Shell 405 catalyst as the means for spontaneously initiating the decomposition reaction. These programs have occurred over the last decade. Even with this experience, it is evident that there is still much that is not understood about the fundamental processes involved in heterogeneous hydrazine catalytic reactors.

The Shell 405 catalyst was developed to satisfy the requirements for a simple, reliable, lightweight, nonpower draining and relatively low cost means of spontaneously decomposing hydrazine. The potential use of hydrazine as a monopropellant was first studied extensively in the USA by JPL during the late 1940's and 1950's. It was found that homogeneous, thermal decomposition of hydrazine proceeded slowly, requiring residence times too large to be practical in most rocket engine applications. Subsequent work evolved several catalysts that could effectively sustain decomposition of liquid hydrazine if the initial reactor bed temperature was maintained in the 600° to 800°F range. For these catalyst systems, however, it was necessary to employ techniques that preheated the bed to initiate and sustain decomposit The complications of using these methods seriously impaired the early acceptance of monopropellant hydrazine for spacecraft propulsion syste... Over the years, efforts were expanded in search for improved spontaneous catalyst with success finally being achieved by the Shell Development Company in what must be considered a true technological breakthrough for that period (1964). The availability of Shell 405 catalyst greatly expanded interest in the application of monopropellant hydrazine propulsion systems, not only because it was a truly spontaneous catalyst, but also because it appeared to be capable of a great many starts.

Coincidentally, the occurrence of the spontaneous catalyst capability was paralleled by a proliferation of unmanned spacecraft missions requiring the use of attitude control and station keeping propulsion systems. The use of Shell 405 catalyst hydrazine systems accelerated, therefore, from the first hurried application in November of 1967 to the number of flight systems in operation at the present time. Because hydrazine thruster technology grew so rapidly, many potential problem areas were bypassed or explored in only enough detail to satisfy specific requirements for a given application. In addition, rapid changes have occurred in thruster performance and life requirements over the last few years. The original specifications for spinning satellites and short-life upper stages required relatively rapid firing rates (on the order of 1 Hz), only a few ambient starts (typically 20 to 50), and only 2,000 to 5,000 pulses. These requirements are simple when compared to the

present needs of three axis stabilized long-life missions that require hundreds of ambient starts (40° to 70°F) and hundreds of thousands of "hot" pulses at varying frequencies. The use of hydrazine thrusters employing Shell 405 catalyst for extended life missions is currently limited by the physical degradation of the catalyst. This program is one part of an extended effort being carried out by AFRPL to improve the life of Shell 405 catalytic hydrazine thrusters.

2. APPROACH

2.1 Objective

The performance of the Shell 405 catalyst deteriorates during
its use for hydrazine decomposition in monopropellant thruster opera-
tion. The overall objective of work under this contract is to investi-
gate external catalyst breakup mechanisms so as to establish an
understanding of this phenomena which can aid in extending catalyst
life during use.

2.2 Program Organization

The External Catalyst Breakup Phenomena program involves the
joint efforts of Exxon Research and Engineering Company (prime contrac-
tor) and McDonnell Douglas Astronautics Company and the Systems Group
of TRW, Inc. A study of Internal Catalyst Breakup Phenomena is being
carried out separately by United Aircraft Research Laboratory under a
different contract (F04611-74-C-0031). The overall effort (i.e., both
internal and external catalyst breakup phenomena work) is coordinated
by the Air Force with the assistance of a Scientific Advisory Board
(SAB). The SAB consists of appropriate Air Force and contractor members
plus the following additional members:

- Mr. S. DeBrock, Lockheed Missiles and Space Corp.
- Mr. M. J. Russi, Aerospace Corp.
- Mr. V. A. Mosely, Bell Aerospace Company
- Dr. J. D. Rockenfeller, Rocket Research Corp.
- Dr. M. Boudart(a), Stanford University
- Dr. D. P. H. Hasselman(a), Lehigh University

Mr. F. S. Forbes, AFRPL, is chairman of the SAB.

The External Catalyst Breakup Phenomena program consists of
three tasks as follows.

Task I - Phenomenological Survey

In Task I a phenomenological survey is to be performed to
identify and describe the more important mechanisms of the external
catalyst breakup process. The objective of this work will be to esta-
blish the foundations for the more extended experimental program in
Task II, and to generate an understanding of the catalyst breakup process.

_ _ _ _ _

(a) Consultant to Exxon Research and Engineering Company.

Three areas of effort will be carried out in Task I. First, a review and analysis of the literature, second, a series of experimental sensitivity tests to screen the breakup hypotheses, and third, a comprehensive assessment of the results of the sensitivity test, literature review and analytical modeling so as to select and rank the breakup mechanisms for additional study in Task II.

Task II - Selected Mechanism Testing

More intensive laboratory testing is to be performed in Task II. This will involve (a) additional investigation of mechanisms or factors which have been shown to be important, and (b) investigation of phenomena occurring in a complex bed environment, rather than just occurring in a single particle. The effect of synergisms or interactions is also to be investigated. Output data involving descriptions of important operating variables is to be generated indicating the level of catalyst degradation to be expected in various regions of catalyst/thruster operation.

Task III - Supporting Analyses

Concurrently with the other tasks, analytical studies are to be conducted to support the experimental activities and also to aid in the assessment of breakup mechanisms by exploring areas not experimentally investigated. The development of a complete catalytic bed design analysis is beyond the scope of this program. However, governing equations and analytical descriptions of phenomena expected during catalyst breakup in simplified situations, are to be developed so at to generate an understanding of driving mechanisms that will form a basis for such a design analysis mode. This work is to provide an assessment of the important factors involved in catalyst fracture.

Task I and Task II efforts are to be carried out in sequence, and primarily will involve work by Exxon Research and TRW. Task III is to be carried out concurrently with Tasks I and II and involves work by McDonnell Douglas Astronautics.

This report is an interim technical report describing work completed in the period of June 1974 to March 1975, and includes the completed Task I effort and the parts of Task III effort carried out in this time frame.

3. TASK I - PHENOMENOLOGICAL SURVEY

3.1 Literature Search

A literature search relative to catalyst breakup phenomena was made. The search included a review of both government and non-government pertinent literature and was primarily based on:

- Lockheed Information Retrieval Service

- APILIT National Retrieval Service

- Reports and Abstracts Furnished by TRW.

The literature was reviewed to examine the available information on possible mechanisms which may contribute to the degradation of Shell 405 hydrazine monopropellant catalytic engines. These encompass both internal (within catalyst particles) and external (particle to particle) phenomena. The results, presented below, include information derived from hydrazine monopropellant engine studies and from other studies which are relevant to the catalyst degradation problem.

3.1.1 Internal Phenomena

3.1.1.1 Reduced Catalyst Internal Porosity

The internal porosity of a catalyst pellet can affect the magnitude of the temperatures and pressures built up during reaction, which in turn, can produce stresses and strains that exceed the tolerable limits of the catalyst structure. This is particularly true if the reaction taking place within the catalyst is exothermic. Prater (47) has shown that significantly higher temperatures can occur inside a catalyst particle relative to the surface bulk fluid temperature during an exothermic reaction. Kesten (32) has applied the Prater equation to the development of a specific model for hydrazine decomposition in Shell 405. The temperature and pressure gradients predicted by these analyses can cause considerable internal stresses within the catalyst structure. Furthermore, extensive thermal and pressure gradients resulting from pore transport limitations during start-up may be considerably higher. This was shown to be the case in studies conducted by Lee, et al (34) on the stability of exothermic reactions in catalysts with transport limitations.

Reductions in total pore volume and changes in pore volume distribution can impede the transfer of heat and pressure generated in the catalyst interstices. Several references can be found to show how exposure of supported catalysts to elevated temperature causes deleterious changes in available micropore volume and pore distribution.

- 19 -

For example, studies by Levy (35) Shachner (60) and Benesi, (3) show
how commercial alumina pellets exposed to high temperatures, undergo
a large reduction in number of micropores along with reductions in
surface area. Sintering is seen to convert several small pores into
fewer larger ones such that the total pore volume is relatively unchanged.
Such changes have been shown to increase the overall density of the
catalyst particle, cause blockage of available active sites and result in
increased thermal and pressure stresses.

Sayer and Southern (75) suggest that the rapid decrease
observed in the surface area of a CNESRO-1 hydrazine catalyst substrate
at temperatures in excess of 1000°C was due to a phase change from the
gamma alumina to the alpha alumina. However, even if such is the case,
the CNESRO-1 catalyst is based on a γ-alumina which is prepared from
aluminum monohydrate (boehmite) while the γ-alumina used for Shell 405
support is prepared from alpha aluminum trihydrate (gibbsite). Their
results are thus not directly applicable to the behavior of Shell 405
at elevated temperature but are nevertheless of interest to the pres-
ent problem.

Papmahl and Rose (86) have shown, by microscopic examination
how catalyst pores could be clogged with fines formed when portions of
the catalyst pellets are crushed or attrited. Such possible clogging
of internal catalyst pores could contribute to increased pressure
build-up within the Shell 405 catalyst and subsequent accelerated
catalyst failure.

In addition, it has been shown that exposure of a supported metal
catalyst to rapid and high temperature changes can cause extensive
migration and growth of metal crystallites such that micropore blockage
can occur. The work of Ruchenstein and Petty (53) has shown this to
be the case for alumina supported platinum catalysts. Localized high
temperatures, achieved in a catalyst pellet at crystallite sites, were
found to cause growth and agglomeration of platinum crystallites. In
some cases the transient temperature spikes were believed to cause
possible detachment of clusters of crystallites. These processes could
be even more severe in a catalyst such as Shell 405 which has an extensive
amount ($\sim$ 30 wt. %) of dispersed metal (iridiu-) throughout the catalyst
structure.

3.1.1.2 Presence of Adsorbed Species

The literature contains numerous references showing how the
adsorption of certain molecular species, present in the reactive system,
can interfere with reaction rates and reduce the activity of heterogeneous
catalyzed systems. In most cases, loss of catalyst activity for the
intended reaction occurs because active catalyst sites are permanently
or temporarily occuppied by adsorbed species, thus rendering them
unavailable for the intended reaction. However, in certain specific

cases, the adsorbed species can itself participate in processes which destroy the catalyst structure. The classic example of this phenomenon is the adsorption of H_2O on alumina substrates at high temperatures. The adsorbed H_2O is seen to catalyze transformations that rapidly reduces the substrate surface area and micropore volume (35)(55).

Adsorption related processes can have deleterious effects on the performance of Shell 405. Kesten (3) has reported that exposure of Shell 405 catalyst to cold, high pressure decomposition products can result in the adsorption of H_2 and NH_3. The adsorption of these gases was seen as reducing the start-up activity of the catalyst and contributing to large particle pressure build-up. Pressure build-up within the particle pores results from the interaction of temporary lost catalyst activity (from adsorption of NH_3 and H_2) and liquid hydrazine flooding of catalyst pores. This is considered more fully in the paragraphs discussing blockage of outer pores by liquid hydrazine. Studies by Sayer (59) and Wood and Bryant (71) also support the theory of considerable ammonia and hydrogen adsorption on Shell 405 with subsequent loss of available activity for low temperature starts. Their work also supported the observations that the adsorption was reversible and that once the catalyst temperature was elevated, desorption of NH_3 and H_2 would take place. However, cumulative physical adsorption of reaction products could conceivably reduce catalyst activity to a point where low temperature starts would no longer be possible.

More severe deleterious adsorption effects with Shell 405 can occur with chemical species such as halogens, oxygen and H_2O. McCullough (37) has shown that traces of Cl_2 in the hydrazine reactor system could cause permanent loss of catalyst activity. Chlorine is believed to react with iridium metal to form a volatile product $IrCl_3$ whereby active metal sizes are completely lost from the catalyst structure. This same mechanism has been shown to be operable in the loss of activity of alumina supported platinum catalyst, used in reforming reactions in the petroleum industry (41). Cl_2 can result from the presence of trace quantities of halogenated solvents such as freons and perchloro ethylene used to clean hydrazine thruster hardware components (37).

In a similar fashion, oxygen can react with iridium metals under certain conditions resulting in conversion to volatile IrO_3 and IrO_2. This process can result in both loss of iridium metal from the catalyst structure and iridium crystallite growth both resulting in reduced hydrazine decomposition activity. This mechanism has been shown to be responsible for the loss of supported iridium-ruthenium catalyst activity in automobile catalytic converters, as well as other high temperature applications (38).

As indicated in previous paragraphs, the adsorption of water on alumina surfaces has been found to rapidly accelerate high temperature sintering. Shell 405 utilizes a gamma-alumina substrate as a support for metallic iridium crystallites and would be expected to be susceptible to this deleterious phenomenon. This has been confirmed in Shell 405 life test studies conducted by Boge (67). Rapid loss in catalyst area was found to take place when sintering occurred in a nitrogen atmosphere containing water vapor. Effects of trace water may have similar though lower magnitude effects.

Trace water vapor may enter the hydrazine thruster system by adsorption on the Shell 405 catalyst surface during preparation, from contamination in the hydrazine itself, or by chemical reaction. Brooks (5) has reported that water vapor can be formed by the reaction of adsorbed O_2 with IrH under conditions were chemisorbed hydrogen (formed during reduction of the catalyst during preparation or in subsequent hydrazine decomposition) is left on the catalyst surface. These sources of water could contribute to degradation of Shell 405 catalyst surface area and activity by the above mechanism.

Carlson (80) has conducted experimental investigations relating the low temperature, high vacuum, hydrazine ignition properties of Shell 405 catalyst to the concentration of adsorbed gas species including O_2, N_2, H_2 and NH_3 present on the catalyst surface. The results of the study indicated that hydrogen could be adsorbed on Shell 405 under high vacuum conditions if the reactor is cooled rapidly. However, no conclusion was reached about any adverse affect of adsorbed hydrogen on ignition delay and catalyst degradation phenomena.

Smith and Solomon (89) relate the catalyst attrition mechanism in hydrazine engines to the irreversible, dissociative adsorption of hydrazine on catalyst sites at temperatures below 450°K.

Paranskii et al (88) has shown that the mechanical strength of promoted alumina catalysts and resistance to abrasion of catalyst particles was reduced by the adsorption of water and hydrocarbons on the catalyst surface. Similar effects may be possible from the adsorption of reaction products or hydrazine contaminants during the firing of hydrazine monopropellant thrusters.

Thus, the adsorption processes discussed above can all contribute to loss in special catalyst activity. This loss in activity in turn can contribute to severe internal particle pressure build-up and subsequent fracture by interaction with the liquid hydrazine blockage of pores discussed below.

3.1.1.3 Blockage of Catalyst External
Pores by Liquid Hydrazine

Kesten (30) has proposed a mechanism whereby the wetting of
liquid hydrazine on the outside of porous Shell 405 catalyst particles
can prevent decomposition gases from escaping the structure, thus causing
severe internal build-up of pressures. Liquid hydrazine is seen as entering
the pores by capillary action and requiring very high gas pressures
for expulsion. Where non-uniform hydrazine wetting occurs, severe
pressure gradients can exist within the particle structure. Motion
picture studies of hydrazine decomposition in a single particle by Sangiovanni
and Kesten (58) have supported this theory; so have mathematical analyses
conducted by the same authors (57).

The interaction of this mechanism with loss of catalyst specific
activity (produced by adsorption or diffusional phenomena discussed
above) can be great; particularly in transient conditions. Lowered
catalyst activity would permit further penetration of the liquid hydrazine
into the catalyst structure, requiring greater internal pressures for
explusion. Further, if the reduction in catalyst activity due to adsorption
were not uniform, larger thermal gradients would be expected. These
effects would be expected to be particularly pronounced during pulse mode
operation, where catalyst particles would be repeatedly subjected to
cyclic exposure to cold hydrazine and hot decomposition gases.

These effects are supported by the work of Lee (34) who studied
the stability of several exothermic reactions in catalyst particles with
external transport limitations. It has also been observed to occur in a
number of liquid phase heterogeneous catalytic industrial operations.

Moynihan and Bjorklund (82) have estimated the internal
pore pressures in Shell 405 resulting from hydrazine adsorption and
decomposition to be of the order of 2000 psi. These high pressures combined
with large thermal gradients, were believed to be responsible for catalyst
breakup in their 1 lbf. test thrusters.

Greer (84) has studied the low temperature (40°F) start
characteristics of hydrazine monopropellant engines using high speed photography
and a plexiglass reactor. He concluded that catalyst attrition was primarily
caused by high pressures generated within the catalyst rather than from
large chamber pressure spikes.

On the other hand, Basmadjian's (87) theoretical analysis of
pressures arising in both the macropore and micropore networks of
catalyst pellets during the rapid venting of high pressure, fixed bed reactors
leads to the conclusion that rapid pressure release should not result
in damage to the pellets since the pressure in the pellet closely
approaches that of the reactor void space. However, Basmadjians analysis
does not consider gas generation by chemical reaction in the micropores
and its applicability to the hydrazine thruster situation is limited.

3.1.1.4 Thermal Stress Fracture

In addition to the phenomena discussed above, the catalyst breakup model includes the effects of thermal stress fracture as a process which itself can contribute to catalyst particles. From this standpoint, it is useful to consider the basic composition of the Shell 405 catalyst from a strength of materials, structural, point of view. Shell 405 consists of a composite structural system of a continuous (though porous) phase of gamma alumina with large amounts of iridium (≈ 30 wt. %) metal located in the pore interstices. Physical properties of these materials are compared in Table 3-1. Alumina is a refractory oxide having a very low thermal conductivity. Iridium is a metal having a high thermal conductivity.

<u>Table 3-1</u>

<u>Physical Properties of Iridium and Sintered Alumina</u>

Property	Iridium	Sintered Alumina
Thermal Conductivity cals/cm-sec	.36	.02-.01
Linear Coefficient of thermal expansion in/in/°F	6.5×10^{-6}	3.9×10^{-6}
Compressive Strength, psi		4×10^{5}
Tensile strength, psi	3.2×10^{3}	4×10^{4}
Youngs modulus, psi	6×10^{5}	5×10^{7}

Though the linear thermal coefficients of expansion are not too dissimilar, significant local thermal stresses, resulting from temperature differences at the iridium alumina boundaries during start-up conditions, would be expected. This is due to the fact that the local heat fluxes produced at the catalyst active sites would be transferred more rapidly into the much more thermally conductive iridium than to the alumina. Furthermore, during pulse mode operation, metal active sites would tend to be surrounded

by hot decomposition gases, while exterior alumina pore walls would tend
to be in contact with the cold, liquid hydrazine feed. This would further
enhance transient differential thermal stresses. Large transient local
temperature gradients at metal active sites, in porous alumina substrates,
have been predicted by the work of Ruchenstein and Petty (53).

In this connection, it should be acknowledged that the analyses of
Prater (47) and Kesten (31) (which predict much lower temperature gradients
for exothermic reactions occurring within catalyst particles) are steady-
state treatments and do not take into consideration local transient
conditions. Ruchenstein and Petty's work (53) show that transient
phenomena, such as the propagation velocity of the heat flux, must be
taken into account to accurately describe the temperature fields inside
a catalyst particle.

In a recent paper, Russi (77) points out that differential
thermal expansion was not an important factor in the degradation of
Shell 405. However, his conclusions were based on heating catalysts
to 1800°F in a quartz cylinder and measuring bed volume shrinkage. The
problem of differential thermal expansion and thermal stresses developed
within the catalyst particles during the rapid (mil sec) temperature
change during start-up was not, however, addressed.

3.1.1.5 Catalyst Contamination

The present MIL-SPEC (MIL-P-26536C, Amendment 1) for monopropellant
hydrazine controls a large number of potential contaminants, namely:

Contaminant	Max Allowed (% by Wt)
Water	1.0
Chloride	0.0005
Aniline	0.50
Iron	0.002
Non-Volatile Residue	0.005
Carbon Dioxide	0.02
Other Volatile Carbonaceous Material	0.02

The required hydrazine purity must be at least 98.5 percent by weight,
There is also a particulate limit of 1 milligram/liter.

Several of the above contaminants can potentially interfere
with the hydrazine decomposition reaction. However, no conclusive results
are presently available as to the deleterious role of specific contaminants.
A process has been developed to purify propellant grade hydrazine as
part of the current Mars Lander Program. However, no specific evidence
is available which would indicate that use of such a propellant would
extend the service life of Shell 405 catalyst.

Christopher and Russell (81) have also studied the effects
of adsorbed hydrazine contaminants on catalyst life. Basically, they
found that the low volatile metal contaminants such as iron, chromium
and zinc appear to deposit on the catalyst, filling the interstitial
spaces around the catalyst grains and/or forming a coating over the
surface of individual particles. This second mode of deposition may
result in reduced catalyst activity and degradation in bed performance.

Chloride contamination of hydrazine, results in formation of
ammonium chloride. This compound has a relatively high vapor pressure
at the reactor operating temperatures and is not believed to reduce
catalyst performance per se (though condensation of NH_4Cl at the orifice
of a test flow reactor has caused orifice clogging).

Marked degradation on catalyst performance, due to the
presence of MMH and water in combination was believed to have been a
result of carbon monoxide adsorption. However, this has not been firmly
established. The authors conclude that further work on the effects
of hydrazine contaminants on catalyst degradation is required to more
fully understand their role.

Barclay (83) reports that Shell 405 catalyst can be deactivated
by large quantities of UDMH. This contamination results in the formation
of carbon which deposits on the catalyst surface. However, his tests
require further work to fully assess the problem of carbon deposition.

Fredrickson (72) reported observing the performance degradation
of Shell 405 in two lbf. engines subjected to 86,000 firings of static
tests. Though the propellant used in the test program was found to be
contaminated with about 1% UDMH, no conclusions were presented as to
any adverse effect of the contaminants upon the catalyst.

3.1.2 External Phenomena

3.1.2.1 Poor Fuel Distribution - Bed "Drilling," Hydrazine Puddling

Poor fuel distribution can result from the above catalyst particle degradation sources which in turn lead to uneven pressure drop through-out the bed. Local formation of voids in one part of the bed, and blocking by fines in another, lead to maldistribution of the fuel, which in turn leads to uneven distribution of pressure and stresses in the catalyst beds. This phenomenon has been shown to contribute to catalyst bed degradation in several studies. In addition, Kesten (33) has shown that non-uniform distribution of hydrazine in catalyst beds can produce high temperature gradients under steady state conditions. More severe thermal gradients can result from poor fuel distribution during transient (start-up) conditions in highly exothermic reaction systems. This was shown by the work of Ruchenstein and Petty (53) and Lee (34).

The concept of local hydrazine "puddling" would contribute to high temperature and pressure gradients during start-up. In this concept, liquid hydrazine is seen accumulating in catalyst bed pockets where specific activity has been impaired (by any of the above discussed mechanisms). When the catalyst temperature is sufficiently elevated to activate these bed pockets, excess hydrazine is available and transient surges in pressure and temperature (pressure and temperature shocks) occur which are frequently above bed steady state conditions. Further-more, the fact that temperature and pressure increases (spiking) occur very rapidly (msecs) means that the catalyst particles are subjected to severe impact loads which intensifies the bed breakdown process.

3.1.2.2 Bed Channeling, Churning and Settling

These phenomena are largely a function of catalyst particle break-down which leads to loss of material and creation of a "loose" bed. In-house studies at Exxon have shown how local fluid flow eddies can produce a "churning" action leading to increased particle to particle abrasion. The settling of small catalyst fragments ("fines") in the interstices of the bed have been observed to cause the channeling of reactants in a number of fixed bed catalytic systems. It is particularly important for systems operating under high pressures and high gas velocities.

Fredrickson (72) reported on the performance of two 5 lbf. engines subjected to 86,000 static firings. Engine degradation was indicated by excessive chamber pressure oscillations, and depressed pressure pulse shape. Post test observations revealed that 80% and 50% of the upper bed catalyst was lost from the two engines respectively. Failure was attributed to inadequate catalyst bed retention, which in turn could cause bed churning and catalyst attrition.

Fredrickson (74) reported that the loss in thrust of an S/N 002 monopropellant hydrazine thrust engine developed by Marqurdt was apparently caused by the formation of excessive fines which decreased catalyst bed porosity. However, no conclusions are presented as to the actual formation of the fines during the testing.

3.1.2.3 Bed Erosion

Erosion of the Shell 405 catalyst bed by high velocity liquid or gaseous hydrazine is also considered to be a possible source of Shell 405 degradation.

However, preliminary high pressure gas attrition tests at Aerospace by King et al. (78) and at Rocket Research (79) indicate that this may have only a secondary contribution to the overall catalyst degradation mechanism.

3.1.3 Other Factors

Other possible phenomena that could contribute to the degradation process, include:

- Catalyst preparation history
- Crystal structure
- Particle geometry

All can effect and interact with most of the above mechanisms as indicated below.

3.1.3.1 Catalyst Preparation History

Clearly, the way in which the catalyst is prepared and the quality control over the preparation processes can be most important. Incomplete removal of halides could result in iridium crystallite growth and migration as well as loss through volatilization; incomplete removal of H_2O can result in accelerated alumina substrate desurfacing as well as destruction of the micropore structure; incomplete catalyst reduction to impaired activity for start-up. In addition, improper pre-attrition techniques can result in producing residual stresses in the final material which could act as built in latent sources of mechanical failure. A few examples cited in the literature illustrate some of the catalyst preparation.

Neuton (73) et al reports that pre-attrition of Shell 405 catalyst at the 90% level appeared to improve the cold start stability of the catalyst and recommended further evaluation of the technique. Pre-attrition is believed to remove the weak or stressed, portions of catalyst particles prior to firing.

Traina and Pernicone (85) have shown that the strength of
alumina supported catalysts, as well as other catalytic properties, were
very dependent on the methods of preparation of the catalyst including
thermal treatments such as drying and calcination and forming treatments
such as grinding, extrusion and tableting, etc.

3.1.3.2 Crystal Structure

With regard to crystal structure, possible alumina substrate
phase changes during operation could weaken the basic catalyst structure.
However, in this connection, most of the references reviewed in this
preliminary literature study indicate that gamma alumina undergoes a
transformation to the alpha phase via a theta phase (54,55). Trans-
formation of the basic Shell 405 substrate gamma alumina to the alpha
phase can occur rapidly in the presence of certain contaminants (such
as H_2O, halides and alkaline earth metals).

3.1.3.3 Particle Geometry

The effect of catalyst particle geometry on its structural
stability has also been shown to be important. Paranski et al (45)
has described how particles of nearly spherical geometry tend to
resist fracture from abrasion and other external forces better than
granules which are irregular and have a high "aspect ratio" (large
l/r). Similar dependence of the susceptibility of fracture to
size and shape are predicted by the work of Chaplin (11) who analyzed
fundamental stress-strain patterns in granular material.

3.2 Sensitivity Testing

As a result of the literature search and other considerations,
a number of areas were chosen for experimental or analytical investiga-
tion or both. These areas and their method of investigation are shown
in Table 3-3. Experimental results are described in this section of the
report. Analytical model results are described in Section 4. Work was
carried out in the areas of:

- Gas Fluid Dynamic Erosion

- Particle Static Pressure Crushing

- Bed Static Pressure Crushing

- Particle Fluidization

- Liquid Fluid Dynamic Erosion

Table 3-3

Interaction Summary for Experimental and Analytical Modeling Work

General Area	Specific Mechanism	Apparatus Used in Experimental Work	Analytical Modeling Work Area
Fluid Dynamic Erosion	Pure Gas per se	HSGET	Fluid Erosion
	Liquid Droplets in Gas	--	Fluid Erosion
	Pulsed Liquid Streams	PLPET	--
	Solid Particles in Gas	--	Fluid Dynamic Erosion
Pressure Crushing	Static Individual Particle	ITI	Stress Failure From Compression Stress
	Static Bed	PCMB/ITI	Failure from Compression
	Dynamic - Normal Transient Pressure Buildup	--	Pressure Shock
	Dynamic - "Pop" Shock	CBPST*	Pressure Shock
Differential Thermal Expansion	Compressive Crushing During Heating	--	Differential Expansion
	Compressive Crushing During Cooldown	--	Differential Expansion
Particle Movement	Incipient Movement Velocity	Modified ILBET	--
	Abrasion in "Fluidized" Bed	Modified ILBET*	--
Thermal Shock	Hot Gas Heat-Up	CBTPT*	Stress Failure From Thermal Shock
	Liquid Quench of Hot Bed	CBTPT*	Stress Failure From Thermal Shock
Internal Pore Pressure Gradients	Rapid External Pressurization or Depressurization	--	Stress Failure From External Pressure Changes
	Pore Pressure Build-Up as a Result of Imbibed Liquid	--	Internal Particle Model

* Experimental work not yet completed.

3.2.1 Sensitivity Testing in the
Gas Fluid Dynamic Erosion Area

The effect of gas fluid dynamic erosion was evaluated using single catalyst particles. This work was done using the High Severity Gas Erosion Tester (HSGET) shown in Figure 3-1. The unit consists of a Hevi-Duty oven with three separate temperature controlled furnaces. The first two sections serve as a pre-heater for the flowing gas. The specimens are held in the third zone. Nitrogen was used as the flowing gas. Individual particles and pellets were held in specially constructed holder assemblies fabricated from 325 mesh type 304 stainless steel screen (see Figures 3-2 and 3-3). Individual particles were photomicrographed, vacuum dried overnight and weighed both before and after exposure to hot flowing gas in the HSGET apparatus. Five replicate samples were used in each run. Total exposure to nitrogen at 1700°F in the HSGET, which is preheated to operating temperatures, was one hour. Variables investigated included superficial gas velocity and catalyst selection parameters.

Tests were conducted at 50, 110 and 250 feet per second superficial gas velocity. All standard sizes of fresh Shell 405 catalyst were tested at 250 feet per second; the 1/8" cylinders, 14 to 18 mesh granules and 25 to 30 mesh granules were also tested at lower velocities. Five replicate runs with individual particles were made in each case. Detailed data is shown in the Appendix. In Table 3-4 is shown the average absolute weight loss for each test and in Table 3-5 the same results are reported on an average percent weight loss basis. Standard deviations calculated from the replicate data on a percentage change in weight basis are also shown in the Appendix Photomicrographs of representative particles (two out of five) for each catalyst size before and after exposure to the hot flowing gas at 250 feet per second are shown in Figures 3-4 to 3-9.

An examination of the weight data indicates that none of the granular Shell 405 gas erosion tests showed a statistically significant average percentage weight loss at any of the gas velocities employed. This was corroborated by an examination of photomicrographs of particles before and after exposure to hot flowing gas, which did not indicate any obvious change in particle morphology. In contrast, the 1/8" x 1/8" cylindrical pellets exhibited a statistically significant (t-test at the 95% confidence limit) average percentage weight loss at all the gas velocities employed. The overall average weight loss with the cylinders was 3.1%. The differences in the weight losses at the different gas velocities was not statistically significant at the 95% confidence level (t-test).

A statistical Analysis of Variance was also performed on results from gas fluid dynamic erosion tests. The calculations were performed using the IBM three star analysis of variance (ANOVA) program.

Figure 3-1

High Severity Gas Erosion Tester (HSGET)
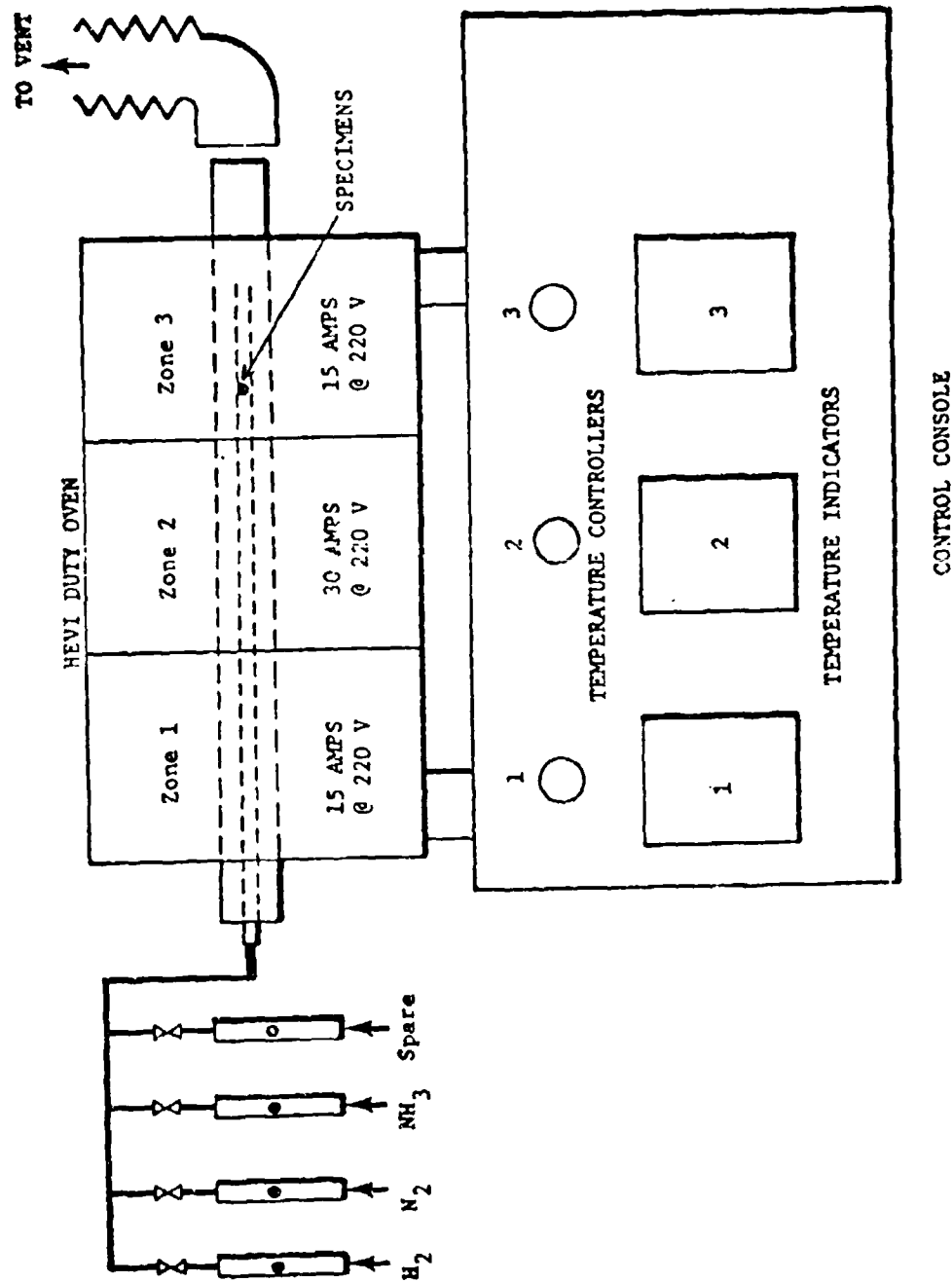
ROCKET PROJECTILE Envelope Assembly

Lower Assembly with Support Tube

Rocket Assembly Superimposed on
Lower Assembly
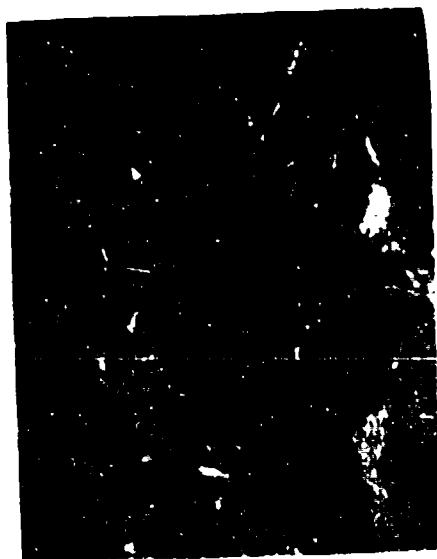
Rear View—Folded Envelope

Side View—Folded Envelope
Enclosing Particle

Figure 3-3

HSGET Cylindrical Pellet Holder Assembly

1/8" x 1/8" Pellet in Assembly String
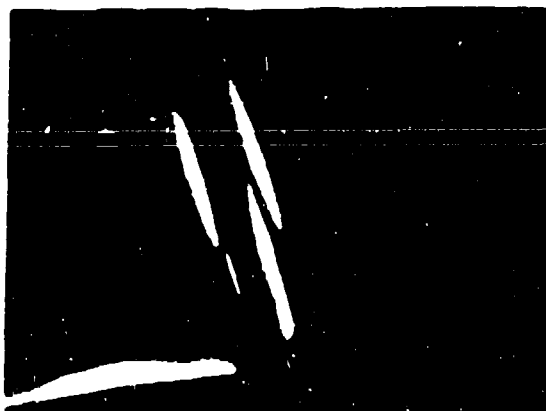
Nichrome Holder Wire

Assembly with 1/8" x 1/8" Pellet

Table 3-4

Summary of Sensitivity Tests in the Gas Fluid Dynamic Erosion Tester

Average Weight Loss in 10^{-5} Grams (a)

Fresh Shell 405 Catalyst Size	Superficial Gas Velocity, feet per second		
	50	110	250
1/8" x 1/8" cylinders	166	137	160
8-12 Mesh	-	--	19
14-18 Mesh	-	0	1
20-25 Mesh	-	-	0
25-30 Mesh	0	0	0
20-30 Mesh	-	-	0

(a) Total weight loss for all specimens in each category divided by the number of specimens. Weight loss after exposure to flowing nitrogen at 1700°F for one hour.

Table 3-5

Summary of Sensitivity Tests in the Gas Fluid Dynamic Erosion Area

Fresh Shell 405 Catalyst Size	Average Percent Weight Loss		
	Superficial Gas Velocity, feet per second		
	50	110	250
1/8" x 1/8" Cylinders	3.28	2.68	3.22
8-12 Mesh	-	-	1.04
14-18 Mesh	-	0	0
20-25 Mesh	-	-	0
25-30 Mesh	0	0	0
20-30 Mesh	-	-	0

● Weight loss after exposure to flowing nitrogen at 1700°F for one hour.
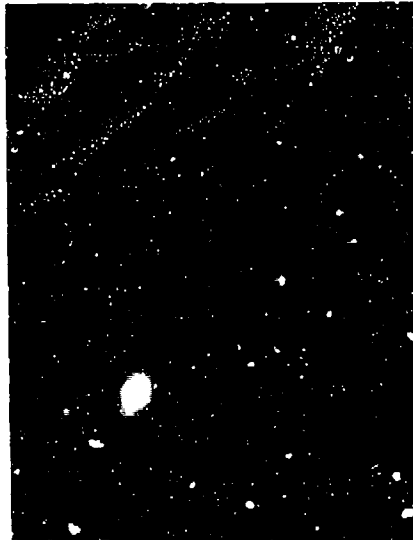
Pallet 1 - Before
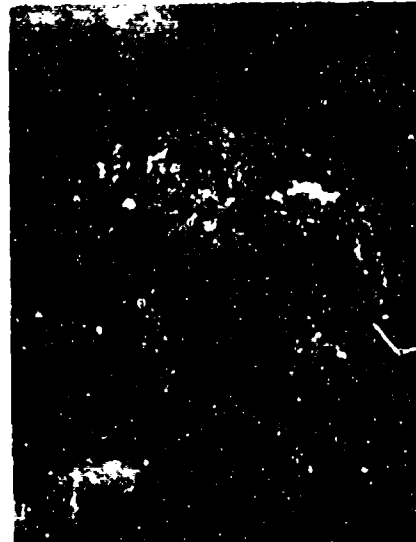
Pellet 1 - After

Pellet 2 - Before

Pallet 2 - After

Figure 3.

... ...
Me... ... ...feet/second
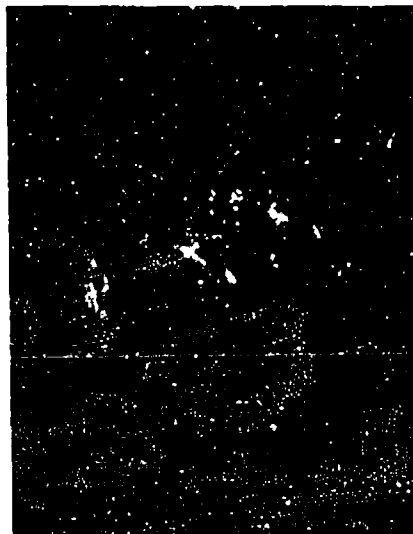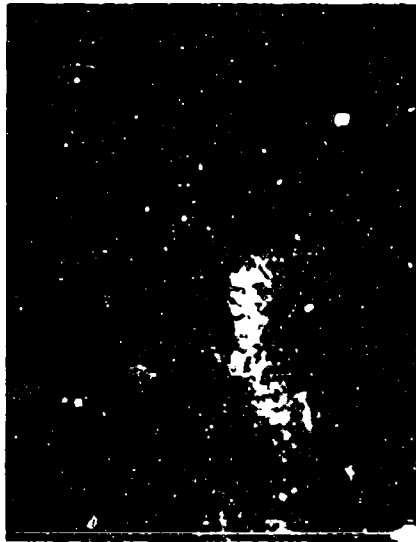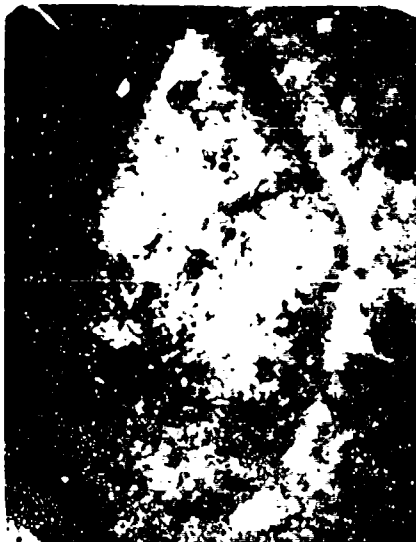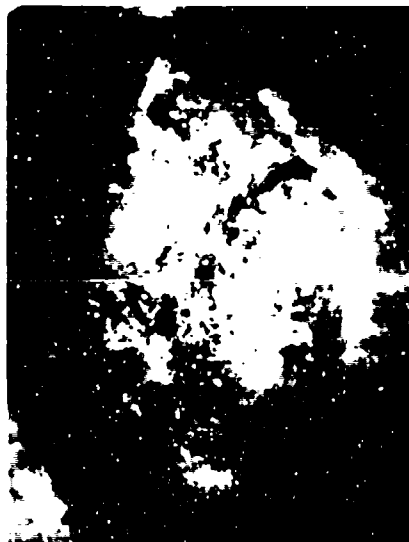
Figure 3-6

Gas Erosion Test: Fresh Shell 405, 14 to 18 Mesh
Particles at 250 feet/second
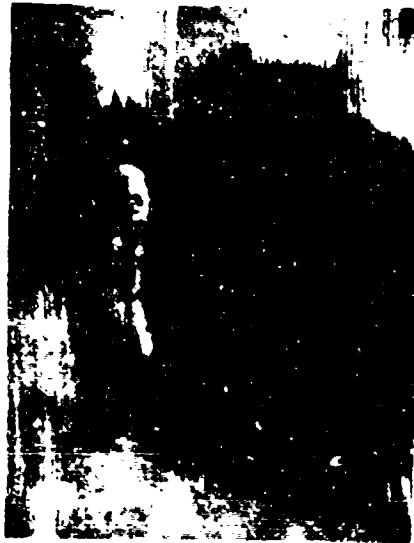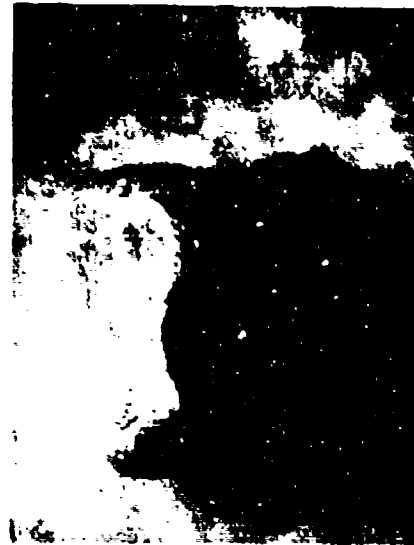
Particle 1 - Before

Particle 1 - After

Particle 2 - Before

Particle 2 - After

Figure 2-7

Gas Erosion Test: Fresh Shell 405, 20 to 25 Mesh
Particles at 250 feet/second
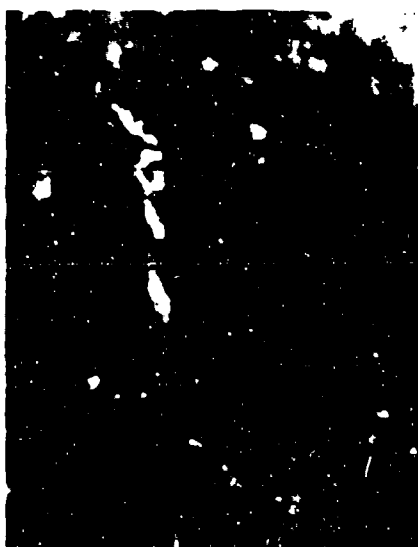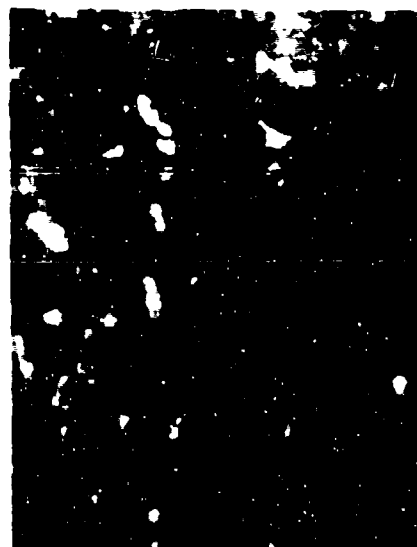
Particle 1 - Before

Particle 1 - After

Particle 3 - Before

Particle 3 - After

Particle 1 - Before

Particle 1 - After

Particle 4 - Before

Particle 4 - After

Figure 3-9

Gas Erosion Test: Fresh Shell 405, 2? to 30 Mesh
Particles at 250 feet/second
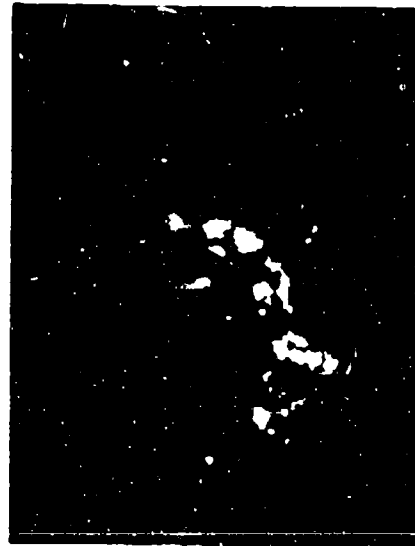
Particle 1 - Before
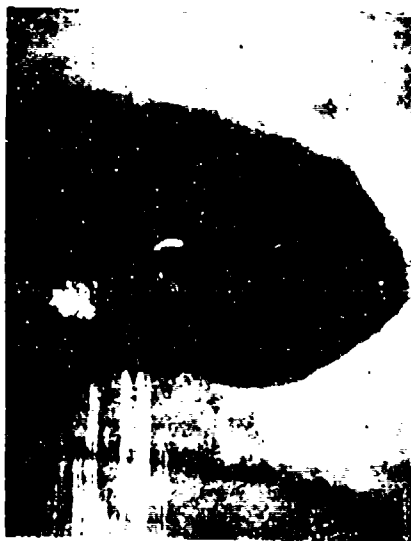
Particle 1 - After

Particle 2 - Before
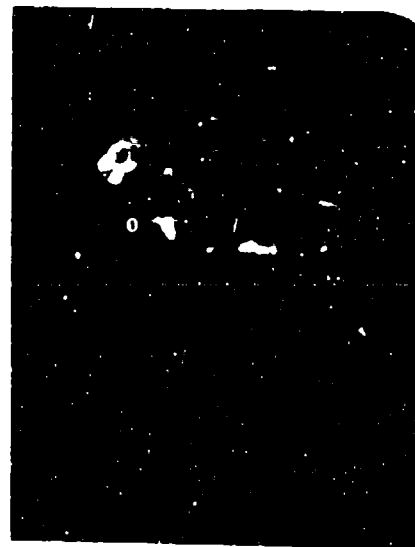
Particle 2 - After

The input data and results are shown in the Appendix. The row variables
tested were 1/8" pellets versus 25-30 mesh particles and the column
variable tested was superficial velocity at three levels for the two
catalyst sizes. Five replicates at each condition was included. F-
tests on the mean squares using the replicate sum of squares results
for the denominator term indicates that only the row effect is signifi-
cant at better than the 95% confidence level. Other factors and
interactions were not significant using this criteria. This analysis
agrees with the previous conclusion based on t-tests of the individual
sets of data that the 1/8" pellets exhibited a significant weight loss
whereas the granular material did not and that this weight loss did not
vary significantly with gas velocity.

Although it is not clear why only the cylindrical pellets
exhibited a weight loss, it is interesting to speculate on possible
causes. The granular Shell 405 catalyst is smaller in size than the
1/8" x 1/8" cylinders and has a "rounded" geometry resulting from the
attrition procedure. The granules are also prepared from a different
alumina source than the cylinders. Thus, the weight loss may not be
the result of gas erosion per se, but simply reflect a loss of volatile
material peculiar to the cylindrical catalyst as a result of heating to
1700°F in nitrogen. This volatile loss would involve a non-water materi-
al as the pellets are adjusted to a common water level before weighting
both before and after exposure to hot flowing gas. Many commercial
pelletized catalysts exhibit a weight loss upon heating to temperatures
in the range of 1700°F (91). The fact that the weight loss did not vary
with gas velocity over the range of 50 to 250 feet per second would tend
to corroborate this interpretation. It is also possible that this dif-
ference resulted from the geometry of the pellets and particles them-
selves. In the HSGET test with the cylindrical pellets, the flowing gas
impinged on the face of the cylinder, rather than on its side. This
suggests the possibility that the cylindrical pellets experienced some
erosion as a result of the formation of a turbulent wake, which did not
develop to the same extent with the more streamlined, smaller granular
particles.

Most important, however, is the fact that the granular Shell
405 catalysts did not exhibit any significant weight loss even after
exposure to gas velocities as high as 250 feet per second for one hour.
These results indicate that gas fluid dynamic erosion per se is not a
major contributor to the degradation of individual catalyst particles.

3.2.2 Sensitivity Testing in the Particle
Static Pressure Crushing Area

Particle pressure crushing studies were carried out in the
Instron Testing Instrument (ITI) shown in a schematic form in Figure 10.
Individual catalyst particles were tested in the ITI on an as-is-basis
so as not to alter their characteristics. Results, thus, are to be

Figure 10

Instron Testing Instrument (ITI)
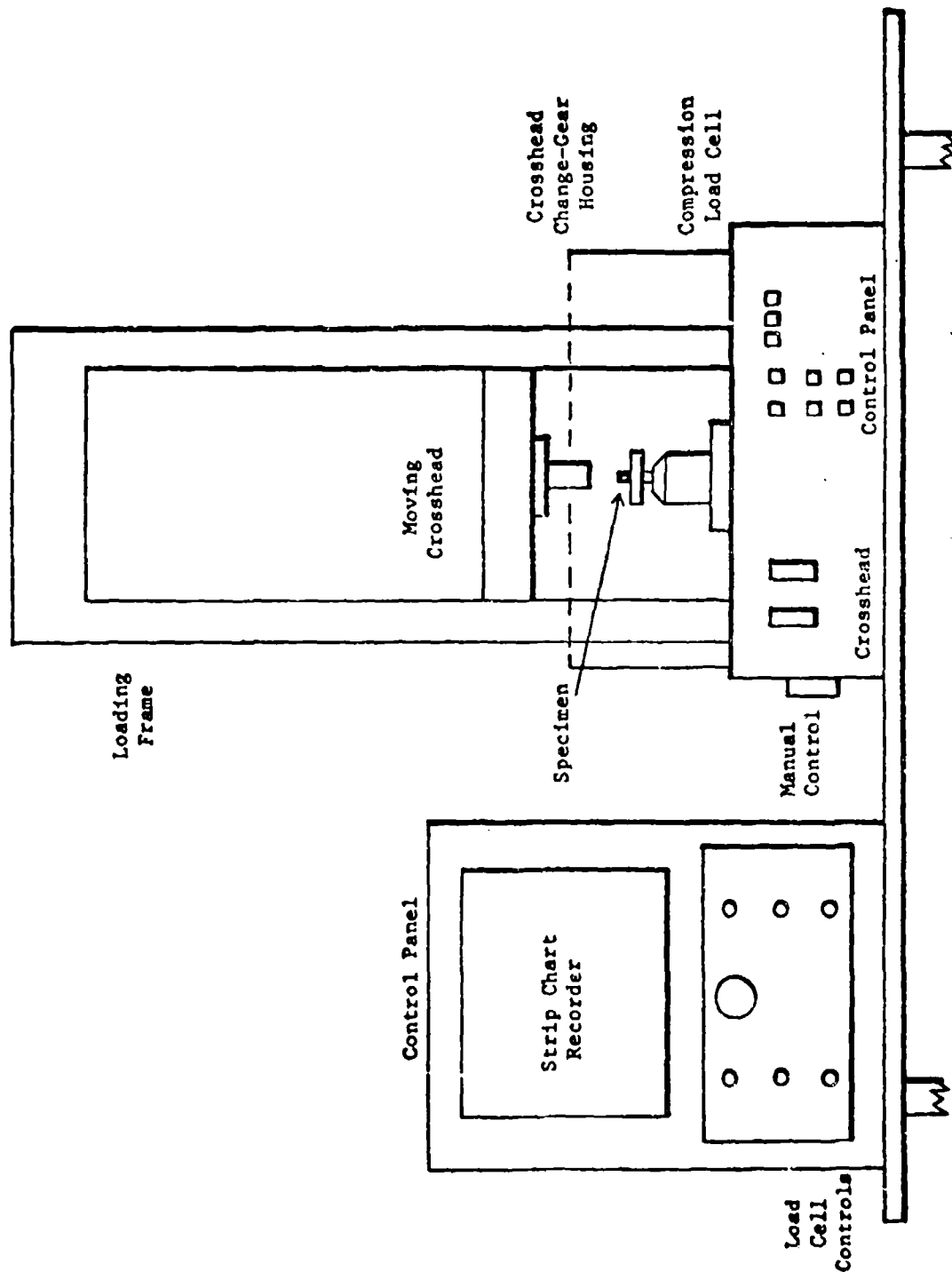
considered as a crushing strength rather than a compressive strength
and have merit on a relative rather than an absolute basis. This is
particularly true of the granular mesh size catalyst specimens since
they have a non-cylindrical geometry and thus do not provide parallel
loading forces when tested in the ITI. The use of replicate testing
and statistical techniques were employed in order to provide as firm a
basis for analyzing the data as possible.

Work on the following factors was carried out:

- Catalyst selection parameters, i.e., different
  catalyst sizes.

- Effect of thruster exposure.

- Effect of water level.

Prior to carrying out the catalyst selection parameters work,
a study was made of a possible effect of catalyst moisture content on
the average crushing strength. Consultant discussions indicated that
such an effect might either (1) be an artifact affecting the measurement
(e.g., by causing particles to move horizontally during the test), or
(2) could reflect an effect of the strongly bound water in the small
angstrom size pores of the alumina. A small effect of water content on
the crushing strength of alumina based hydrotreating catalysts were re-
cently reported in the literature (92). Thus, in addition to a possible
variable influencing ITI measurement results, such an effect could have
significant bearing on interpreting crush strength results since a
catalyst after its initial firing in a space environment would be ex-
pected to have a very low moisture content. For this study, Fresh Shell
405 1/8" cylinders and 14-18 mesh catalyst were employed along with
Harshaw AL1602 alumina 1/8" cylinders. The specimens were tested (1) as-
is, (2) after drying in a vacuum oven and (3) after saturation by water
vapor at 80°F. Replicate tests with sample sizes of up to 15 tests were
employed. Results of this study are shown in Table 3-6. Detailed data
are contained in the Appendix.

An examination of the average crushing strengths in Table 3-6
indicated no obvious effect of water level on both the Shell 405 catalyst
cylinders and mesh granules and the Harshaw alumina cylinders. Statis-
tical t-tests on the variations of means for each material indicated they
were not statistically different. An examination of the standard devia-
tions indicates that the vacuum oven dried material in all three cases
had a higher standard deviation than the as-is and water saturated
samples. Statistical F-tests on these differences in variances indicated
that none of these differences were significant at the 95% confidence
level.

Table 3-6

Investigation of the Possible Effect of Specimen Water Content on iTI Crush Strength Measurement

		"As Is"[a]	Dried in Vacuum Oven[b]	Water Saturated[c]
Fresh Shell 405 1/8 x 1/8 Cylinders	Average Crush Strength lbs	34.4	34.9	35.0
	Sample Size	10	15	15
	Standard Deviation, lbs	6.08	7.54	6.43
Fresh Shell 405 14-18 Mesh	Average Crush Strength, lbs	1.99	1.59	1.17
	Sample Size	5	10	10
	Standard Deviation, lbs	.85	.98	.61
Harshaw Alumina AL 1602 1/8 x 1/8 cylinders	Average Crush Strength, lbs	26.6	28.8	24.6
	Sample Size	10	10	9
	Standard Deviation, lbs	5.65	9.42	5.64

(a) Tested as is after removal from their containers.
(b) Tested after drying in a vacuum oven overnight at 110°C and 120 mm Hg total pressure.
(c) Tested after being saturated with water vapor at 80°F and 1 atm total pressure.

The data obtained with the 1/8" cylinders and 14-18 mesh fresh Shell 405 at various water levels was pooled into a single set of data and an average crushing strength and standard deviation calculated for the resultant sample size of 40 and 25 replicate measurements, respectively Twenty-five replicate measurements were also made on other mesh size Shell 405 catalyst. Results of these tests are shown in Table 3-7. As would be expected because of geometric effects, the standard deviations of the granular specimens are much larger compared to their mean value. This is shown below:

Specimen	Standard Deviation as % of Average Crushing Strength
• 1/8" x 1/8" cylinders	
Fresh Shell 405	19.0
Al 1602 Alumina	26.0
• Fresh Shell 405 granules	
8-12 Mesh	40.1
14-18 Mesh	56.6
20-25 Mesh	65.1
25-30 Mesh	48.2
20-30 Mesh	65.0

In Table 3-8 are shown the results of tests with the various mesh size of alumina support before attrition, while in Table 3-9 are shown the results on the corresponding material after 50% attrition. In Table 3-10 is shown a comparison of the effect of catalyst preparation steps on particle average compressive crushing strength of the various sizes of granular material. In Table 3-11 is shown a comparison of the cylindrical alumina pellets before and after iridium addition. The difference between the average crushing strengths within a given size of material were subjected to statistical analysis (t-tests at the 95% confidence level) to see if these differences are statistically significant. A summary of these statistical tests are shown in Table 3-12.

Table 3-7

Particle Compressive Crushing Strength of Fresh Shell 405
Catalyst in the ITI

	1/8" x 1/8" Cylinder	8-12 Mesh	14-18 Mesh	20-25 Mesh	25-30 Mesh	20-30 Mesh
Average Crushing Strength, lbs	34.8	4.26	1.50	0.74	0.56	0.61
Sample Size	40	25	25	25	25	25
Standard Deviation, lbs	6.62	1.75	0.85	0.48	0.27	0.40
Cumulative Distribution of Crushing Strength, lbs (a)						
1%	19.4	0.30	-	-	-	-
5%	24.0	1.45	0.11	-	.11	-
10%	26.3	2.12	0.41	.12	.22	0.10
50%	34.8	4.36	1.50	.74	.56	0.61
90%	43.3	6.60	2.59	1.35	.90	1.12
95%	45.6	7.25	2.89	1.52	1.00	1.27
99%	50.2	8.42	3.48	1.85	1.18	1.54

(a) - Calculated from measured mean and standard deviation assuming a normal distribution.

- 48 -

Table 3-8

Particle Compressive Strength of Alumina Support Before Attrition

	Mesh Size				
	8-12	14-18	20-25	25-30	20-30
Average Crushing Strength, lbs.	2.26	1.09	0.39	0.40	0.45
Sample size	25	25	25	25	25
Standard Deviation, lbs.	1.37	0.68	0.26	0.17	0.20
Distribution of Crushing Strength, lbs. (a)					
1%	-	-	-	-	-
5%	0.02	-	-	0.12	0.12
10%	0.51	0.17	.06	0.18	0.20
50%	2.26	1.09	0.39	0.40	0.45
90%	4.01	1.96	0.72	0.62	0.70
95%	4.50	2.20	0.81	0.68	0.78
99%	5.44	2.68	1.00	0.80	0.91

(a) Calculated from measured mean and standard deviation assuming a normal distribution.

Table 3-9

Particle Compressive Strength of Alumina Support After 50% Attrition

	Mesh Size				
	8-12	14-18	20-25	25-30	20-30
Average Crushing Strength, lbs.	3.16	1.86	0.72	0.50	0.46
Sample size	25	25	25	25	25
Standard Diviation, lbs.	1.17	0.86	.39	.26	.28
Distribution of Crushing Strength, lbs. (a)					
1%	0.39	-	-	-	-
5%	1.20	0.45	0.09	0.07	-
10%	1.62	0.76	0.22	0.17	0.10
50%	3.12	1.86	0.72	0.50	0.46
90%	4.62	2.96	1.22	0.83	0.82
95%	5.04	3.27	1.36	0.93	0.92
99%	5.85	3.87	1.63	1.11	1.11

(a) calculated from measured mean and standard deviation assuming a normal distribution

Table 3-10

Effect of Catalyst Preparation Steps on
Particle Average Compressive Crushing Strength

Average Crushing Strength - lbs. (a)

Material	Mesh Size				
	8-12	14-19	20-25	25-30	20-30
Alumina Support before attrition	2.26	1.09	0.39	0.40	0.45
Alumina Support after 50% attrition	3.16	1.86	0.72	0.50	0.46
Attrited Support after iridium addition (fresh Shell 405)	4.26	1.50	0.74	0.56	0.61

(a) average crushing strength based on 25 replicate measurements

Table 3-11

Effect of Iridium Addition on Average
Compressive Crushing Strength of 1/8" x 1/8" Cylinders

Material	Average Compressive Crushing Strength, lbs.	Sample Size	Standard Deviation, lbs.
1/8" x 1/8" alumina support	34.6	25	9.89
1/3" x 1/8" alumina support after iridium addition (fresh Shell 405)	34.8	40	6.62

Table 3-12

Summary of Statistical Tests on the
Significance of Differences Between Particle
Average Compressive Crushing Strength

Size	Is the Difference Statistically Significant? (a)	
	Comparison of Material Before and After 50% Attrition	Comparison of Material Before and After Metal Addition
1/8" x 1/8" cylinders	-	No
8-12 Mesh	Yes	Yes
14-18 Mesh	Yes	No
20-25 Mesh	Yes	No
25-30 Mesh	No	No
20-30 Mesh	No	No

(a) Based on a t-test using the measured means and standard deviations at the 95% confidence level (single sided t-test at .025).

It can be seen from examining Tables 3-10, 11 and 12 that the addition of the iridium metal to the alumina support in general did not result in any significant increase in particle crushing strength. In contrast, the use of the attrition procedure during the preparation of the catalyst support in general improves the average crushing strength, with the improvement with the larger granular sizes (i.e., 8-12, 14-18, and 20-25 mesh) being statistically significant.

Mesh Size	Increase in Crushing Strength of 50% Attrited Support over Support Before Attrition
8-12	38%
14-18	70%
20-25	84%
25-30	25%
20-30	2%

These latter two effects presumably reflect the loss of the weaker granular material during both the grinding process involved in the initial mesh size selection and in the attrition procedure where at least 50% of the weaker material is rejected. In contrast to the improvement in average crush strength, as shown in Table 3-13, the attrition procedure did not improve the scatter in the individual values (i.e., reduce the standard deviation), so that both the attrited supported and the corresponding metal loaded catalyst still have a relatively wide variation in individual particle crushing strengths. A wide variation in individual crushing strengths is deleterious since it means (as shown in Table 3-7) that an aggregate bed of individual particles will contain an appreciable number of particles with individual crushing strengths much lower than that represented by the average crushing strength (50% value). These results suggest that preparation techniques that would reduce the standard deviation or variation in individual crushing strengths could offer the possibility of significant improvements in aggregate or bed performance.

A short study was also made of the effect of repeated loading on the crushing strength of fresh Shell 405 catalyst. This was done by repeated axial loading of the 1/8" x 1/8" cylindrical Shell 405 catalyst to 50% of the average compressive crushing strength. Specimens were exposed to 10, 25, and 50 repeated loadings and then loaded to failure so as to measure the crushing strength. Results of these tests are shown in Table 14. Statistical t-tests at the 95% confidence level indicated that none of these values are statistically different from the mean value for the catalyst which had not been subjected to repeated loadings.

Table 3-13

**Effect of Catalyst Preparation Steps on the
Scatter in Individual Particle Compressive Crushing Strengths**

Standard Deviation of Individual
Crushing Strength – lbs.

Material	Mesh Size				
	8-12	14-18	20-25	25-30	20-30
Alumina support before attrition	1.37	0.68	0.26	0.17	0.20
Alumina support after 50% attrition	1.17	0.86	0.39	0.26	0.28
Attrited support after iridium addition (fresh Shell 405)	1.75	0.85	0.48	0.27	0.40

Table 3-14

Effect of Multiple Loading on Compressive Crushing
Strength of Fresh Shell 405 1/8" x 1/8" Cylinders

Number of repeated compressive loadings (a)	Compressive Crushing Strength, lbs.
0	34.8
10	34.9 (b)
25	42.0 (b)
50	35.8 (b)

(a) Cylindrical pellet axially loaded repeatedly to 50% of average
    failure compressive crushing strength followed by complete
    pressure release, then loaded to failure to measure crushing
    strength.

(b) Not statistically different from mean value for no repeated
    loading based on a t-test at the 95% confidence limit using
    the measured standard deviation value for fresh Shell 405
    1/8" x 1/8" cylinders.

A number of specimens of Shell 405 catalyst used in thrusters were made available by TRW. Samples were taken from this material and tested in the ITI. A comparison of the crushing strength properties of these catalysts exposed to a hydrazine catalyst chamber environment versus corresponding fresh catalyst properties is shown in Table 3-15. A comparison of results from a 14-18 mesh sample exposed to 250 seconds of steady state firing spread over 51 cold starts against results from a fresh catalyst shows no significant difference in either average crushing strength or the variance (standard deviation) of the strengths (based on a t-test and an F-test respectively). In contrast, the used 1/8" cylindrical catalyst pellets showed a much lower average crush strength and larger variation in individual particle crush strengths than did the fresh cylinders. A t-test on the difference between the two means was significant at the 95% confidence level (calculated t-test = 3.42; $t_{40, .025} = 2.02$). Similarly an F-test on the two variances indicated the difference was significant at the 95% confidence level (calculated F-test = 3.02; $F_{10, 40, .05} = 2.08$).

Two samples of used 18-20 mesh Shell 405 catalyst were also received from TRW. The first sample was taken from the downstream portion of the bed in a 5 lb thruster which saw 84,000 pulses. The second sample was taken from the upper portion of the bed near the injector of a 5 lb thruster which saw 210,000 pulses. Results of ITI measurements on particles taken from these samples are shown in Table 3-16. Surprisingly the catalyst exposed to the higher number of pulses near the injector section of the bed had the higher average crush strength. A statistical t-test on the difference between these two means was significant at the 95% confidence level (calculated t-test = 2.61; $t_{18, .025} = 2.10$). Similarly an F-test on the difference between the variances (standard deviations) of these two samples was also significant at the 95% confidence level (calculated F-test = 4.16; $F_{10, 10, .05} = 2.98$). Although no fresh 18 to 20 mesh Shell 405 particulates were tested, an interpolation of the data contained in Table 3-7 suggests that such a mesh size would have an average crushing strength of approximately 1 pound. This suggests that the downstream bed samples exposed to 94,000 pulses (Sample 1, Table 3-16) have suffered a loss in particle crushing strength, whereas the upper bed samples exposed to 210,000 pulses (Sample 2, Table 3-16) did not.

In general, the results suggest that exposure to a thruster environment can cause changes in particle crush strength. Particularly damaging is the situation where both the mean crush strength decreases and the standard deviation of the crush strength values increases, the net result of which is a sharp increase in the percentage of very weak particles.

Table 3-15

Comparison of Particle Crushing Strength
of Fresh Versus Used Shell 405 Catalyst

		Fresh	Used
1/8" x 1/8"	Average Crushing Strength, lbs.	34.8	21.9[a]
	Sample Size	40	10
	Standard Deviation lbs	6.62	11.5
14-18 Mesh	Average Crushing Strength, lbs	1.50	1.72[b]
	Sample Size	25	10
	Standard Deviation	0.85	0.99

(a) TRW sample. Detailed history not available, however,
estimated at a few thousand seconds steady state operation.

(b) TRW sample. Approximately 250 seconds of steady state
firing spread over 51 cold starts.

Table 3-16

Comparison of Particle Crushing Strength of
Two Samples of Used 18-20 Mesh Shell 405 Catalysts

	Sample 1	Sample 2
Sample History	TRW Sample. 84,000 pulses in 5 lbf thruster in November 1972 Sample from downstream end of bed.	TRW Sample. 210,000 pulses in 5 lbf thruster in August 1973. Sample from upper portion of bed near the injector.
Average Crushing Strength, lbs[a]	0.55	1.02
Sample Size	10	10
Standard Deviation lbs.	0.25	0.51

(a) Samples dried in vacuum oven overnight at 110°C and 120 mm Hg
Total pressure.

3.2.3 Sensitivity Testing in
the Bed Crushing Area

Sensitivity tests involving the static pressure crushing of a small bed of granular catalyst were added to the program. Because of uncertainties in available 20-25 mesh results, data from this mesh size fresh Shell 405 catalyst was emphasized. Data was also obtained with 25-30 mesh material. The data was obtained using the Pressure Crushing Mini-Bed (PCMB) shown in a schematic in Figure 3-11. For the mesh sizes employed this apparatus provides a ratio of bed diameter to particle diameter ranging from approximately 8 to 10. Sufficient catalyst was employed to yield bed depths ranging from 3/4 to 1 inch, which resulted in ratios of bed length to bed diameter ranging from 3 to 4. The PCMB was axially loaded in compression using the Instron Instrument (ITI).

The following procedure was adopted in obtaining the data. The fresh Shell 405 catalyst was first screened and any material outside the cited mesh size was rejected. Approximately 0.9 to 1.0 g of proper mesh size catalyst was charged to the reactor, and the reactor tapped until the bed settled to a constant volume. The movable upper assembly was placed in the PCMB and a sequential series of measurements was made with the same sample at progressively higher bed pressures. Two series of runs were made with the 20 to 25 mesh catalyst, the first at bed pressures of 22, 92, 200, and 322 psi, and the second at 22, 50, and 100 psi. A single run series was made with 25 to 30 mesh fresh Shell 405 at bed pressures of 25, 45, 98, 204, and 324 psi. In the sequential run series the bed is loaded to the lowest bed pressure first and then held under this load for 20 minutes. The load is removed and the bed contents screened and the weight of the resultant fractions determined. The reactor is then repacked with the surviving original mesh size material and tapped to constant volume. The PCMB is first loaded to the initial pressure load and held for ten minutes, then loaded to the second highest bed pressure and held there for 20 minutes. The load is then removed and the bed contents screened and weighed. As the surviving bed material is subjected to higher and higher pressures, it is always loaded in sequence to the previous loads employed and held at these loads for 10 minutes prior to a 20 minute loading time at the higher pressure. Detailed data obtained from the sequential runs are shown in the appendix.

For the runs with 20 to 25 mesh catalyst, the on 25 mesh and through 25 mesh material was first measured, following which the through 25 mesh material was further divided into an on 30 and through 30 mesh size material. These results are summarized in Tables 17 and 18. Material balances are also shown for each mesh size separation. Excellent material balances were obtained, averaging approximately 99%. Results are shown for both individual loading pressure results, and also on a cumulative basis for the sequence of pressures employed. In Figure 3-12 is plotted the cumulative weight percentage of fresh Shell 405 through both 25 and 30 mesh for the pressures employed. In Figure 3-13 the through 30 mesh data is plotted on an enlarged scale. The exponential increase in the weight of material through a given mesh size as pressure is increased as shown in Figure 3-12 is characteristic of the general experience with catalysts under pressure loading.

Figure 3-11

Pressure Crushing Mini-Bed (PCMB)

Movable Upper Assembly

Bed Diameter, D = 0.25"

Bed Container

Catalyst Bed
(Length, L, > 3/4")

Bed L/D > 3

Fixed Lower
Assembly
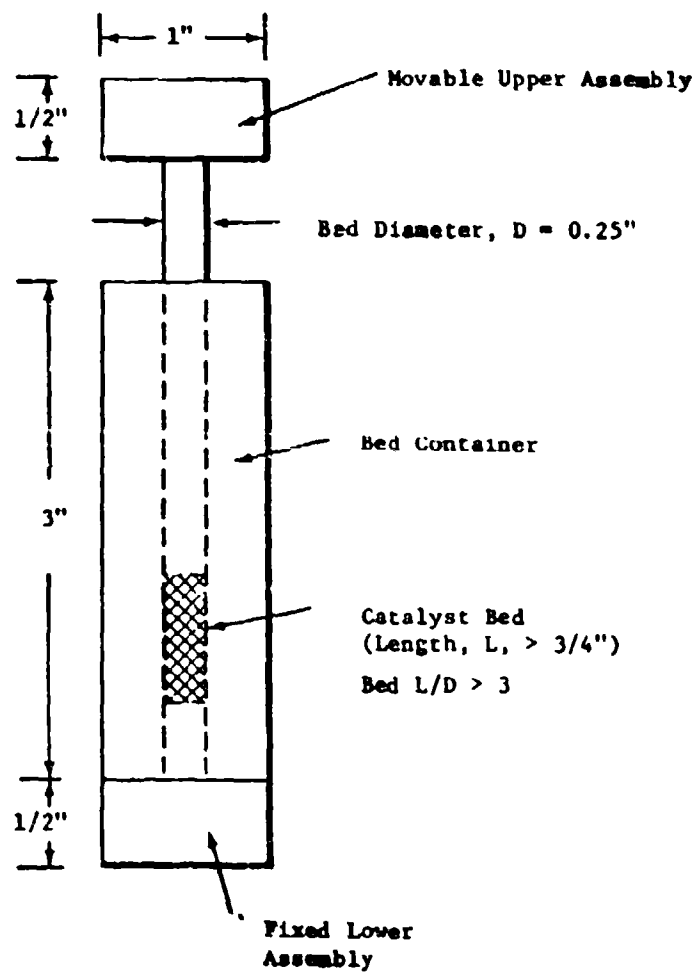
Figure 3-17

Fines Production with Sequential Mini-Bed Compressive Crushing of 20-25 Mesh Fresh Shell 405 Catalyst

		Bed Pressure, lb/in^2		
		22	50	99
Individual Measurement	Wt. % on 25 Mesh	98.30	98.73	96.23
	Wt. % Through 25 Mesh	1.70	1.27	3.77
	Material Balance, %	100.1	99.8	100.0
Cumulative Wt. % Through 25 Mesh		1.70	2.97	6.74
Individual Measurement	Wt. % on 30 Mesh	1.19	1.04	3.73
	Wt. % Through 30 Mesh	0.51	0.23	0.04
	Material Balance, %	97.5	97.4	100.0
Cumulative Wt. % Through 30 Mesh		0.51	0.74	0.78

Percentages are all based on the weight of starting 20-25 mesh material. Material balances are equal to recovered weight divided by starting weight x 100 for given separation.

Figure 3-18

Fines Production with Sequential Mini-Bed
Compressive Crushing of 20-25 Mesh
Fresh Shell 405 Catalyst

		Bed Pressure, lb/in^2			
		21.9	91.8	200	322
Individual Measurement	Wt. % on 25 Mesh	95.69	97.19	97.09	65.88
	Wt. % Through 25 Mesh	4.31	2.81	2.91	34.12
	Material Balance, %	100.9	99.9	99.6	97.4
Cumulative Wt. % Through 25 Mesh		4.31	7.12	10.03	44.15
Individual Measurement	Wt. % on 30 Mesh	4.04	2.69	1.96	11.68
	Wt. % Through 30 Mesh	0.27	0.12	0.95	22.44
	Material Balance, %	100.0	99.8	100.0	95.1
Cumulative Wt. % Through 30 Mesh		0.27	0.39	1.34	23.78

Percentages are all based on weight of starting 20-25 mesh catalyst.
Material balances are equal to recovered weight divided by starting
weight x 100 for given separation.

Figure 3-12

Sequential Mini-Bed Crushing of 20-25 Mesh
Fresh Shell 405 Catalyst

THROUGH
25 MESH
($\leq$ 0.71 mm)

THROUGH
30 MESH
($\leq$ 0.59 mm)

BED PRESSURE, lb/in^2

CUMULATIVE WT. % THROUGH INDICATED MESH SIZE
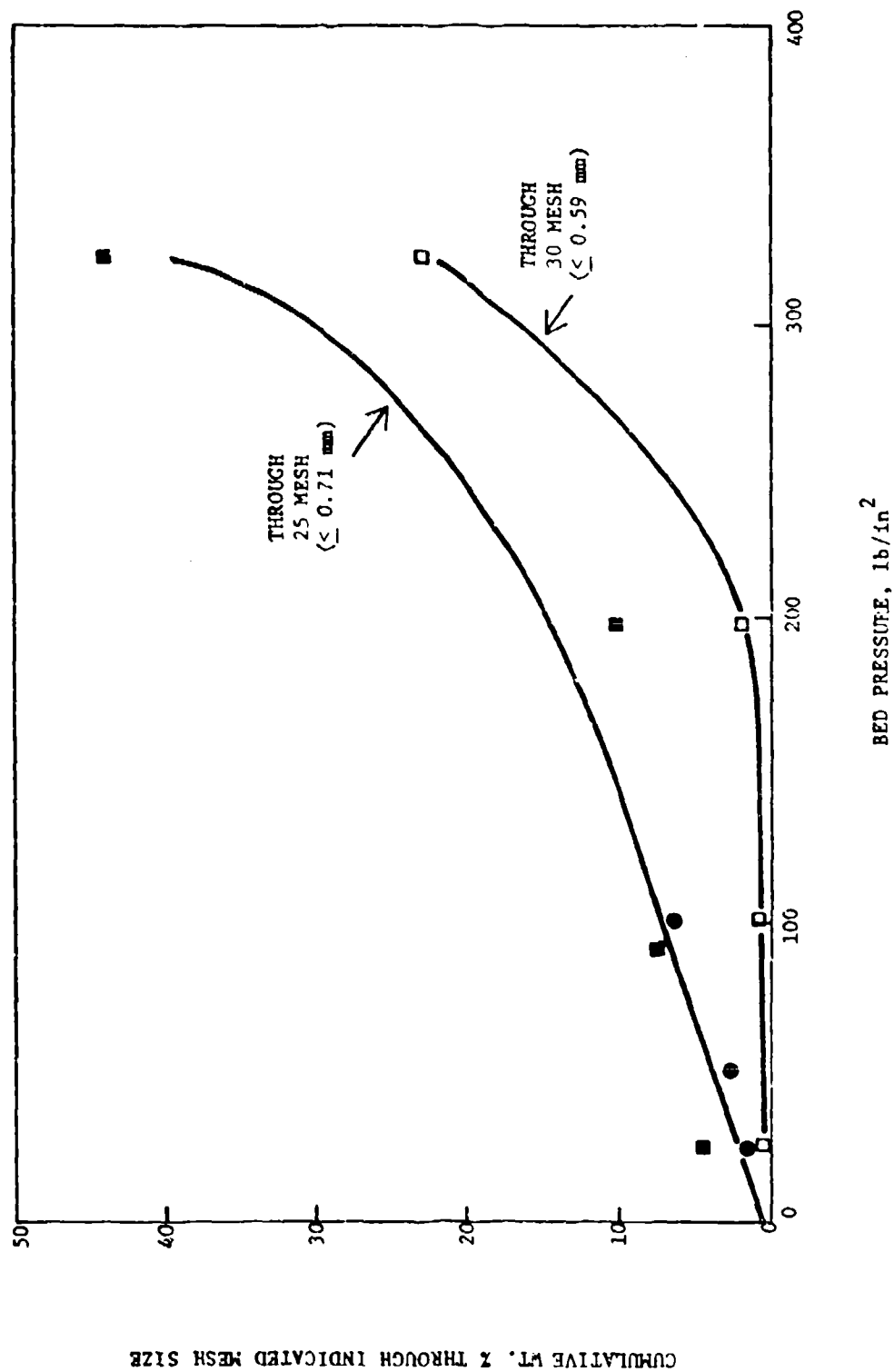
Figure 3-13

Sequential Mini-Bed Crushing of 20-25 Mesh
Fresh Shell 405 Catalyst
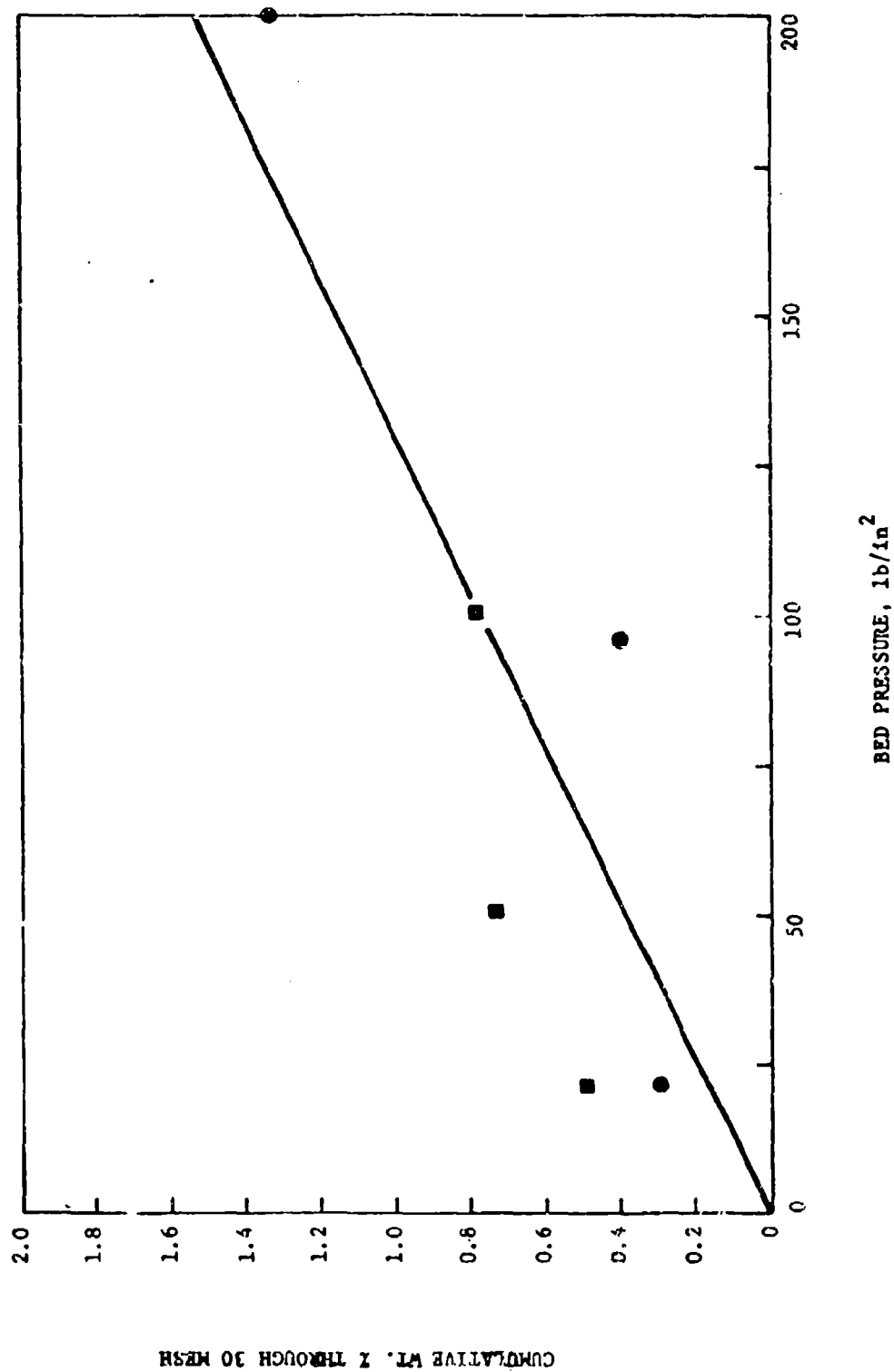
Results for the run with 25 to 30 mesh fresh Shell 405 are
shown in Table 3-19. For this run, there was only sufficient material
for an accurate on 35 mesh through 35 mesh separation at the highest
pressure employed (i.e., 324 psi). In Figure 3-14 are plotted the cumu-
lative weight percentages through 30 mesh obtained at the various
pressures, along with an estimate of the corresponding through 35 mesh
material.

The results of these tests indicate that 20-25 mesh Shell 405
catalyst exhibits a reduction in particle size at low pressures (i.e.,
below 100 psi). At 100 psi with the 20-25 mesh catalyst, 7 wt. % of
material exhibits a measurable size reduction (i.e., passes through 25
mesh) while 0.8 wt. % of the material passes through the next lowest
mesh size (i.e., 30 mesh). In contrast, with the 25 to 30 mesh material
at 100 psi only 0.8 wt. % exhibits any size reduction (i.e., passes
through 30 mesh) while the material passing through the next lowest
mesh size (i.e., 35 mesh) was too low to accurately measure.

3.2.4 Sensitivity Testing in the Particle Fluidization Area

Sensitivity tests in the particle fluidization area were carried
out. In the terminology used by engineers who design fixed bed catalytic
reactors, bed fluidization simply implies any movement of catalyst parti-
cles as a result of gas flow either in void spaces inadvertently formed
within the bed or in a contiguous volume such as the inlet sections above
the catalyst bed where either catalyst particles or the ceramic distri-
butor balls which are used could experience movement. Commercial exper-
ience with fixed beds indicate that once bed fluidization begins catalyst
degradation by impact fracture and particle to particle abrasion is gen-
erally quite serious and often catastrophic. Thus, design practice is
aimed at identifying conditions to avoid bed fluidization via control of
injector design and flow rates to avoid incipient bed fluidization velo-
cities.

Incipient particle movement velocities of various granular Shell
405 catalyst were measured in the modified ILBET apparatus shown in a
schematic in Figure 3-15. This unit employs a simple right angle, center
axis, cylindrical pipe gas inlet. The scaling parameters (i.e., the
ratio of the dimensions of the vessel, pipe gas inlet, catalyst particles,
separation distance between bed and inlet, and bed depth) employed are
listed in Table 3-20, along with typical values employed in larger equip-
ment used to establish commercial design criteria. It can be seen that,
in general, the scaling parameters are quite similar. The top of the
catalyst bed is visually observed and the incipient fluidization velocity
was defined as the lowest velocity at which any particle on the top of
the bed first experienced movement, as the gas velocity is progressively
increased. Replicate measurements are being made at each set of conditions.

Table 3-19

Fines Production with Sequential Mini-Bed
Compressive Crushing of 25-30 Mesh
Fresh Shell 405 Catalyst

		Bed Pressure, lb/in^2				
		25	44.9	97.9	204	324
Individual Measurement	Wt. % on 30 Mesh	99.53	99.93	99.75	99.30	98.71
	Wt. % Through 30 Mesh	0.47	0.07	0.25	0.70	1.29
	Material Balance, %	100.0	100.1	99.9	99.9	99.6
Cumulative Wt. % Through 30 Mesh		0.47	0.54	0.79	1.49	2.78
Individual Measurement	Wt. % on 35 Mesh	-	-	-	-	0.64
	Wt. % Through 35 Mesh	-	-	-	-	0.65
	Material Balance, %	-	-	-	—	114.2

Percentages are all based on weight of starting 25-30 mesh material.
Material balances are equal to recovered weight divided by starting
weight x 100 for given separation.

Figure 3-14

Sequential Mini-Bed Crushing of 25-30 Mesh
Fresh Shell 405 Catalyst
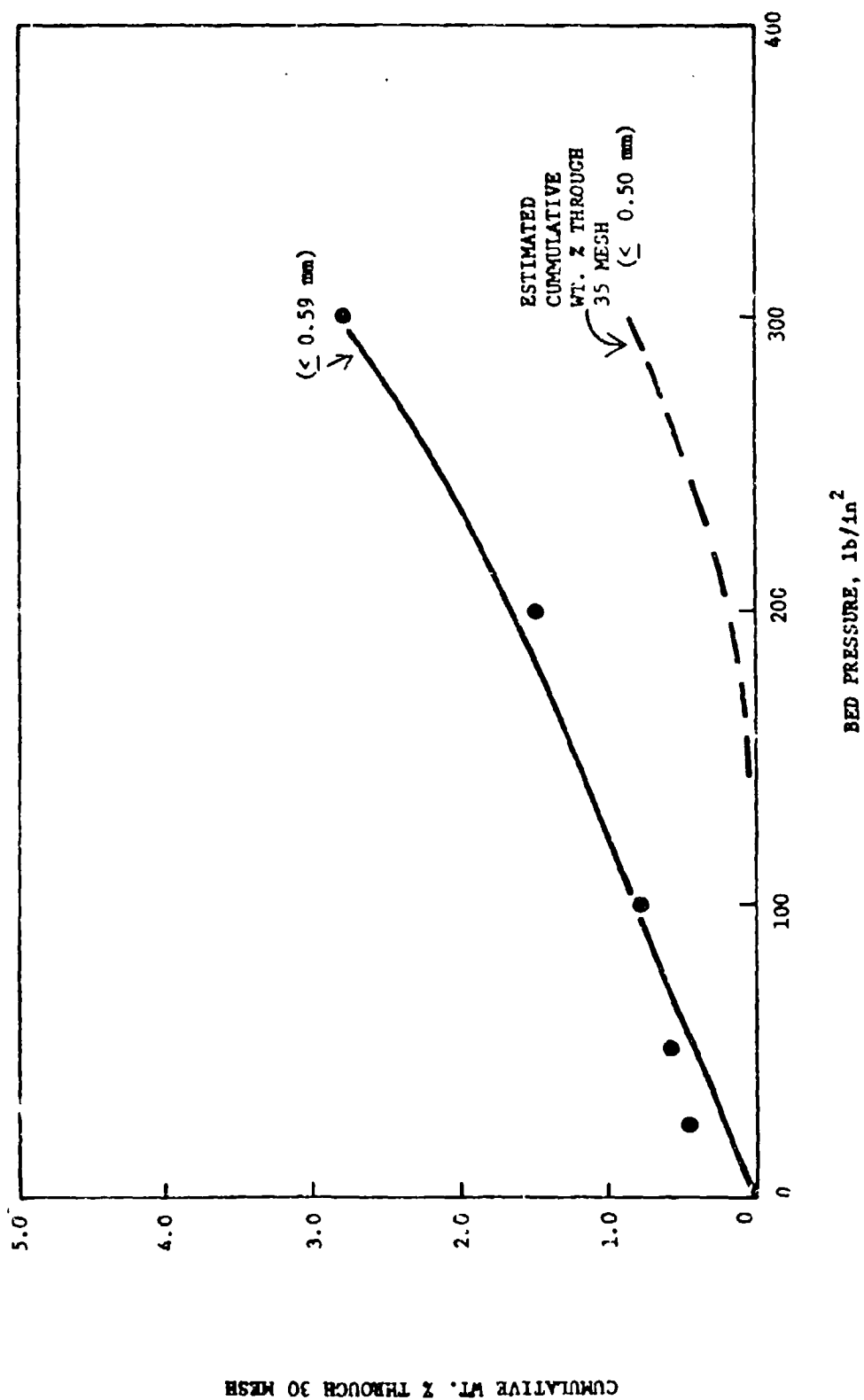
Figure 3-15

Modified ILBET Apparatus for
Incipient Particle Movement
Velocity Measurement

BED VESSEL
(inner diameter,
D_V = 25 mm)

CYLINDRICAL
PIPE GAS INLET
(inner diameter, D_o = 5 mm)

CATALYST BED
(depth, D_L, 15 to 20 mm)

100 MESH
SCREEN SUPPORT
BETWEEN WASHERS

H

SEPARATION
DISTANCE, H,
BETWEEN INLET
AND CATALYST BED

H_2

He

EFFLUENT TO VENT
OR WET TEST METER

- 69 -
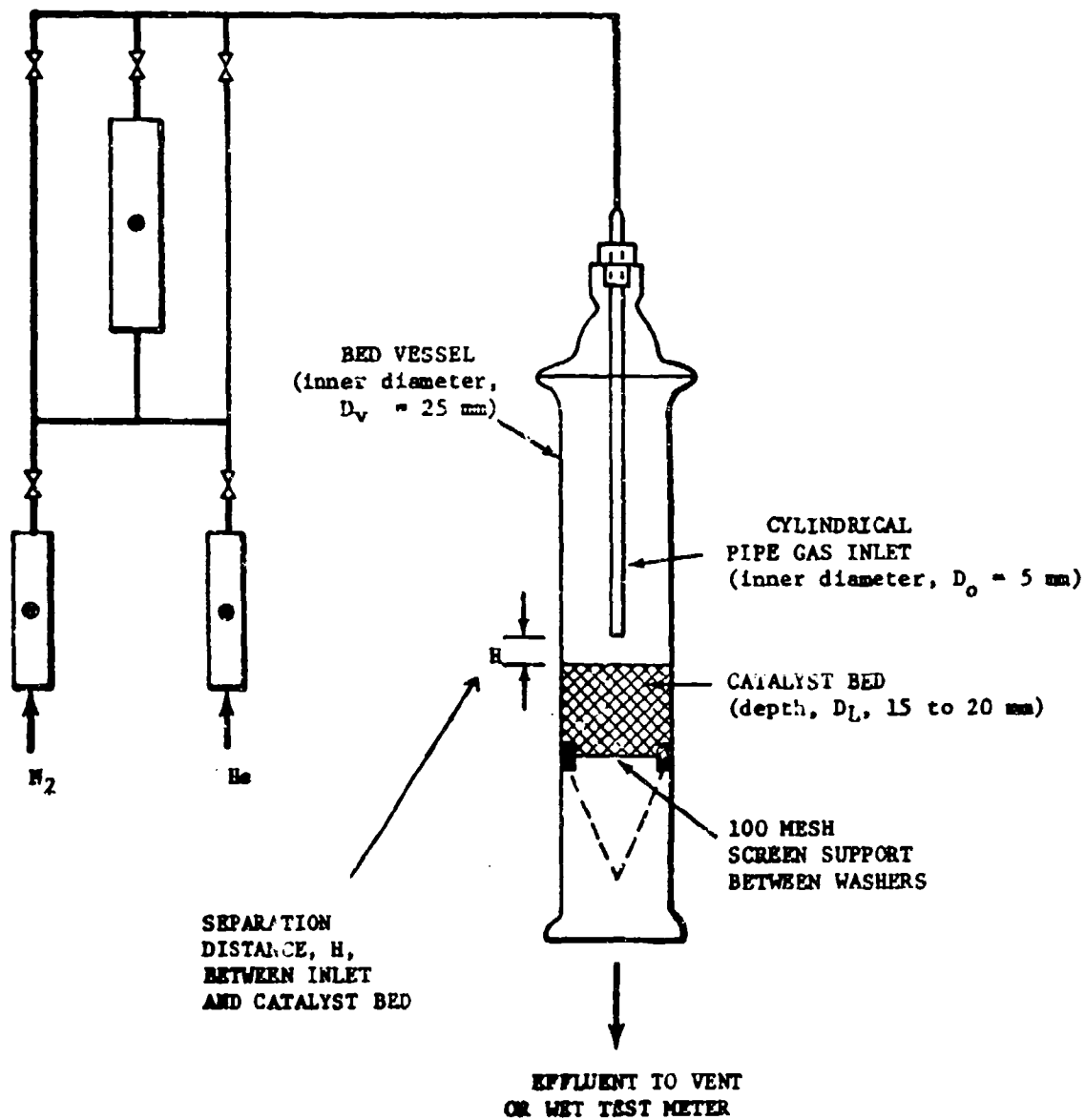
Table 3-20

Comparison of Scaling Parameters Used
In Incipient Particle Movement Study

Scaling Parameter	Range of Values	
	ILBET Used For Particle Fluidization	Typical Lab Vessel Used to Establish Commercial Design Practice
D_v/D_o	5	~ 6
D_o/D_p	2.5 to 7	3 to 12
D_L/D_p	10 to 20	15 to 30
H/Do	2	~ 2

Terminology: D_v = inner diameter of bed vessel
D_o = inner diameter of pipe type inlet
D_L = catalyst bed depth
H = separation distance between bed and inlet
D_p = particle diameter

Pure nitrogen, pure helium and helium-nitrogen blends were used to provide data on the effect of gas density. In addition to the effect of gas density, catalyst selection parameters were also investigated.

The minimum inlet distributor superficial velocity for particle movement was measured for fresh Shell 405 particles of 8 to 12 mesh, 14 to 18 mesh and 20 to 30 mesh size. The detailed data obtained with pure helium, pure nitrogen, and helium-nitrogen blends are shown in the Appendix. In Table 21 is summarized the average inlet velocity and standard deviation of the velocity determined from the replicate measurements with pure nitrogen and helium. These values were determined from a sample size of ten replicate measurements. Statistically significant (t-tests at the 95% confidence level) differences exist between the average velocities found for the various mesh sizes and the two gases employed.

A correlation of incipient fluidization data was made employing the following equation:

$$V_g = K \left[g \ D_p \ \frac{(\rho_p - \rho_g)}{\rho_g} \right]^{1/2} \qquad (3-1)$$

where: V_g = incipient movement velocity

g = gravity constant

D_p = diameter of particle

ρ_g = vapor density

ρ_p = particle density

K = emperical correlating constant to be derived from the data.

Since the density for gases is much lower than the particle density, the equation was simplified as follows:

$$V_g = K' \left(\frac{D_p}{\rho_g} \right)^{1/2} \qquad (3-2)$$

where $K' = K(g\rho_p)^{1/2}$

Table 3-21

Particle Fluidization: Effect of Particle Size
and Gas Density on Minimum Inlet Superficial
Velocity for Particle Movement

| | | Fresh Shell 405 Particle Size | | |
		8–12 Mesh	14–18 Mesh	20–30 Mesh
Pure Nitrogen	Average Velocity M/sec (a)	5.49	4.03	2.28
	Sample Size	10	10	10
	Standard Deviation M/sec	1.49	0.47	0.47
Pure Helium	Average Velocity M/sec (a)	12.18	9.61	6.72
	Sample Size	10	10	10
	Standard Deviation M/sec	1.22	1.51	1.30

(a) Average minimum superficial velocity in the inlet distributor
tube which causes any particle movement, meters per second.

The incipient movement velocity was estimated in terms of a horizontal or surface velocity from the superficial inlet velocity using a literature correlation of maximum surface vapor velocity or a function of inlet velocity and inlet geometry. This correlation is shown in Figure 16. For the conditions employed in the present study, this correlation predicts that the horizontal or surface velocity will be 85% of the inlet superficial velocity. Average incipient movement velocities calculated from this correlation are shown in Table 3-22, and both the pure nitrogen and helium results and the results from the helium-nitrogen blends. Also shown in Table 3-22, are average gas compositions and an average catalyst particle diameter for the mesh sizes employed. The average incipient particle movement velocity in terms of feet per second was then plotted as a function of $(D_p/\rho_g)^{1/2}$. This correlation is shown in Figure 17, and is applicable to a unit value gravity environment.

It could appear that, in general, thruster gas velocities will be above the incipient particle movement velocity. As an example, a hydrogen-nitrogen gas mixture (67% H_2 – 33% N_2) at 10 atmospheres and 925°C will have an approximate 1.1 g/liter density. For the largest granular size employed, i.e., 8-12 mesh, this would yield an $(Dp/\rho_g)^{1/2}$ value of approximately 1.35. From Figure 3-17, which assumes a unit gravitational field, this would correspond to a incipient movement velocity of approximately 12 feet/second. The highest anticipated satellite gravitational field is 5.0 G, for an on-orbit spinner, and this higher gravity would raise this incipient particle movement velocity to approximately 28 feet per second. Lower gravitational fields, smaller catalyst particle sizes, and higher gas densities at higher pressures will all directionally lower the incipient fluidization velocity. Assuming that a thruster gas velocity of 110 feet per second is representative, it can be seen that Shell 405 granules are exposed to velocities much higher than the incipient particle movement velocity, and that particle movement would be possible once sufficient void space occurs in the catalyst bed.

Maximum Surface Vapor
Velocity for Impinging Jets
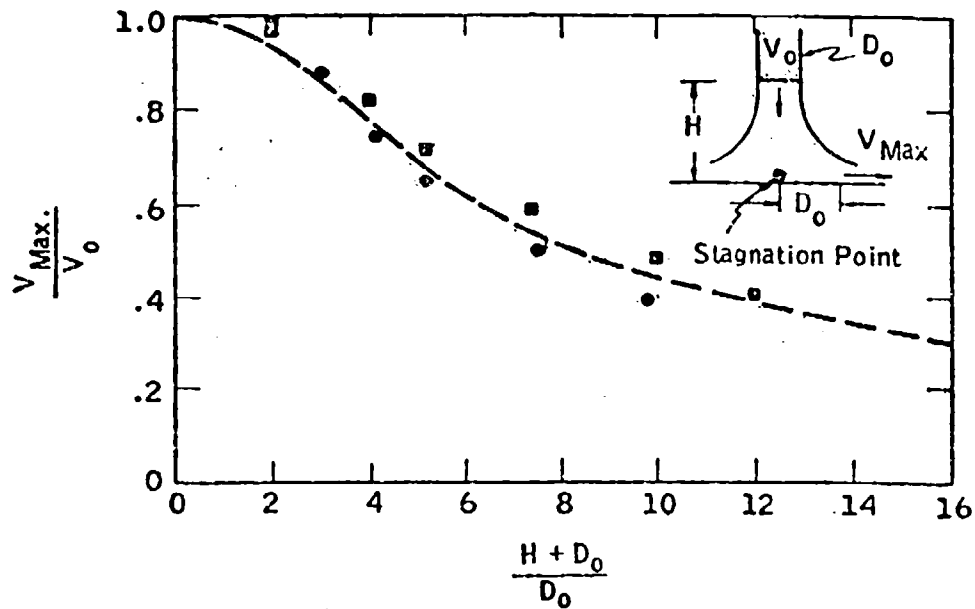
Legend

■   Impingement Jet Data From A 16" Ducted Fan

●   Impingement Jet Data From A 4" Uniform Jet

Source: R. E. Kuhn, NASA   TN D-56,
         September, 1959.

Table 3-22

Summary of Particle Fluidization Parameters

Fresh Shell 405 Particle Size	Average Gas Comp. % N₂ in N₂-He	Average Particle Diameter Dp, mm (a)	Gas Density g/l	Average Incipient Particle Movement Velocity, ft/sec (b)	$(D_p/\rho_g)^{1/2}$ $(mm-1/g)^{1/2}$
8-12	100	2.00	1.16	16.57	1.31
14-18	100	1.19	1.16	11.24	1.01
20-30	100	0.71	1.16	6.36	0.78
8-12	0	2.00	0.16	33.98	3.54
14-18	0	1.19	0.16	26.81	2.73
20-30	0	0.71	0.16	18.75	2.11
8-12	85.0	2.00	1.01	17.94	1.41
14-18	63.0	1.19	0.78	11.52	1.24
20-30	63.3	0.71	0.78	8.26	0.95
8-12	22.3	2.00	0.38	18.83	2.29
14-18	26.2	1.19	0.42	10.99	1.68
20-30	30.2	0.71	0.46	7.37	1.24

(a) Average Dp for 8-12 mesh assumed as 2.00 mm (10 mesh opening), for 14-18 mesh as 1.19 mm (16 mesh opening), for 20-30 mesh as 0.71 mm (25 mesh opening).

(b) A horizontal velocity which is assumed to be 85% of average inlet distribution superficial gas velocity for H+Do/Do = 3.

Figure 3-17

Correlation of Incipient Particle Movement Velocity
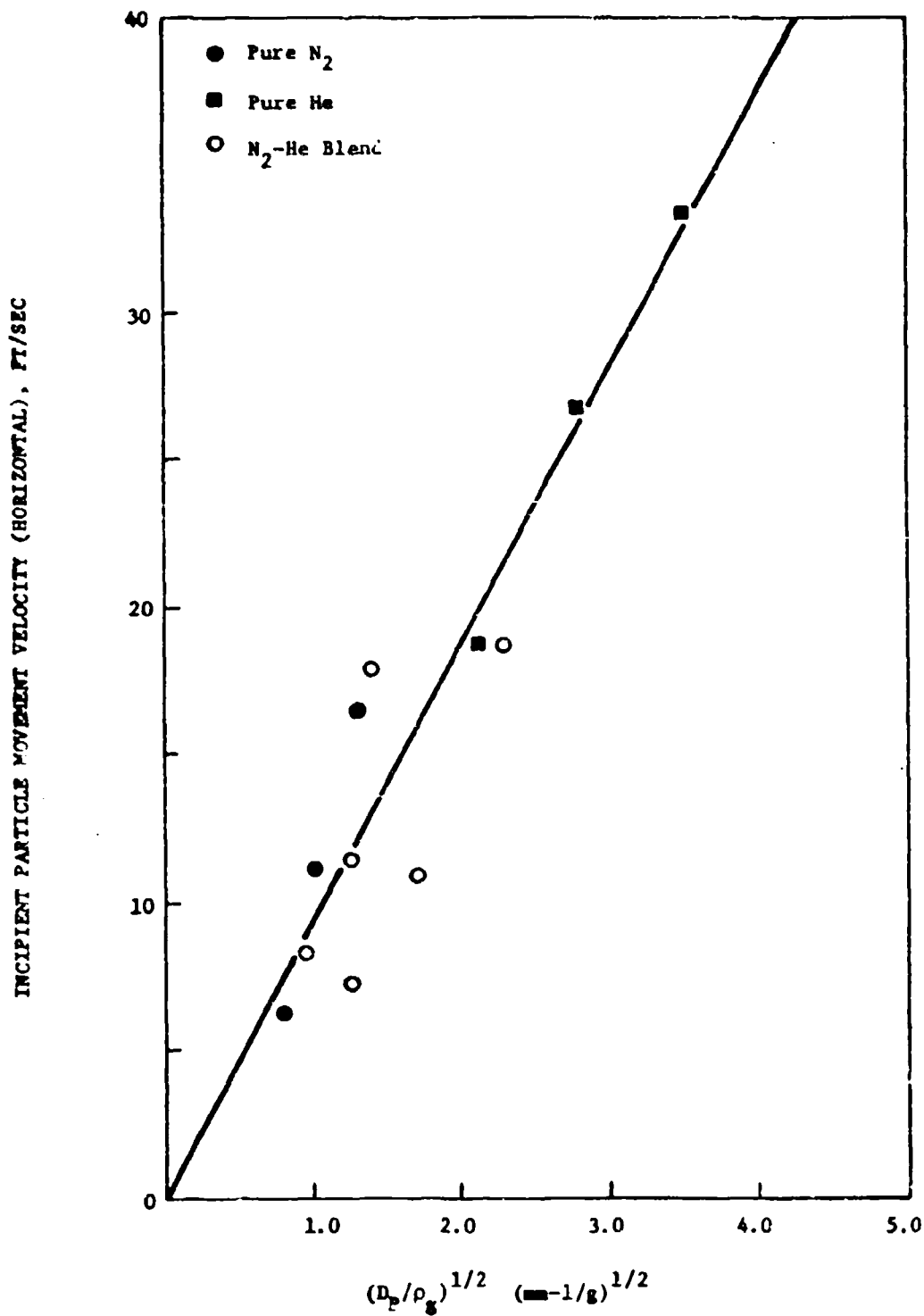
3.2.5 Sensitivity Testing in the
Liquid Fluid Dynamic Erosion Area

Sensitivity tests in the liquid fluid dynamic erosion area were carried out. In line with Air Force and Scientific Advisory Board recommendations, a test involving individual catalyst particles subjected to a pulsed, liquid flow was developed and substituted for the ILBET liquid erosion test originally planned. This work was carried out in the Pulsed Liquid Particle Erosion Test (PLPET) apparatus shown in Figure 3-18. In this test, individual catalyst particles were passed through a stream of flowing liquids at a speed which could be varied by changing the stirrer speed. A flat nozzle was employed so as to produce as near a rectangular flow of liquid as possible. The stream angle was adjusted so that the catalyst particle struck the liquid stream at a right angle. The velocity of the liquid stream was maintained high enough to insure that the stream geometry was restored before the next impact of the particle (the stream advanced a minimum of 7 cm in the time required to complete a revolution of the arm which was 1 cm in diameter).

The 1/8" x 1/8" cylindrical particles were held in a small clamp which was attached to the moving arm. Granular 8-12 mesh catalyst particles were first attached to a small wooden dowel via the use of glue, and the dowel held in a small clamp attached to the moving arm. In Figure 3-19 are shown photomicrographs of the catalyst holder assembly. In the case of the 8-12 mesh catalyst particles, the glue was removed from the catalyst particles via a combustion technique prior to making the final weight measurement. This combustion technique consisted of burning off the glue and a small portion of the dowel attached to the glue (the major portion of the dowel was simply cut off) in a laboratory furnace with flowing air at 1300°F. Blank measurements of dowel glued particles indicated this technique was capable of effecting complete glue and dowel removal. In order to eliminate any thermal effects, the catalyst particles were pre-exposed to 1300°F air before being exposed in the PLPET apparatus, and its water level held constant before any weight measurement was made. Initial runs using 1-methylnaphthalene as the liquid indicated this fluid had some solvent power relative to the glues tried, which tended to loosen the particles from the dowel at high speeds. In order to solve this problem, water was substituted as the fluid. Similarly, early runs with the combustion furnace at 1700°F indicated that Shell 405 catalyst exhibited some spontaneous weight loss simply from exposure to flowing air at this temperature, necessitating a reduction of the combustion temperature to 1300°F. This loss presumedly resulted from the volatility of iridium oxide at this temperature (94 to 97). Glue and dowel removal was still effected at this lower temperature. Replicate experiments were made in all cases.

Figure 3-18

Pulsed Liquid Particle Erosion Tester (PLPET)
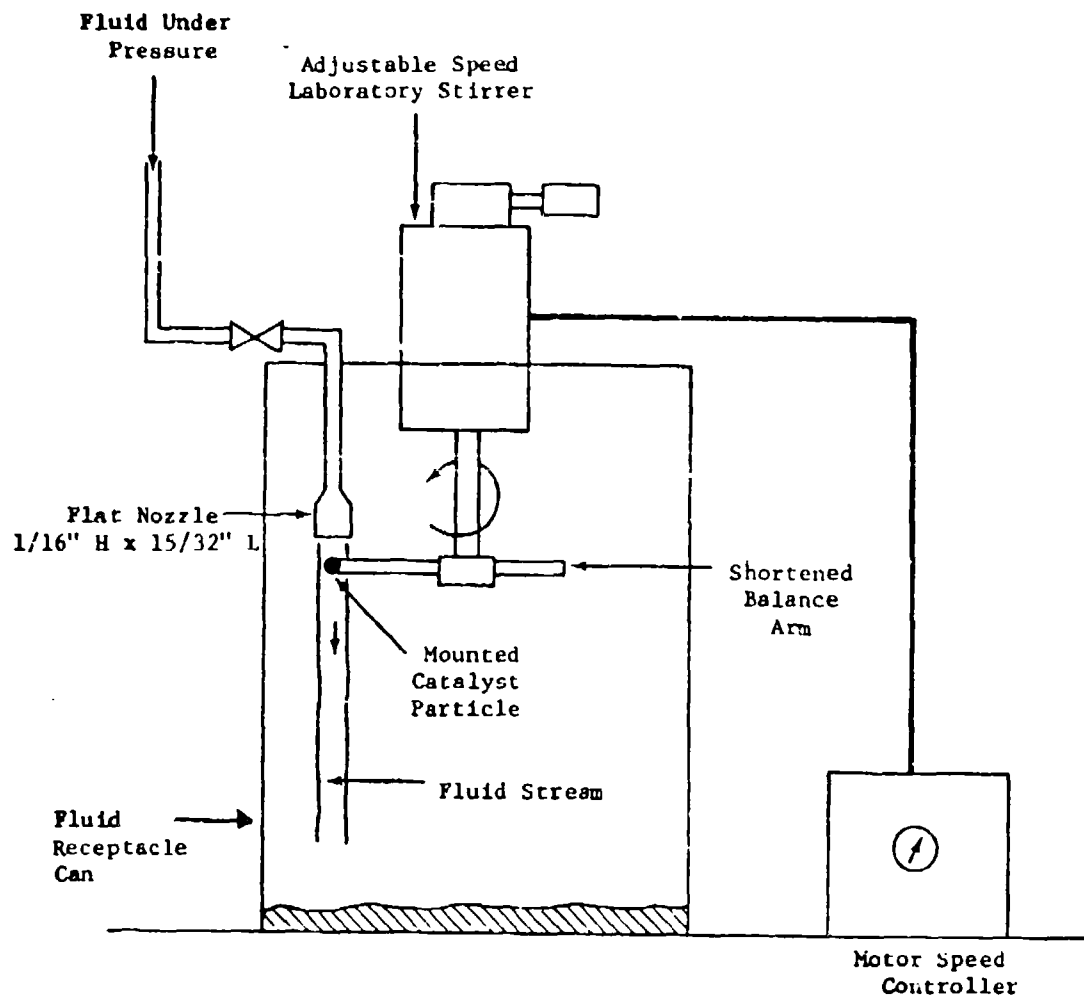
Figure 3-19

PLPET Catalyst Holder
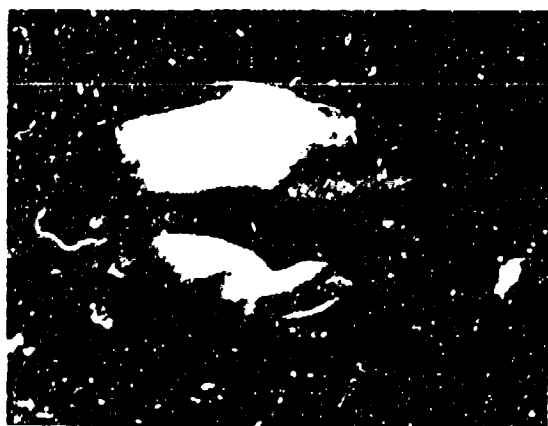
The effect of the number of pulses up to 500,000 pulses was investigated using Fresh Shell 405 1/8" x 1/8" cylinders at 100 feet per second liquid velocity. Results of these tests are shown in Table 23. Individual data is tabulated in the Appendix. In general, the average weight loss increased with increasing number of pulses, although the difference between the average weight loss at 100,000 and 500,000 pulses was not statistically significant, principally because of the rather large variation in individual pellet results after exposure to 500,000 pulses (see detailed data in the Appendix). Photomicrographs of representative pellets taken before and after exposure to pulsed liquid flow are shown in Figures 3-20 to 3-22. Evidence of the effects of liquid erosion on the face of the pellets exposed to 100,000 and 500,000 pulses can be clearly seen.

Table 3-23

Effect of the Number of Pulses at a Fixed Velocity (a,b)

	Number of Pulses		
	8,200	100,000	500,000
Average Weight Loss, %	0.30	0.90	1.06
Sample Size	5	5	5
Standard Deviation, wt % loss	0.17	0.08	1.09

(a) Fresh Shell 405 1/8" . 1/8" cylinders
(b) Velocity of liquid relative to particle, 0 feet per second

The effect of pulsed liquid erosion was investigated further in the PLPET apparatus using the following variables:

- Liquid velocity
- Number of pulses
- Catalyst selection parameters

Figure 2-22

Liquid Erosion Test — Columbium 1/8" x 1/8"
Cylinders at 100 Percent Density and 8,200 Pulses
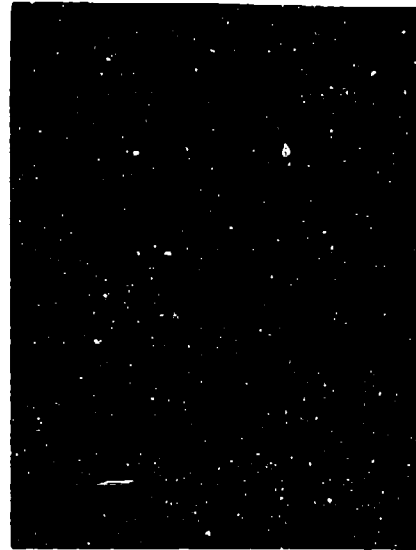
Pellet 1 – Before

Pellet 1 – After
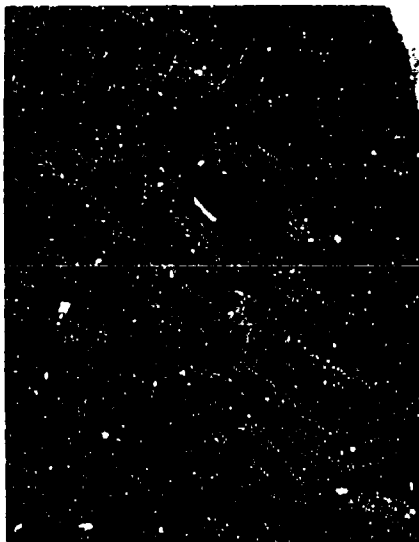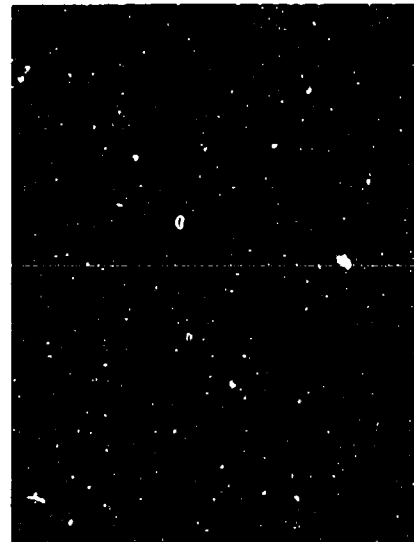
Pellet 3 – Before

Pellet 3 – After

Figure 3-21

Liquid Erosion Test: Rene Shell 405 1/8" x 1/8"
Cylinders at 100 Feet per Second and 100,000 Pulses
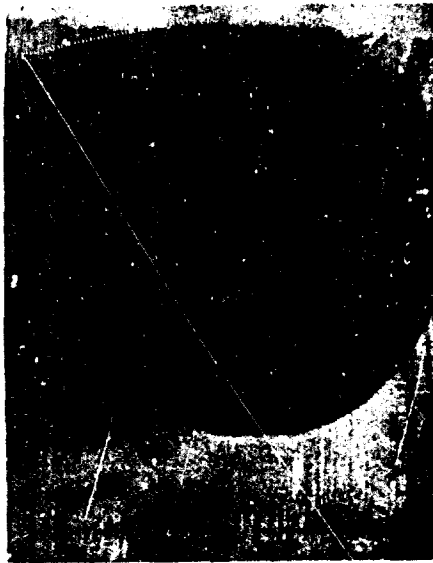
Pellet 3 - Before
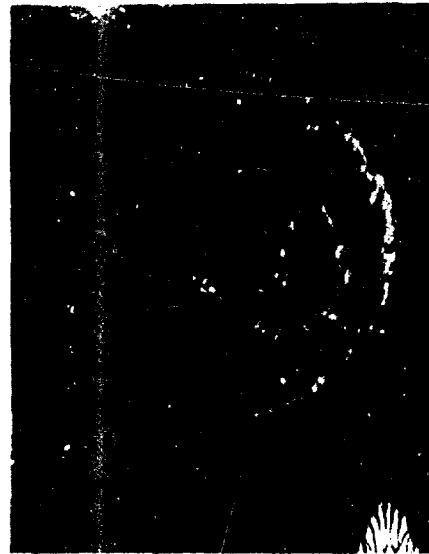
Pellet 3 - After
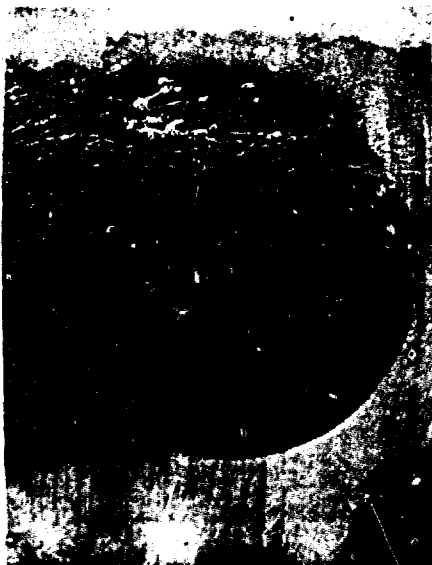
Pellet 5 - Before

Pellet 5 - After

Liquid Erosion Tests ████████████████ 303 1/8" x 1/8"
Cylinders at 10th ██████████████ and 100,000 Pulses

Bullet 3 - Before

Bullet 3 - After

Bullet 3 - Before
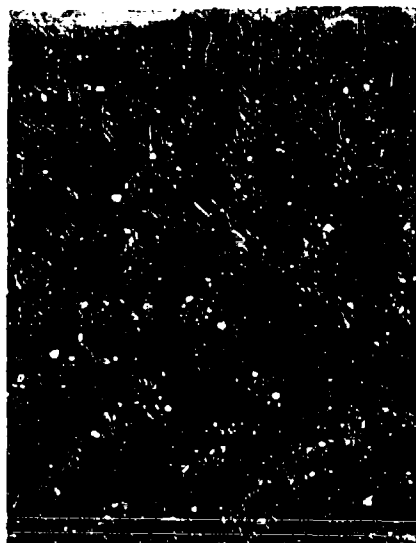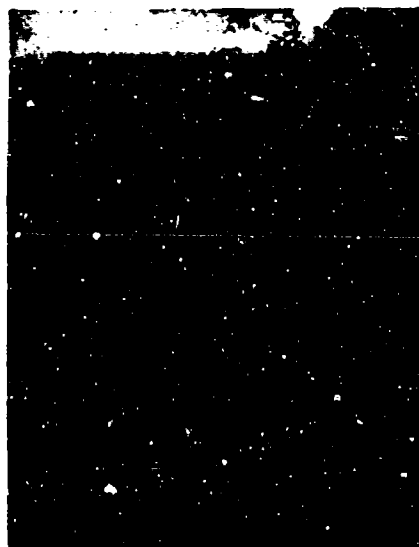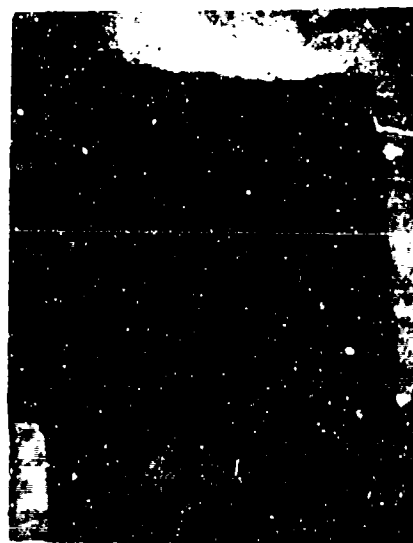
Bullet 3 - After

Each variable was tested at two levels i.e. 55 and 100 feet per second liquid velocity, 8,200 and 100,000 pulses and 1/8" x 1/8" cylinders and 8-12 mesh particles. Individual tests were replicated. The program was planned thus as a 2^3 full factorial statistically designed experiment with replication. This experimental design made possible a statistical analysis for all main effects and two and three factor interactions. A summary of average weight losses for each condition tested is shown in Table 3-24. Photomicrographs of representative catalyst pellets or particles both before and after exposure to the pulsed liquid flow at 55 feet per second are shown in Figures 3-23 to 3-26. Detailed data are tabulated in the Appendix. The average weight loss data as a function of velocity is plotted in Figure 3-29 for the 1/8" cylinders and in Figure 3-30 for the 8-12 mesh granules. Examination of the data indicates that the weight loss for the 8-12 mesh granules was greater than for the 1/8" cylinders at a fixed velocity and number of pulses, and that the weight loss increased with velocity and number of pulses as would be expected.

As indicated previously, photomicrographs of the 1/8" x 1/8" cylinders exposed to a liquid velocity of 100 feet per second and 100,000 and high pulses clearly show signs of pronounced "pitting" on the pellet face exposed to the liquid stream. Photomicrographs of the 8 to 12 mesh granules similarly exposed to a liquid velocity of 100 feet per second and 100,000 pulses do not show evidence of pronounced "pitting", although weight measurements indicate the weight loss at equivalent conditions for the granules was at least as great as for the pellets. Similarly, photomicrographs of both pellets and granules exposed to lower velocities and numbers of pulses do not show signs of pronounced "pitting", although small weight losses were observed.

A statistical Analysis of Variance (ANOVA) was performed on the data (93). The individual data used in the ANOVA is shown in the Appendix, along with the means associated with the three main effects. In Table 3-25 is shown a summary of the ANOVA calculations. Variance ratio tests (F-distribution) were performed on the resultant mean squares using the replicate mean square to determine the residual error. All three main effects (i.e., effect of number of pulses, velocity, and catalyst type) were significant at the 95% confidence level. None of the interactions (i.e., the three two-factor interactions and the one three-factor interaction) were significant at this confidence level.

In general, although pulsed liquid stream erosion was shown to effect particle weight loss, the magnitude of the loss was low with the fresh catalysts tested to date. For example, with a granular catalyst exposed to 100,000 pulses, the average weight loss can be held to only 0.7 wt % if the linear velocity is restricted to a maximum of 50 feet per second. Thus, if liquid injection velocities are held below 50 feet per second, the weight losses experienced by fresh granular catalysts at the bed inlet during a cold start attributable to pulsed, liquid stream erosion per se will be small. The effect of pulsed liquid stream erosion on granular catalysts exposed to aging in a thruster environment, however, remains to be determined. This will be experimentally investigated later in the program.

Table 3-24

Effect of Velocity, Number of Pulses and Catalyst Selection on Liquid Erosion in PLPET

Number of Pulses		Velocity of Liquid Relative To Particle			
		55 Feet per Second		100 Feet per Second	
		1/8" x 1/8" Cylinders	8-12 Mesh Granules	1/8" x 1/8" Cylinders	8-12 Mesh Granules
8,200	Avg. Weight Loss %	0.12	0.25	0.30	0.69
	Sample Size	5	4	5	4
	Standard Deviation	0.06	0.40	0.17	0.28
100,000	Avg. Weight Loss %	0.61	0.79	0.90	1.35
	Sample Size	4	5	5	5
	Standard Deviation	1.08	0.32	0.08	0.22

Pallet 1 - Before

Pallet 1 - After
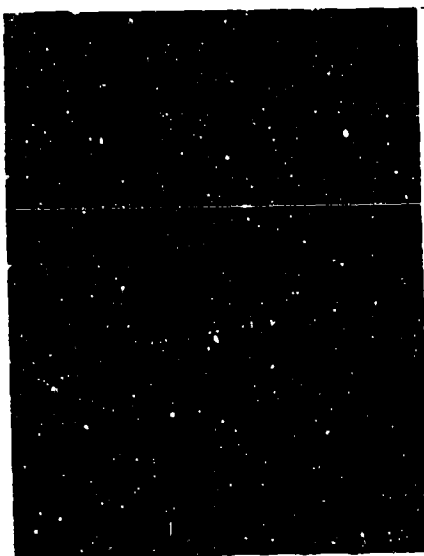
Pallet 5 - Before

Pallet 5 - After

Figure 3.18
Liquid Erosion Test: Armco Stainless 403 1/8" x 1/8"
Cylinders at 55 Feet per Second and 100,000 Pulses
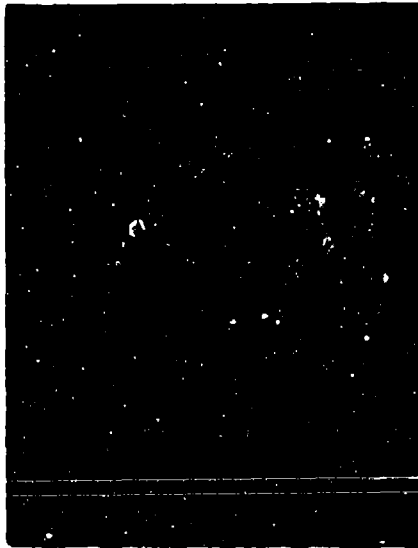
Pellet 1 - Before

Pellet 1 - After
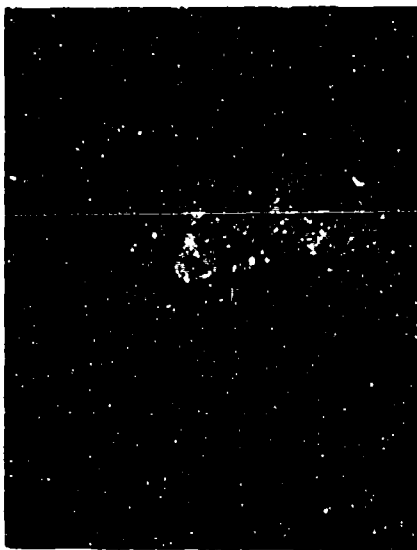
Pellet 4 - Before
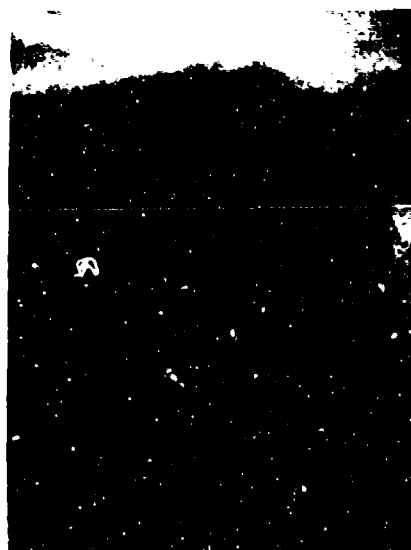
Pellet 4 - After

Particle 4 - Before
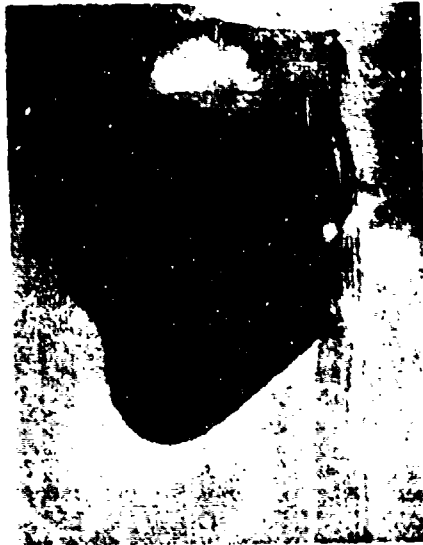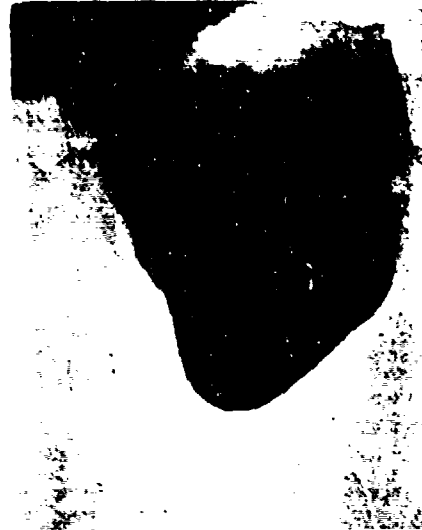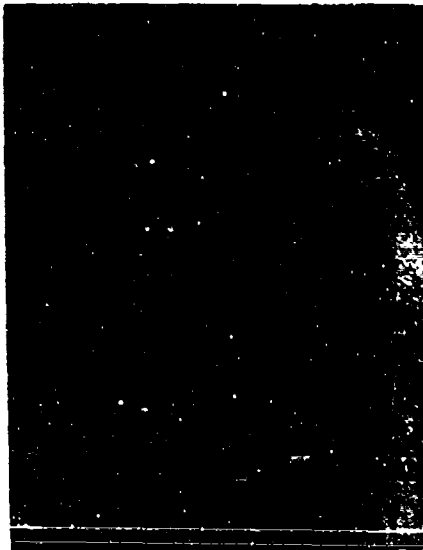
Particle 4 - After
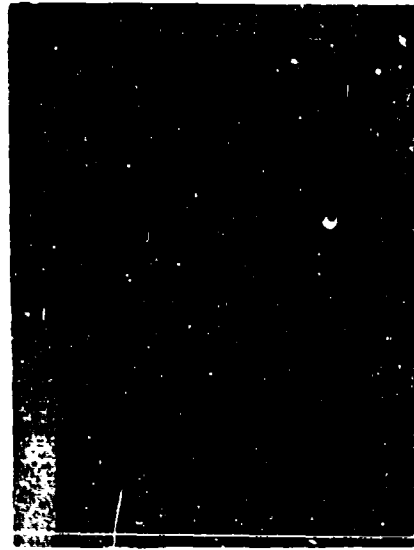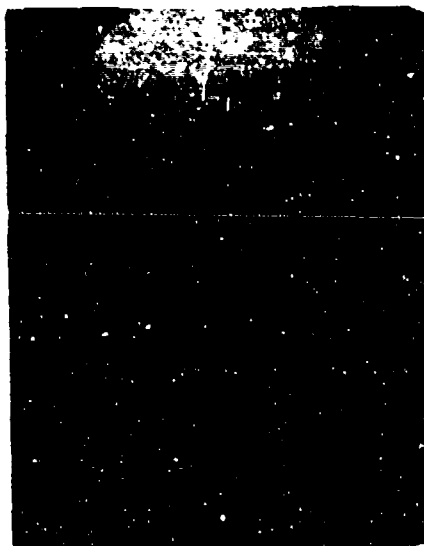
Particle 5 - Before
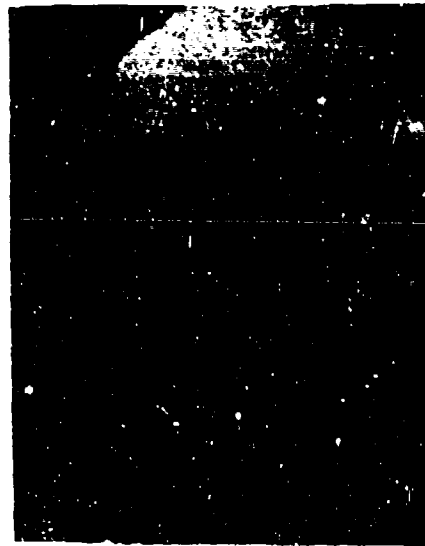
Particle 5 - After

Figure 2-27

Liquid Erosion Test: Beach Shell 405 8 to 12 Mesh
Particles at 100 Feet per Second and 8,200 Pulses

Particle 3 - Before

Particle 3 - After

Particle 4 - Before
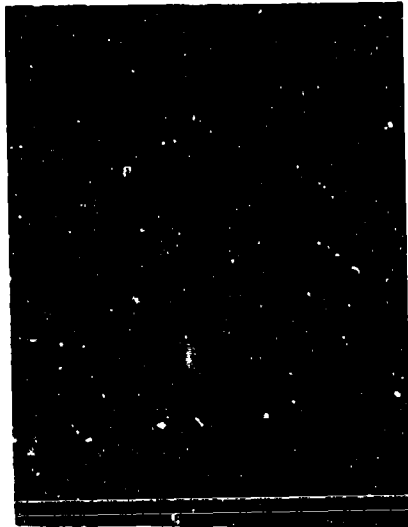
Particle 4 - After

Particle 1 - Before

Particle 1 - After

Particle 3 - Before
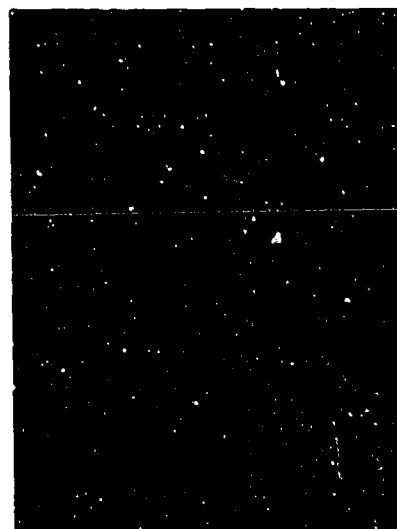
Particle 3 - After

Figure 3-29

Liquid Dynamic Erosion of Fresh Shell 405
1/8" x 1/3" Cylinders
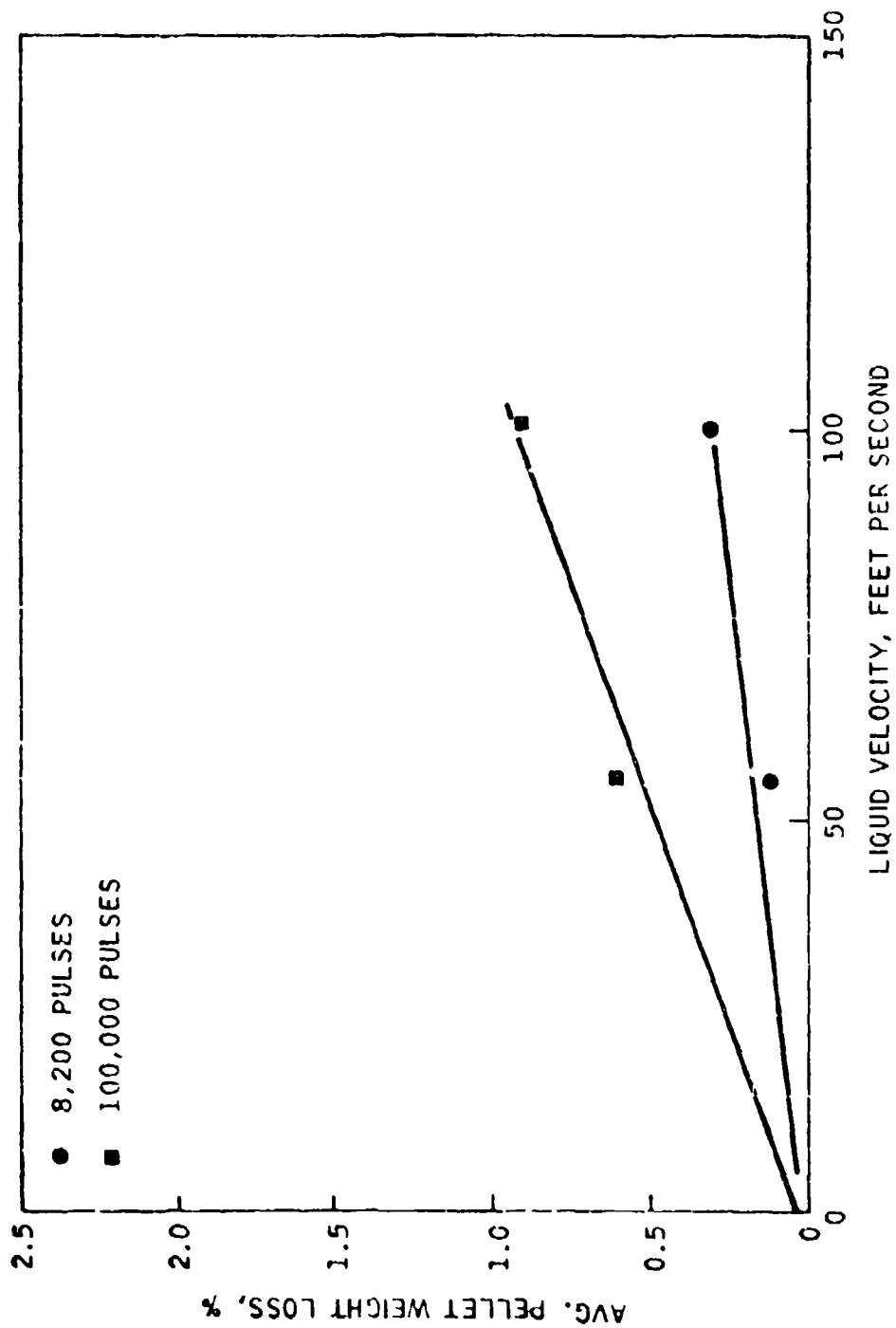
Figure 3-30

Liquid Dynamic Erosion of Fresh Shell 405
8 to 12 Mesh Particles
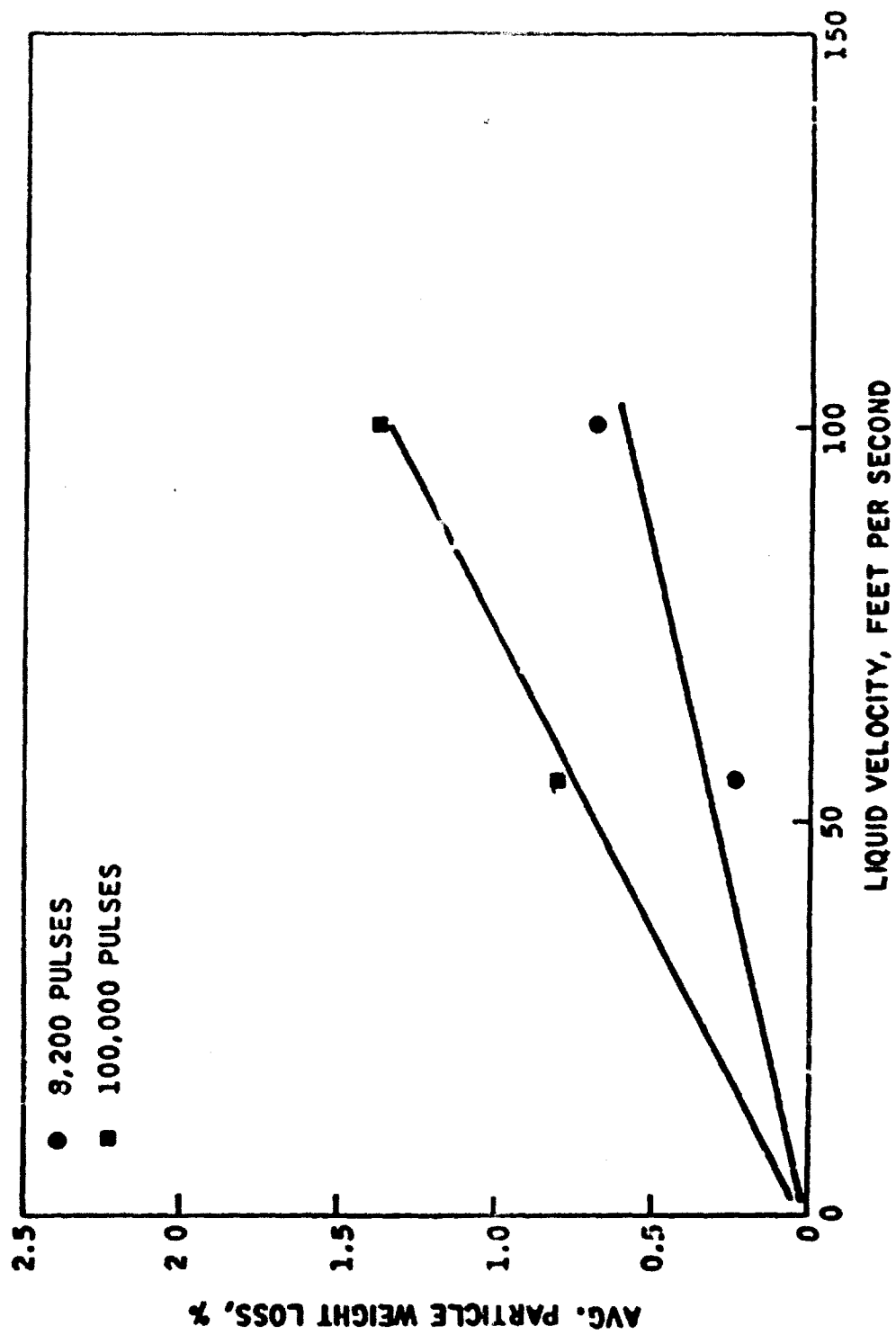
Table 3-25

Analysis of Variance (ANOVA) Summary

Pulsed Liquid Erosion Data

Source of Variation	Sum of Squares	Degrees of Freedom	Mean Square
Pulse Number	3.26041	1	3.26041
Velocity	1.35424	1	1.35424
Catalyst Type	0.82944	1	0.82944
Pulse Number x Velocity Interaction	0.03025	1	0.03025
Pulse Number x Catalyst Type Interaction	0.00961	1	0.00961
Velocity x Catalyst Type Interaction	0.16900	1	0.16900
Pulse Number x Catalyst Type x Velocity Interaction	0.00009	1	0.00009
Replicates	4.98215	32	0.15569
TOTAL	10.63518	39	--

3.2.6 Thermal Shock

It was proposed in the modified program plan (revision of 18 February 1975) to investigate two areas related to the general problem of thermal shock. The first was termed "Hot Gas Thermal Shock" and involved the investigation of the effect of repeated thermal cycling of a bed under varying pressure loads. It, thus, is representative of the thermal cycling fatigue experienced by a lower bed section during repeated cold starts. The second was termed "Liquid Quench Thermal Shock" and involved the investigation of the effect of the injection of a cold liquid onto a hot catalyst bed. It, thus, is representative of an upper bed section during a hot start.

Air Force directions of 7 March 1975, however, indicated that other work was to be substituted for the thermal shock study originally planned while awaiting thermal shock results from United Aircraft Research. These thermal shock studies will be carried out later in the program.

3.3 Estimation of Catalyst Strength of Material Properties

Strength of material properties are important parameters in interpretating both experimental and analytical results. Determination of the true strength of material properties of the small, irregularly shaped Shell 405 catalyst particles is a difficult task. To help overcome this difficulty, Dr. D. P. H. Hasselman, Director of the Ceramics Research Laboratory, Lehigh University was retained to (1) provide expert opinion and advice in this area, and (2) to estimate a number of material properties of individual catalyst particles. Dr. Hasselman's reports describing this effort are contained in the Appendix.

Experimental measurements were also made using the ITI to help estimate Shell 405 catalyst properties. Stress-strain measurements were made on Shell 405 1/8" x 1/8" cylinders in compression. Blank measurements were also made. These measurements yielded a Youngs Modulus of approximately 300,000 psi. A measurement was also made using the PCRB/ITI to determine a bed modulus using 20 to 25 mesh Shell 405 catalyst at pressures up to 1,000 psi. This experiment yielded a bed modulus of approximately 25,000 psi. A modulus of this magnitude indicates that a bed subjected to a 100 psi load will compact approximately 0.4%.

4. ANALYTICAL MODELING

4.1 Introduction

4.1.1 Organization of the Effort

Analytical modeling supporting studies were carried out by
McDonnell Douglas Astronautics Company (MDAC). The MDAC Study Manager for
this project was Mr. R. J. Hoffman, Project Thermodynamics Engineer--Plume
Effects, Aero/Thermodynamics and Nuclear Effects Department. Mr. W. T. Webber
of the same department acted as Principal Investigator for the study and
performed the analyses of the internal particle behavior and of pressure
shocks. Mr. S. A. Schechter of the Structures Department performed the
analyses of stresses from thermal shock, internal pressure, particle-to-
particle contact, and examined the mechanical failure mechanism. Mr. D. Quan
of the Propulsion Department performed the analyses related to differential
expansion. The analysis of fluid erosion was done by Dr. W. D. English
of the Propulsion Department.

4.1.2 The General Purpose and Limitations

Analytical modeling studies in general were conducted both to
support experimental activities and to explore areas not investigated
experimentally. In order to carry out these supporting analyses a number
of assumptions had to be made in regards to (1) the nature of the governing
equations and analytical descriptions of the phenomena involved (2) typical
values for thruster parameters such as catalyst size, bed loading etc. and
(3) the various physical properties of Shell 405 granules, particularly in
the strength of materials area. It was recognized a priori (1) that the
decisions made in the areas of thruster parameters would not be universally
applicable (2) true strength of material properties of granular Shell 405
catalyst were generally not available, and (3) our knowledge of the detailed
processes involved in various proposed catalyst breakup mechanisms is often
incomplete. Thus, the modeling work described in this report was not intended
to provide universal and final answers to all catalyst breakup and thruster
design problems but rather to provide appropriate and timely support to
the overall effort, and particularly to the phenomenological survey portion of
the program.

4.1.3 General Description

The areas involved in analytical modeling are shown in Table 4.1.
The interrelationship between the experimental studies and supporting analyses
were previously shown in Table 3-3. These studies had a number of objectives. First,
they were designed to aid in the discrimination of important highly destructive mech-

- 96 -

anisms from the less important mechanisms, so as to help guide the direction of the concurrent and subsequent experimental tasks in the direction of the most important phenomena. Second, these studies were designed to aid in the interpretation and correlation of the results of the experimental studies. Third, and perhaps most important, the analytical models were to be the means of extending the findings of experimental results to other operating conditions, and to aid in predicting how catalyst failure can be controlled by appropriate choices of engine design and operational parameters.

Although the analyses have been broken into several categories, the majority have a common meeting ground in the limited physical strength of the catalyst.   Whenever the local stresses developed in the catalyst material exceed certain values, local failure and loss of material will result.

The stresses at the contact points between two adjoining catalyst particles are amenable to analysis by Hertzian contact theory to determine these local stresses, regardless of whether the contact forces are produced by steady gas pressure drop through the bed, pressure shocks acting upon the bed, differential expansion tending to compact the bed, or.even the impact of two colliding particles. Stresses may be generated in the interior of the particle by rapid external heating or cooling, rapid externally applied pressurization or depressurization, or by the local generation of heat or gas pressure interior to the particle, from the decomposition of liquid hydrazine which has flowed into the interior of the particle under the action of surface tension forces or externally applied pressure. In any of these cases, the radial temperature or pressure profile suffices to determine the radial and tangential stress field interior to the particle.

Thermally derived stresses, pressure derived stresses, and point-to-point contact derived stresses may be calculated individually, and then superposed to yield the total stress field, and this will show synergistic effects when several processes act together to exceed a failure stress that would not have been attained by any of the processes acting singly.

The thermally induced free volume changes of the bed and chamber hardware during a startup and shutdown may be calculated from the sequence of time-varying temperature profiles in each. These profiles are obtained from existing computer programs described the thermochemistry and the flow through the bed. To obtain bed compression stress from the volume change requires a bed deformation theory, since loaded granular materials are inherently nonlinear in deflection, and do not have constant elastic moduli. Evaluating the local stresses in the particles at locations of point-to-point contact also requires a structural model.

The erosion by gas-entrained hydrazine droplets or solid particles carried through the bed requires a still different bed model. Mass losses may be calculated by knowledge of the effects of particle velocity and impact angle upon the local mass-loss ratio, the abrasion resistance property of the substrate, and the variation of this property with temperature. These are combined with the calculated gas velocity profile, catalyst temperature profile, and hydrazine quality profiles in the catalyst bed, to give a numerical solution by marching through the bed. Primary and secondary particles are carried along in these calculations in marching from the injector end to the downstream end of the catalyst pack. Impacts are presumed to occur at each new layer of catalyst particles which is encountered.

Table 4-1

Supporting Analyses

1. Thermal Shock Stresses in Individual Catalyst Particles

    A. Calculate time-dependent temperature profiles in individual
        catalyst particles.

    B. Calculate stresses resulting from the temperature profiles.

2. Internal Pressure Stresses in Individual Catalyst Particles

    A. Calculate time-dependent pressure profiles in individual
        catalyst particles.

    B. Calculate stresses resulting from the pressure profiles.

3. Differential Thermal Expansion of Catalyst Bed and Chamber

    A. Calculate time-dependent temperature, pressure, and velocity
        distributions in the bed during a smooth start transient.

    B. Calculate temperature distributions in chamber hardware.

    C. Calculate time-dependent differential bed compression.

    D. Calculate stresses in individual particles resulting from bed
        compression.

4. Fluid Dynamic Erosion

    A. Calculate time-dependent temperature, pressure, and velocity
        distribution in the bed during start transients and steady-
        state operation.

    B. Calculate erosion rate of catalyst particles based upon impinge-
        ment of gas carrying entrained droplets and particles.

5. Pressure Shocks in Bed

    A. Calculate time-dependent flow processes in bed during hard start.

    B. Calculate bed compression from pressure distribution.

    C. Calculate particle stresses resulting from bed compression.

4.2 Structures Analyses

4.2.1 Stress Failure Model

The purpose of the stress failure analysis was to develop a failure model for the Shell 405 catalyst by extending the uniaxial compressive failure value, which was experimentally measured using 1/8" x 1/8" cylinders, to a multiaxial, tension-compression failure surface, suitable for use for other shapes of catalyst particles, and for other modes of stress application.

In the failure tests described in Section 3.2 the 1/8" cylindrical pellets were loaded in uniaxial compression. The failure stress for fresh Shell 405 catalyst was 2836 psi with a standard deviation of 19 percent. The failure level for used material was 1785 psi with a standard deviation of 53 percent. The typical failure was a crack in the direction of the load in each pellet, shown schematically in Figure 4.1. This type of overall (macroscopic) fracture is typical in porous brittle materials (99). The failure is due to the local (micromechanical) tensile stresses which occur at the surface of the internal pores at 90° to the load direction.

In the remaining analyses, a failure criteria is required to assess the severity of the macroscopic or gross stress states produced by the thermal, internal pressure and contact loadings. As only uniaxial compressive failure data were available, the simple local maximum tensile stress around the pores was selected as the failure mode. The pore shape, a cylindrical pore, was selected from a microscopic examination of the material. If more types of failure test data were available, e.g., tensile, biaxial, etc., then a more complicated two or even three dimensional failure model could be developed.

The solution of the stress state in the substrate material around a cylindrical pore in a semi-infinite media in uniaxial stress was obtained from Reference 101. The stress state produced at the pore boundary by biaxial loading of the porous material was obtained by superposition of two stress states produced by uniaxial loading, with one rotated 90 degrees to the other.

For circular cylindrical void in a semi-infinite medium under macroscopic biaxial tensile loads, S_1 and S_2, the maximum micromechanical tensile stress is circumferential, at the surface of the void. The distribution is easily found from the Reference 101 solutions to be

$$\sigma_r = S_1 (1 + 2 \cos 2\theta) + S_2 (1 - 2 \cos 2\theta) \qquad (4.2-1)$$
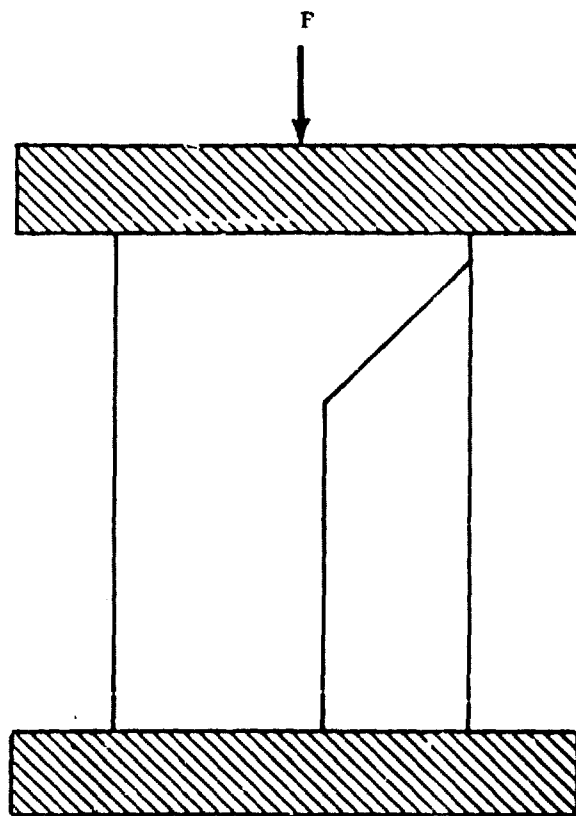
Figure 4-1.   Failure in a Brittle Porous Material.

and the maxima are $(\sigma_\theta)_{max} = \begin{cases} 3\ S_1 - S_2, & \text{at } \theta = \pm \frac{\pi}{2}, \text{ for } S_1 > S_2 \\ 3\ S_2 - S_1, & \text{at } \theta = 0,\ \pi\ \text{ for } S_2 > S_1 \end{cases}$ (4.2-2)

where θ is the angle around the void, and $\theta = 0$ is aligned with S_1, as shown in Figure 4-2.

Note that since the radial stress is zero at the surface, the micromechanical stress state is uniaxial at the surface, even though the macroscopic load is biaxial. Thus we can relate the biaxial tension-compression macroscopic failure criterion desired to a micromechanical uniaxial tensile failure.

The macroscopic failure stress measured for the fresh material under uniaxial compression ($S_1 = 2836$ and $S_2 = 0$), shows the micromechanical tensile failure strength (from equation (4.2-2)) $(\sigma_0)_{max}$ is 945 psi. The macroscopic failure stress measured for the used material under uniaxial compression ($S_1 = 1785$ psia and $S_2 = 0$) shows the micromechanical tensile failure strength (from equation 4.2-2) is 595 psi. The corresponding biaxial macroscopic failure envelope generated by equation (4.2-2) is shown in figures 4-3 and 4-4. The details of the shape of the envelope will change if different assumptions are made for pore shape but the basic failure envelope shape will remain (102). The complete solution for the arbitrary elliptical void was solved in Reference 102. For an elliptical hole under uniaxial tension with the major axis, a, normal to the load and a minor axis, b, the maximum tension is

$$\sigma = S\ (1 + 2\ \frac{a}{b}) \qquad\qquad (4.2-3)$$

Two-dimensional stress distributions caused by stress boundary conditions do not involve the elastic constants. In the general three-dimensional case the solution does depend on the elastic constants, in particular on Poisson's ratio, ν. In the following micromechanical three-dimensional analysis, the Poisson's ratio used is that of the solid material surrounding the pores, denoted ν_s. In the later macroscopic analysis of the stresses produced by thermal, pressure, and contact loadings, the Poisson's ratio used is that of the overall porous medium. The Poisson's ratio, ν_s, of the substrate material is known, 0.32 for temperatures up to 1800°F. The Poisson's ratio of the actual catalyst is not known.

The peak micromechanical σ_{max} tensile stress for a spherical void in a solid body under uniaxial compression stress S, seen from Reference 101, is

$$\sigma_{max} = \frac{15\ \nu_s - 3}{2\ (7 - 5\ \nu_s)}\ S \qquad\qquad (4.2-4)$$

Figure 4-2
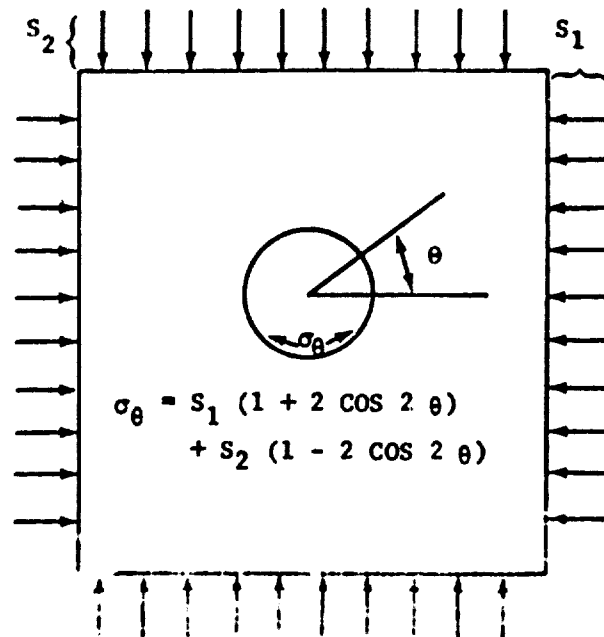
Figure 4-2. The Stress Distribution Around a Cylindrical Hole in Biaxial Stress.

$$\sigma_\theta = S_1 (1 + 2 \cos 2\theta)$$
$$+ S_2 (1 - 2 \cos 2\theta)$$
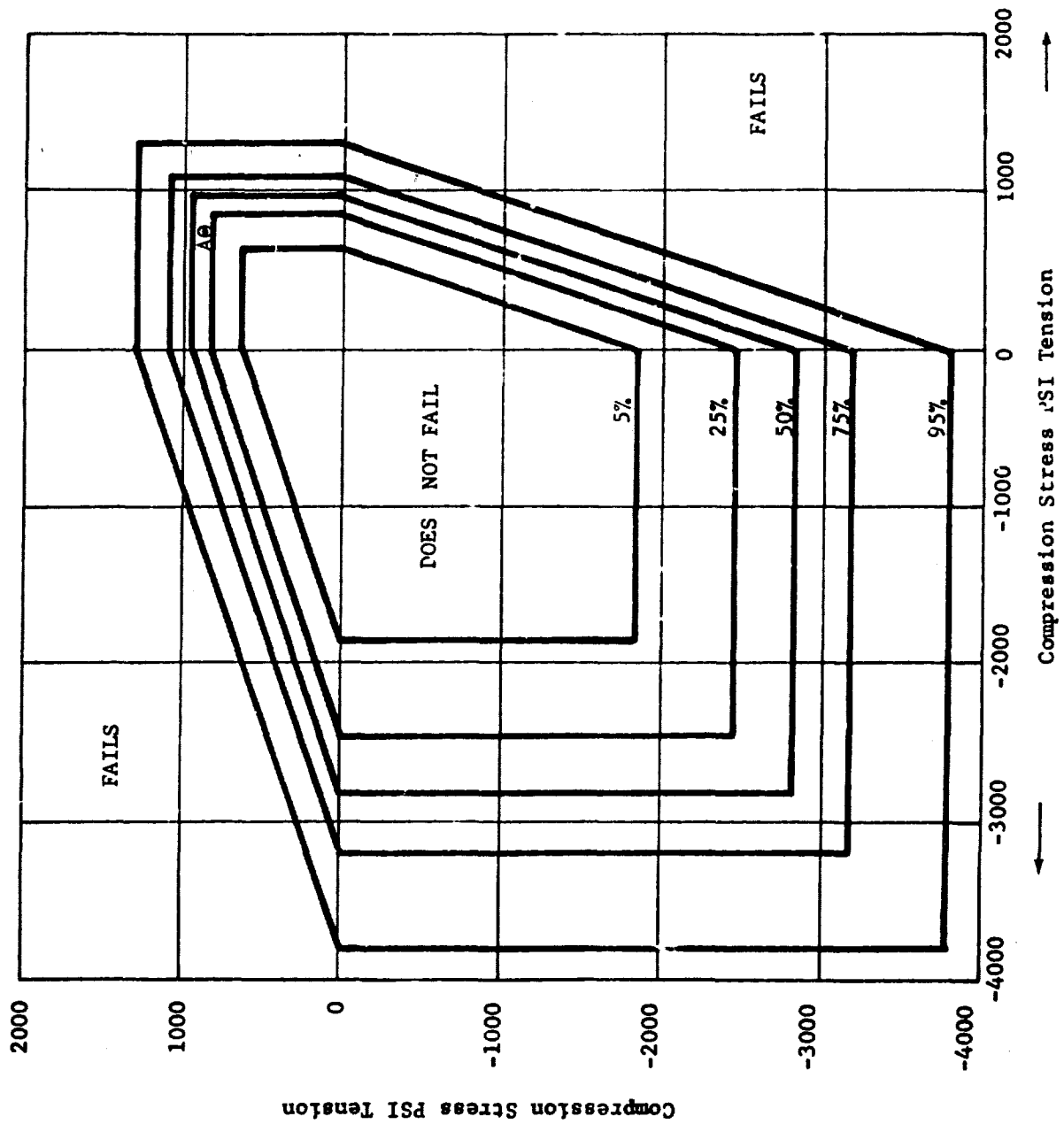
Figure 4-3. Failure Surface for Biaxial Loading - Fresh Shell 405.
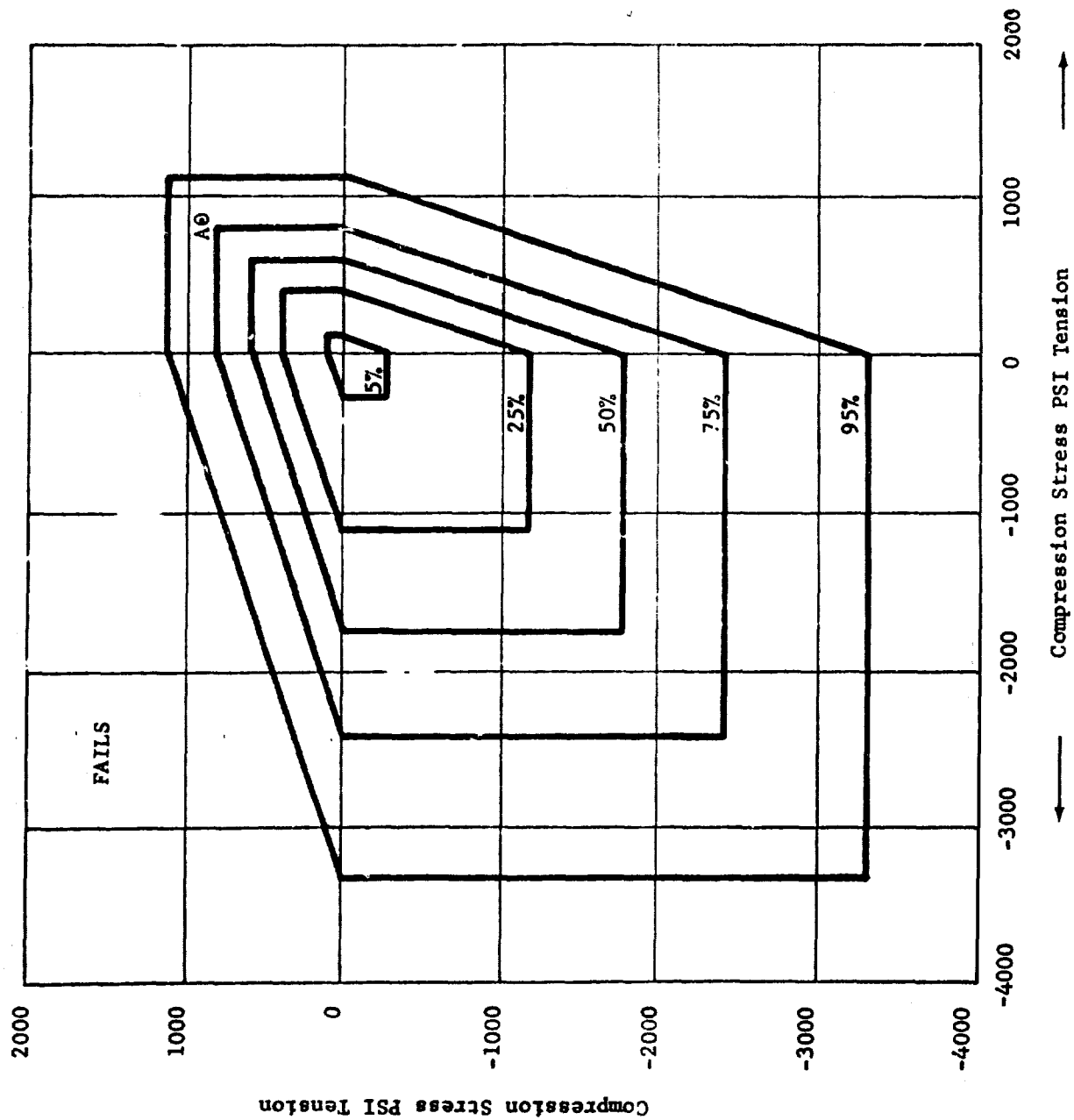
Figure 4-4. Failure Surface for Biaxial Loading - Used Shell 405.

For $\nu_S = 0.32$, $\sigma_{max} = 0.7225S$. The tensile stress produced by a biaxial load could be obtained by superposition as done for equation 4.2-1. However, the solution for the maxima is somewhat complicated, and has not yet been worked out. The micromechanical tensile failure stress for a spherical void is 2048 psi. This is more than two times the failure stress of a cylindrical void, 945 psi. This difference indicates the dependence of the failure criteria used here on the assumption made regarding pore shape, and points up the need for failure tests using biaxial and, if possible, triaxial, stress states. Even uniaxial tensile failure test data would greatly reduce the uncertainties.

4.2.2 Temperature Profiles Developed Inside a Catalyst Particle by External Heating or Cooling

The temperature profiles developed when an initially cold catalyst particle is externally heated, or when a uniformly hot catalyst particle is externally cooled is a function of two dimensionless moduli, the Biot number and the Fourier number.

The Biot number expresses the effect of the external thermal resistance on the transient temperature profiles which are developed inside the thermally conductive body, and is especially important for the real case where heat is transferred to (from) the body from a hot (cold) fluid flowing past the body. The Biot number is, roughly speaking, the ratio of external thermal conductance to internal thermal conductance. If, for instance, a cold, thermally resistive sphere were exposed to a hot external fluid of infinite conductance, the exterior boundary of the sphere would instantly assume the high external temperature, and the thermal gradient in the outermost lamina of the sphere would be infinite. This would correspond to an infinite Biot number. If, instead, the interior of the sphere had infinite conductance, while the conductance of the hot fluid surrounding it was finite, the sphere would heat up uniformly, with no internal gradients. This would correspond to a Biot number of zero. The Biot number is:

$$Bi = \frac{hr}{kp} \qquad (4.2-5)$$

where r is the radius of the particle
$\quad$ kp is the thermal conductivity of the particle
$\quad$ h is the heat transfer coefficient for the convected fluid
$\quad\quad$ surrounding the particle. h is defined by the equation

$$q/\wedge = h \, \Delta T \qquad (4.2-6)$$

the value of h is generally estimated in terms of a dimensionless Nusselt number:

$$Nu = \frac{hD}{k_F} \qquad (4.2\text{-}7)$$

where D = diameter of the particle
k_F = thermal conductivity of the fluid flowing around the particle.

The Nusselt number is generally estimated from a correlation involving Reynolds number and Prandtl number. An acceptable correlation for sphere is:

$$Nu = 2 + .6\ Re^{1/2}\ Pr^{1/3} \qquad (4.2\text{-}8)$$

Reynolds Number is defined:

$$Re = \frac{\rho V D}{\mu} = \frac{GD}{\mu} \qquad (4.2\text{-}9)$$

where ρ is density of the fluid
V is velocity of the fluid
D is diameter of the particle
μ is viscosity of the fluid

and Prandtl number is:

$$Pr = \frac{C_p\ \mu}{k_F} \qquad (4.2\text{-}10)$$

where C_p is specific heat of the fluid at constant pressure
μ is viscosity of the fluid
k_F is thermal conductivity of the fluid

For hydrazine decomposition products the following estimates of physical properties were assumed:

C_p = .725 cal/gram °K
μ = 6.66 x 10^{-4} poise
k = 5.56 x 10^{-4} cal/cm sec °K

$$P_r = \frac{.725 \times 6.66 \times 10^{-4}}{6.56 \times 10^{-4}} = .736$$

For a conservative catalyst bed design, the following values were assumed:

$$G = .05\ \frac{pounds}{in^2\ sec} = 3.5\ \frac{gram}{cm^2\ sec}$$

$$D = .10\ cm\ (25\ mesh)$$

then, $$Re = \frac{3.5 \times .10}{6.66 \times 10^{-4}} = 526.$$

The Nusselt Number may now be calculated

$$Nu = 2 + .6(526.)^{1/2}(.736)^{1/3} = 14.4$$

This permits calculation of the heat transfer coefficient:

$$h = \frac{Nu\ K}{D} = \frac{14.4 \times 6.56 \times 10^{-4}}{.1} = .0944\ \frac{cal}{cm^{2 \circ}K}$$

To estimate the Biot number it is necessary to have a value for the thermal conductivity of the catalyst. Values may be found in the literature which vary from .005 to .05 $\frac{cal}{cm\ sec^{\circ}K}$ hence the Biot number for the external heating of the particle will fall within the range:

$$Bi = \frac{.0944 \times .05}{.05} = .0944$$

to

$$Bi = \frac{.0944 \times .05}{.005} = .944$$

Obviously if different values are used for pellet radius or bed loading (chamber pressure or contraction area ratio) then the Biot number will vary correspondingly.

To estimate the Biot number for the cooling of a hot particle being quenched in liquid hydrazine, a value for the maximum heat transfer coefficient for boiling heat transfer to the quench liquid must be obtained. Experimental investigations of boiling heat transfer to water show that the heat transfer rate increases rapidly with temperature difference until a threshold value is reached, whereupon the heat transfer changes from nucleate boiling to film-boiling, and the heat transfer rate decreases enormously. At the maximum value, just before the transition, the temperature difference is approximately 150°F (83°C) and the heat transfer rate is approximately 410,000 BTU/hr-ft^2 (30.9 cal/cm^2 sec). The corresponding value for heat transfer coefficient is:

$$h = \frac{30.9}{83.} = .37\ cal/cm^{2 \circ}C$$

If we presume that this same value will be obtained with boiling hydrazine instead of water, then the Biot number may be estimated (using high and low estimates for thermal conductivity of the catalyst):

$$Bi = \frac{.37 \times .05}{.05} = .37$$

$$Bi = \frac{.37 \times .05}{.005} = .37$$

Hence external cooling by cold hydrazine results in a Biot number approximately four times higher than external heating by hot product gases.

The Fourier number is the undimensionalized time in which a transient heating or cooling event may be measured. The time required to heat an object is proportional to its heat storage capability:

$$\Delta H = AL\rho C_p \Delta T \qquad (4.2\text{-}11)$$

where

ΔH is stored heat
A is cross-sectional area of the element
L is the length of the element
ρ is the density of the material
C_p is the specific heat of the material
ΔT is change in temperature

The time required to heat an object is inversely proportional to its heat conduction rate $\overset{\circ}{H}$, where

$$\overset{\circ}{H} = \frac{A\,K_t}{L}\,\Delta T \qquad (4.2\text{-}12)$$

where K_t is thermal conductivity

Combining the expressions, and introducing a parameter of proportionality:

$$t = Fo\,\frac{\rho Cp\,L^2}{K_t} \qquad (4.2\text{-}13)$$

The parameter in this expression, Fo, is called the Fourier number, and expresses the extent of completion of the thermal transient.

For a particle of catalyst:

$\rho = 3.4$ gram/cm^3
$Cp = .22$ calories/gram K
$L(radius) = .05$ cm (25 mesh)
$K = .01$ (median value) calories/cm sec °K

$$Fo = \frac{Kt}{\rho CpL^2} = \frac{.01\,t}{3.4 \times 22 \times .05^2} = 5.4\,t$$

With the Biot number and Fourier number identified, it is easy to look up the solutions for the transient temperature profiles inside the catalyst particles in standard reference texts, (Reference 103). A family of profiles for a Biot number of 1.0 similar to a worst-case for external heating is shown in Figure 4-5. A family of profiles for a Biot number of 4.0, similar to a worst-case for external cooling is shown in Figure 4-6.
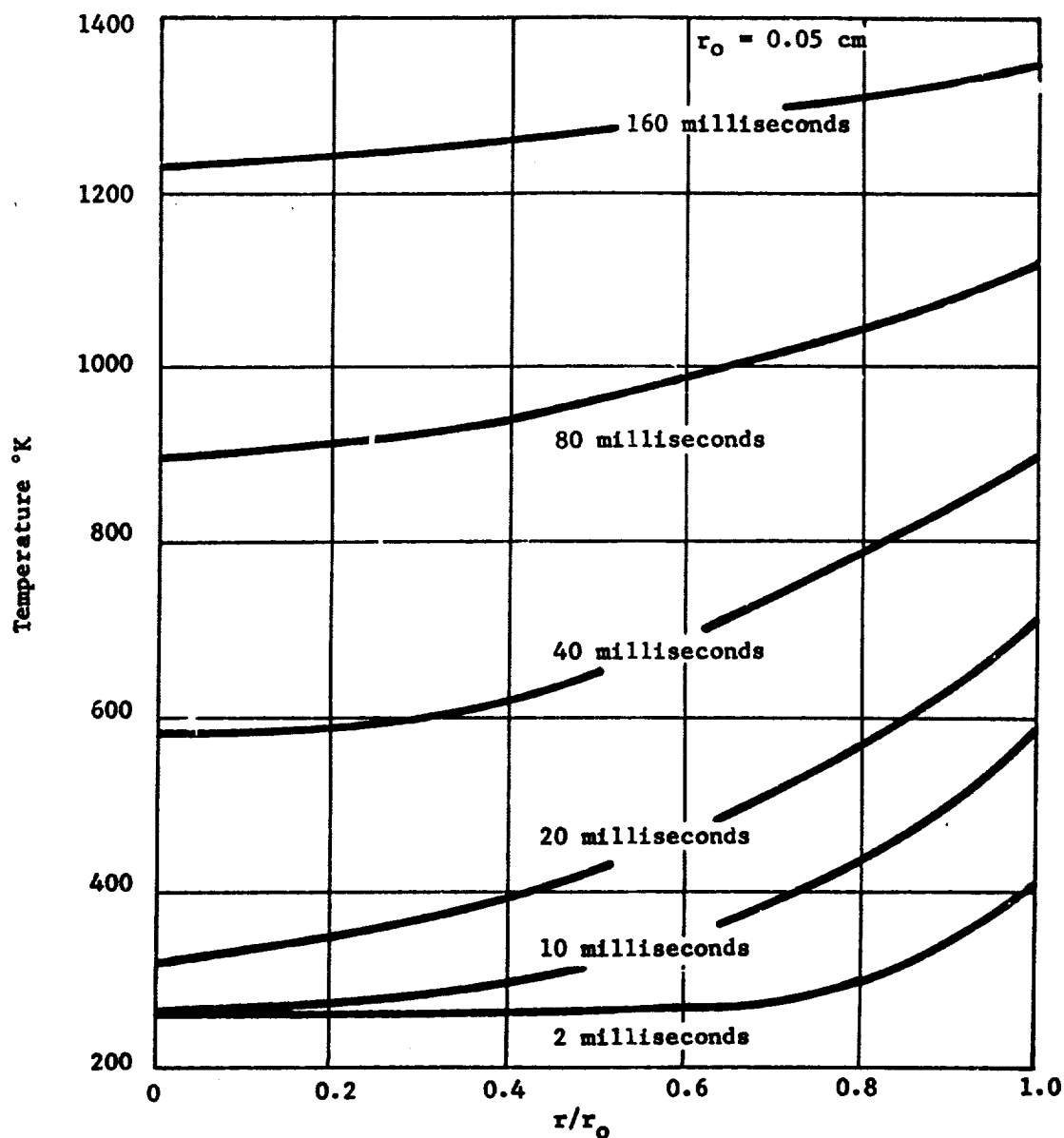
Figure 4-5. Temperature Profiles in an Externally Heated Spherical Pellet as a Function of Time During Heating.

Biot Number = 1.0

Hot Gas Temperature = 1473°K
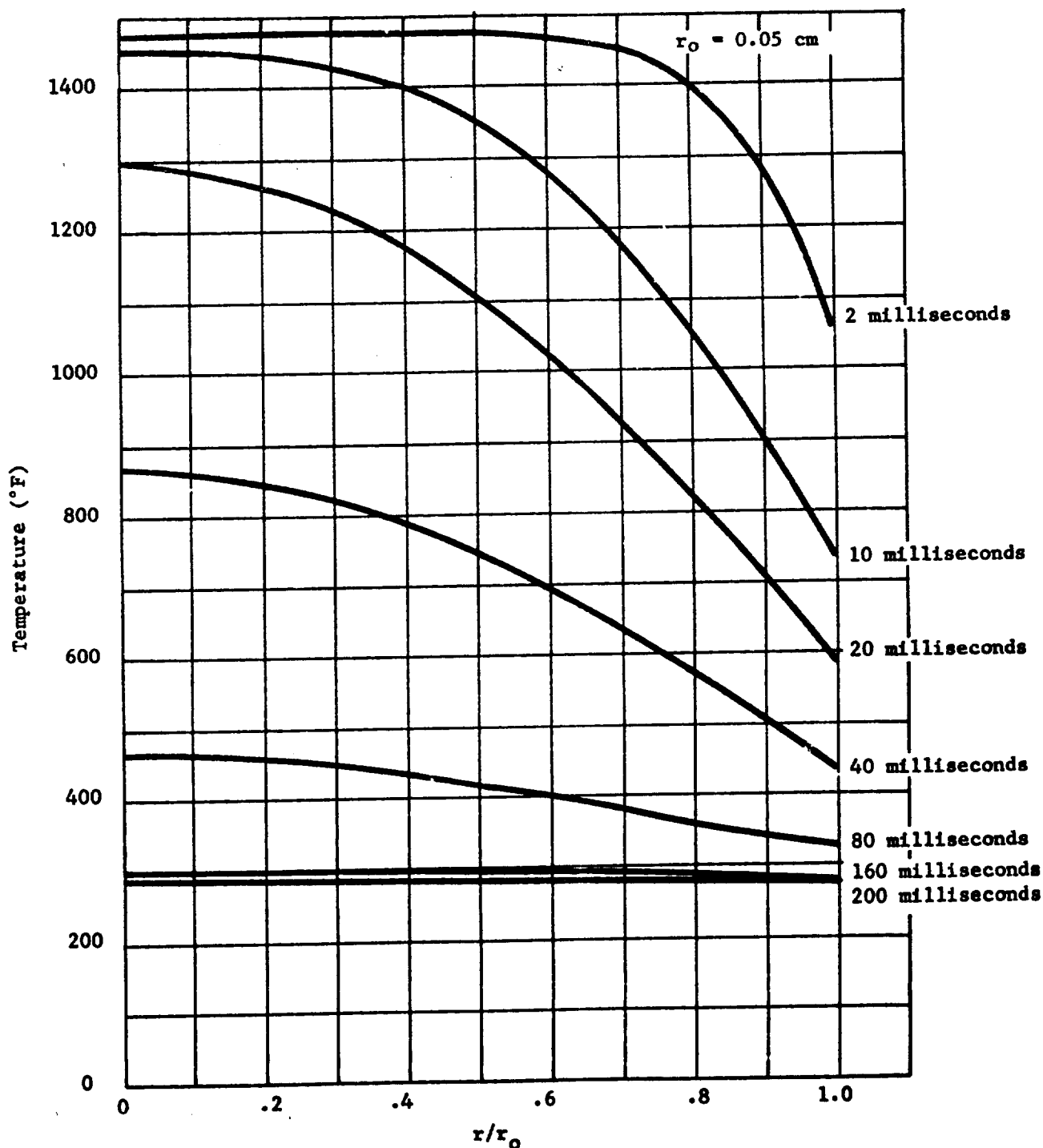
Figure 4-6. Temperature Profiles in an Externally Cooled Spherical Pellet as a Function of Time.

Biot Number = 4.0, corresponding to maximum rate nucleate boiling heat transfer.

- 110 -

4.2.3 Particle Stresses Resulting From Thermal Shock

The stresses which result from internal temperature profiles developed in a catalyst particle may be calculated for spherical, isotropic homogeneous materials. The loads were assumed to be spherically symmetric. Then for an arbitrary temperature profile, $T(r)$, the radial and tangential stresses which are classical elastic solutions from Reference 101 are

$$\sigma_r(r) = \frac{2\alpha E}{1-\nu_p} \left[\frac{1}{r_0^3} \int_0^{r_0} T(r)\, r^2 dr - \frac{1}{r^3} \int_0^r T(r) r^2 dr \right] \qquad (4.2\text{-}14)$$

and

$$\sigma_t(r) = \frac{\alpha E}{1-\nu_p} \left[\frac{2}{r_0^3} \int_0^{r_0} T(r) r^2 dr + \frac{1}{r^3} \int_0^r T(r) r^2 dr - T(r) \right] \qquad (4.2\text{-}15)$$

where

σ_r = radial stress (psi)
σ_t = tangential stress (psi)
α = coefficient of thermal expansion of the porous sphere (in/in °F)
E_p = Young's modulus of the porous medium (psi)
ν_p = Poisson's ratio of the porous medium
r = radius (in)
r_0 = outer radius of the sphere (in)

To show the types of stress distributions and some general results from the above equations, consider the temperature profile

$$T = A \left(\frac{r}{r_0} \right)^n \qquad (4.2\text{-}16)$$

which allows closed-form solutions. This function is sketched in Figure 4-7. The total temperature difference is always A, while the abruptness of the temperature rise increases as n is increased. Thus the effects of A and n upon thermal stresses calculated using these profiles reveals the affect of total temperature difference in the particle, and the effect of varying temperature gradient in the particle. The above distribution produces a radial stress field which is

$$\sigma_r = \frac{2\alpha EA}{(1-\nu_p)(n+3)} \left[1 - \frac{r}{r_0}^n \right] \qquad (4.2\text{-}17)$$

- 111 -

The maximum absolute value of the radial stress which occurs at $r = 0$ is

$$\sigma_r = \frac{2\alpha EA}{(1-\nu_p)(n+3)} \qquad (4.2\text{-}18)$$

This stress is tensile for A 0 (heating) and compression for A 0 (cooling). The transverse stress σ_t from equation 4.2-15 becomes

$$\sigma_t = \frac{\alpha EA}{(1-\nu_p)(n+3)} \left\{ 2 - (n+2) \left(\frac{r}{r_0}\right)^n \right\} \qquad (4.2\text{-}19)$$

Therefore, for $A > 0$ this starts as a tensile stress at $r = 0$ of the same magnitude as $\sigma_r(o)$ and reaches a compressive maximum at $r = r_0$ of

$$\sigma_t = \frac{\alpha EAn}{(1-\nu_p)(n+3)} \qquad (4.2\text{-}20)$$

at the surface. For cooling $(A < 0)$ σ_t starts in compression at $r = 0$ and goes to tension at the outer surface. Therefore, the ratio of the maximum tensile stress to maximum compressive stress is, for heating 2/n.

From equations (18) and (20) it can be seen that the maximum stresses are directly proportional to the temperature difference, A, between the outside and inside of the sphere. For $r = 0$, the center of the sphere, the stress state is hydrostatic $(\sigma_r = \sigma_t)$, and when $A > 0$ (heating) tensile stresses are produced. Also, at $r = 0$ the steeper the gradient (the larger n is) the smaller the stress. If $A < 0$ (cooling) this stress state would be compressive. Since it is a hydrostatic compressive stress, no failures occur on cooling. Therefore, at $r = 0$, the heating condition $(A > 0)$ is the only one which can produce a failure.

At the surface of the sphere, $r = r_0$, the radial stress, σ_r, is zero. The transverse stress for heating $(A > 0)$ is negative (compression). Since this is a uniaxial stress state, a failure can occur. The magnitude of the compression is $\frac{n}{2} \sigma_r$. Near the surface σ_r is small, but tensile, and thus will reduce the amount of the σ_t compressive stress required to produce a failure, thus a failure could initiate below but near the surface. On cooling $(A < 0)$ the surface will be in tension, hence the failure will only occur at the exterior of the sphere and propagate inwards. The magnitude of surface stress is proportional to the temperature difference and the ratio (n/n+3). Since (n/n+3) increases as n increases, the steeper the gradient, the greater the surface stress.

Now consider a specific heatup/cooldown case in a 20-25 mesh catalyst particle. The radial and tangential stress solutions for the typical temperature profiles for heat-up, Figure 4-5 and cooldown, Figure 4-6, are shown in Figures 4-8 to 4-11. These show the greatest temperature difference on heating occurs at 20 milliseconds, which produces the greatest tensile and compressive stress. On cooldown the greatest tensile stress occurs at 10 milliseconds.

- 112 -

$$T = A \left(\frac{r}{r_0} \right)^n$$
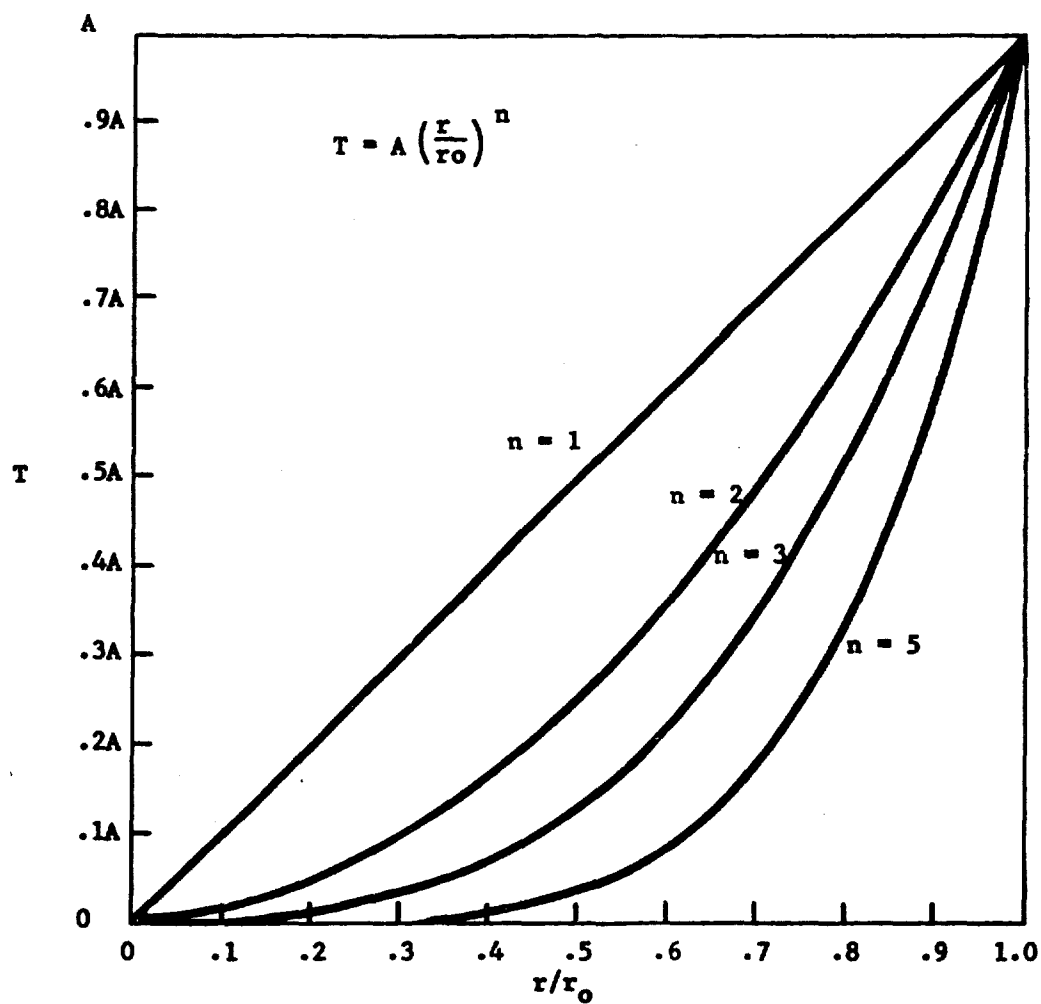
Figure 4-7. Arbitrary Temperature Profiles for Estimating Effects of Thermal Stress.

- 113 -
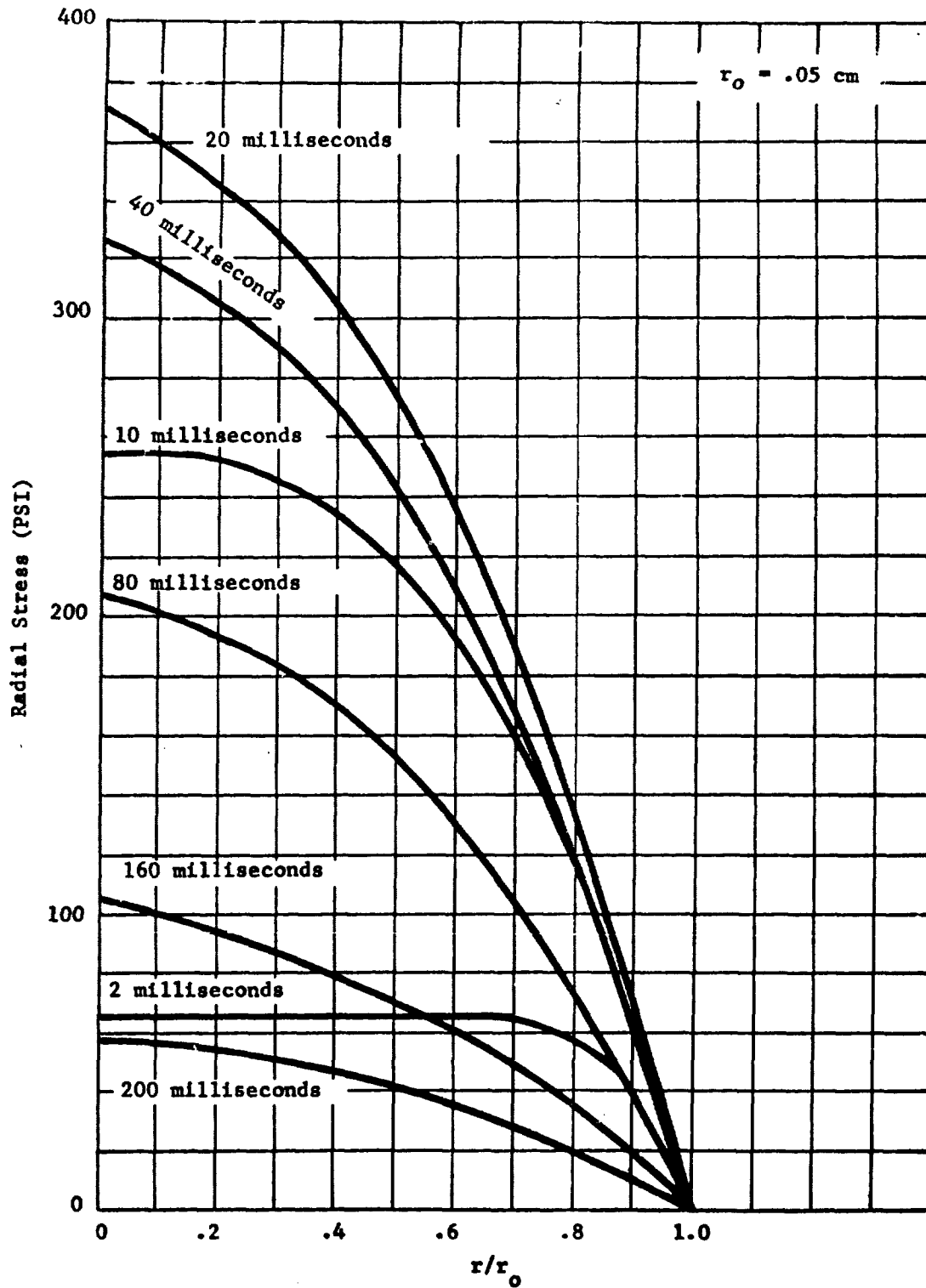
Figure 4-8. Radial Stress As A Function of Time Produced by Heating
G = .05 pounds/in², Gas Temp. = 1473°K, Particle Temp. = 273°K
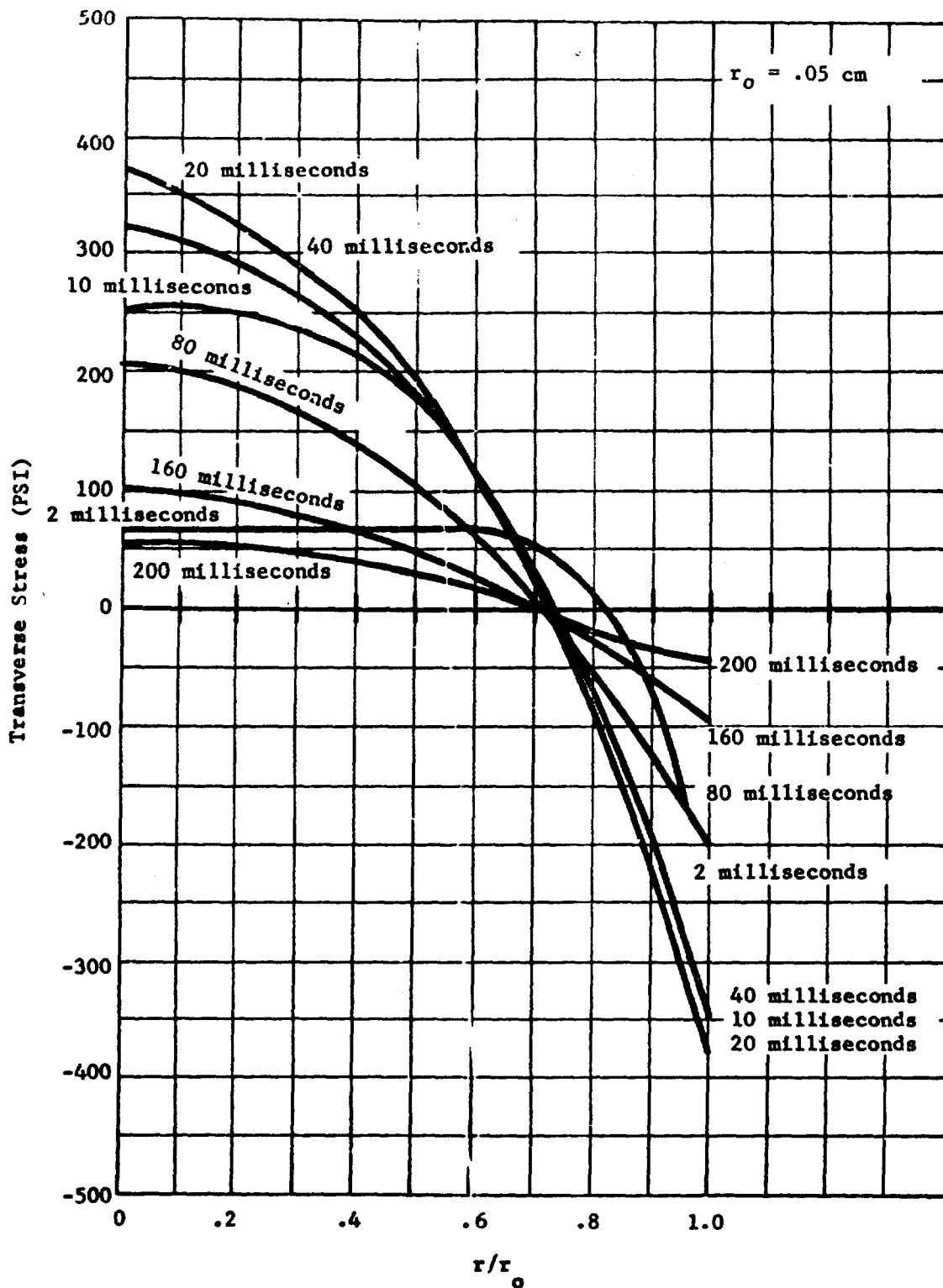
Figure 4-9. Transverse Stress as a Function of Time Produced by Heating.

$G = .05$ pounds/in^2-sec. Gas Temp. $= 1473°K$, Particle Temp. $= 273°K$
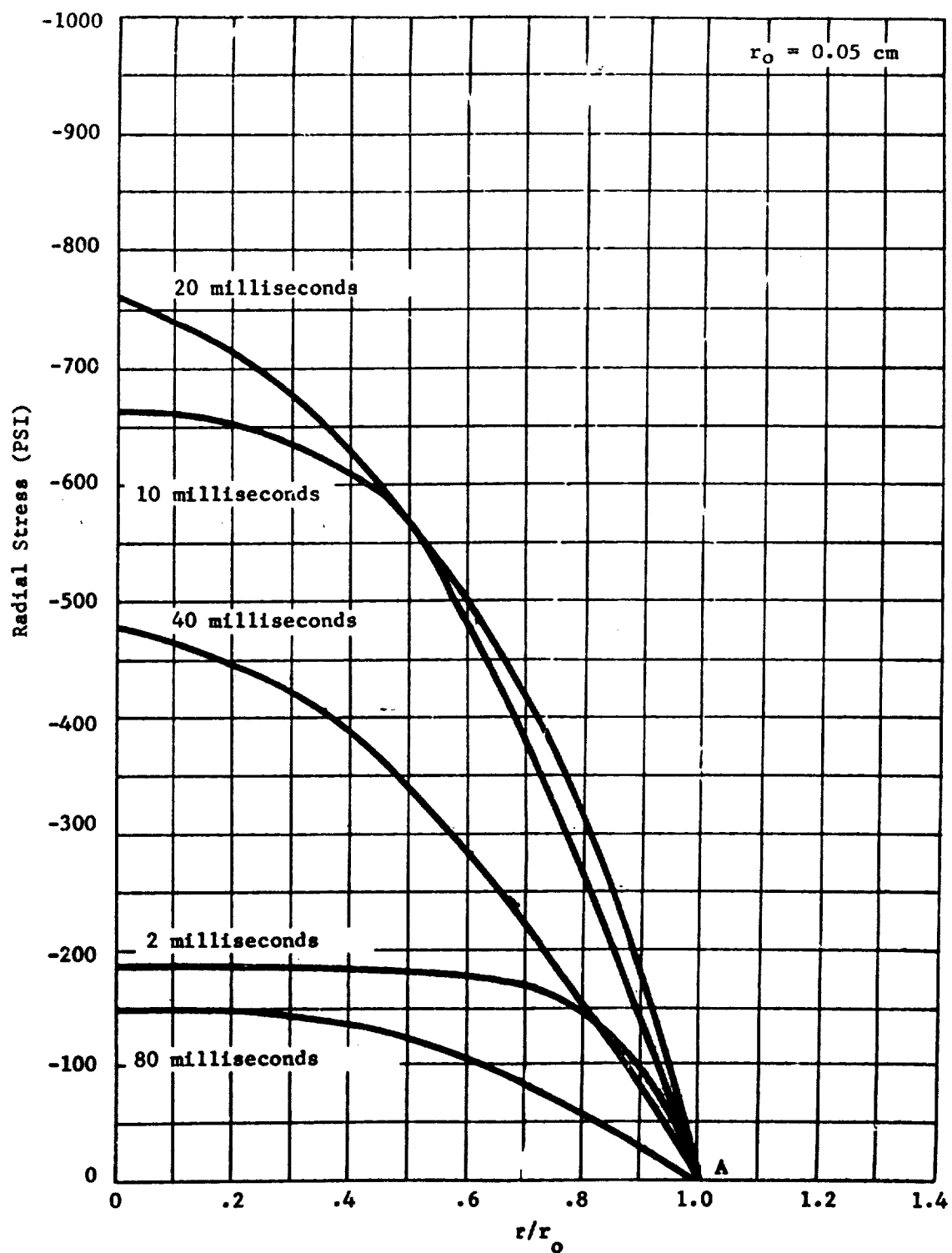
Figure 4-10. Radial Stress as a Function of Time Produced by Cooldown. Maximum Rate Nucleate Boiling Heat Transfer.
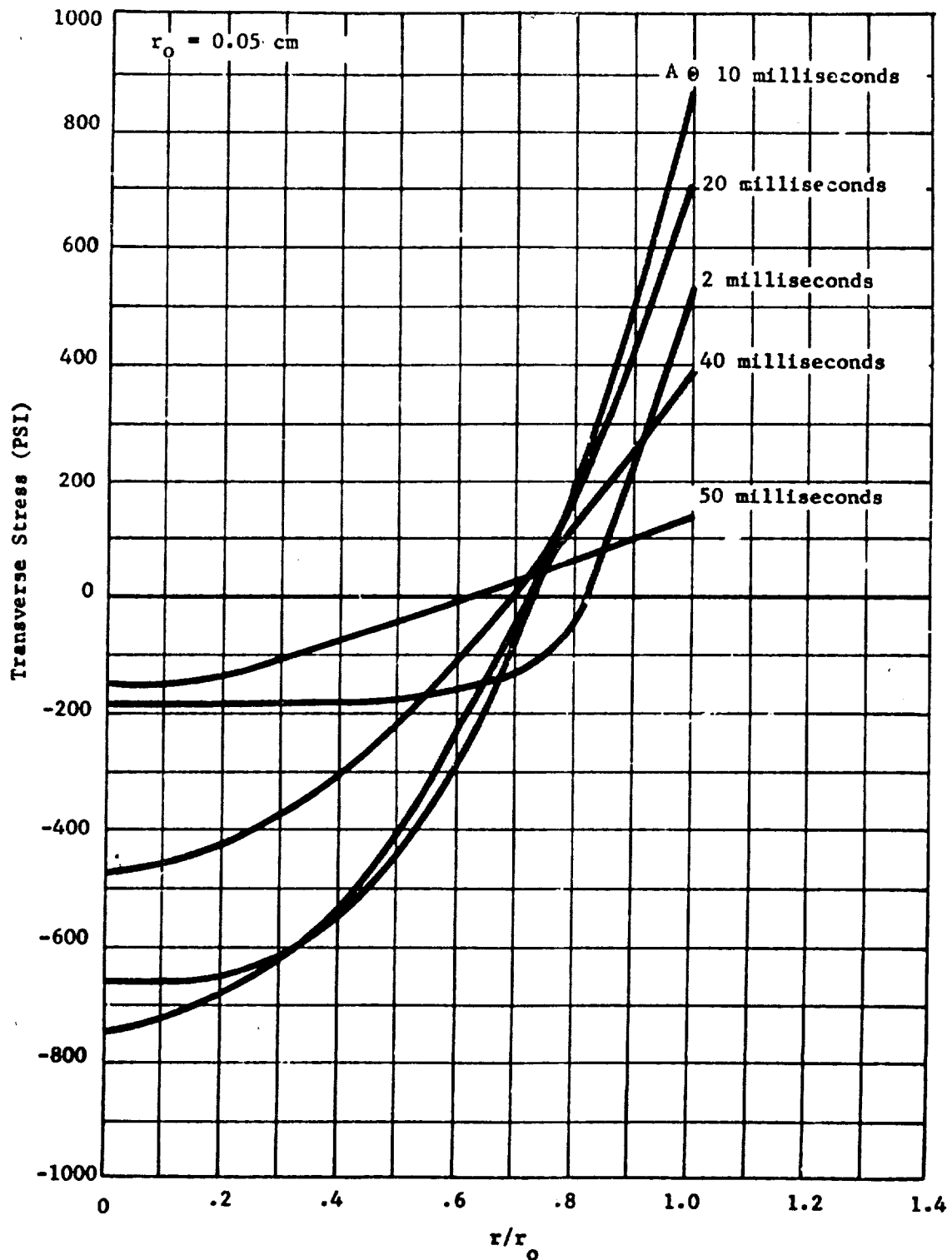
Figure 4-11. Transverse Stress as a Function of Time Produced by Cooldown.
Maximum Rate Nucleate Boiling Heat Transfer.

- 117 -

On heating, for $\nu_p = 0.3$ (see the failure section for a discussion of the Poisson's ratio ν), the maximum tensile stress is 380 psi which is hydrostatic $\sigma_r = \sigma_\theta$. Although this is a triaxial stress state, it is well below failure for the two dimensional equal-load ($S_1 = S_2$) biaxial limit, so the heating case does not appear to be a possible point of failure.

On cooldown, the maximal tensile stress occurs at the outer radius. The maximum tensile stress occurs at 10 milliseconds and is 885 psi. The stress state at this point is biaxial, with the stresses being equal in the two transverse directions and $\sigma_r = 0$. This is illustrated as Point "A" in figures 4-3, 4-4, 4-10, and 4-11. Therefore, between 25% and 50% failure would be expected for the virgin material. If used material were cooled down, since the mean failure stress is lower and the scatter is larger, between 75% and 95% failures would be predicted with this material. It should be reiterated that this is for the particular situation of 20-25 mesh, initial temperature of 1473°K (2191°F) and flow conditions such that the quenching liquid remained in the nucleate boiling regime, rather than film boiling.

These conclusions were drawn assuming $\nu_p = 0.3$. The tensile stresses which would be predicted decrease as ν_p decreases. If $\nu_p = 0.1$, then the maximum tensile stress on cooldown would decrease from 885 psi to 688 psi and fewer failures would be expected in either fresh or used materials. However, this latter value of Poisson's ratio appears much too low based on estimates made by Professor Hasselman (see Section 3.3), who predicts a value of 0.25 which is much closer to the original assumption of 0.3. The uncertainties in the predictions which arise from lack of accurate values for tensile failure stresses and Poisson's ratio, point up the need for experimental determinations of these important material properties.

In general, the results indicate that failure as a result of hot gas thermal shock during heating is unlikely, where failure from liquid quench thermal shock during cooldown is distinctly possible.

4.2.4 Pressure Profiles Developed Inside a Catalyst Particle by External Pressurization or Depressurization

If the boundary of a porous, permeable catalyst particle is suddenly exposed to a high pressure gas, a series of transient pressure profiled are developed in the particle, until pressure equilibration is finally obtained. If a catalyst particle has fully pressure-equilibrated at a high pressure, and suddenly has the boundary pressure reduced to a low value, the same sort of process occurs, with the flows being in the reverse direction. The processes of mass flow of gas through the permeable material, and accumulation of mass in the porosity volume, is quite analogous to the transient response to external heating or cooling. To determine the relevant time scale for the pressurization or depressurization process, a dimensionless parameter similar to the Fourier number may be developed.

The accumulation of gas mass in an element of porous solid is:

$$\Delta M = \frac{AL \; \phi \; M_w \; \Delta P}{RT} \qquad (4.2\text{-}21)$$

where ϕ is porosity
M_w is molecular weight of the gas
ΔP is change of pressure
R is gas constant
T is temperature

The mass transport rate by D'Arcy flow is

$$\dot{M} = \frac{A \; K_m \; M_w \; P \; \Delta P}{\mu \; L \; R \; T} \qquad (4.2\text{-}22)$$

where Km is permeability in cm^2
μ is viscosity of the fluid

Dividing one expression by the other gives a dimensionless group analogous to the Fourier Number:

$$N_m = \frac{K_m \; P \; t}{\phi \; \mu \; L^2} \qquad (4.2\text{-}23)$$

To find the appropriate time scale for particle pressurization or depressurization, it is only necessary to evaluate t in the above expression. Since the most damaging temperature distributions were obtained at a Fo of about 0.1, it is reasonable to evaluate the expression for pressure at the same value.

$$t = \frac{\phi \; \mu \; L^2 \; N_m}{Km \; P}$$

$\phi = .26$
$\mu = 6.66 \times 10^{-4}$ poise
$L = .05$ cm
$Km = .1$ Darcy $= 9.869 \times 10^{-10}$ cm^2
$P = 100$ psia $- 6.8947 \times 10^6$ dyne/cm^2

$$t = \frac{.26 \times 6.66 \times 10^{-4} \times .05^2 \times .1}{9.869 \times 10^{-10} \times 6.8947 \times 10^6} = 6.36 \times 10^{-6} \text{ second}$$

Hence, the pressure equilibration process is very rapid compared to the thermal equilibration process. The time scale for the depressurization of a thrust chamber at the termination of a pulse is on the order of 1 to 100 milliseconds. This is so much slower a process than the time required for depressurization of a pellet that we must conclude that no internal pressure stresses will occur during a normal cutoff. Very rapid pressurization of a pellet could take place, by local detonations or shock waves in the chamber. Since the catalyst is relatively strong in compression, a steep fronted wave of over a thousand psi would be required to cause any damage by pressure-generated stresses in the individual particles. Explosions of this amplitude would produce much more destructive effects by producing compaction pressures within the bed, so the effects of externally impressed pressure upon the individual particle may be identified as non-destructive. The worst-case pressure profiles and internal stress levels which would be generated by 1000 psi pressurization or depressurization episodes are illustrated in Figures 4-12 and 4-13. Rapid pressurization will be assessed experimentally during the "pop" shock tests to be conducted by TRW.

4.2.5 Particle Stresses Resulting from Internal Pressure During Pressurization or Depressurization in the Absence of Liquid

The stresses resulting from internal pressure may be calculated in a manner quite similar to those for the temperature gradient. The total stress per unit area, e.g., τ_r is the sum of the average stress in the solid material, e.g., σ_r plus the average stress, $-fp$, caused by the pore pressure. (Reference 104) i.e.,

$$\tau_r = \sigma_r - fp \qquad (4.2\text{-}24)$$

where p = pressure in the pore (psi)
       f = void fraction

Note that pressure is considered positive in compression and stress is considered positive in tension. The average stress in the solid material (per unit area of porous material) is what controls failure. Using equation (24), one finds that for an arbitrary point symmetric pressure profile $p(r)$ in a sphere of radius r_0 where the external pressure on the outer surface is equal to $p(r_0)$, the radial and tangential stresses are:

$$\sigma_r(r) = \frac{2(1-2\nu)}{1-\nu} f \left[\frac{1}{r_0^3} \int_0^{r_0} p(r)r^2 dr - \frac{1}{r^3} \int_0^r p(r)r^2 dr \right] + fp(r) - p(r_0) \qquad (4.2\text{-}25)$$

and

$$\sigma_t(r) = \left(\frac{1-2\nu}{1-\nu}\right) f \left[\frac{2}{r_0^3} \int_0^{r_0} p(r)r^2 dr + \frac{1}{r^3} \int_0^r p(r)r^2 dr \right] + \left(\frac{\nu}{1-\nu}\right) fp(r) - p(r_0) \qquad (4.2\text{-}26)$$

For the purposes of equations 25 and 26 the pressure, $p(r)$, is the absolute pressure.

- 120 -
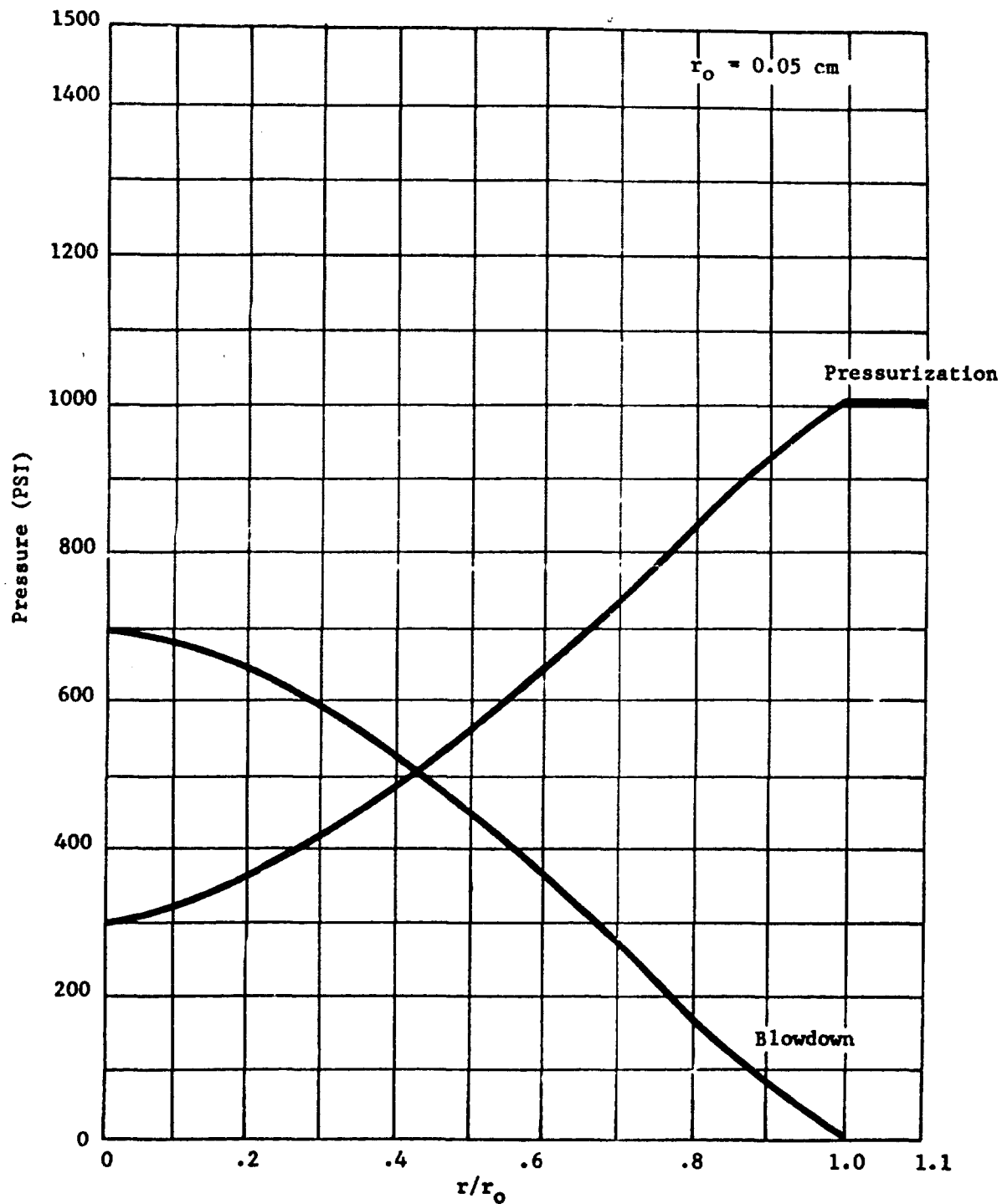
Figure 4-12. Worst-Case Pressure Profiles Due to Pressurization and Blowdown.
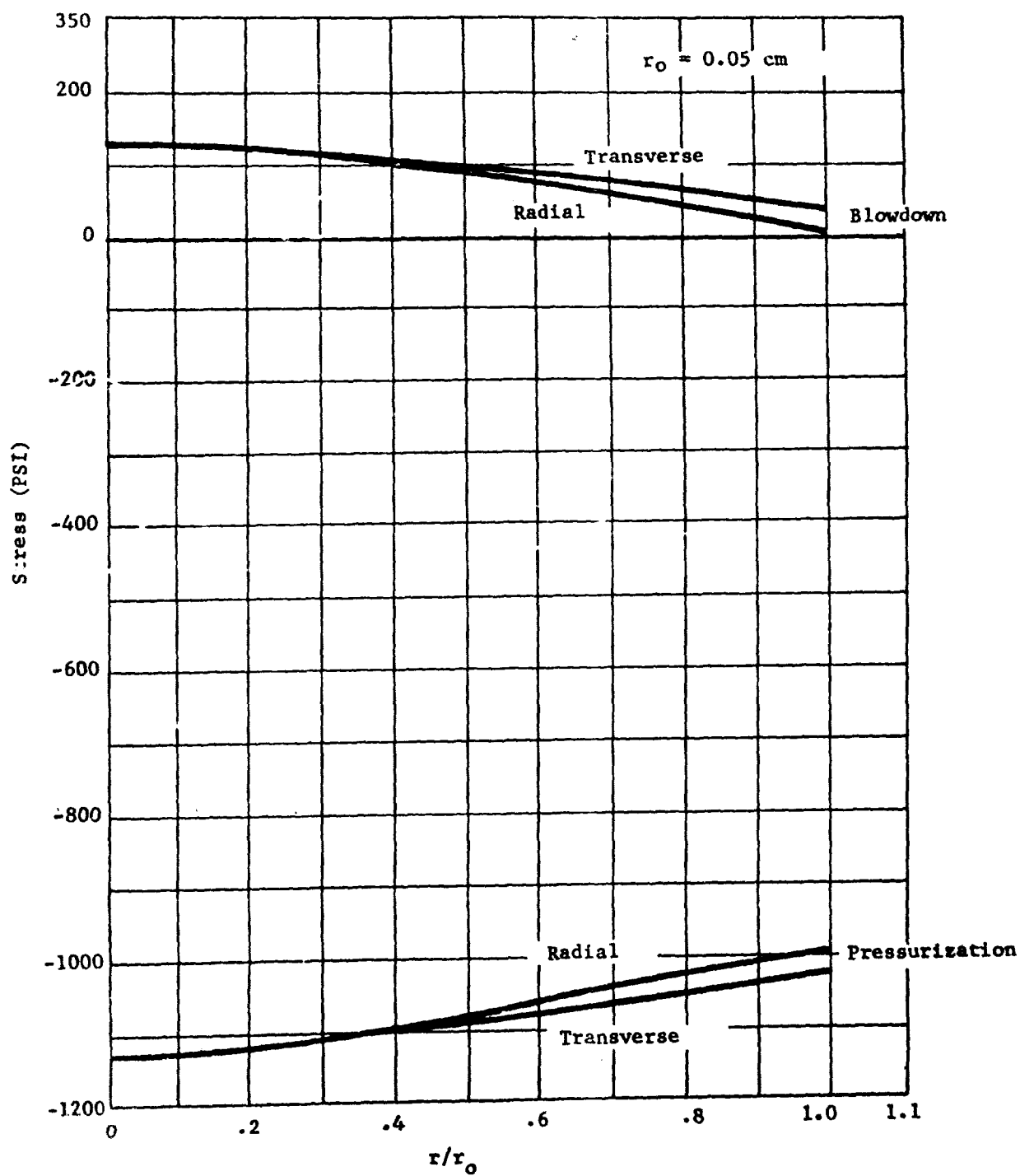
Figure 4-13. Stresses Produced by the Pressurization and Blowdown in Shell 405 Catalyst.

The effect of the internal pressure profiles on the stress in the substrate material can be studied by looking at the solution to two pressure cases, one which represents pressurization to 1000 psi and the other blowdown to 0 psi, and as shown in Figure 4-12. The stress distributuons produced by these pressure profiles are shown in Figure 4-13. On pressurization to 1000 psi, the stresses are compressive in the body, and almost hydrostatic. On blowdown, the stresses are tensile, but are very low, even for this steep profile.

Because the stress-state in the body during pressurization is almost hydrostatic compression no material failure is expected. The stress state during blowdown is almost hydrostatic tension. The stress levels in the matrix are much lower than would be needed to produce failure, using the biaxial failure envelope given in Figure 4-3. Therefore, if these are the worst case pressure profiles, then the internal pressure stress should not produce material failure.

The solutions to equations (14), (15), (25), and (26) have been combined in a small computer program which solves both the thermal and internal pressure problems. The solution for the combined problem is obtained by superposition of the solutions. A pair of simultaneous pressure and temperature profiles are shown in Figure 4-14 and the corresponding combined stresses in Figure 4-15. These are typical profiles and are just to illustrate the principle of superposition. The resultant stress distributions shown in Figure 4-15 show the related magnitude of the thermal and internal pressure solutions. These solutions show that for our material and the pressure and temperature profiles of interest, the worst case thermally generated stresses are greater than those generated by the worst case internal pressure distribution due to pressurization and blowdown.

In general, it is concluded that the pore pressure gradients present in the catalyst particle during either rapid gas pressurization or depressurization in the absence of liquid will not cause particle failure.

4.2.6 Particle Stresses From Bed Compression

Whenever the bed of catalyst pellets is made to bear a compressive load, local stresses are produced at the tiny areas where the pellets actually come into contact with each other. It is the local stresses produced in the pellets at these points of contact which can cause local failure and the loss of material associated with bed compression stress. There are four relationships which must be determined to define the effects of compression:

1. What is the relationship between bed compression pressure and the normal force developed between adjoining particles (required for the analysis of flow-induced pressure loadings acting on the bed, and also for differential thermal expansion).

- 123 -
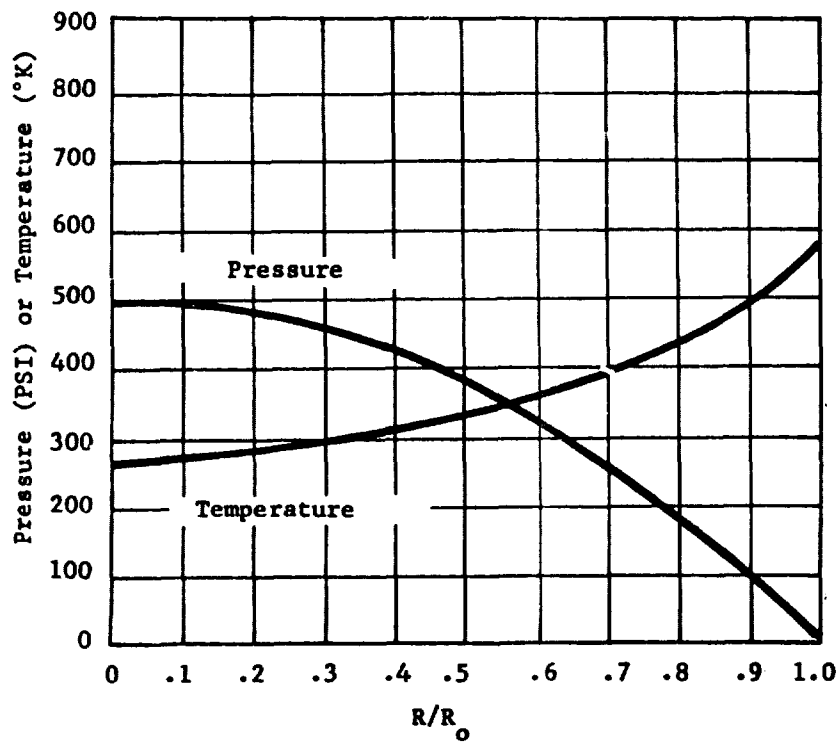
Figure 4-14. Pressure and Temperature Profiles
to Determine the Radial and Transverse
Stress Distributions.
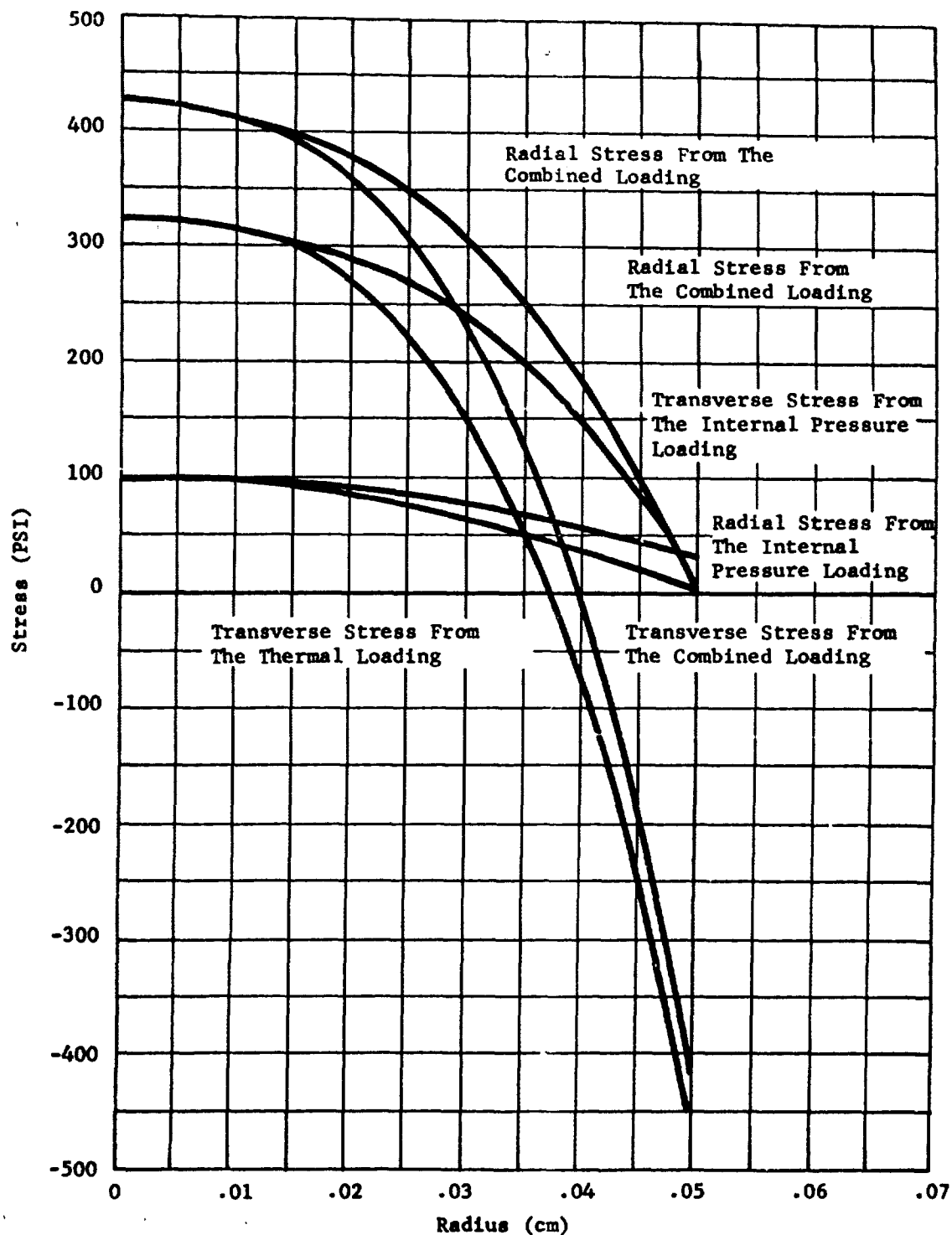
Figure 4-15. Radial and Transverse Stresses as a Function or Radius For Simultaneous Thermal and Internal Pressure Loading.

2. What is the relationship between bed volume change and the resulting bed compaction pressure (required for the problem of differential thermal expansion).

3. What are the distributions of stresses produced in a particle by a given level of normal force applied by another identical particle.

4. What is the volume of material which will fail as a result of the stress distributions produced in the particle, and what happens to the smaller fractured particles i.e. are they blown out of the catalyst bed or trapped in bed interstices.

4.2.6.1 Particle-to-Particle Forces
Resulting from Bed Compression

We will assume that the bed is composed of identical spheres arranged in a face-centered cubic array, (theoretical closest packing) as illustrated in Figure 4-16. It may be seen that Sphere E is in contact with twelve other adjoining spheres, and that all the bed compression forces acting upon Sphere E must be supported by these twelve points of contact. Let us assume that the spheres are frictionless at the points of contact, so that all of the points of contact produce only forces normal to the surfaces. From considerations of symmetry, the forces acting on the x, y, and z faces of the unit cube will be equal, i.e., the bed compression will act like a hydrostatic pressure. The force acting on the z-normal face will be equal to the bed compression stress multiplied by the area of the z-normal face of the unit cube. The length of the diagonal across this face includes the diameter of Sphere E and the radii of Spheres B and D, hence the length of the diagonal is 4R where R is the radius of the spheres. The length of the side of the unit cube, then, must be $2\sqrt{2}R$, and the area of the face must be $8 R^2$. If the bed compression stress is P, then the force exerted on the z-normal face of the unit cube is $8 R^2 P$. This force in the z direction will be shared between the upper cut portions of Spheres E, A, B, C, and D, with Sphere E supplying one half of the total projected area in the plane. The force borne by Sphere E will be one half the total or $4 R^2 P$.

Since we have hypothesized frictionless contacts, with only normal forces, none of the z-directed force acting upon Sphere E can be balanced by its contacts with Spheres A, B, C, or D, hence, all of the support for Sphere E in the z direction must come from its contacts with Spheres F, G, and the other two equivalent hidden spheres. Each point of contact must contribute one quarter of the total z-directed force or $R^2 P$. It may be seen that the forces acting between Sphere E and the spheres below it, are elevated 45° from the x-y plane, and hence each particle-to-particle force F is $R^2 P$ divided by the cosine of 45°, hence:
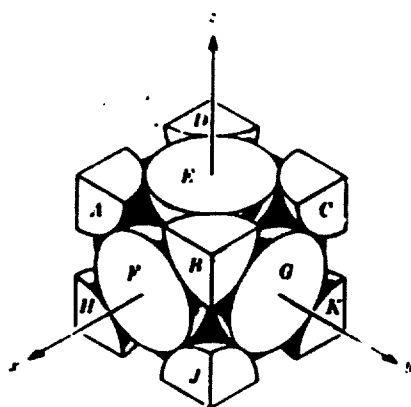
Figure 4-16. Unit Cube from a Face-Centered Cubic Array
of Identical Spheres.

$$F = \sqrt{2} \, R^2 P \qquad\qquad (4.2-27)$$

where F is the force between the particles
       R is the radius of the spheres
       P is the pressure applied to the bed

This derivation closely follows Reference 105. The relationship given in Equation 4.2-27 was also shown to be valid for hexagonal-close packing, (106). In a later section a method for determining the applicability of Equation 4.2-27 to our problem will be presented.

4.2.6.2 Stress Produced in the Particle from Point-to-Point Contact

The stresses from particle-to-particle contact, due to bed compression, may be calculated from Hertz contact theory. The Hertz contact analysis defines the stress distribution in a semi-infinite body due to the pressure distribution produced by a spherical indentor. The solution can be extended to the contact between two spheres if the radius of contact, a, is small compared to the radius of the body, R_o, as shown in Figure 4-17. The solution is shown in Reference 101. If the approximation R_o a is large is not valid, then the solution can only be obtained by the use of complex computer codes.

The solution to the contact problem as presented in Reference 101, assumed the displacements of points within the contact area, a, Figure 4-17, that were required to bring the points, on the surface of each sphere at R = a, into contact. Hertz assumed the stress distribution within the contact area was hemispherical, with the maximum occurring at the center of the contact area. The displacements predicted by the assumed stress distribution agree with those calculated to bring the points on the surface of the spheres in contact. Knowing the stress distribution and the contact force, F, the maximum contact stress was shown in Reference 101 to be:

$$q_o = \frac{3}{2} \, \frac{F}{\pi a^2} \qquad\qquad (4.2-28)$$

with a radius of contact of

$$a = \sqrt[3]{\frac{3}{4} \, \frac{(1-\nu^2)}{E} \, FR_o} \qquad\qquad (4.2-29)$$

where ν is Poisson's ratio
      E is Young's Modulus
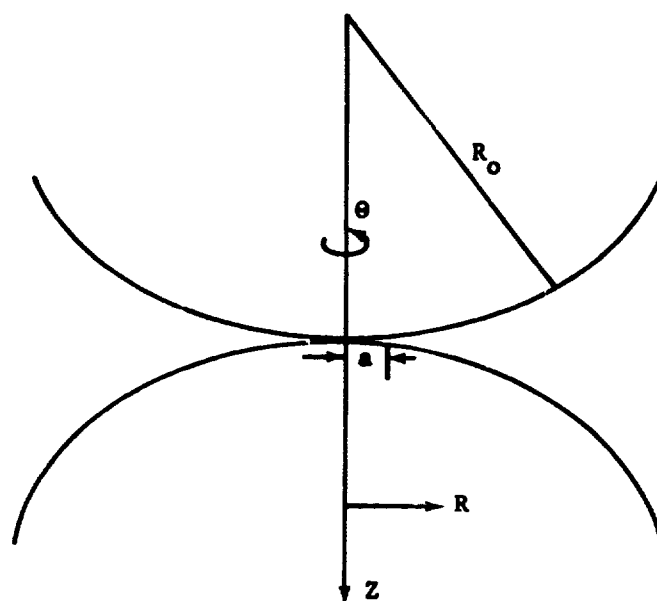
Figure 4-17. Schematic of the Contact Problem.

To relate the contact stresses to the bed pressures a relationship such as Equation (4.2-27) is required. For the remainder of the analysis of the contact problem, the bed will be assumed to be either a face-centered cubic or a hexagonal close packed sphere aggregate. Therefore, the contact stress and radius of contact can be related directly to the bed pressure by using Equations (4.2-27), (4.2-28) and (4.2-29).

For our case, using the Poisson's ratio of the porous sphere, ν_p, as described in the failure section, and solving Equations (4.2-28) and (4.2-29) and using F from Equation (4.2-27) yields.

$$q_o = 0.6492 \sqrt[3]{\frac{E^2 P}{(1-\nu_p^2)^2}} \tag{4.2-30}$$

and

$$a = 1.0198R \sqrt[3]{\frac{P}{E}(1-\nu_p^2} \tag{4.2-31}$$

With the values of q_o and a, the resultant three-dimensional stress distributions in a semi-infinite flat body produced by a spherical indentor can be calculated by using the relationships developed by Love, Reference 107. Love showed the stresses are

$$\sigma_R = q_o \left\{ \frac{(1-2\nu_p)a^2}{3R^2} \left[1 - \left(\frac{z}{\psi}\right)^3\right] + (1+\nu_p)\frac{z}{a}\tan - \left(\frac{a}{\psi}\right) \right. \tag{4.2-32}$$

$$\left. + (1-\nu_p)\frac{z\sqrt{4}}{a^2+\psi} - 2\frac{z}{\sqrt{\psi}} + \frac{a^2 z^3}{(\psi^2 + a^2 z^2)\sqrt{\psi}} \right\} \tag{4.2-33}$$

$$\sigma_\theta = q_o \left\{ -\frac{(1-2\nu_p)a^2}{3R^2} \left[1 - \left(\frac{z}{\psi}\right)^3\right] + (1+\nu_p)\frac{z}{a}\tan^{-1}\left(\frac{a}{\psi}\right) \right.$$

$$\left. - (1-\nu_p)\frac{z\sqrt{\psi}}{a^2+\psi} - 2\nu\frac{z}{\sqrt{\psi}} \right\}$$

$$\sigma_z = -p_o \frac{a^2 z^3}{(\psi^2 + a^2 z^2)\sqrt{\psi}} \qquad (4.2\text{-}34)$$

$$\tau_{rz} = -p_o \frac{a^2 R z^2 \sqrt{\psi}}{(\psi^2 + a^2 z^2)(R^2 + \psi^2)} \qquad (4.2\text{-}35)$$

$$\tau_0 = \tau_\theta = 0$$

where

$$\psi = \frac{1}{2}\left\{ R^2 + z^2 - a^2 + \sqrt{(R^2 + z^2 - a^2)^2 + 4a^2 z^2} \right\} \qquad (4.2\text{-}36)$$

The q_o used in this analysis is that from two spheres in point-to-point contact, given Equation 20.

The amplitude of the stresses presented in Equations (4.2-32 to 4.2-37), as discussed in Reference 101, decrease very rapidly as R/a increase from 1.0, where R is the distance from the center of contact as shown in Figure 4-16. At the surface, for R/a > 3., the σ_r/q_o < 0.02. Therefore, if R/a is large, the effect of the curvature of the bodies can be neglected. In our case, for 10 psi in the bed, R/a > 31. Therefore, the use of the contact solution and the stress distributions in a flat semi-infinite half space should produce very good results for the stresses produced by the point-to-point contact of two spheres of Shell 405 catalyst.

The discussion of the results of the contact solution in Reference 101 show the maximum compressive stress, q_o, occurs in the Z direction, see Figure 4-17 and at the center of the contact area R = o, Z = 0 and is given by Equation 4.2-36. The stresses in theother two orthogonal directions in the R-O plane, at the same location are also compressive and related to the maximum stress, Reference 101 is

$$\sigma_r = \sigma_\theta = \frac{1 + 2\nu_p}{2} q_o \qquad (4.2\text{-}38)$$

The contact load goes to zero at the edge of the contact area, R = a. This is the location of the maximum tensile stress

$$\sigma_r = \frac{1 - 2\nu_p}{3} q_o \qquad (4.2\text{-}39)$$

At the same location, $Z = 0$, $R = a$, the σ_θ stress is equal to $-\sigma_r$ and $\sigma_Z = 0$. This is equivalent to a state of pure shear in the $r-\theta$ plane at that location. The effect of Poisson's ratio and the location of possible failures will be discussed later.

A computer program developed under another program, contract No. DNA001-72-C-0024, was modified to calculate the total stresses due to contact forces, thermal gradients and internal pressures. The solutions discussed below were generated by this program.

The effect of the Poisson's ratio, ν_p, of the porous material on the maximum contact stress, from Equation (4.2-30), as shown in Figure 4-18 is small. Figure 4-18 does show the maximum contact stress, q_o, increases very rapidly for very low bed stresses.

At the center of the contact area, $R=Z=0$, the effect of ν_p on the other two orthogonal stresses, σ_R and σ_θ, in the $r-\theta$ plane, given by Equation (4.2-30), is shown in Figure 4-19. These orthogonal stresses are also compressive at this point and can vary from $q_o/2$ for $\nu_p = 0$ to q_o for $\nu_p = 0.5$. Therefore, the center of the contact area is in a compressive state. The failure model, developed in this Section, for a two dimensional stress state indicates the failure, probability maximizes at the center of contact, and at the edge of the contact area. The effect of ν_p on the maximum tensile stress, σ_R from Equation (4.2-39) is shown in Figure 4-20. Changing the value of ν_p from 0.3 to 0.1 can double the tensile stress. The other stress in the $r-\theta$ plane, σ_θ, is compressive with a magnitude equal to σ_R. This is a state of pure shear at this location.

The stress distributions for σ_Z, σ_R, and σ_θ along the contact surface, $Z=0$, as a function of R, where R and Z are defined in Figure 4-17, are shown in Figure 4-21. These stress distributions were calculated using the computer program mentioned earlier, for 10 psi bed pressure, $\nu_p = 0.3$ and $E = 300,000$ psi. At $R=0$, the center of contact, the stresses are all compressive. The σ_θ and σ_Z stresses remain compressive throughout the contact area, $R/a \leq 1$. The σ_Z stress becomes zero on the surface outside the contact area, R/a 1, as would be expected as no surface loads are being applied. The σ_θ stress remains compressive for all R/a. The σ_R stress starts as a compressive stress and becomes tensile only near the edge of the contact area. The exact location is dependent on the material properties. For $R/a > 1$, outside the contact area, at $Z=0$, $\sigma_R = -\sigma_\theta$ decrease very rapidly, as shown in Figure 4-21, as R/a increases from 1.0

For any given level of bed compaction pressure, the radial distribution of surface stress in the vicinity of the particle-to-particle contact may be obtained by referring to 4-18 to find q_o and 4-21 to find σ_r/q_o and σ_θ/q_o versus radius (i.e. R/a). The values for σ_r and σ_θ which result may be plotted over the biaxial failure surface (illustrated previously as figures 4-3 and 4-4) to indicate the probability of failure at various locations within or adjacent to the area where the particles are in contact. This has been done in figure 4-22. The points marked A, B, C, D E, F and G represent the values for σ_r and σ_θ at values for R/a of 0.0, 0.25, 0.50, 0.75, 1.0,
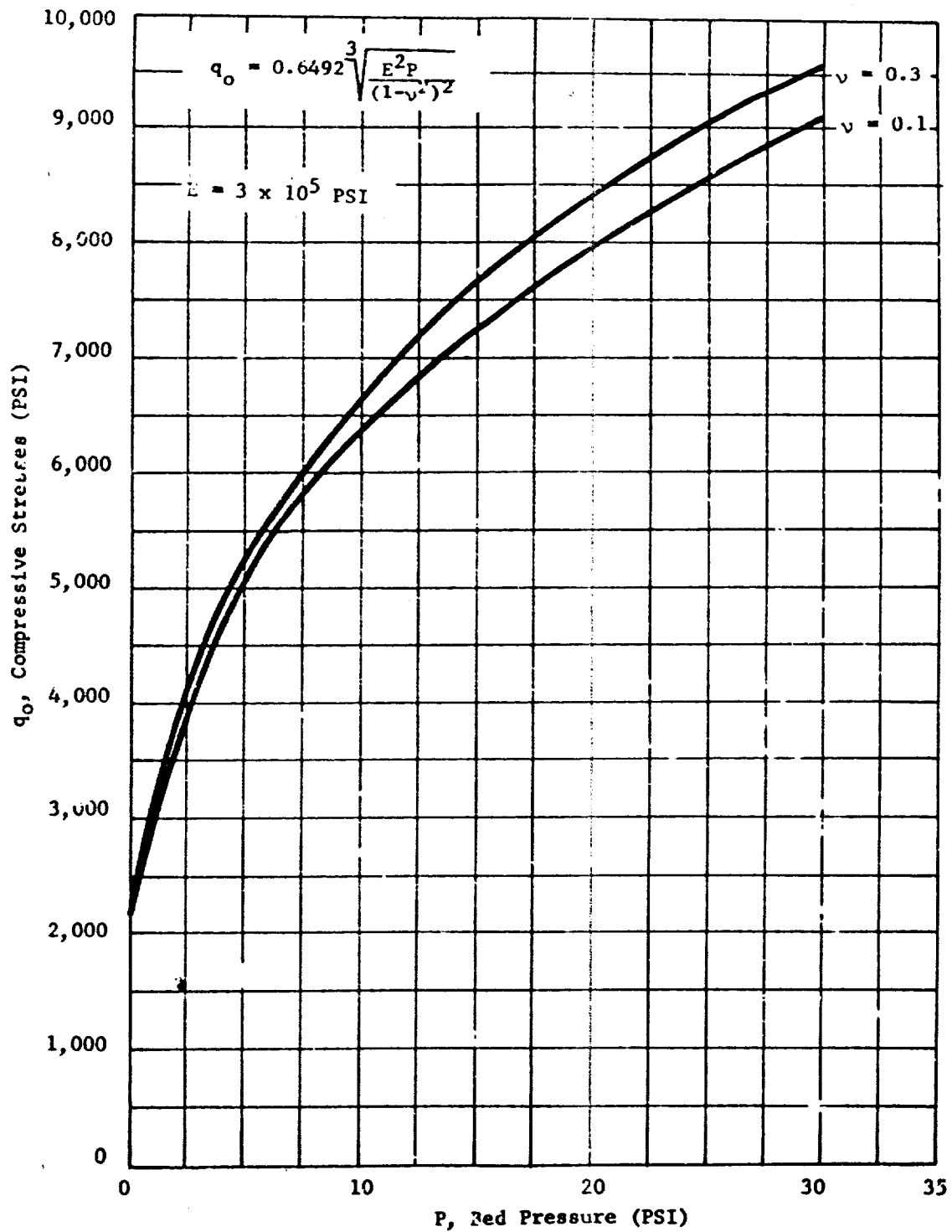
Figure 4-18. Maximum Contact Stress as a Function of the Mean Bed Pressure at the Center of the Contact Area.
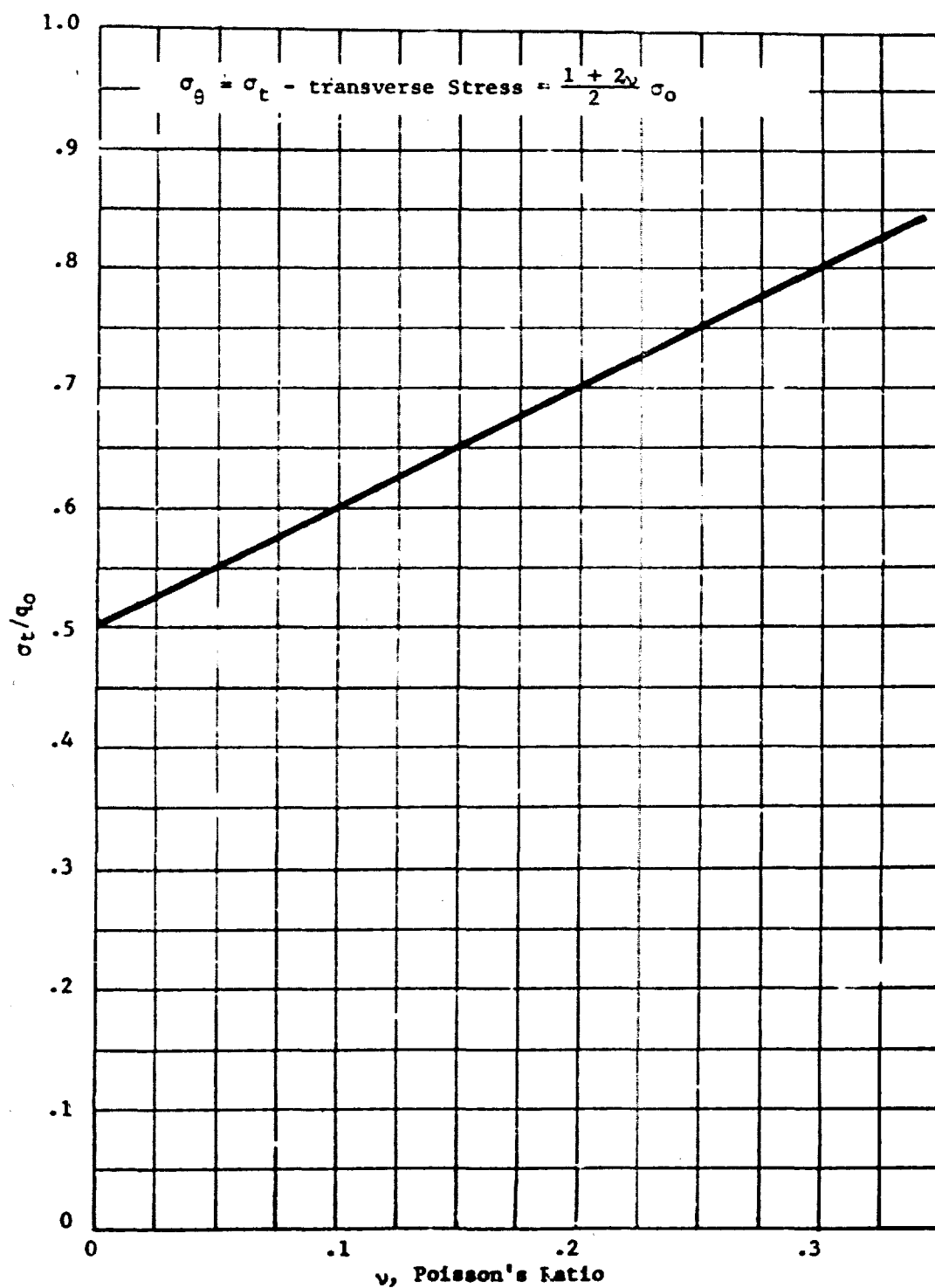
Figure 4-19. Effect of Poissons Ratio on the Transverse Stresses at The Center of the Contact Area.
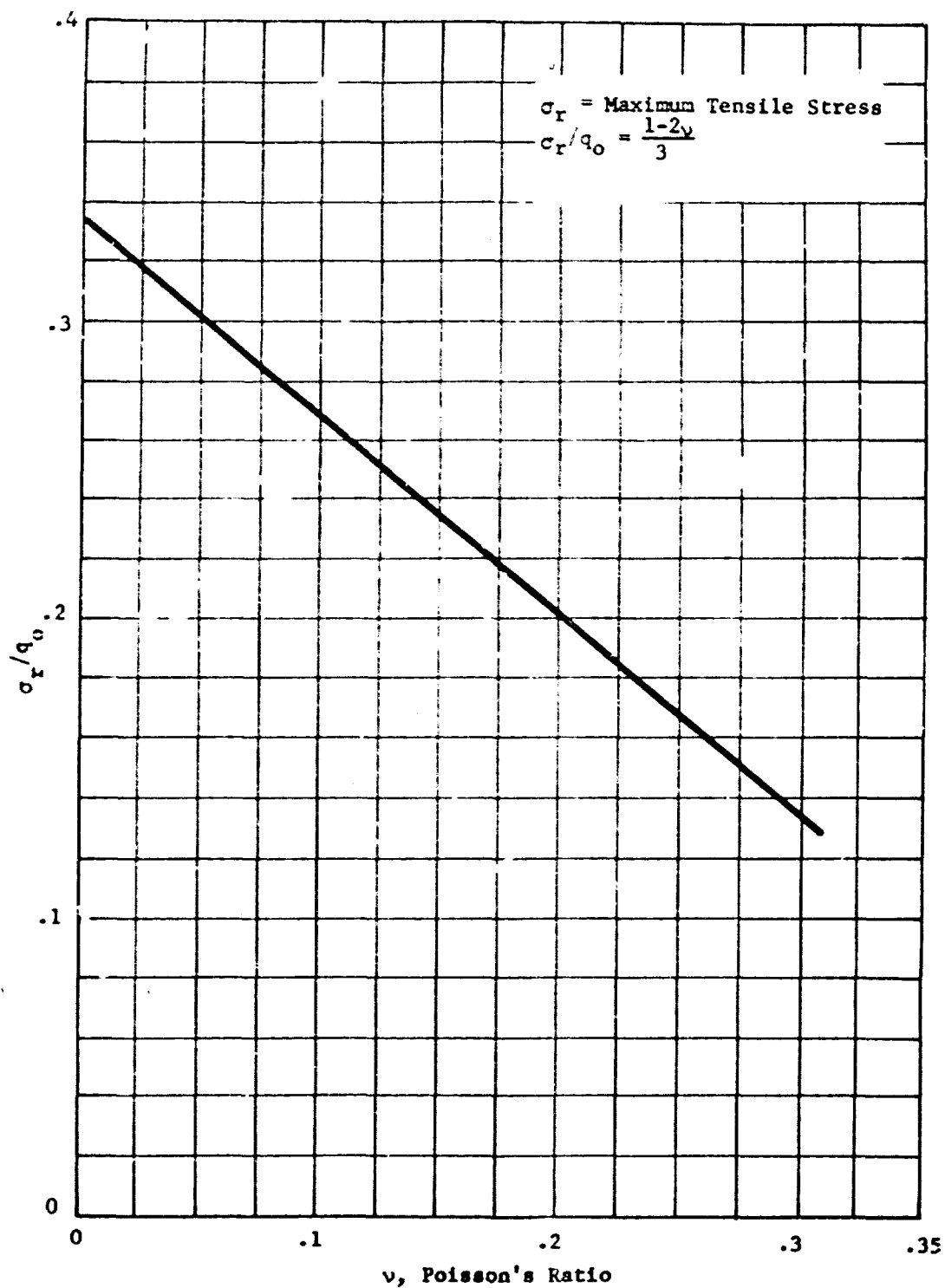
Figure 4-20. Effect of Poisson's Ratio on the Maximum Tensile Stress, at the Edge of the Contact Area.
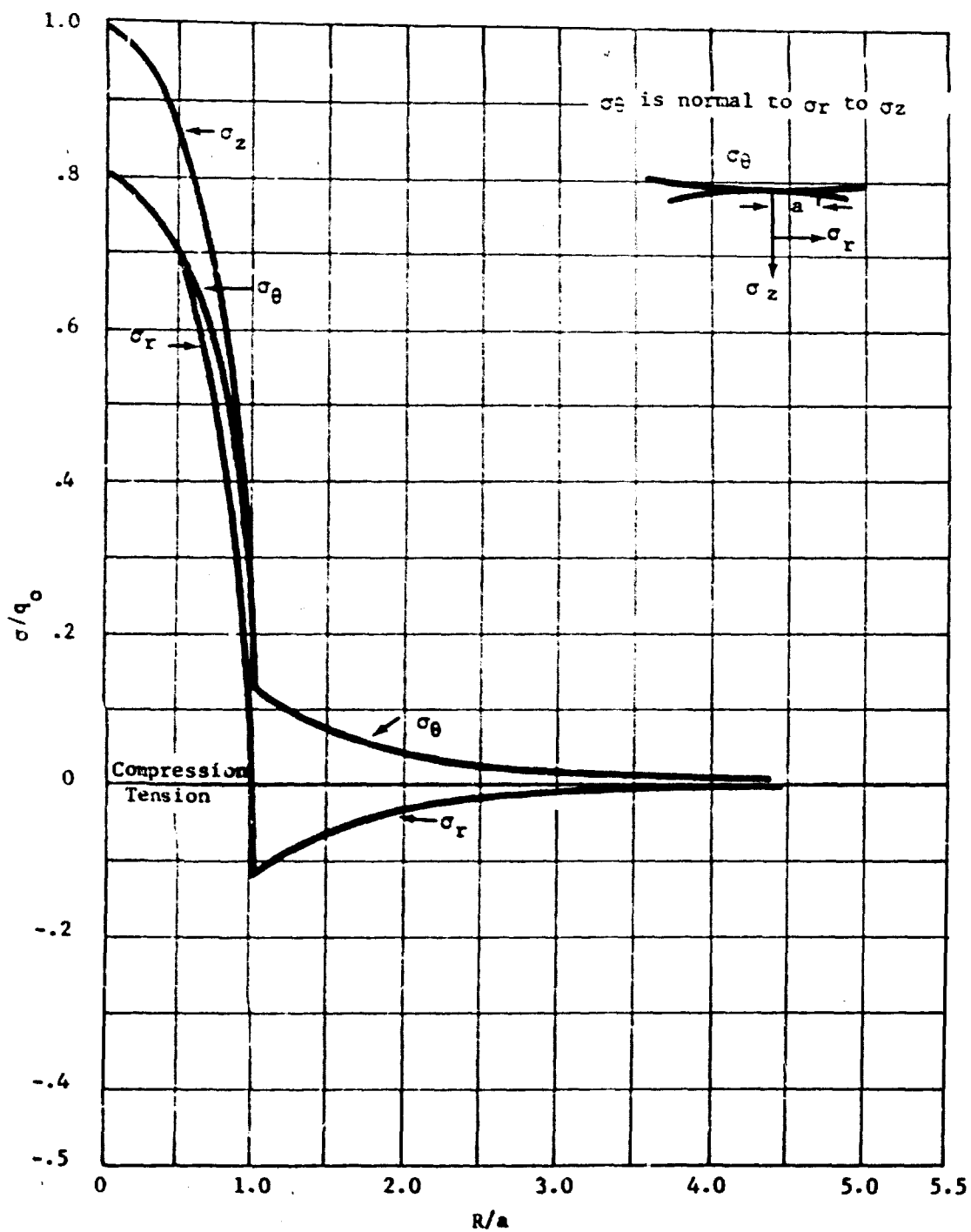
Figure 4-21. Stress Distribution on the Surface of Two Spheres of
Fresh Shell 405 Catalyst with a Bed Pressure of
10 psi for $\nu_p = 0.3$.
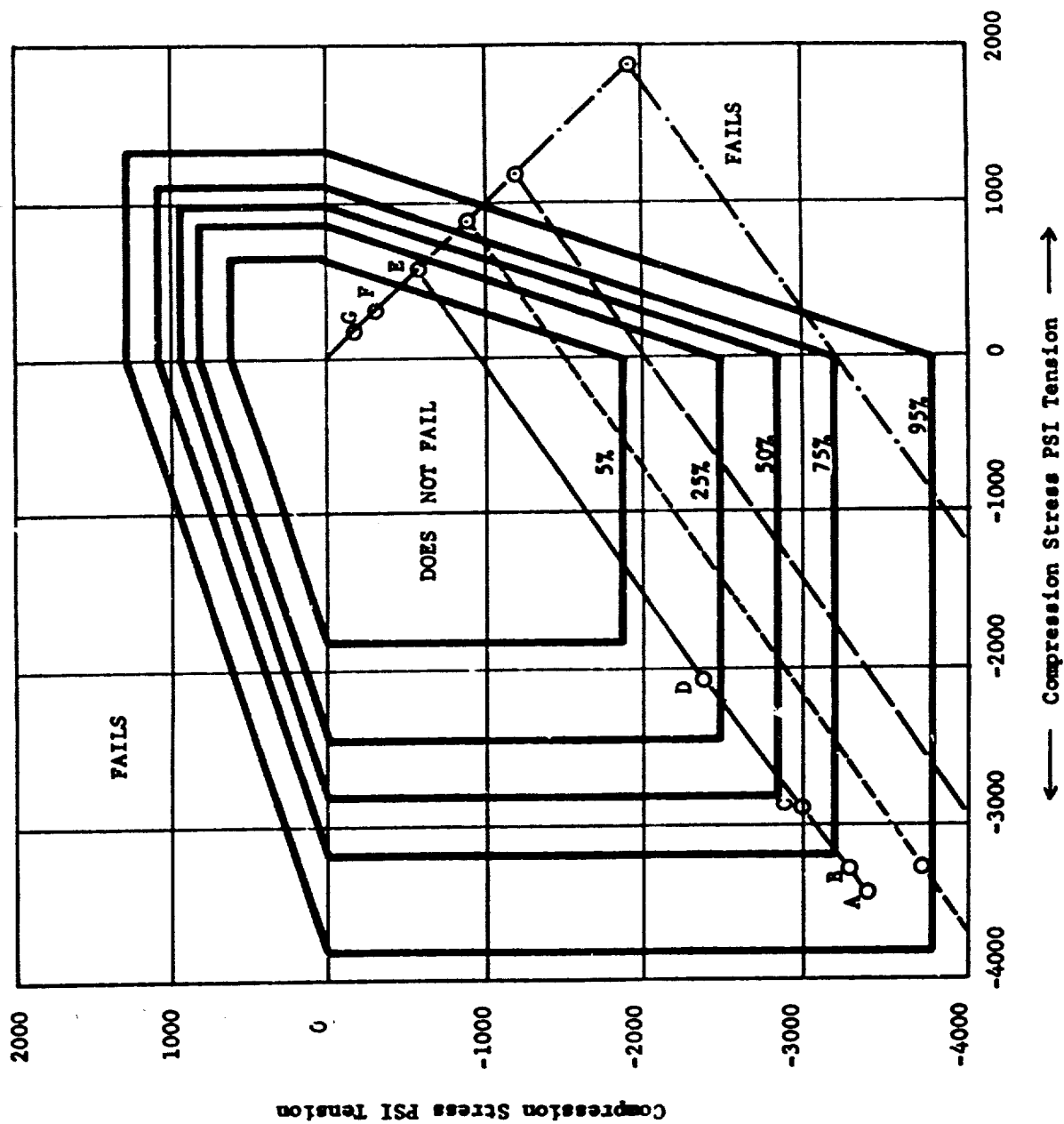
Figure 4-22. Failure Surface - Fresh Shell 405.
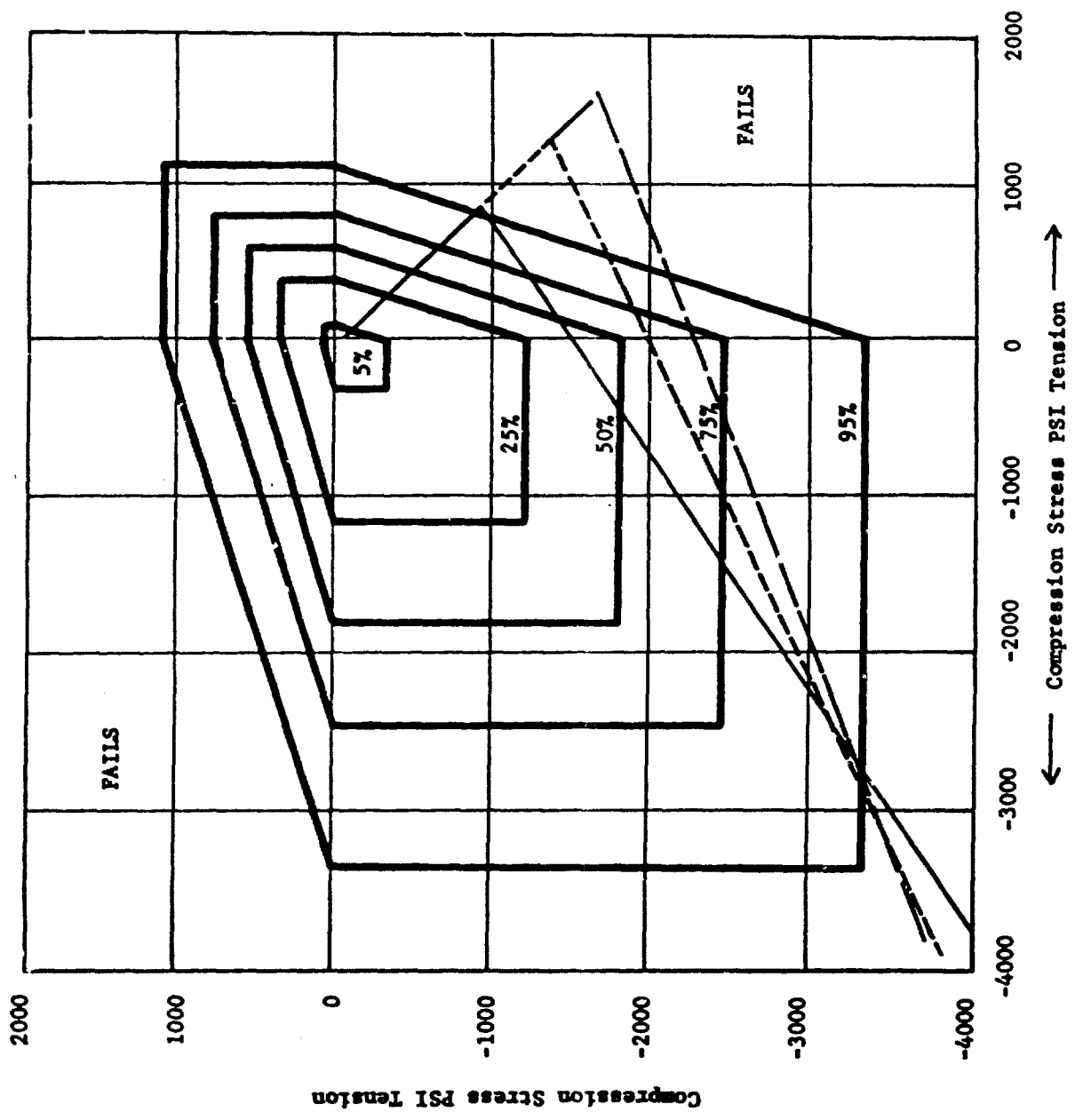
Figure 4-23. Failure Surface - Used Shell 405.
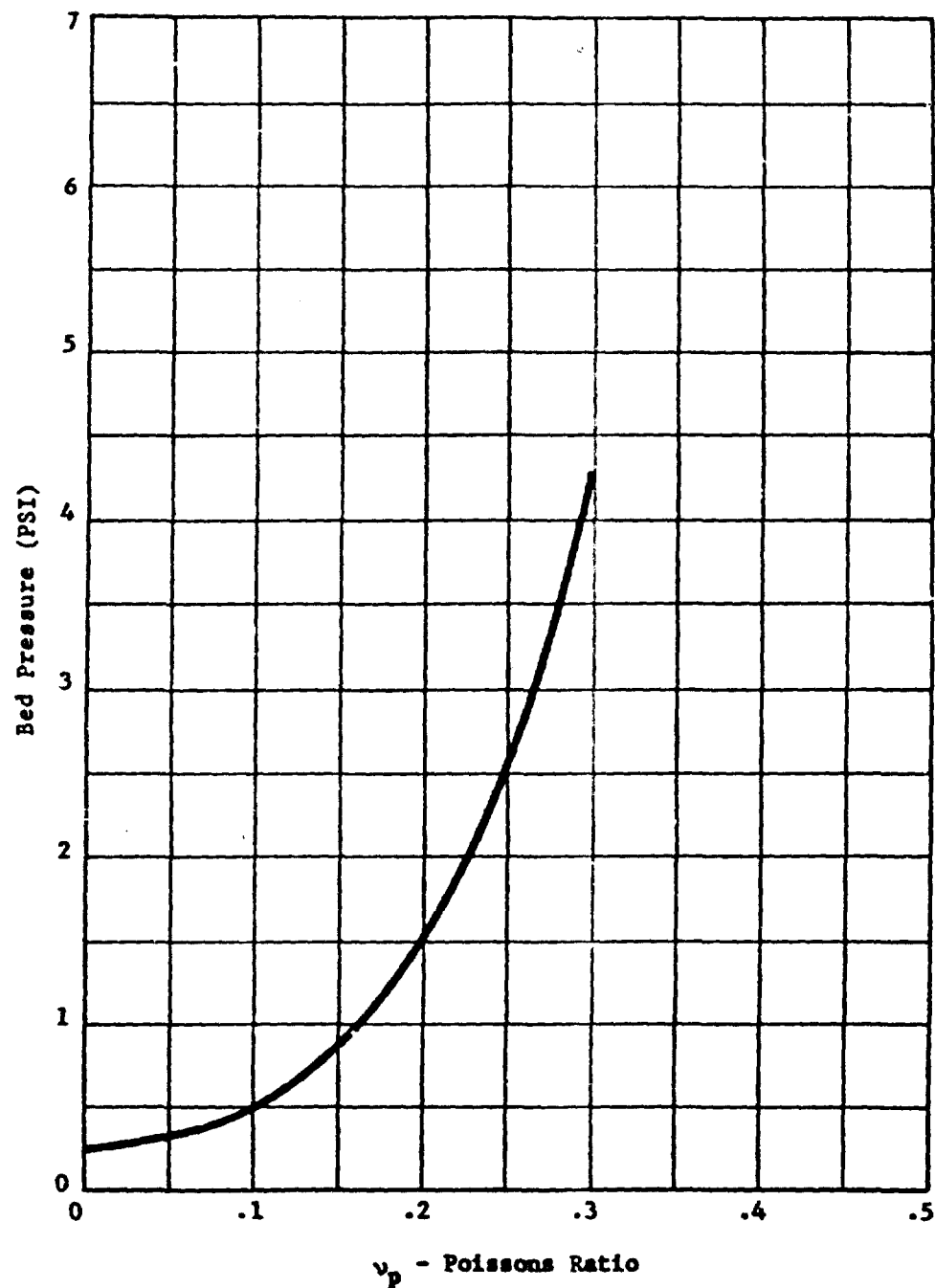
Figure 4-24. Bed Pressure Required to Produce Catalyst Failure as a Function of Poisson's Ratio.

In an earlier section a two-dimensional failure model was developed from a uniaxial compressive stress failure load and several assumptions about the pore shape and distribution. In view of the uncertainties of the pore shape, pore distribution in this material the extension of this single failure point to a three dimensional failure model was not felt justified. Therefore, no estimates of failure volumes were generated.

Future studies should be directed to obtain additional failure data, e.g., tensile, biaxial, etc., from which a three-dimensional failure model can be constructed. With the three-dimensional failure model and the stress distributions generated from the earlier analysis the volume of failed material can be predicted as a function of bed pressure.

Considering the predicted stresses produced by the thermal loading, the internal pressure loading and the particle-to-particle contact loading, the contact problem appears to be the most damaging. Thus, the calculations indicate, using reasonable assumptions regarding catalyst properties such as Poisson ratio, that failure resulting from static pressure forces causing excessive particle to particle contact loading in all probability is a significant mechanism in catalyst breakup. The results suggest that longer engine life could be obtained if the contact area between particles were increased, which will require a redesign of the shape of the catalyst, or by techniques to isolate the particles from each other.

4.2.6.3 Relationship Between Bed Volume and Bed Compaction Pressure

In this section the relationship between the change in bed volume as a function of bed pressure for a sphere pack is presented. This relationship shows the relation between the pressure and volume change in nonlinear. The relationship also gives a simple method of checking the accuracy of the sphere pack assumptions used to calculate point-to-point contact forces from bed compaction pressure.

The relationship for the change in the bulk volume of a pack of identical, isotropic elastic spheres under an external pressure P was solved by Brandt, Reference 111. The solution was generated by using Hertz contact theory. The Hertz theory, as presented in Reference 101, shows the change in radius of one of the spherical particles at the point of contact decreases by the amount

$$\Delta R = \left(\frac{3 \ (1-\nu^2) \ F}{4 \ ER^{1/2}} \right)^{2/3} \tag{4.2-40}$$

where   F = the contact force (lbs)
        ν = Poisson's ratios of the spheres
        R = radius of the spheres (in.)
        E = Young's modulus (lbs/in^2)

Since the displacement is not linear with load, the volume change is also not expected to be linear with load. Brandt, Reference 111, using Hertz contact theory and a sophisticated energy technique showed for an aggregate of equal sized particles, in random packing, the relationship between the mean pressure in the bed and the bed volume change is

$$\frac{\Delta v}{v_o} = 3 \left[\frac{1.75 \, (1-v_p^2)}{E} \right]^{2/3} P^{2/3} \tag{4.2-41}$$

where P = pressure in the bed (psi)
Δ_v = the volume change of the bed (in)
v_o = the initial volume of the bed (in)
E = Young's modulus (psi)
v_p = Poisson's ratio of the porous sphere

This relationship was generalized in Reference 111 for a fluid filled bed, but the relationships are quite complicated and are not presented. Equation 4.2-41 shows that while the particles within the sphere pack remain elastic the pack does not follow a linear load volume relationship. If the change in volume ($\Delta v/v$) is plotted versus $P^{2/3}$ (the bed pressure to the 2/3 power) then a linear relationship is expected. Therefore, from Equation 4.2-41, nonlinear bed pressure volume relationship, even for elastic materials, is expected.

The accuracy of Equation 4.2-41 was tested (Reference 112) for low modulus (scft spheres ($E/(1-v)^2$ = 0.54 x 10^4 psi) and high modulus (hard) spheres ($E/(1-v)^2$ = 33 x 10^6 psi). Good correlation was obtained for the soft spheres while poor correlation was obtained for the hard spheres. This can be attributed to the random nonuniformities in the radius of the sphere which had a better chance to be evened out with the soft spheres than with the hard sphere at low pressures (Reference 106).

The non-uniform radius and size problem was considered in Reference 113. The model developed, also using Hertz contact theory, for spheres not in perfect contact as was assumed earlier, allows for an increasing number of contacts between the spheres as the pressure increases. The pressure-volume relationship in Reference 16 is

$$\frac{\Delta v}{v} = \begin{cases} a \, P^{2/3} & p \leqslant p_1 \\ b \, P^{2/3} & p > p_1 \end{cases} \tag{4.2-42}$$

- 142 -

where   a, b are functions of the material properties of the
        spheres.
        pi is the bed pressure required to close all the gaps
        due to the initial nonuniformities of the spheres.

        Good qualitative correlation with Ottawa sand was achieved with
Equation 42. To determine if our material follows the 2/3 law of either
Equation 42-41 or 4.2-42, more experimental compression tests should be
done on particle beds of Shell 405. If significant deviation is found
from Equation 4.2-41, the contact force given in Equation 4.2-23 should
be modified. It was suggested in Reference 113 that the sphere radius be
changed to an effective radius of curvature at the contact point which
is determined experimentally.

4.3   Internal Particle Model

        When liquid hydrazine contacts a cold pellet of Shell 405 catalyst,
a series of processes occur: imbibition of the liquid due to surface tension
forces, decomposition of hydrazine to evolve heat and decomposition products,
transport of heat, liquid and gases due to temperature and pressure gradient,
and change of phase or change of physical properties associated with the
increase in temperature and pressure. If sufficiently high temperatures and
pressures are developed internally, they may be destructive to the catalyst
pellet. To evaluate these processes in a quantitative way, a mathematical
model of the internal particle processes had to be developed, capable of
calculating the sequence of pressure and temperature profiles which are
generated in the particle. These temperature and pressure profiles, once
computed, may be transformed to radial and tangential stress profiles using
the methods described in an earlier section of this report. Because of
the complexity of the flow, state, and reaction rate processes, it is
necessary to perform the calculations by a finite-difference approach,
using digital computer numerical integration to obtain solutions.

4.3.1   Flow Through A Porous Media

        When a pressure gradient causes a single fluid phase to flow through
a porous medium completely saturated with the fluid, under conditions where
viscous, continuum flow is obtained, the flow rate is defined by D'arcy's
Law

$$Q = \frac{K_w A}{\mu} \frac{dP}{dL}$$ (4.3-1)

or

$$\dot{M} = \frac{K_w A \rho}{\mu} \frac{dP}{dL}$$ (4.3-2)

where Q is volumetric flow rate

A is the cross-sectional area of the porous body

μ is the viscosity of the fluid

$\dfrac{dP}{dL}$ is the pressure gradient through the medium

K_m is thepermeability, a property of the porous medium

ρ is the density of the fluid

When a catalyst particle is exposed to a reactive gas at its outer boundary in a system where appreciable pressure gradients <u>do not</u> exist, as is the case in many commercial chemical reactors, then the transport of reactant species into the catalyst pore volume takes place principally by molecular diffusion, driven by concentration gradient. Analyses of commercial catalyst pellet behavior has traditionally been based upon molecular diffusion as the principal (or only) transport mechanism. In contrast, when a Shell 405 pellet is wetted by liquid hydrazine, and then permitted to react, there are large pressure gradients developed, first by the capillary imbibition pressure or the liquid, and later by the high pressure gases generated by the decomposition of hydrazine which has flowed to the interior of the particle. D'Arcy flow and molecular diffusion may be compared to determine their relative importance in determining mass transport in a particle of Shell 405 catalyst. Molecular diffusion follows Fick's law:

$$\dot{M} = DA \frac{d\rho}{dL} = \frac{DA\, M_v}{RT}\, \frac{dP}{dL} \qquad (4.3-3)$$

where D is the diffusion coefficient

A is the cross-sectional area

ρ is density of the diffusing component

L is distance

M_v is molecular weight

R is gas constant

T is temperature

When the flow rate associated with D'Arcy's Law is divided by the rate of molecular diffusion:

$$\frac{\dot{M}_{flow}}{\dot{M}_{diff}} = \frac{K_m P}{D\mu} \qquad (4.3-4)$$

The values for the properties during the pressure buildup in a practicle assumed were:

$K_m = .1$ Darcy $= 9.869 \times 10^{-10}$ cm^2

$p = 1000$ psi $= 6.895 \times 10^7$ dyne/cm^2

$D = .482$ cm^2/sec

$\mu = .00119$ poise

$$\frac{\dot{M}_{flow}}{\dot{M}_{diff}} = \frac{9.869 \times 10^{-10} \times 6.895 \times 10^7}{.482 \times .000119} = 1186$$

The D'Arcy flow process is three orders of decimal magnitude greater than molecular diffusion, hence we feel justified in ignoring molecular diffusion in our model, and retaining only D'Arcy flow.

When two fluid phases are present simultaneously in a porous medium, then the presence of phase A reduces the permeability of the medium for the flow of phase B and vice-versa. The permeability for the flow of each phase is a fraction of the single-phase permeability, and this fraction is called the relative permeability. The relative permeability is a function of the saturation of the two phases, where saturation is defined as the volume fraction of the total pore volume occupied by the phase. Figure 4-25 shows the experimental relative permeability of the alumina to n-decane in the presence of air (Reference 117). By definition, the relative permeability to the flow of the liquid is 100 percent when the liquid saturation is 100 percent; however, the relative permeability falls to zero when the liquid saturation is still 30 percent. This indicates that if a wetting liquid penetrates into the interior of a porous particle, it cannot subsequently be entirely removed by a flow process, such as expulsion by the flow of gas past it, but rather can only be removed by evaporation or chemical reaction in situ. Figure 4-26 shows that when two phases are present in a porous medium, each interferes with the flow of the other, but that the effect is not necessarily symmetric between the wetting phase and the nonwetting phase (Reference 118). The sum of the two relative permeabilities at most saturations is usually well under 100 percent.

4.3.2 Klinkenberg Effect, Non-Continuum Flow of Gases

When the pore sizes in a porous medium become so small as to be comparable to the mean free path of the molecules of the fluid, then non-continuum flow effects become important. For flow through pipes or other man-made hardware of a simple known shape and size, the Knudsen number can readily be calculated. When the shapes and pore size distributions are no better known than is the case for a sample of porous medium, however, an experimental approach is necessary to define the effects of non-continuum flow. Figure 4-27 shows the variation in experimentally observed permeability when several gases having different molecular properties are flowed through a fine-grained porous medium at various pressures (Reference 110). The increase in observed permeability as the pressure decreases is the result of non-continuum flow becoming important in an increasing fraction of the pores in the total ensemble of pore sizes in the medium. The experimentally determined non-continuum flow effect can be described by the relationship

$$K_g = K_c \left(1 + \frac{b}{p}\right) \tag{4.3-5}$$

where K_g is the gas permeability with non-continuum effects
   K_c is gas permeability under continuum conditions
   P is the gas pressure
   b is a coefficient for a given gas and medium

The constant b in the above equation depends on the mean free path of the gas and the size of the openings in the porous medium. Since permeability also varies with the pore size, it would be expected that the Klinkenberg factor, b, could be correlated with the permeability. Figure 4-28 shows such a correlation (Reference 120).

In our model of the processes occurring in the pellet, the flow of liquid hydrazine and of hydrazine vapor or product gases considers the time-varying distribution of saturation within the pellet and considers the resultant local relative permeability for liquid and gas, and the extent of non-continuous flow in the gas phase through the Klinkenberg correction.

4.3.3 Imbibition Pressure

When a non-wetting fluid, such as mercury, is injected into a porous medium, displacing a wetting fluid phase, a considerable pressure may be required to introduce the non-wetting fluid, the pressure varying as a function of the saturation of the porous medium. Conversely, a wetting fluid phase will be preferentially drawn into a sample of porous medium, spontaneously generating a pressure which expells any non-wetting phase which may be present. These pressures can be measured to fefine the imbibition characteristics of the porous medium. Figure 4-29 shows raw experimental data obtained when a particular sandstone samples was injected with mercury, and when the same sample spontaneously imbibed water to displace hydrocarbon. The shape of the curves is the same for the two different fluids, with only the scale factor differing to correspond to the different values for the interfacial tension and contact angle, i.e., $\sigma\cos\theta$/. (Reference 121) H. C. Leverett proposed the J-function to correlate imbibition pressure data (Reference 122):

$$J(s) = \frac{P_c}{\sigma\cos\theta} \left(\frac{K}{\phi}\right)^{1/2} \qquad (4.3-6)$$

where: P_c is imbibition pressure
σ is interfacial tension
θ is contact angle
K is permeability of the medium
ϕ is porosity of the medium.

It is instructive to compare this equation, rearranged:

$$P_c = \frac{\sigma\cos\theta}{\left(\frac{K}{\phi}\right)^{1/2}} J(s) \qquad (4.3-7)$$

With the equation for the pressure difference across a meniscus in a capillary:

$$P_c = \frac{\sigma\cos\theta}{r} \qquad (4.3-8)$$

The $\left(\frac{K}{\phi}\right)^{1/2}$ term is approximately proportional to the mean value of pore
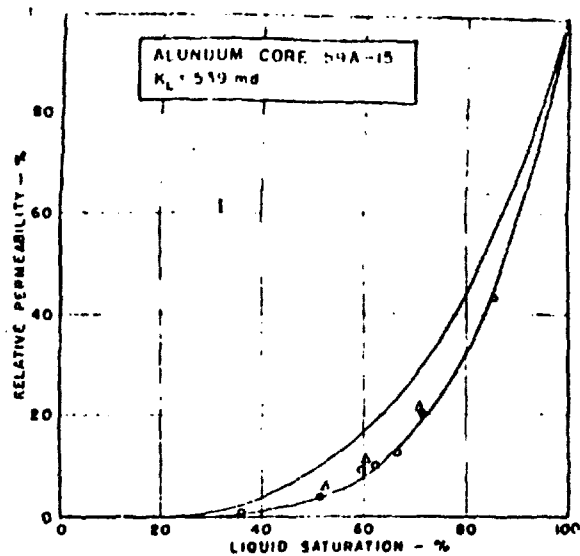
Figure 4-25
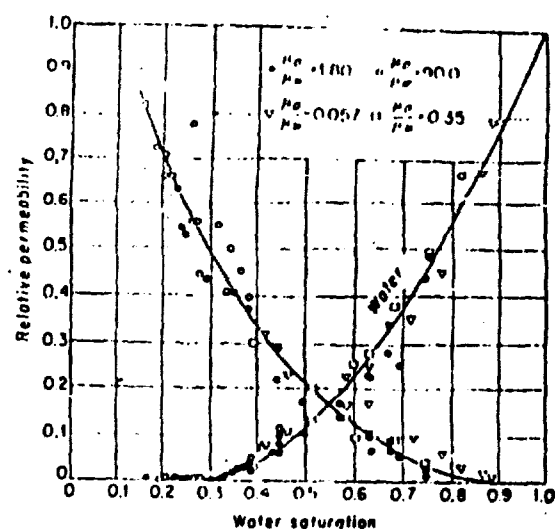
Figure 4-26
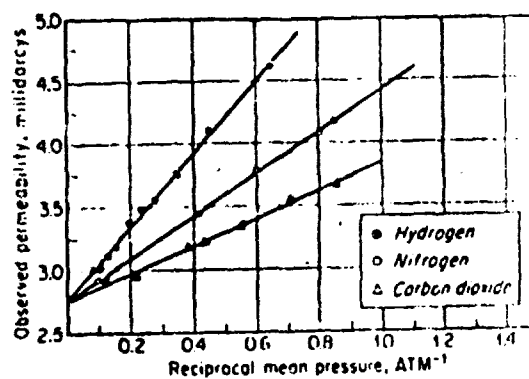
Permeability of core sample L to hydrogen, nitrogen, and carbon dioxide at different pressures. Permeability to isooctane, 2.55 millidarcys. (*From Klinkenberg.*[])

Figure 4-27
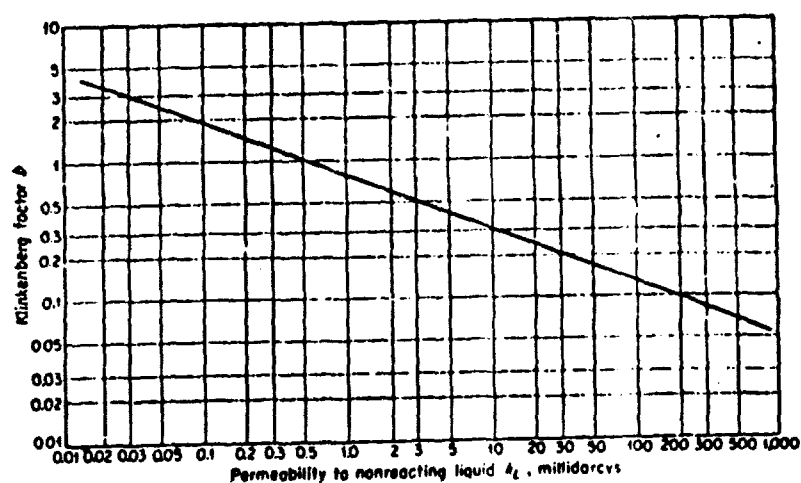
Correlation of Klinkenberg factor b with permeability. (*From American Petroleum Institute.*[])

Figure 4-28
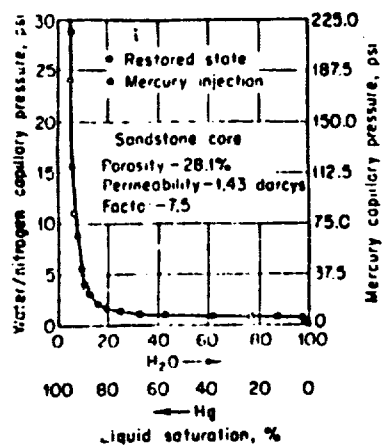
Figure 4-29
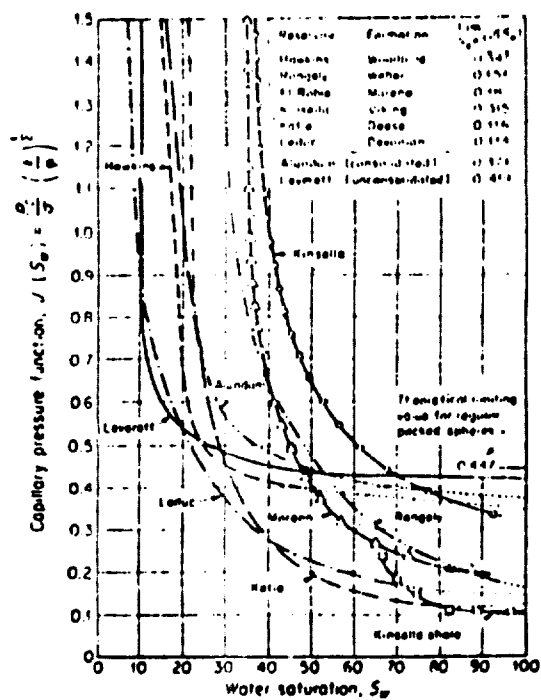
Figure 4-30

radius, and the undimensional function J(s) describes the effect of pore diameter distribution, relative to the mean, over the entire pore volume. Figure 4-30 illustrates J-functions for a wide variety of different materials, including a porous alumina (Reference 123). The J-function for the alumina used in our model is taken from the experimental measurements of pore size distribution versus cumulative pore volume in Shell 405 done at U.A.R.L. (Reference 124) (Figure 4-31). This can be converted to a curve of capillary imbibition pressure versus saturation, or J-function versus saturation by using Equations 8 and 6 (Figure 4-32). The capillary pressure curve presumes room-temperature liquid hydrazine, having a surface tension of 65.7 dyne/cm and a zero wetting angle. The J-function curve presumes a permeability of 100 millidarcy and a porosity of .25. The imbibition pressures used in our model vary with time and location in the pellet according to the local values for saturation and temperature-dependent interfacial tension.

4.3.4 Thermal Effects

The MDAC internal particle model calculates the convection of heat due to flow of both liquid and gas, the conduction of heat through the particle, and the effects of local heat evolution or absorption due to decomposition reactions and hydrazine phase change. If the catalyst pellet were in the environment typical of most commercial gas-phase catalytic reactor, then pressure gradients would be small, D'Arcy flow of fluid through the particle would be small, and heat convection could be ignored. For a particle of Shell 405 catalyst exposed to liquid hydrazine, however, these assumptions are not valid, as can be shown:

Conduction of Heat:

$$\overset{o}{Q} = K_t \ A\frac{T}{L} \tag{4.3-9}$$

Convection of heat:

$$\overset{o}{H} = \frac{K_m}{\mu} \rho A C_p T\frac{\Delta P}{\Delta L} \tag{4.3-10}$$

Take the ratio of convection to conduction:

$$\frac{\overset{o}{H}}{Q^o} = \frac{K_m}{K_t} \rho \ \frac{C_p}{\mu} \ T \ \frac{\Delta P}{\Delta T} \tag{4.3-11}$$

Use reasonable values for properties:

K_m = .1 Darcy = $9.869*10^{-10} cm^2$

ρ_{gas} = .0122 gramcm^3

$C_{p_{gas}}$ = .679 cal/gram °K

T = 728.8 °K

ΔP = 1000 psi = $6.8947*10^7$ dyne/cm^2

K_t = .01 cal/sec cm °K

μ = .005 poise

ΔT = 728.8 °K

- 149 -
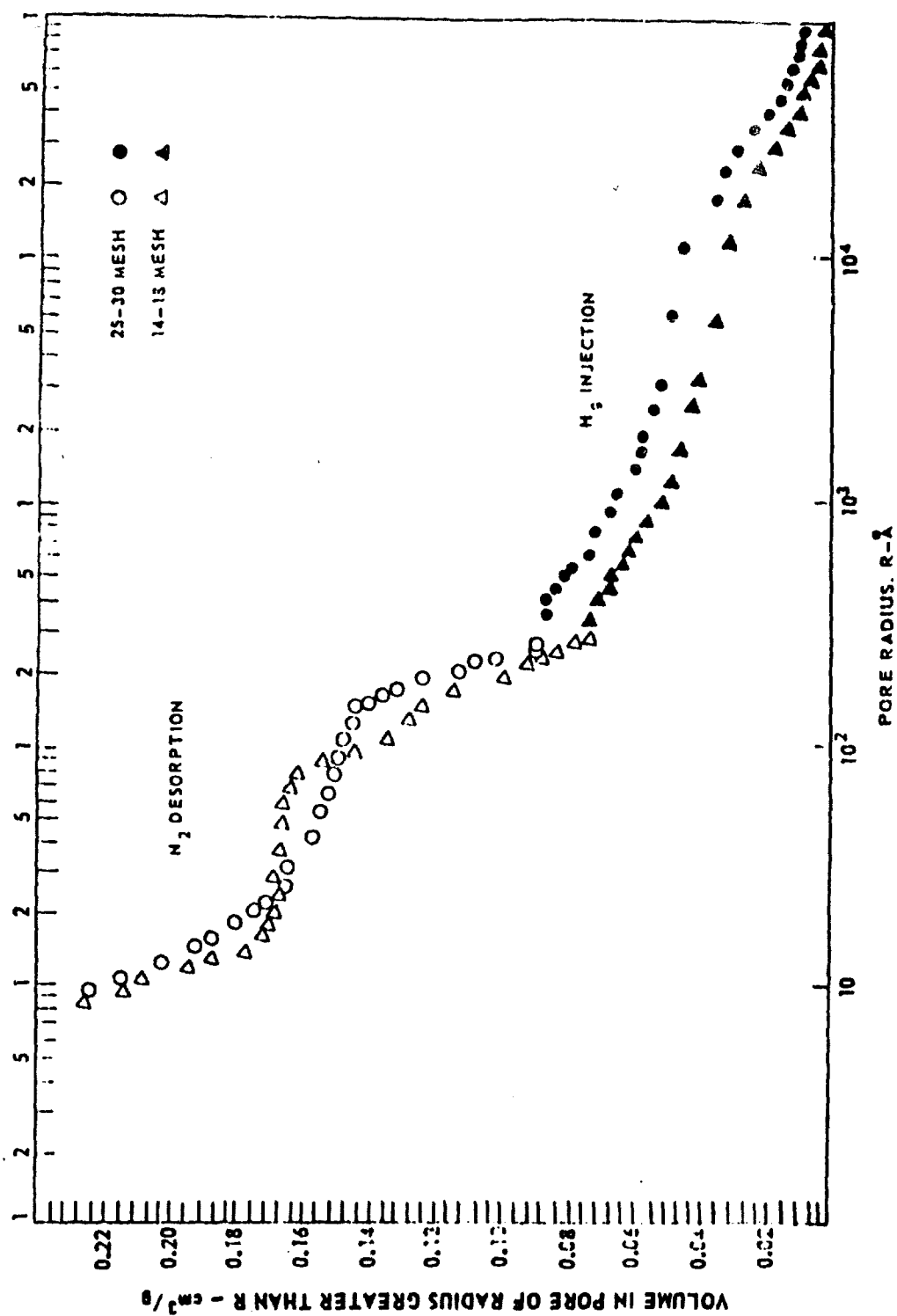
Figure 4-31. Cumulative Pore Size Distribution for Shell 405 Catalyst.

Figure 4-32
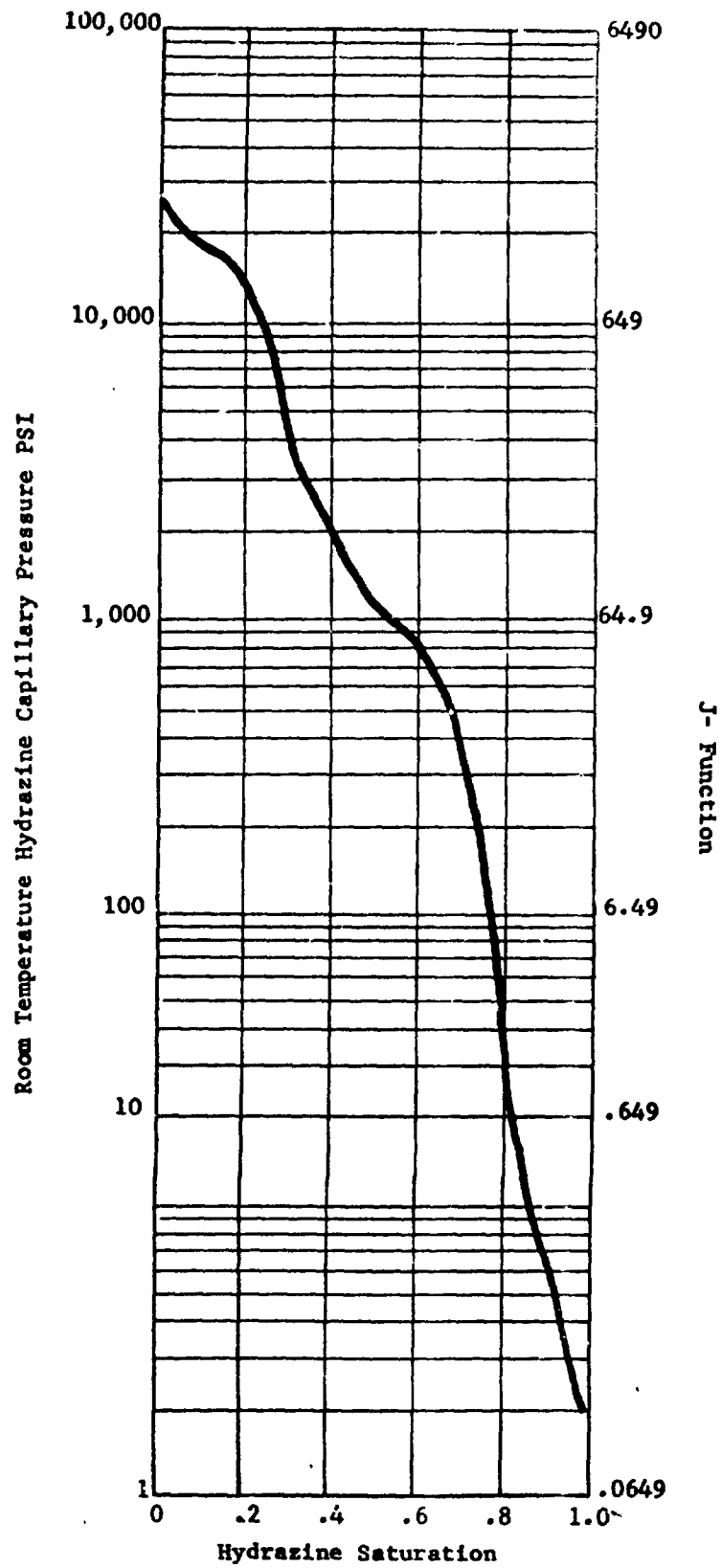
Evaluate the ratio of convective to conductive heat transport

$$\frac{H}{Q} = \frac{9.869 \times 10^{-10} \times .0122 \times .679 \times 728.8 \times 6.8947 \times 10^7}{.01 \times .005 \times 728.8} = 11.$$

Convective heat transfer is seen to be an order of magnitude more important than conduction under the particular conditions chosen for this comparison. Obviously, either process can be important, under the appropriate conditions, and the importance at any particular time and location will depend upon the particular values in the catalyst pellet being analyzed.

In the solution of the internal particle processes, the viscosity of the liquid and gas, the interfacial tension, the vapor pressure, the specific enthalpies, etc., are calculated as functions of local time-varying temperature using correlations developed for the NDAC TCC computer program[Reference 125]. Both the homogeneous gas phase decomposition rate of hydrazine and the heterogeneous, surface catalyzed decomposition are calculated using global Arrhenius equations, taken from the work done at U.A.R.L. For the sake of simplicity, the decomposition is assumed to be one-step:

$$N_2H_4 \longrightarrow N_2 + 2H_2 \qquad\qquad (4.3\text{-}12)$$

4.3.5 Finite Difference Model

The interior of the pellet is represented by a linear sequence of nodal points and internodal paths extending from the external environment (boundary conditions) to the center of the sphere, as in Figure 4-33.

The internodal paths transmit gas (product gas plus hydrazine vapor), liquid hydrazine, heat and enthalpy. The nodal points accumulate gas, liquid and enthalpy and effectuate phase change and chemical reaction. The nodes possess extensive and intrinsic state properties: hydrazine mass, product gas mass, enthalpy, temperature, pressure and saturation.

The types of behavior associated with nodal points and internodal paths is illustrated conceptually in Figure 4-34. Thermal equilibrium between liquid, solid, and gas phases is presumed at each nodal point. Phase equilibrium between hydrazine liquid and vapor is also presumed. The fluid temperatures and vapor concentrations flowing from a nodal point are those of the nodal point. Viscosities and densities used in internodal flow calculations are arithmetic-means of the adjoining nodes. Relative permeabilities are those characteristic of the saturation in the upstream nodal point.

The approximate forms of the more important governing equations are listed below.

Each node has state properties associated with it.
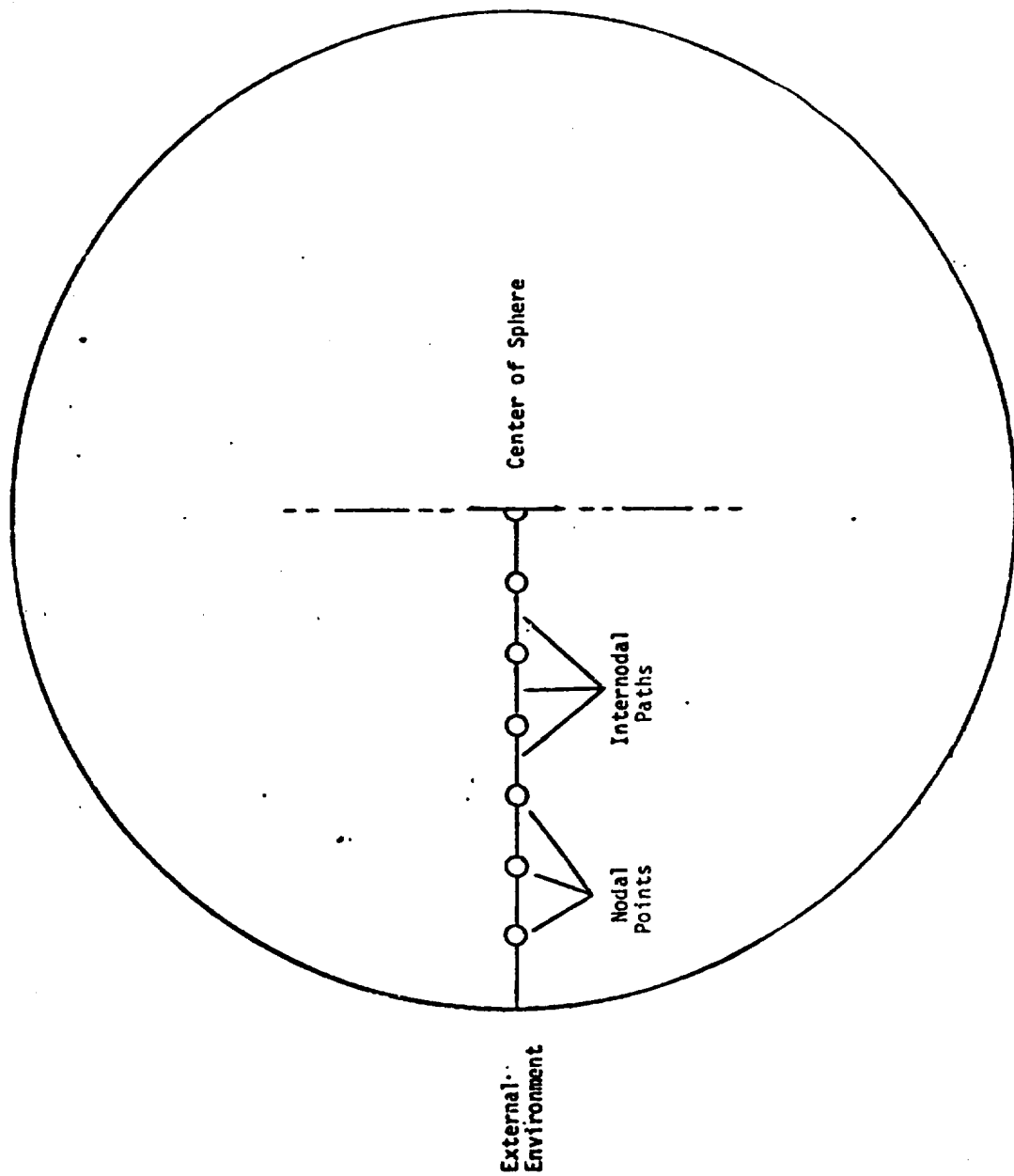
Figure 4-33. Pellet Internal Model.

- 153 -
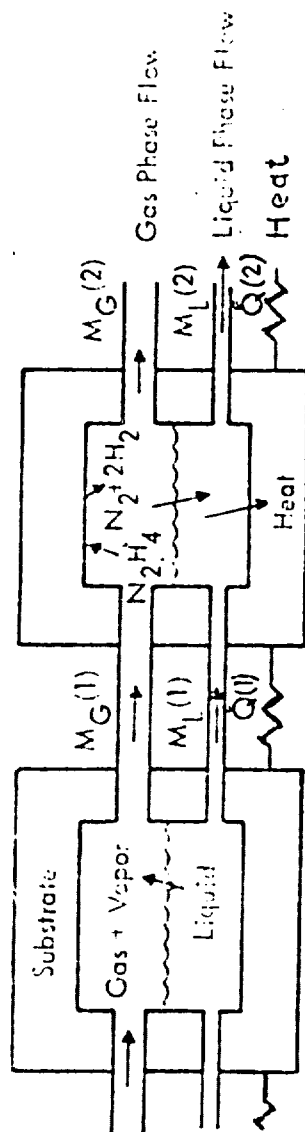
Figure 4-34. Nodal Behavior.

$$\text{Nodal enthalpy} = H_n = H_{Substrate} + H_{Liquid} + H_{gas} \qquad (4.3\text{-}13)$$

$$H_{Substrate} = \rho_s V(1-\phi)\, h_s(T)$$

ρ_s = density of solid phase $\qquad\qquad\qquad\qquad$ (4.3-14)

V = nodal volume = volume of spherical shell

ϕ = porosity = pore volume/nodal volume

$h_s(T)$ = specific enthalpy of solid phase at temperature T

$$H_{Liquid} = \rho\, V \phi S\, h(t) \qquad\qquad\qquad\qquad (4.3\text{-}15)$$

S = liquid saturation = liquid volume/pore volume

$h\ (T)$ = specific enthalpy of liquid phase at temperature T

$$H_{gas} = \rho_g\, V\, \phi(1-S)\, h_g(T) \qquad\qquad (4.3\text{-}16)$$

$h_g(T)$ = specific enthalpy of gas phase at temperature T

Nodal temperature is the value of T, found iteratively, which satisfies the above enthalpy relation when nodal enthalpy is known. The enthalpy versus temperature iteration is done while maintaining phase equilibrium between the liquid and vapor phase of hydrazine.

$$\text{Nodal pressure} = P_n = P_{gas} + P_{vapor} \qquad\qquad (4.3\text{-}17)$$

$$P_{gas} = \frac{N_g R\, T_n}{M_{w_g} V} \phi\,(1-S) \qquad\qquad (4.3\text{-}18)$$

N_g is mass of gas in the node

R is the gas constant

M_{w_g} is Mean Molecular Weight of the gas

$$P_{vapor} = f(T_n) \qquad\qquad\qquad\qquad (4.3\text{-}19)$$

$f(T_n)$ is the vapor pressure of hydrazine

Generating a New Value for Nodal Enthalpy in Node 2 of Conceptual Illustration

$$H_{n(t*\Delta t)} = H_{n(t)} + \text{inflowed enthalpy} - \text{outflowed enthalpy} + \text{enthalpy of reaction}$$
$$+ \text{inflowed heat} - \text{outflowed heat} \qquad\qquad (4.3\text{-}20)$$

$$\text{Inflowed enthalpy} = \overset{o}{M}_g(1) \cdot h_g(1) \cdot \Delta t + \overset{o}{M}_\ell(1) \cdot h_\ell(1) \cdot \Delta t \qquad (4.3\text{-}21)$$

$$\text{Outflowed enthalpy} = \overset{o}{M}_g(2) \cdot h_g(2) \cdot \Delta t + \overset{o}{M}_\ell(2) \cdot h_\ell(2) \cdot \Delta t \qquad (4.3\text{-}22)$$

$$\text{Enthalpy of reaction} = \overset{o}{M}_r(2) \cdot h_r \cdot \Delta t \qquad\qquad (4.2\text{-}23)$$

- 155 -

$\overset{o}{M}_r(2)$ is reaction rate of hydrazine in Node 2

h_r is specific heat release of hydrazine decomposition reaction

Δt is the time interval: used for numerical integration

Inflowed heat $= K_r \, (A(1)/L(1)) \cdot (T(1)-T(2)) \cdot \Delta t$ (4.3-24)

Outflowed heat $= K_T \, (A(2)/L(2)) \cdot (T(2)-T(3)) \cdot \Delta t$ (4.3-25)

Gas Phase Flow Rate into Node 2 of Conceptual Illustration

$$\overset{o}{M}_g(1) = \rho_g \; g = \frac{K_a K_{r_g} K_k \, A \, (P_1 - P_2) \; g}{\mu_g \; L}$$ (4.3-26)

K_a = permeability of the substrate

K_{r_g} = relative permeability for gas (empirical function of saturation)

K_k = Klinkenberg rarefaction correction $= (1 + \dfrac{b}{P})$ 4.3-27)

       b is the Klinkenberg constant for the substrate

A = cross-sectional path area

ρ_g = mean density of gas phase materials in Nodes 1 and 2

μ_g = mean viscosity of gases in Nodes 1 and 2 (empirical function of temperature)

L = path length

Generating a New Value for Nodal Gas Mass

$M_{g(t+\Delta t)} = N_{g(t)}$ + inflowed gas - outflowed gas + gas formed by reaction (4.3-28)

inflowed gas $= \overset{o}{H}_g(1) \cdot \dfrac{N_g(1)}{N_g(1) + N_v(1)} \cdot \Delta t$ (4.3-29)

N_g is mass of product gases

M_v is mass of hydrazine vapor

outflowed gas $= \overset{o}{N}_g(2) \cdot \dfrac{N_g(1)}{N_g(\;) + N_v(\;)} \cdot \Delta t$ (4.3-30)

gas from reaction $= \overset{o}{N}_r(2) \cdot \Delta t$ (4.3-31)

Liquid Phase Flow Rate into Mode 2 of Conceptual Illustration

$$\overset{o}{M}_{\ell}(1) = \rho_{\ell} q_{\ell} = \frac{K_a K_{r_e} \; A(P_1 - P_2) - (I_1 - I_2)\rho_{\ell}}{\mu \ell L} \qquad (4.3\text{-}32)$$

K_r = relative permeability for liquid (empirical function of saturation) evaluated for saturation of Mode 1

$$I_1 = \text{imbibition pressure} = \frac{\sigma_1 \cos\theta}{(\frac{K}{\phi})^{1/2}} \; J(S_1) \qquad (4.3\text{-}33)$$

$J(S_1)$ = J-function evaluated at saturation of Mode 1

σ_1 = interfacial tension at the temperature of Mode 1

Generating a New Value for Total Hydrazine in Mode 2

$$M_{H(t+\Delta t)} = M_{H(t)} + \text{inflowed hydrazine} - \text{outflowed hydrazine} - \qquad (4.3\text{-}34)$$
$$\text{hydrazine reacted}$$

$$\text{Inflowed hydrazine} = M_{\ell}(1) \cdot \Delta t + H_g(1) \cdot \frac{M_v(1)}{M_g(1) + M_v(1)} \cdot \Delta t \qquad (4.3\text{-}35)$$

$$\text{Outflowed hydrazine} = M_{\ell}(2) \cdot \Delta t + M_g(2) \cdot \frac{M_v(2)}{M_g(2) + M_v(2)} \cdot \Delta t \qquad (4.3\text{-}36)$$

$$\text{Hydrazine reacted} = M_r(2) \cdot \Delta t$$

Generating a New Value for Liquid Mass, Vapor Mass, Saturation

New values are found for liquid and vapor hydrazine by iteratively determining nodal temperature to agree with nodal enthalpy while maintaining hydrazine phase equilibrium.

$$M_v = \frac{P_{vapor} \cdot M_w \; V \phi \; (1-S)}{RT} \qquad (4.3\text{-}37)$$

$$M_{\ell} = M_H - M_v \qquad (4.3\text{-}38)$$

$$V_{\ell} = M_{\ell}/\rho_{\Omega} \text{ where V is liquid volume,} \quad \text{is liquid} \qquad (4.3\text{-}39)$$
$$\text{density (empirical function of temperature)}$$

$$S = V_{\ell}/V \text{ where S is liquid saturation} \qquad (4.3\text{-}40)$$

Obviously an iterative approach is required to obtain S together with T and P from enthalpy, and known phase behavior.

The hydrazine vapor concentration is

$$\rho_v = \frac{P_{vapor} \; M_w}{RT} \qquad (4.3\text{-}41)$$

Estimating The Chemical Reaction Rate

$$M_r = M_{r_{heterogeneous}} + M_{r_{homogeneous}} \tag{4.3-42}$$

$$M_{r_{het}} = V_n \phi(1-S) \, \rho_v * 10^{10} \, e^{-\frac{2758}{RT}} \tag{4.3-43}$$

V_n = nodal volume

ρ_v = hydrazine vapor concentration

$$M_{r_{hom}} = V_n \, \phi(1-S) \, \rho_v * 2.14 \times 10^{10} \, e^{-\frac{36,400}{RT}} \tag{4.3-44}$$

Initial Conditions

The interior of the particle may be set to a uniform initial value for temperature, pressure, and liquid hydrazine saturation.

Boundary Conditions

In addition to the internal behavior of the catalyst, it is necessary to impose conditions at the boundary. The boundary temperature and pressure may be specified in an arbitrary time-dependent way by designating eleven equally timed values, for temperature and pressure, with linear interpolation with time between specified points. A time may be specified, for the boundary to "dry up." The boundary will be wetted with liquid hydrazine before this time, and will contact only dry product gas after this time.

4.3.6 Results from the Operation of the Internal Particle Model

Although the MDAC internal particle model is not completley developed and verified by comparison with experimental data, test cases were nevertheless run with the model. The results obtained from the small number of test cases which have been calculated to date, however indicate the nature of the processes which occur when a particle of cold Shell 405 catalyst is wetted with liquid hydrazine. The sample case described as an illustrative example (Figure 4-35) is based upon a particle of 25 mesh Shell 405. The initial pressure is .001 psi and the initial temperature is 300°K. At time zero the boundary condition is changed to liquid hydrazine at 300°K and 1 psia.

The liquid imbibition proceeds very rapidly, concurrent with pressure build-up in the particle. On the order of .2 microseconds after start, the first gas commences to flow out of the particle. The internal gas pressure at this time is about 12 psia. The liquid hydrazine continues to flow inward very rapidly countercurrent to the outward flow of gas. This countercurrent flow is possible because the gas flow is driven by pressure gradient alone, while the liquid flow is driven by the sum of pressure gradient and capillary imbibition pressure gradient. Both phases can flow independently, because of the modest liquid saturation of the outermost laminae, which gives appreciable relative permeability
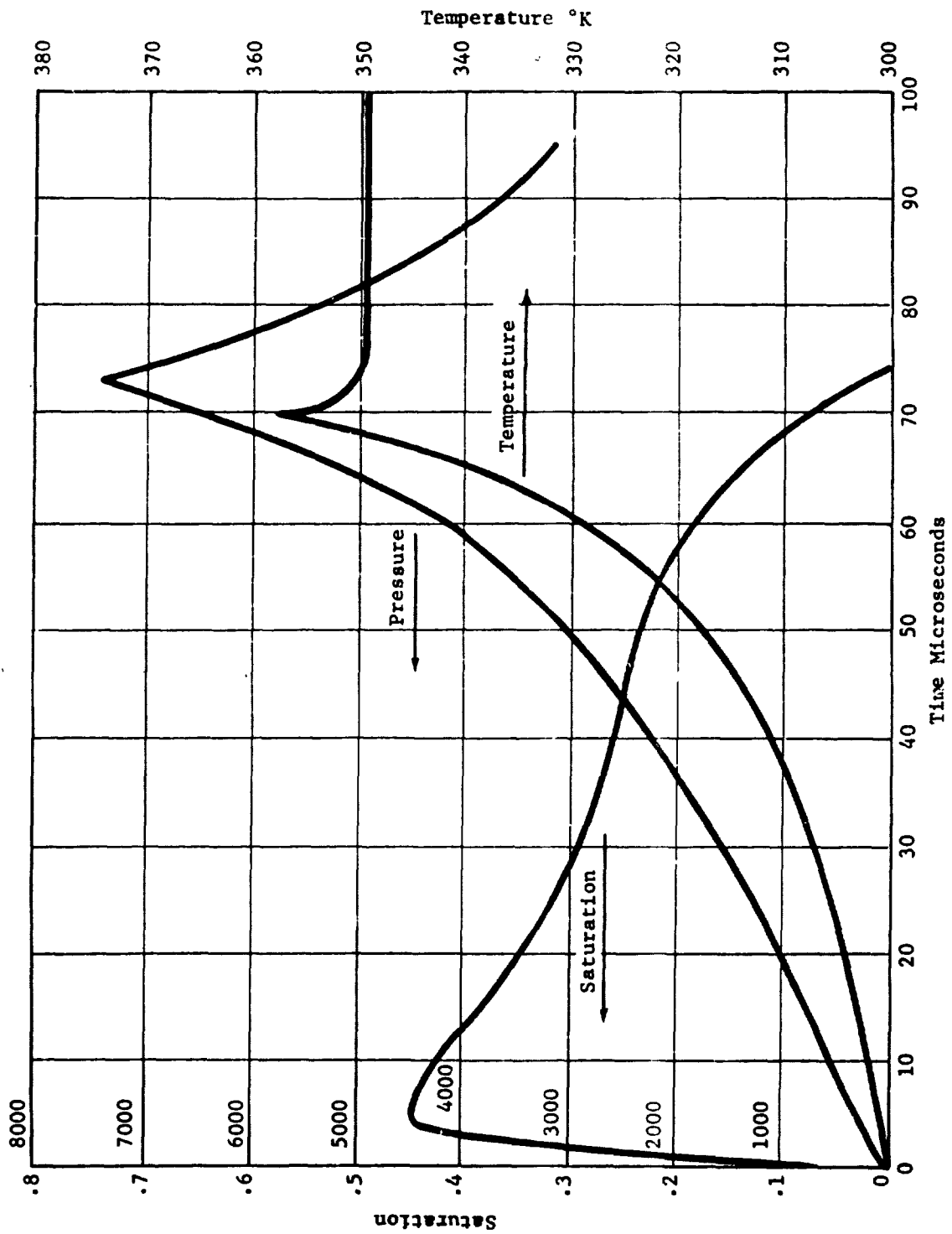
Figure 4-35. Internal Particle Model Illustrative Case.

for both liquid and gas, i.e., the presence of either phase at this time does not completely block the flow of the other phase.

At a time 4.0 microseconds after start, the liquid influx at the boundary is first cut off. At this time the internal gas pressure of 270 psia is finally able to overcome the liquid imbibition pressure, which is now much reduced from its earlier values, because of the high liquid saturation of the outermost portions of the particle (65 percent liquid saturation). At this time the volume mean saturation of the entire particle is 44 percent and the temperature rise is still less than 1 degree.

The flow of liquid hydrazine at the outer boundary of the pellet reverses as the internal gas pressure continues to rise. At 12.19 microseconds after start the maximum outward flow rate of liquid hydrazine is attained. At this time the liquid saturation at the surface of the particle is decreasing, and the liquid relative permeability is declining faster than the outward pressure gradient is increasing. Liquid hydrazine from the outer layer of the pellet continues to be drawn from the outer laminae toward the center by the imbibition pressure gradient.

The outward flow of liquid hydrazine from the outer boundary of the pellet does not cease until 38.39 microseconds after start, when the liquid saturation in the surface layer has decreased below 30 percent, which reduces the liquid relative permeability to zero.

The most interesting aspect of the particles' behavior at this time is the increasing temperature due to the exothermic decomposition of hydrazine in the interior of the particle. As the temperature increases, both the vapor pressure of the hydrazine and the reaction rate of the hydrazine vapor increase rapidly, with the result that the rate of temperature rise is accelerated still further.

The "thermal explosion" is culminated at 70 microseconds after start, as the last of the liquid hydrazine in the pellet is consumed. The peak pressure is 7390 psia.

Following the pressure peak, the passive blowdown of the particle begins, and by 95 microseconds after start, the pressure has declined to 3171 psia.

The stress imposed upon the catalyst particle by a pressure excursion of this sort is easily calculated. The pressure profile in the interior of the particle is remarkably flat during the time that the highest pressures are attained. According to the equations for stress generated by internal pressure (4.2-25 and 4.2-26), for the case of constant pressure profiles,

$$\sigma_r = f \cdot p \qquad\qquad (4.3\text{-}46)$$

$$\sigma_\theta = f \cdot p \qquad\qquad (4.3\text{-}47)$$

where σ_r is radial stress in the particle
σ_θ is tangential stress in the particle
f is the porosity of the particle
p is the internal pressure

- 160 -

For a catalyst particle porosity of .26, the maximum stresses are each calculated to be 1921 psi, and directed in tension. This stress level should produce failure according to our best estimate of the failure model for Shell 405 (Figures 4-3 and 4-4), however, it should be remembered that it is rather hazardous to estimate a failure in biaxial tension solely from experimental failure tests performed in uniaxial compression.

In general, based on the initial results of the internal particle processes model, it can be seen that contact with liquid hydrazine results in imbibition followed by in-situ decomposition which can produce internal particle pressures capable of causing particle destruction.

Engineering Remedies

One way to avoid the internal pressure generation which arises from liquid imbibition is to prevent the liquid hydrazine from actually contacting the catalyst. A possible method of accomplishing this would be to arrange thermally conductive metal screens ahead of the catalyst pack, to transport heat from the zone of heat release to an upstream location where the liquid hydrazine could be prevaporized. An alternate method to prevaporize the hydrazine might be to provide an open volume of sufficient length between the injector and the upstream end of the pack to vaporize the hydrazine spray droplets during their passage through the product gases. Due to the high latent heat of evaporation of hydrazine, and the complexities of either of these processes during cold start transients, either of these approaches would involve major problems in engineering analysis. Once the catalyst particles are heated to a temperature 20 percent to 50 percent (on an absolute scale of temperature) above the boiling temperature of hydrazine at the existing chamber pressure, the hydrazine will film-bind and refuse to wet the surface of the catalyst (References 126-128). This should protect hot catalyst from liquid imbibition effects. In addition theoretical considerations infer that smaller or more permeable catalyst particle sizes should result in lower peak pressures.

4.4 Differential Thermal Expansion

One of the mechanisms that may cause or contribute to catalyst breakup is differential thermal expansion. Differences between the thermal expansion rates for the catalyst bed and chamber walls can result in application of compressive forces to the bed and/or the creation of voids in the catalyst bed which, in turn, produces considerable particle abrasion, settling and channeling. The differential expansion is compounded by the simultaneous effect of chamber strain associated with the internal pressure forces. The differential expansion phenomenon normally occurs during the initial ambient start of a firing sequence and during cooldown after the last pulse.

This section presents the differential thermal and pressure expansion analysis of a monopropellant hydrazine catalyst thruster. An evaluation of the effects of various operating and design parameters on the thermal response of the catalyst bed and chamber wall and the resulting net expansion (or contraction) is also presented.

4.4.1 Method of Calculations

Kesten's (Reference 124) analysis of catalyzed hydrazine decomposition

reactors was used to obtain the temperature distributions in the catalyst bed. Calculations of the temperature and reactant concentration distribution as functions of time and axial position in typical reaction chamber configurations can be made with Kesten's steady state and transient computer programs. The steady state calculations are required to provide certain inputs to the transient program. Kesten's transient program was used to give a representation of the thermal transient in the catalyst bed and chamber wall. For computational purposes the catalyst bed is divided into nodal segments (usually around 50 segments) and temperature and pressure calculations are made for these segments as a function of time.

For this study, the transient computer program was modified to include the calculation of thermal expansion. Corresponding to the nodal particle temperatures at each selected time point, the linear deformation, δ_T, is calculated by the relation

$$\delta_T = \alpha L \ (\Delta T) \tag{4.4-1}$$

in which α is the coefficient of linear expansion, L is a length and ΔT is the temperature change. Calculating the dimensional change of each segment in this manner, the incremental volume change is obtained. The change in bed volume is summed from the inlet position to the end of the bed for every selected time increment.

Thermal expansion of the chamber wall is calculated from the wall temperatures predicted by Kesten's computer program. Kesten calculates the chamber wall temperature assuming Newtonian heating or cooling, i.e., internal resistance (L/KA) << surface resistance (1/hA_1) where K is the wall thermal conductivity, A is the conducting area, h is the surface conductance, and A_1 is the surface area. For the thin-wall, metallic chambers of typical flight reactors, this level of approximation is adequate for providing qualitative information on the effects of various design variables on the differential thermal expansion. With this assumption the temperature in the chamber wall is uniform and is calculated by the equation

$$M_W C_W \frac{dT_W}{dt} = \pi d_c \int_o^L h_W \ (T_i - T_W) \ dz \tag{4.4-2}$$

where

T_W = Wall temperature

T_i = Interstitial phase temperature

t = Time

M_W = Thermal mass of chamber wall

C_W = Specific heat of chamber wall

d_c = Diameter

h_W = Heat transfer coefficient between bulk fluid and wall

z = Axial distance

L = Length of reaction chamber

- 162 -

The equation is valid if the outer wall surface is insulated. Heat loss from the chamber wall to the surrounding atmosphere can be accounted for by adding a term to the right side of the above equation. Heat loss by natural convection and radiation to space were the only heat transfer modes considered and can be represented by the form $-h_a A_W (T_W - T_a)^{1.25}$ or $-\sigma \epsilon A_W (T_W^4 - T_a^4)$, respectively where h_a is the natural convection heat transfer coefficient, A_W is the chamber wall surface area, T_a is the ambient temperature, σ is the Boltzmann constant, and ϵ is the wall emissivity.

The time dependent free chamber volume is based on the wall thermal expansion and the simultaneous effect of chamber strain associated with the internal pressure forces. For a cylindrical chamber the pressure deformation is calculated by

$$\delta_p = \frac{PD^2}{2tE} \qquad (4.4-3)$$

where P is the chamber pressure, D is the diameter, t is the wall thickness and E is Young's modulus.

4.4.2 Results of Calculations

Calculations were made for a monopropellant hydrazine reactor with the modified transient computer program to evaluate the effects of various system parameters on the differential expansion of the catalyst bed and chamber walls. Table 4-2 summarizes the base line operating and design characteristics which were used for the calculation. The catalyst bed is cylindrically shaped with two layers of Shell-405 catalyst. The overall bed length is 2 inches with the upper bed consisting of 25-30 mesh particles in the first 0.2 inch and 1/8 inch pellets for the remainder of the bed. The vacuum thrust is 5 lb$_f$ and the bed loading is 0.05 lb/in^2-sec which results in a chamber diameter of 0.84 inches (nozzle area ratio of 2). Chamber wall material is Haynes Alloy 25 (L605) which is a common structural material for monopropellant applications. The structural thickness of the chamber wall is sized from hoop stress considerations unless the value calculated is less than the minimum handling thickness of 0.05 inches. The wall heat transfer mode assumed for the base line calculations is natural convection.

Figure 4-36 illustrates the cold (ambient) start temperature histories in the catalyst bed and chamber wall for the baseline conditions. The temperature response of the catalyst particles varies along the length of the bed with the response decreasing with distance from the inlet end. As expected the chamber wall temperature lags behind the catalyst particle temperatures. Corresponding to the temperature histories in the bed and chamber wall, the volume change is presented in Figure 4-37. Although the chamber wall temperature is always less than the catalyst bed on start-up, the volume increase in the chamber is greater than the volume increase in the catalyst bed after 0.7 seconds. This is the result of the wall coefficient of thermal expansion being four times that of the catalyst particle. Prior to 0.7 seconds the catalyst bed is compressed by differential thermal expansion between the bed and chamber wall. The chamber wall volume change shown in Figure 4-37 includes the volume increase due to internal pressure forces. The pressure induced volume change is significant only during the first 0.2 seconds of operation. After 5 seconds, the contribution of the pressure strain is only one percent of the total wall volume increase.
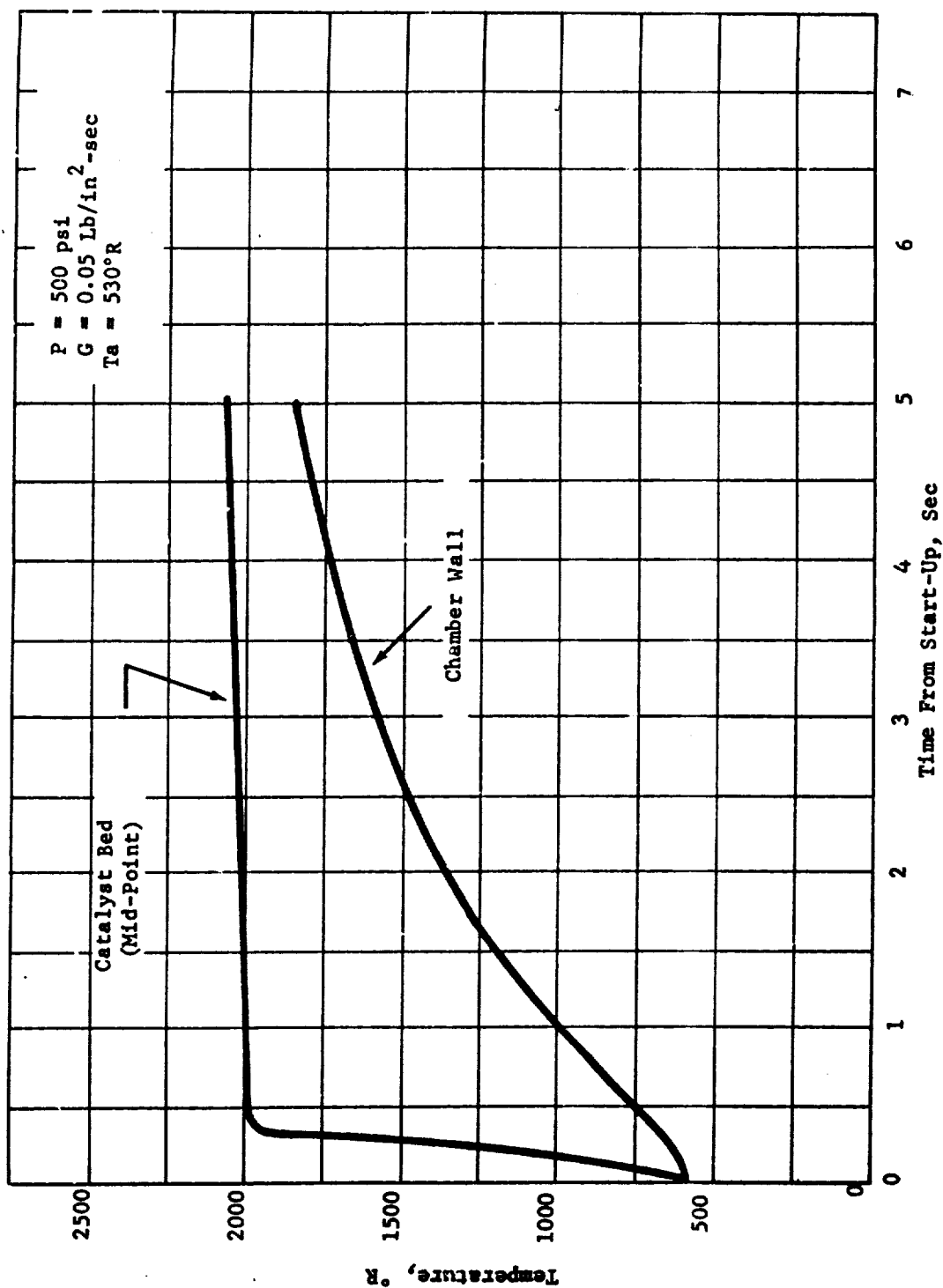
Figure 4-36. Start-Up Temperature Response.
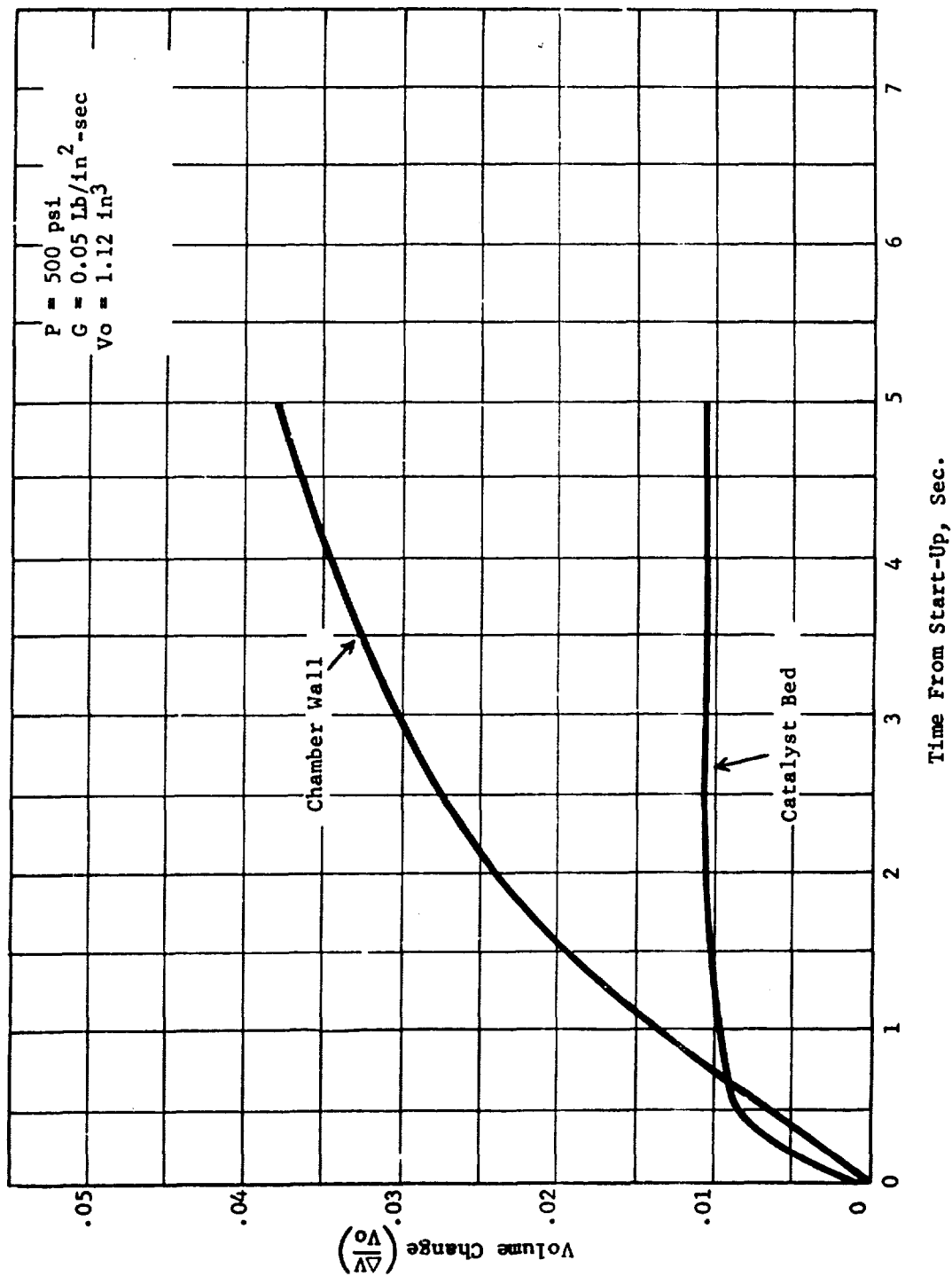
Figure 4-37. Catalyst Bed and Chamber Wall Expansion Histories.

The reactor temperatures at the end of the on pulse form the initial conditions for the cooldown period as shown in Figure 4-38. Translating the temperatures into volume changes produces the results shown in Figure 4-39. It can be seen that the dilation of the catalyst bed at the end of the on pulse is maintained throughout shutdown. This assumes that there is no repacking of the catalyst bed from pressure forces on the bed or by mechanical devices, such as springs. If the volume change shown in Figure 4-39 is re-calculated so that the change is relative to the volume at the end of the on pulse rather than the original volume, a net compression of the catalyst bed occurs during cooldown.

4.4.2.1 Effect of Bed Loading

The effect of varying the bed loading, with all other conditions taken as those of the base line, on the start-up differential expansion is illustrated in Figures 4-40 and 4-41. A compression of the catalyst bed occurs initially but changes to a dilation 0.7 sec after start-up. The magnitude of the peak compression and dilation increases with increasing bed loading. This trend is caused by the faster temperature response at increasing bed loading of (1) the catalyst bed initially, and (2) the chamber wall after the normal thermal lag. The loose bed condition at the end of the on pulse is maintained during cooldown for all values of bed loading investigated if the bed is not repacked. Allowing bed repacking a greater compression takes place at higher bed loading as illustrated in Figure 4-42. This effect of bed loading will diminish if the bed length is optimized for each bed loading value. The bed length is more nearly optimized in terms of gas temperature for the highest bed loading of 0.10 lb/in^2-sec. At lower bed loadings the ammonia dissociation increases with a subsequent lowering of the bed exit gas temperature. Reducing the bed length to maintain a constant ammonia dissociation will have the effect of narrowing the differential expansion differences near steady state conditions and on cooldown.

4.4.2.1 Effect of Chamber Inlet Pressure

Pressure effects on the start-up differential expansion is shown in Figure 4-43. The contribution of pressure induced strains is clearly illustrated in the figure. The sharp initial rise in the net volume change is produced by the buildup in chamber pressure. This phase is followed by bed compression as the catalyst bed begins to increase in temperature. As the wall begins to respond to the hydrazine decomposition environment, the wall thermal expansion becomes dominant. Pressure does not have a strong effect on the bed compression portion of the volume change cycle other than to vary the compression duration. Bed void volume increases as the pressure is increased. The increased wall heat transfer at higher pressures accounts for the greater bed void volume as steady state is approached.

An interesting result is obtained during cooldown if the volume change is taken relative to the beginning of the shutdown cycle. Figure 4-44 shows that the bed is compressed at higher pressures while a loose bed is obtained at the 200 psi pressure condition. For the relatively low bed loading (G = 0.01 lb/in^2-sec) and pressure (200 psi) case, the chamber wall temperature is still increasing after shutdown occurs. Therefore, the chamber wall volume continues to increase for another 3 seconds after reactor shutdown.
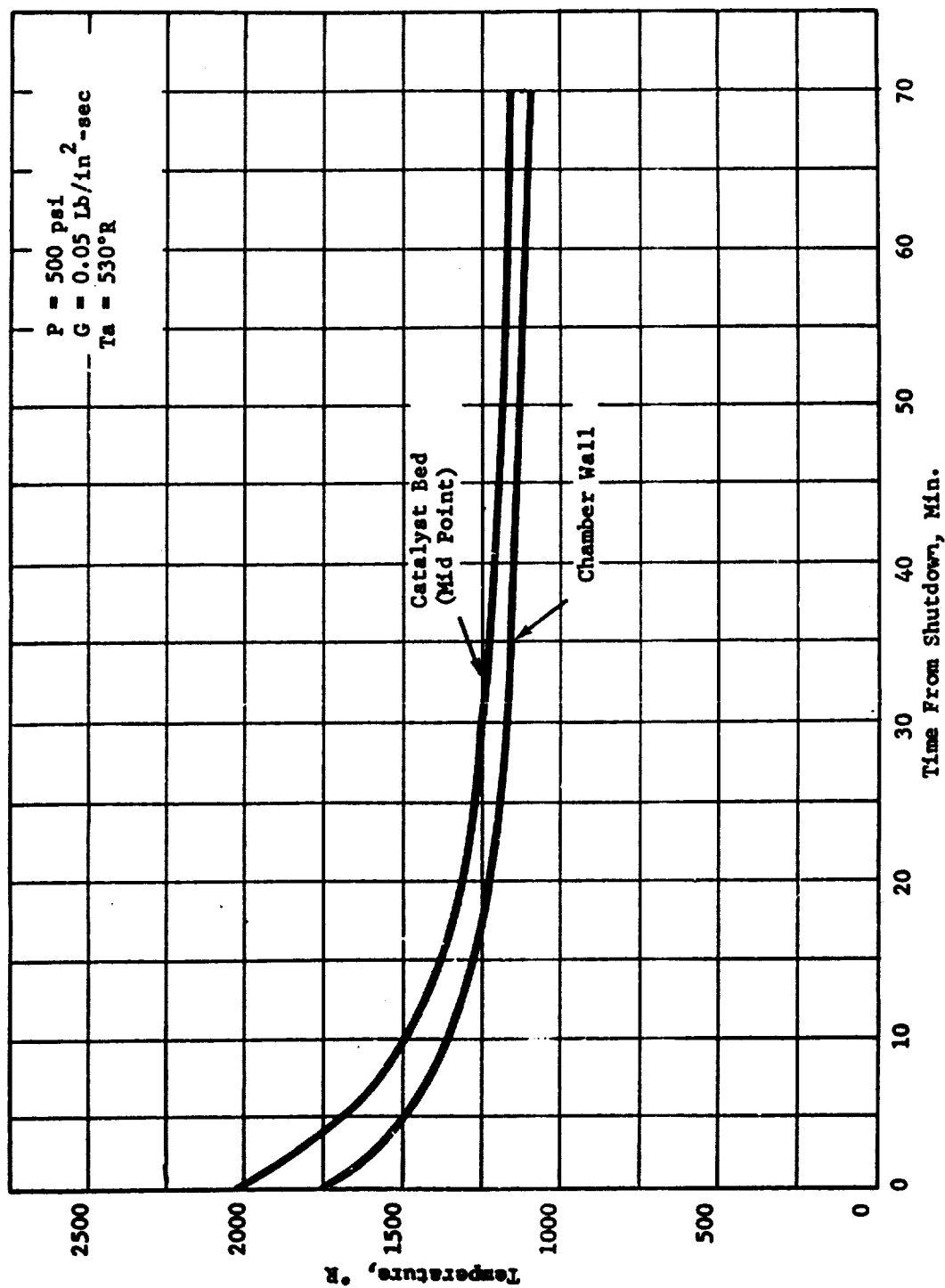
Figure 4-38. Cooldown Temperature Histories.
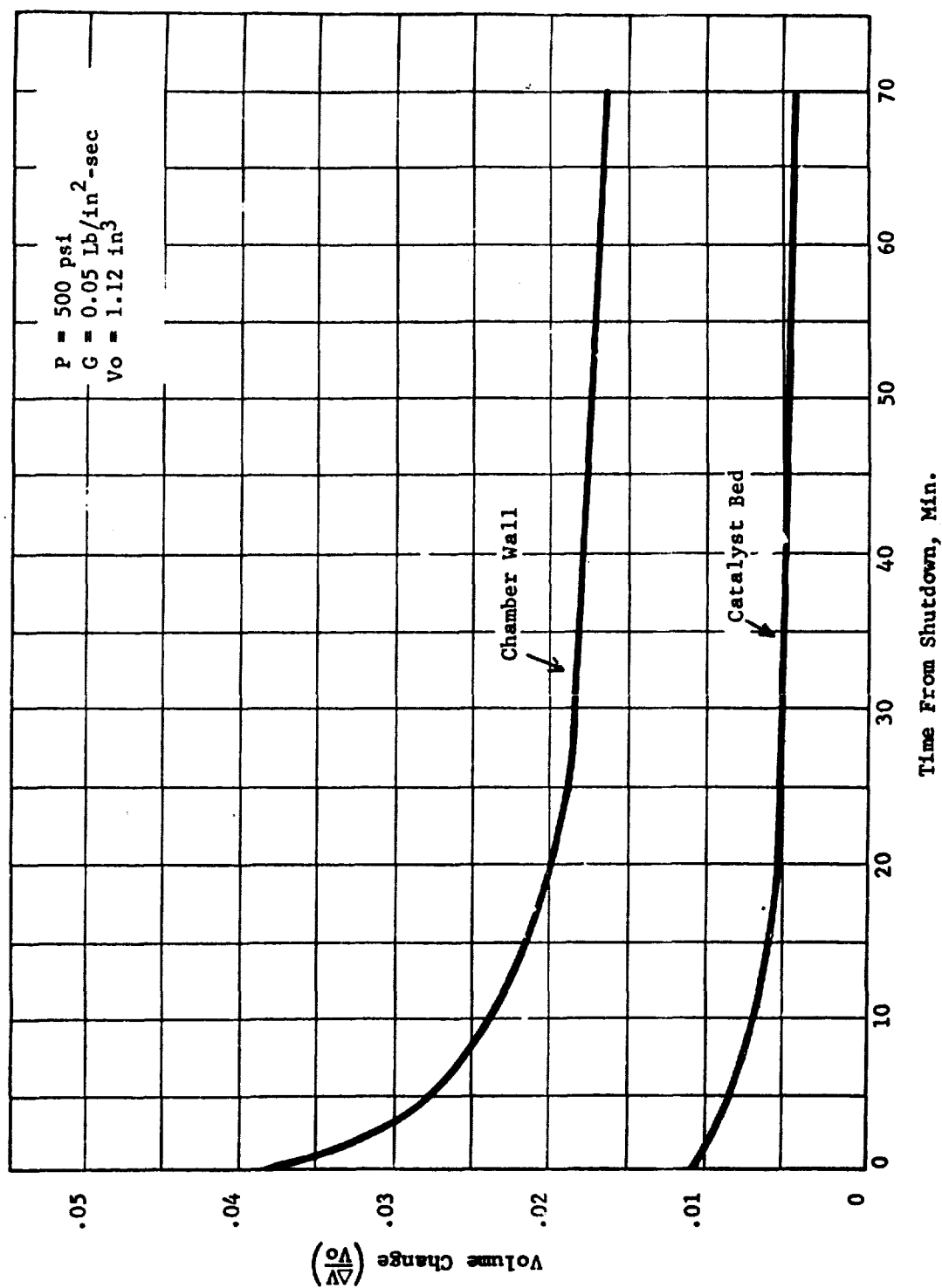
Figure 4-39. Catalyst Bed and Chamber Wall Contraction During Cooldown.
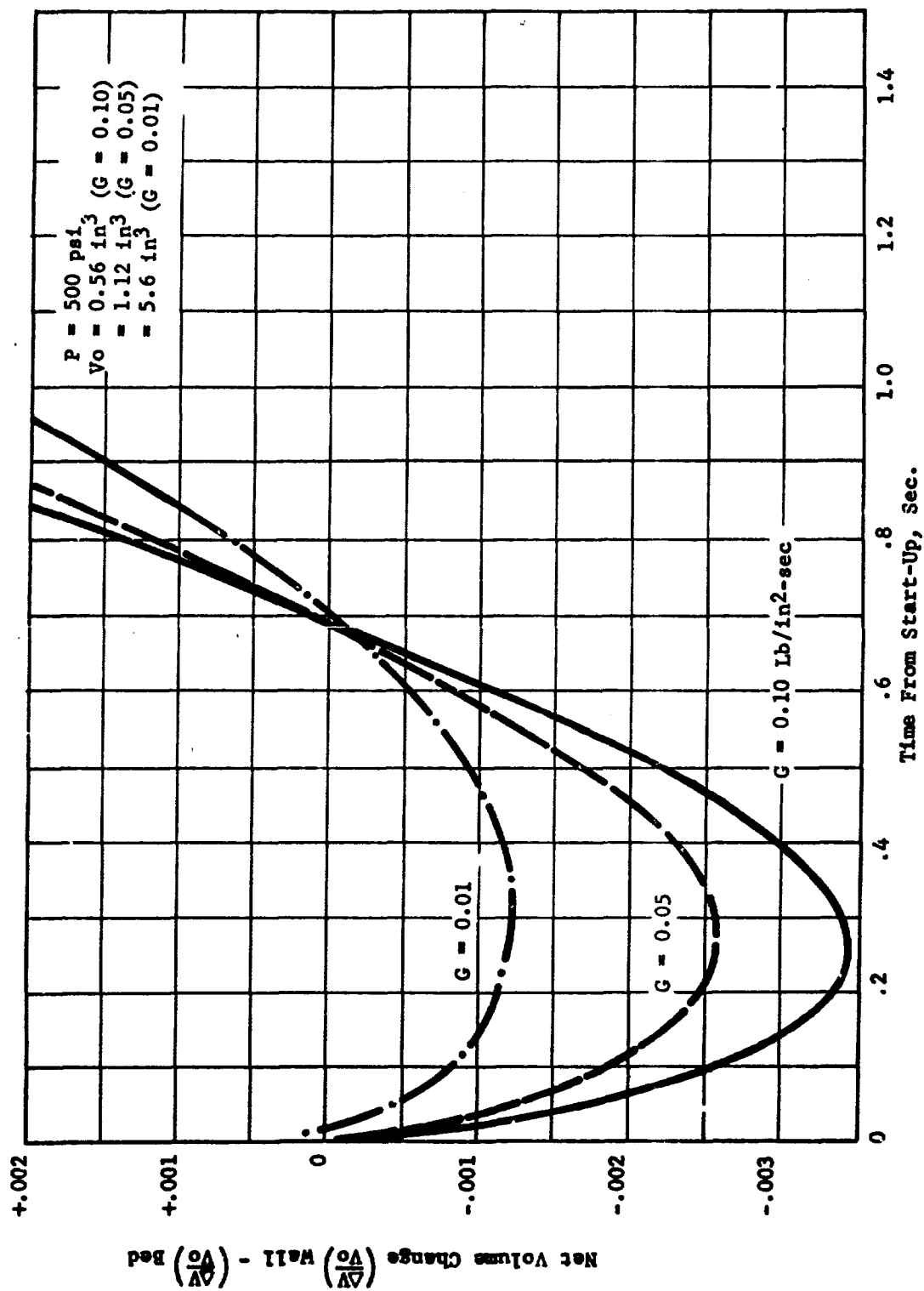
Figure 4-40. Effect of Bed Loading on Differential Expansion.
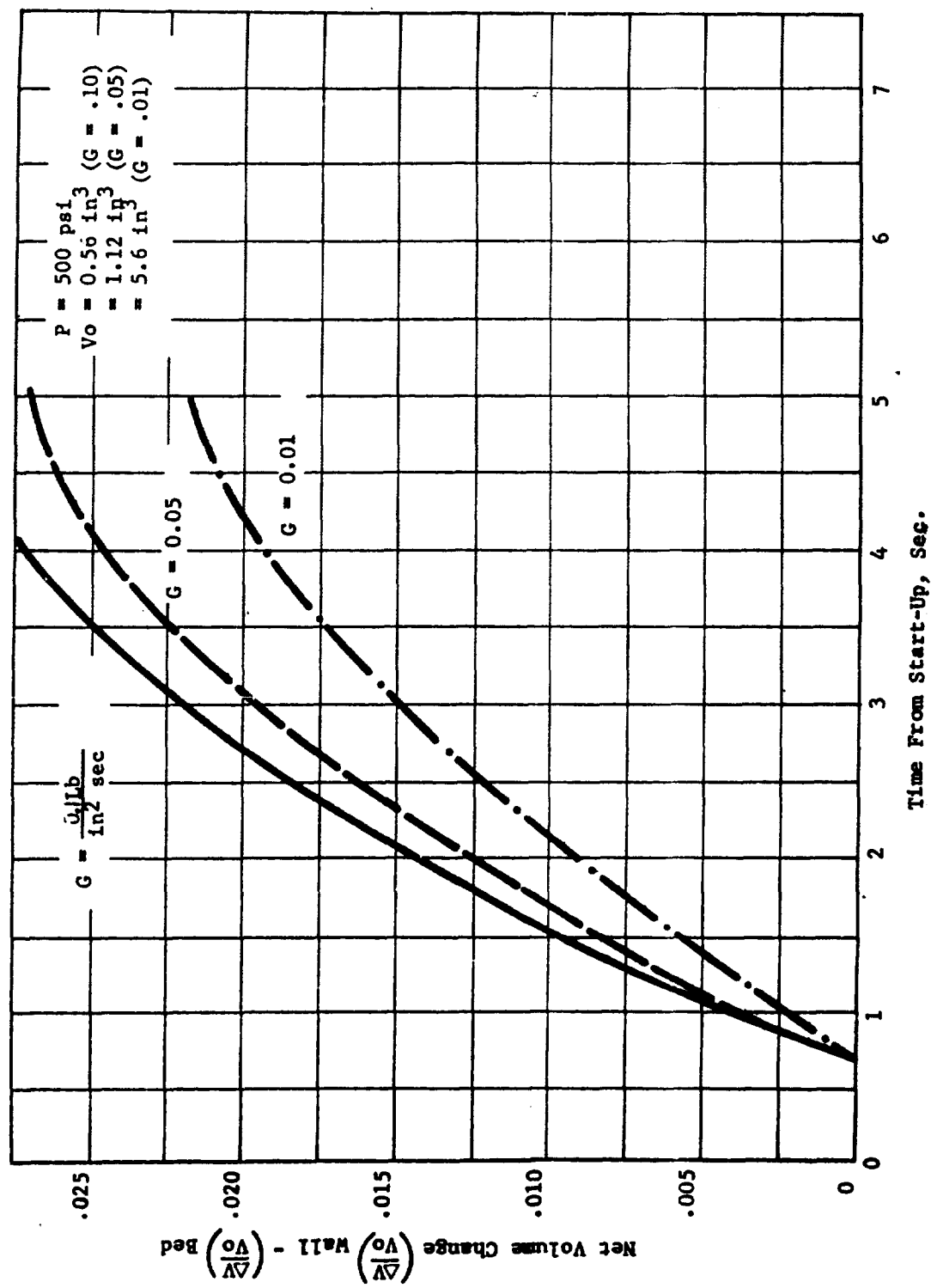
Figure 4-41. Effect of Bed Loading on Differential Expansion - Near Steady State
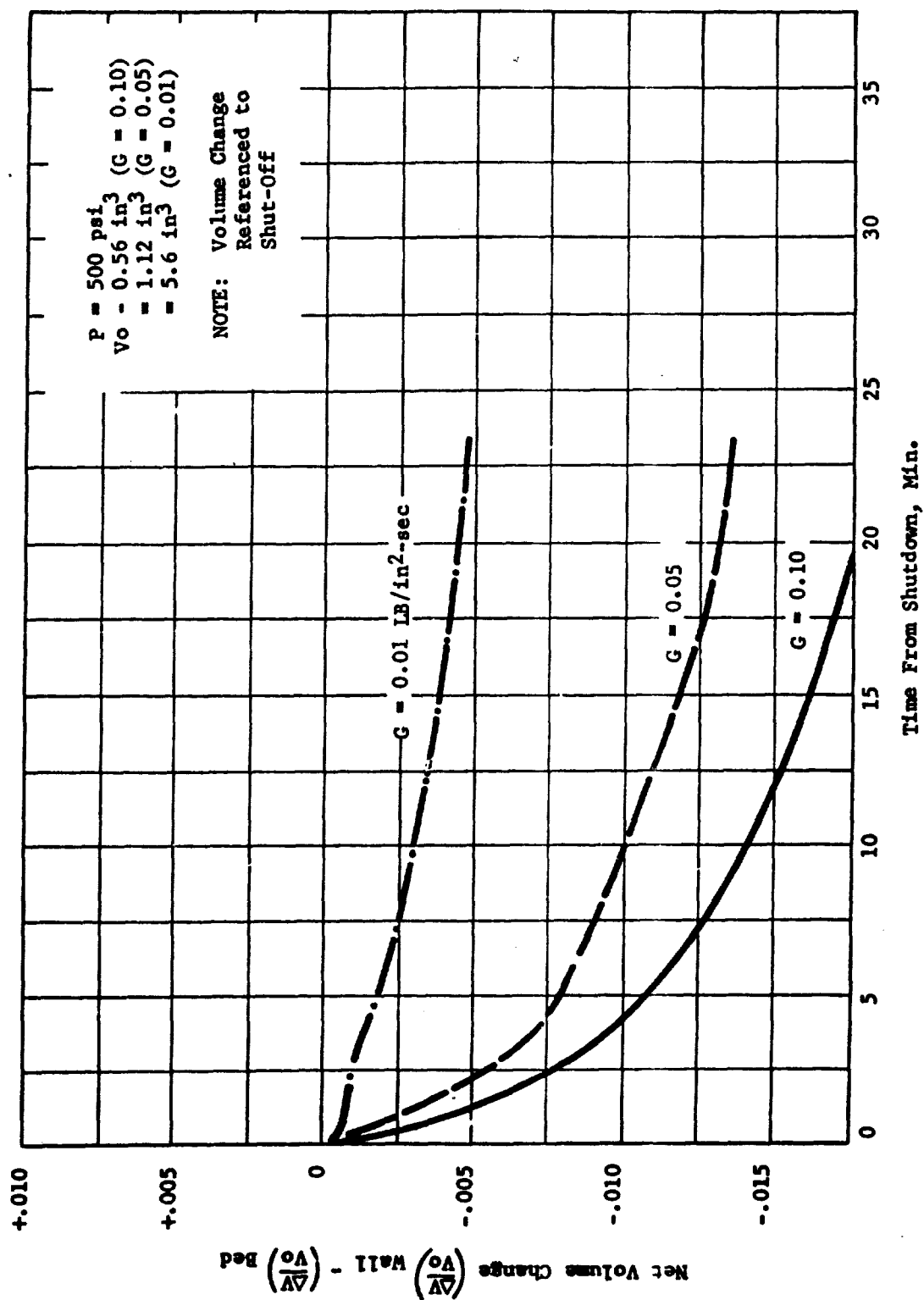
Figure 4-42. Effect of Bed Loading on Cooldown Differential Expansion.
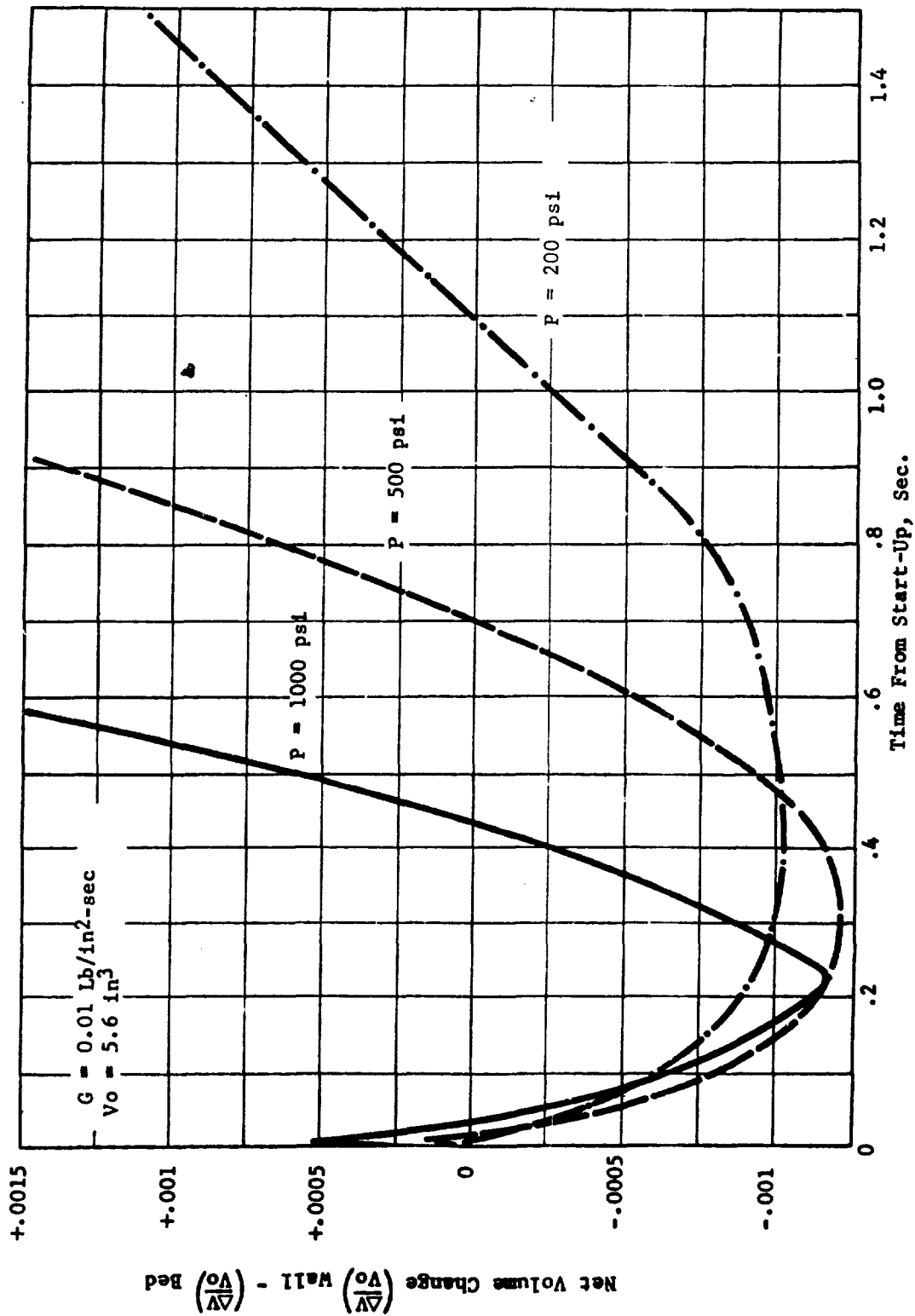
Figure 4-43. Effect of Pressure on Start-Up Differential Expansion.
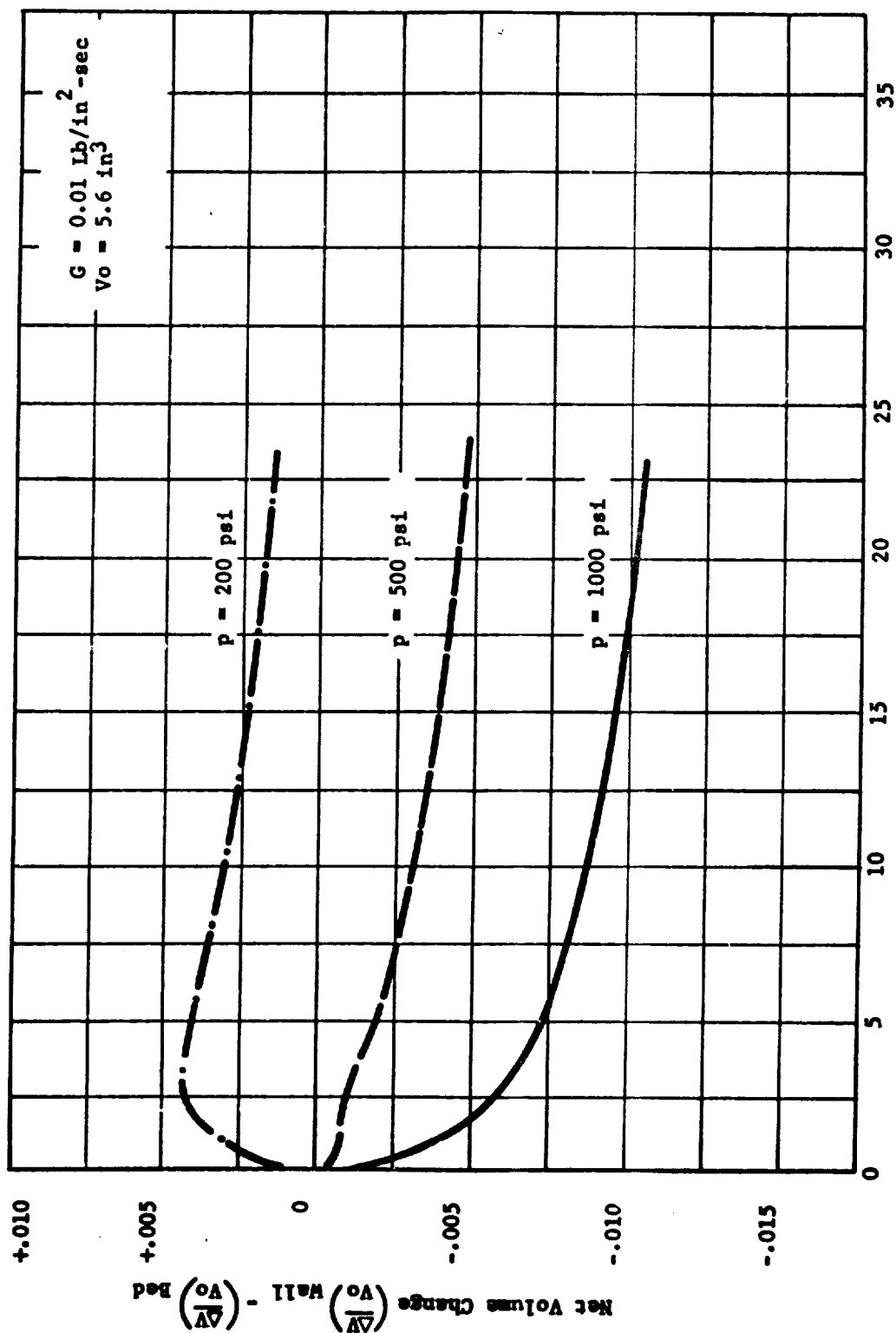
Figure 4-44. Effect of Pressure on Cooldown Differential Expansion.

Table 4-2

Conditions Used in Differential Thermal Expansion Calculation

Catalyst Type	Shell-405
Catalyst Size	
Upper Bed	25-30 Mesh
Lower Bed	1/8 in Pellets
Catalyst Bed Total Length	2 In
Upper Bed Length	0.2 In
Vacuum Thrust	5 Lb_f
Pressure	500 PSI
Bed Loading	0.05 LB/In^2-Sec
Chamber Material	L605
Chamber Wall Thickness	0.050 In
Bed Diameter	0.844 In
Chamber Wall Cooling	Natural Convection

4.4.2.3 Effect of Thrust

As anticipated, the higher surface-to-volume ratio of the smaller reactors leads to gerater heat losses from the chamber wall. As shown in Figure 4-45, the resulting lower wall temperatures produce a greater bed compression but a smaller bed void later on in the starting pulse. The differences in volume between the two illustrated thrust values is less than the effects of bed loading and pressure previously shown. Since the thrust variation was made at constant bed loading the results of the variation are also applicable to a change in bed diameter.

4.4.2.4 Effect of Case Material

Selection of a thrust chamber material for monopropellant applications is usually based on strength properties, resistance to nitriding and oxidation, and compatibility with hydrazine. Nickel or Cobalt base superalloys are usually chosen for the engine material and the coefficient of thermal expansion of these materials show little variation. As the chamber material coefficient of expansion approaches that of the catalyst particles, the steady state bed dilation would diminish. However, the transient bed compression condition would be increased in magnitude.

4.4.3 Effects of Differential Thermal Expansion/Contraction on the Catalyst

If we assume a bed compaction law of the form discussed in the section on particle stresses:

$$\frac{\Delta V}{V} = K \ P^{2/3} \qquad \qquad \bullet \qquad (4.4\text{-}4)$$

where

$\qquad$ V = Bed volume

$\qquad$ P = Bed compaction pressure

The value for K may be obtained from the Exxon experimental measurement of 4 percent bed compression at a pressure of 1000 psi. When this is done, and the equation restated, pressure due to bed compression may be calculated:

$$P = 125,000 \left(\frac{\Delta V}{V}\right)^{1.5} \qquad \qquad (4.4\text{-}5)$$

Figure 4-40 shows that the start transients in engines having bed loadings of .01, .05 and .10 lb/in^2 sec. will produce bed compressions ($\Delta V/V$) of .0012, .0026, and .0034 respectively. These compactions, using the above expression should correspond to bed pressures of 5.2 psi, 16.6 psi and 24.8 psi.
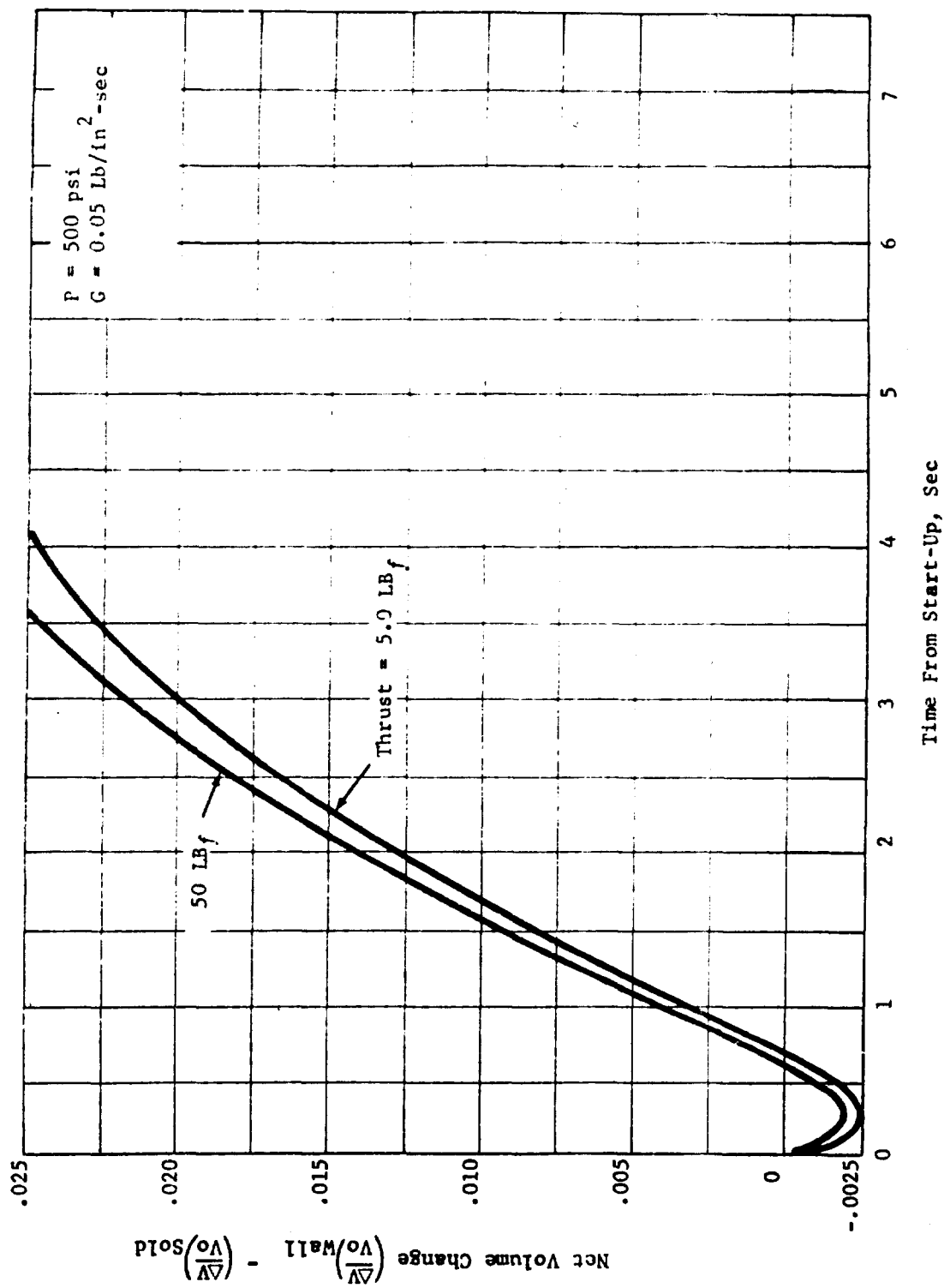
Figure 4-45. Effect of Thrust on Start-Up Differential Expansion.

The expression (taken from a previous section, equation 4.2-27) for the force acting on a pellet in a bed at a location of point-to-point contact is:

$$F = \sqrt{2} \, R^2 \, P \qquad (4.4\text{-}6)$$

where

F is contact force at a point of contact

R is radius of the pellet

P is bed compaction pressure

Using the values

P = 24.8 psi

R = .02 inch (25 mesh)

$F = 2 \quad .02^2 \times 24.8 = .014$ pounds.

This is well under the .61 pounds of compressive force which is given in Table 3-10 as the average force required to completely crush a 20-30 mesh particle. Hence it may be concluded that the differential thermal expansion of a single cold start by itself will not be adequate to cause catastrophic destruction of the catalyst pack.

Referring to Figure 4-18 of the section on particle stresses, however, indicates that a bed compression stress of 25 psi produces a local peak stress of 9000 psi in the catalyst pellet at the center of the point of contact. Referring to Figure 4-22 of the same section shows that 25 psi of bed compression is sufficient to initiate failure in either used or new catalyst material, hence local failure and mass loss at points of contact should be expected from 25 psi of bed compression stress. This conclusion is experimentally confirmed by the bed crushing tests of Figure 3-13 which indicated that approximately 0.4 percent of the bed mass should be lost from a 25 psi compression of the bed.

When the engine cools off from the maximum thermal dilation which occurs at steady-state, the bed may be subjected to compression stresses if it has repacked itself during this period of maximum dilation. According to Figure 4-42, engines having bed loadings of .01, .05 and .10 will give bed compressions of .004, .013, and .0175 in the first twenty minutes after cutoff. These correspond to bed pressures of 31.6 psi, 185 psi and 289 psi. The highest of these bed compression pressures is sufficient to crush 15 percent of the catalyst in the bed according to bed pressure crushing experimental results of Figure 3-12. The largest unknown in this process appears to be the flow behavior of the catalyst bed under pressure in the thruster environment e.g. will it repack during a dilation phase. Regarding this latter point, it should be noted that on occasion when a used thruster is opened, the catalyst bed is so tightly packed that it will not flow under the force of gravity alone.

In general, it can be seen that the pressure crushing forces which result from differential thermal expansion effects are potentially significant factors in catalyst breakup.

4.5 Fluid Erosion

The objective of this section is to determine the amount of wear caused by particulate contaminants carried in the propellant stream under various design and operating conditions. To do this a computer program was developed, capable of calculating the erosion wear of catalyst pellets under a variety of conditions. This computer program was then exercised with input parameters selected to represent specific design and/or operating conditions of interest, to determine the amount of damage to the bed with the various conditions.

4.5.1 Program Development

Nielsen and Gilchrist (Reference 129) have postulated that abrasion wear of a substrate by impinging particles occurs by a combination of two mechanisms: (1) cutting wear, in which the impinging particle digs into the surface, like a machine cutting tool; (2) deformation wear (work hardening due to repeated deformation, then cracking of the surface layers) which is due to impact alone. (The term "fatigue wear" will be used for deformation wear in this report.) Cutting wear is at a maximum at relatively low angles of attack (ca 30°) on the substrate, and falls to zero at angles near 90°; fatigue wear exhibits the opposite dependence on angle of attack, reaching a maximum of 90°. The wear in all cases is proportional to the kinetic energy of the impinging particles.

Nielsen and Gilchrist correlated published literature and their own experiments by the equation

$$W = \frac{MV^2 \cos^2 \alpha \, \sin n\alpha}{2\alpha} + \frac{M \, (V \sin \alpha - K)^2}{2\epsilon} \qquad (4.5\text{-}1)$$

in which W is the "erosion" [pounds (mass) of substrate removed] caused by impact of M pounds (mass) of particles at angle of attack α and average particle velocity V feet/second; K is a cut-off velocity, below which no fatigue wear occurs; n is a material-dependent constant; o and ϵ, the wear rate constants, are the amount of kinetic energy which must be "absorbed" by the surface to release one unit mass of eroded material. The first term of the Nielsen-Gilchrist equation calculates cutting wear; the second term calculated fatigue.

4.5.1.1 Catalyst Bed Configuration Assumptions

The arrangement of catalyst pellets in a well-packed bed consists of a series of layers of pellets, each layer made up on an approximate hexagonal arrangement, with triangular interstice passages between the pellets. The passages are perpendicular to the plane of the layer. Figure 4-46 is a sketch of this structure, using spherical pellets for the example, and viewing the spheres cut through on their equators.

Figure 4-46

Pellet Configuration
Hexagonal Packing
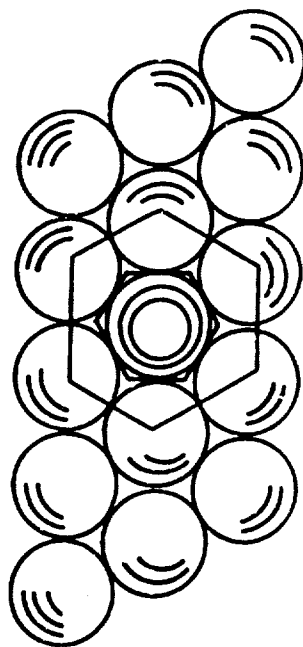
Pellets of one layer fit in the "cavities" formed between pellets in adjacent layers, as shown in Figure 4-47. In this position, the upper surface of each pellet in layer 2 is directly below and perpendicular to the passage between the pellets in layer 1. The optimum configuration of the layers places a second layer pellet behind 50% of the passages through layer 1; the remainder of the passages through layer 2 lie directly above similar passages through layer 2. The arrangement of "blocked" and "open" passages is symmetrical, as sketched in Figure 4-48.

4.5.1.2 Effect of Temperature on the Fatigue Wear Coefficient

The Nielsen-Gilchrist equation does not include consideration of the effects of temperature on the abrasion process, and little of the published work on change of abrasion with change of substrate temperature is applicable for the purposes of this program. It has become accepted that surface wear rates of most materials for many types of wear are inversely proportion to the surface hardness (References 130 and 131). If this relationship is accepted, then the change of wear rate with temperature will be related to the change of surface hardness with temperature.

4.5.1.3 Threshold Velocity for Fatigue Wear

The factor K in the Nielsen-Gilchrist equation is based on the assumption that fatigue wear ceases abruptly if the velocity of impingement falls below come lower limit equal to K (which is material dependent). Examination of published data demonstrated that there is no true cutoff, but rather a rapid decrease in damage below a threshold velocity. If the fatigue wear constant, ϵ, (units are ft lbs/lb) is calculated as a function of velocity, it is found that ϵ increases abruptly below a certain velocity, but does not become infinite (Figure 4-49). The slopes of the portion of the plots below the velocity limit were found to be parallel for glass, plastics (TFE and Acrylic), and the metals aluminum, copper and steel.

The velocity threshold at which the curve breaks ranges from 180 to 1000 ft/sec, and of course the plateau value for ϵ depends on the substrate material.

4.5.2 Method of Calculation

The algorithm for calculation of particle impingement erosion was developed using the following assumptions.

Erosion (or abrasion wear) is presumed to be caused solely by condensed phase (liquid or solid) materials carried by a flow of gas or vapor. No wear is calculated for solid particles suspended in liquid hydrazine. Under the conditions which apply in a rocket engine catalyst pack, the cutting wear term of the Nielsen-Gilchrist equation is relatively unimportant, and is assumed equal to zero. Liquid droplets are presumed to arise from incomplete vaporization of the hydrazine. The Kesten steady state program supplies values for the amount of liquid at specified locations in the catalyst bed. The data from the Kesten program are interpolated for the required locations.

Figure 4-47

Multi-Layer
Pellet Configuration

Back Row

Front Row

First
Layer

Second
Layer

Side View

Back Row

Second Layer

Front
Row

Bottom View
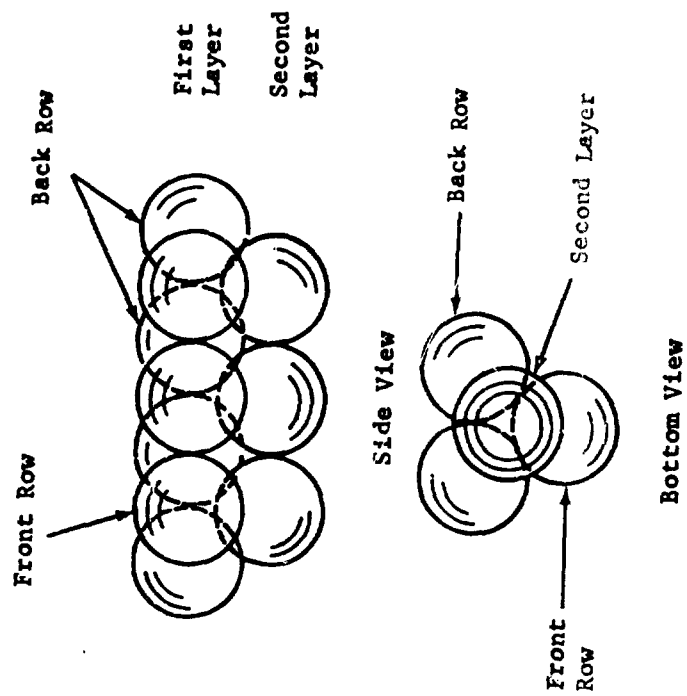
Figure 4-48

Impingement Focusing

Blocked Passage ◀   ◁ Open Passage

Top View
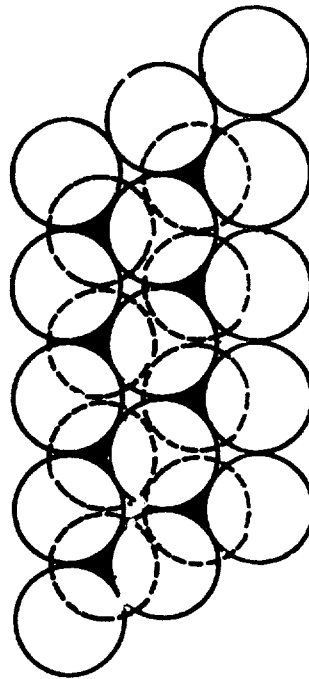
Dashed Circles are Pellets in Second Layer.

Solid particles are presumed to arise from three sources; contaminants in the hydrazine, particles generated in the bed by compression, rubbing, thermomechanical shock and pore pressure imbalance, which may be supplied as auxiliary input from the other processes considered in this study, and particles generated by particle impingement erosion at other locations upstream in the bed.

Droplets and particles are presumed to travel at the same velocity as the gas/vapor in which they are carried, i.e., newly generated particles are presumed to accelerate instantaneously to the stream velocity.

The fatigue wear term in the Nielsen-Gilchrist equation is used as the model for calculating wear, with the following modifications; the constant K is eliminated and the fatigue wear coefficient, ϵ, is treated as a function of velocity for impingement velocities less than K:

$$\epsilon_V = \epsilon_0 * (\frac{Velocity}{Limit\ Velocity})^{-3.5625} \qquad (4.5-2)$$

The value of ϵ is also regarded as a function of the substrate (pellet) temperature

$$\epsilon_{T,V} = -2.82 \times 10^{-4} (T-T_o)\ \epsilon_V \qquad (4.5-3)$$

The variation in pellet temperatures with axial locations and operating times is used for the calculation of ϵ, and are taken from the output from the Kesten-U.A.R.L. transient computer program. The data are interpolated to obtain the time and location required.

The temperatures of the vapor and of the impinging particles are not presumed to affect the wear rate as calculated by this model. Impingement velocities are calculated as follows.

The unimpeded mass flow rate of the liquid hydrazine upstream of the catalyst bed is input to the program. The total cross section area of all the passages through a layer of pellets at the narrowest point (maximum cross section of the pellets) is calculated, assuming a circular cross section for the pellets and hexagonal packing. Because of conservation of mass, the same total mass of fluid must flow through the restricted area as through the unimpeded area ahead of the bed. Therefore, the velocity must be increased by a factor equal to the cross section without pellets divided by the minimum area through the pellet layer. The unimpeded velocity is calculated from the mass flow rate, then the velocity through the layer is calculated by multiplying by the area ratio. The liquid impingement velocity at any layer is taken as the maximum velocity through the preceding layer. The volume of a unit mass of liquid hydrazine is expanded to the volume of gas/vapor at the local pressure, temperature and composition, assuming ideal gas law behavior and the exit composition of reaction products, and correcting for vapor quality. The gas velocity is then calculated by multiplying the liquid velocity by the relative volume increase.

Figure 4-49

Fatigue Wear Factor for Glass as a Function of Impinging Particle Velocity
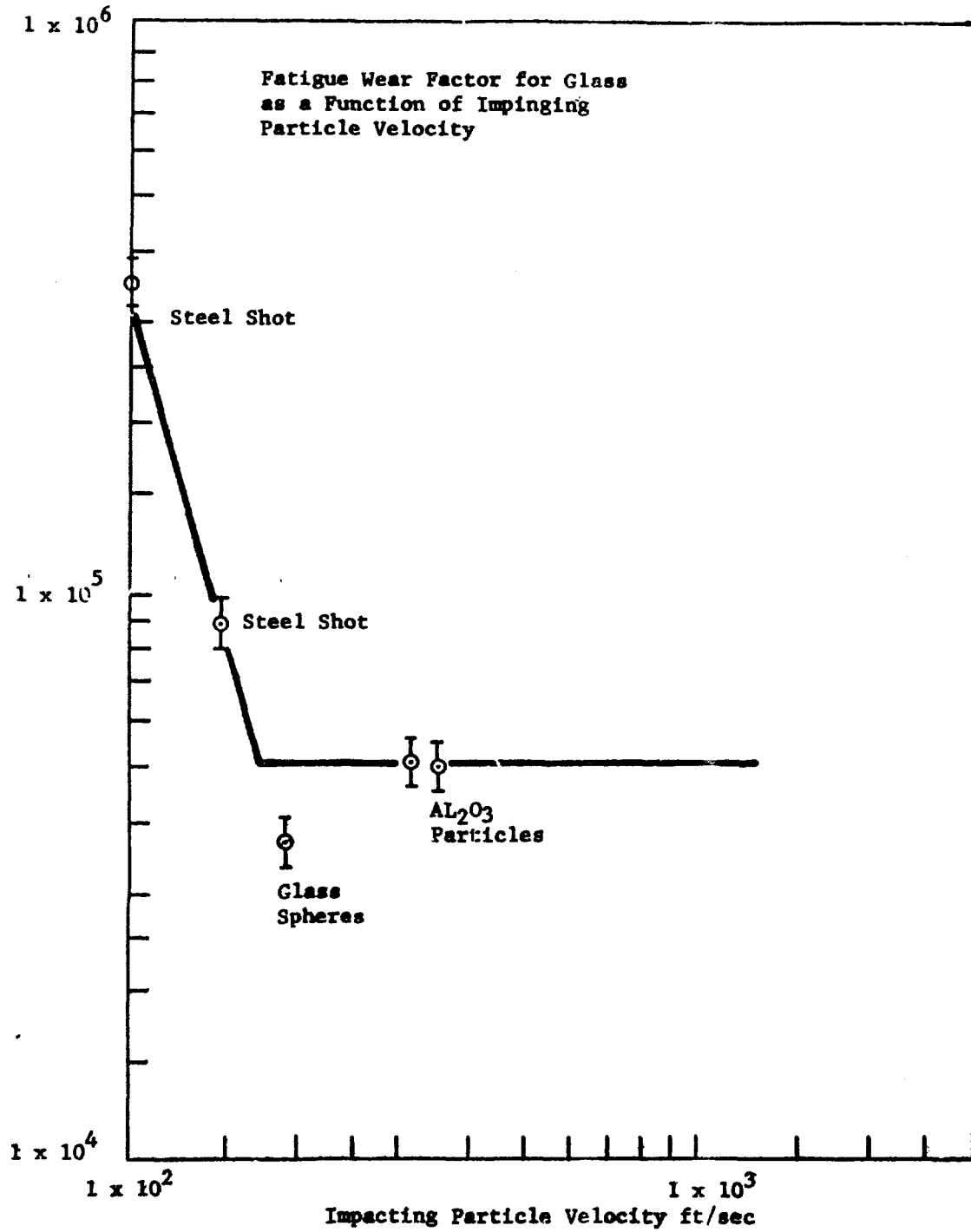
A simple model of the catalyst bed is assumed. This is illustrated in Figure 4-50. The pellets are assumed to be spherical, with a radius which will result in the same volume per pellet as the average for the actual pellets. If the bed being modeled consists of only a single type of pellet, it is necessary to input the data on pellet characteristics twice, and to assume a fictitious division between the two sections. Eleven stations along the bed are selected for calculation of damage. Two of these are invariant; the first station is always the second layer of pellets in the forward section, and the fifth station is always the front layer of the aft section. The remaining stations are automatically selected to select four equally spaced locations in the forward bed and seven equally spaced locations in the aft bed.

The operating time is divided into 17 increments. The first four increments are equally spaced in the start-up transient, the last four increments are equally spaced in the tail-off transient, and the remaining nine increments are equally spaced in the steady state operating period. The tail-off is considered to be complete when the chamber pressure drops to atmospheric; it does not include the extended cooldown period when there is no flow. Any of these periods can be assigned a zero duration in the data input, in which case the time increments are assigned to another period.

Calculation Sequence

1. Read in data defining bed configuration, pellet specification, propellant specifications, operation parameters, and bed conditions during operation.

2. Establish calculation locations and time increments.

3. Calculate specific details of bed structure including layer spacing, interstice volume, passage area, number of pellet layers per section, etc.

4. Calculate the velocity of liquid hydrazine flow.

5. Calculate the time for a volume of hydrazine equal to pore volume of the bed to flow through the bed (wave duration).

6. For time increments 1 to 17 carry out the following calculations (7-22).

7. For calculation locations 1 to 11 carry out the following calculations (8-17).

8. Interpolate the time-location-temperature table to determine the substrate temperature.

9. Interpolate the propellant quality-location table to determine the propellant quality.

10. Interpolate the intra-bed particle generation-time-location table to find the generated particle concentration.

11. Calculate the mass of impinging particles and droplets.
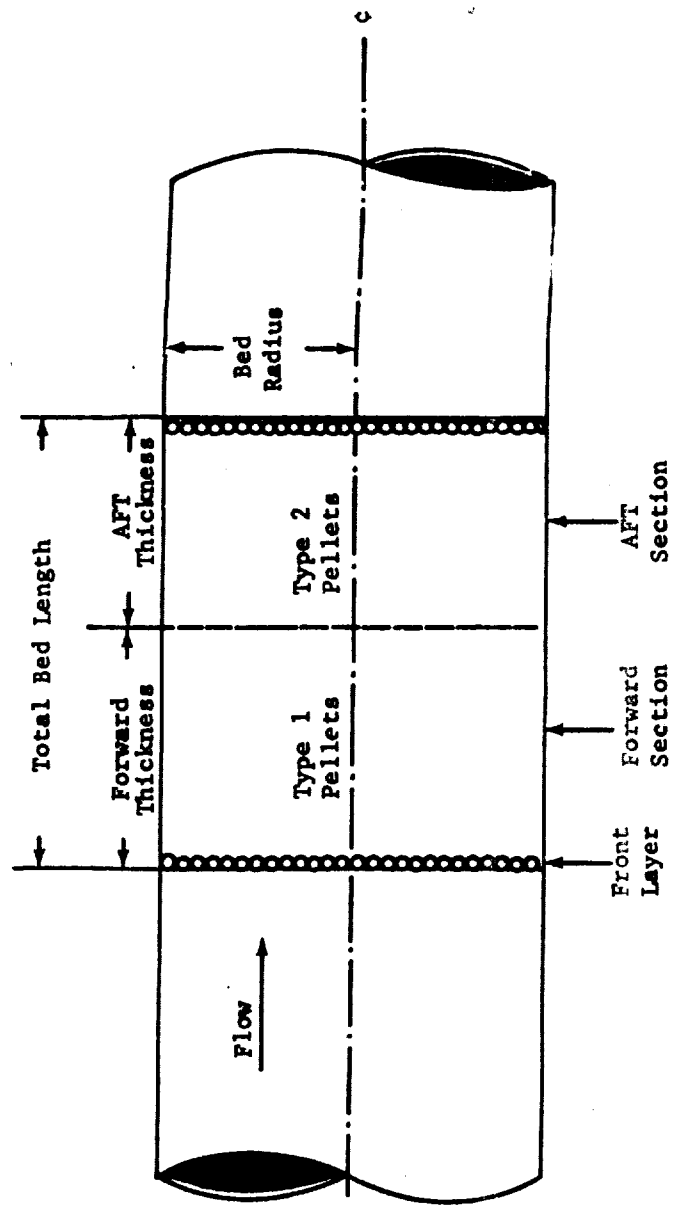
Figure 4-50. Catalyst Bed Model.

12. Calculate the impingement velocity.

13. Calculate the wear rate factor corrected for velocity and substrate temperature.

14. Calculate the wear during a time equal to the wave duration.

15. Calculate the wear rate.

16. Calculate the damage (amount of material removed).

17. Add the material removed to the mass of impinging particles and integrate the wear forward to the next station, layer by layer.

18. Average the wear rate between the last time increment and the current time increment, and calculate the damage over the time increment.

19. Calculate the average pellet dimensions in each bed section at the end of the time increment.

20. Recalculate the bed parameters: length, pellets per layer, layers persection.

21. Print notice of extreme wear (5% change).

22. Use new bed and pellet parameters as basic condition for calculations at the next time increment.

23. Calculate the total change.

24. List results; final condition of bed, total mass and volume change, wear at selected locations at each time increment.

25. Plot results.

26. Test for new case. Reset variables and read in new data if another case is to be run.

Input Data Values Used to Run the Computer Program

The program has been run using a single nominal engine and pulse, varying only the solid contaminant concentrations in the hydrazine supply. The basic data are the following.

1. Bed/pellet description:
   Bed radius 0.10656 meter (4.195 inch)
   Bed length 0.05596 meter (2.203 inch)
   Forward Section length 0.00508 meter (.20 inch)
   Aft Section length 0.0508 meter (2.0 inch)
   Pellet Radius, Forward Section 0.00305 meter (.012 inch)
   Pellet Radius, Aft Section 0.001951 meter (.079 inch)

2. Propellant properties:
    Flow Rate 35.13 kg/sec-m^2 (.05 Pounds/Square inch-second)
    Density 1008.3 kg/m^3 (1.0083 gm/cc)
    Chamber Pressure 3.446 x 10^7 N/m^2 (4989 psi)

3. Times
    Start-up 0.0115 sec
    Steady State 5.0 sec
    Tailoff 0.022 sec

The times were selected from the output of the Kesten Transient program
which was executed with the same bed, pellet and propellant data to supply
the time-location-pellet temperature table required as input by ABRADE.
Propellant quality vs location was obtained from a run of the Kesten One-Deminsional
Steady-State program.

Values for the important wear rate coefficients ϵ (energy/unit mass
removed), VLL (velocity lower limit, the velocity below which ϵ is no longer
constant), EXP (the slope of the dϵ/dV curve), and TFACT, (the change in ϵ
with temperature) for the catalyst pellets could not be found in the literature,
and the values used for the calculations were estimated from analogous materials
and related properties.

$$\epsilon = 0.477904 \text{ JOULE/KG}$$
$$EXP = -3.5625$$
$$VLL = 25.5 \text{ M/SEC}$$
$$TFACT = -2.82 \times 10^{-4} \text{ JOULE/KG-DEG}$$

When the program was operated with these data as input, and with clean
hydrazine (no particles), a value of zero was calculated for total damage.
Using the same basic data, but including particle contaminants in the hydrazine
resulted in mass loss calculated for the pellets. For a particle mass fraction
concentration of 1×10^{-4} the calculated damage during the 5-second pulse was
5×10^{-3} percent.

4.5.3 Results

The ABRADE program to calculate abrasion wear by particles carried in
the gas phase has been coded and executed. Calculations by the program are in
accord with experience in that there is negligible erosion damage from operation
of the bed even with a cold start. Particulate material carried in the gas
stream is needed for appreciable wear. The numerical values obtained appear
to be reasonable. The results calculated are compromised by the necessity to
estimate the most important of the physical properties. It would be desirable
to determine actual values for ϵ for pellets at several flow rates and substrate
temperatures, to provide real values for the coefficients used in ABRADE.

4.5.3.1 Parametric Variation Study

An evaluation was conducted to determine the effects of several
parameters on the wear of catalyst pellets, by calculation of the wear at
several levels of the parameters. The parameters studied in this fashion
include:

1. Solid contaminant concentration in propellant.
2. Propellant quality (vapor/liquid) distribution.
3. Propellant flow rate.
4. Chamber pressure.
5. Bed L/d ratio at constant volume.

The various parameters affected the wear to different degrees. The results for each analysis are discussed below. In all cases, the parameters under study were held constant. The values described above for the standard test case were used.

Contaminant Concentration

A set of eight runs were conducted in which the concentration of solid particulate contaminant in the incoming liquid propellant was varied over the range 0 to 0.1 kg/m^3 (mass fraction range 0 to 1×10^{-4}). Two additional runs were conducted at the highest concentration with 5 pulses and 10 pulses. The wear was found to vary linearly with particle concentration, and it became significant (1×10^{-4} percent in a single 5 second pulse) at about 0.5 PPM. The results are plotted in Figure 4-51. The wear for multiple pulses at the higher concentrations of particles was not linear with the number of pulses, due to progressive degradation of the bed. There was a multiplication factor of 1.06/pulse for 5 pulses and 1.08/pulse for 10 pulses.

Liquid Droplet Concentration

A set of four runs were conducted in which the fraction of injected hydrazine moving as droplets at various locations was varied. The liquid droplet particle concentrations were:

1. 50 percent liquid at 1.1747×10^{-4} meters. (.00462 inch), 0 percent liquid at 1.1790×10^{-4} meters (.00464 inches).

2. 50 percent liquid at 2.5×10^{-4} meters (.00984 inch), 0 percent liquid at 4.3×10^{-4} meters (.01693 inch).

3. 50 percent liquid at 6.2×10^{-4} meters (.02441 inch), 0 percent liquid at 1.2×10^{-3} meters (.04724 inch).

Only in the last case did the calculations indicate any wear, and in that case the wear was 0.23 percent in one 5 sec pulse, which is quite significant.

An implicit assumption in this calculation is that any liquid present is carried as droplets in the gas/vapor, and condensed state flow along surfaces is not considered.

Figure 4-51
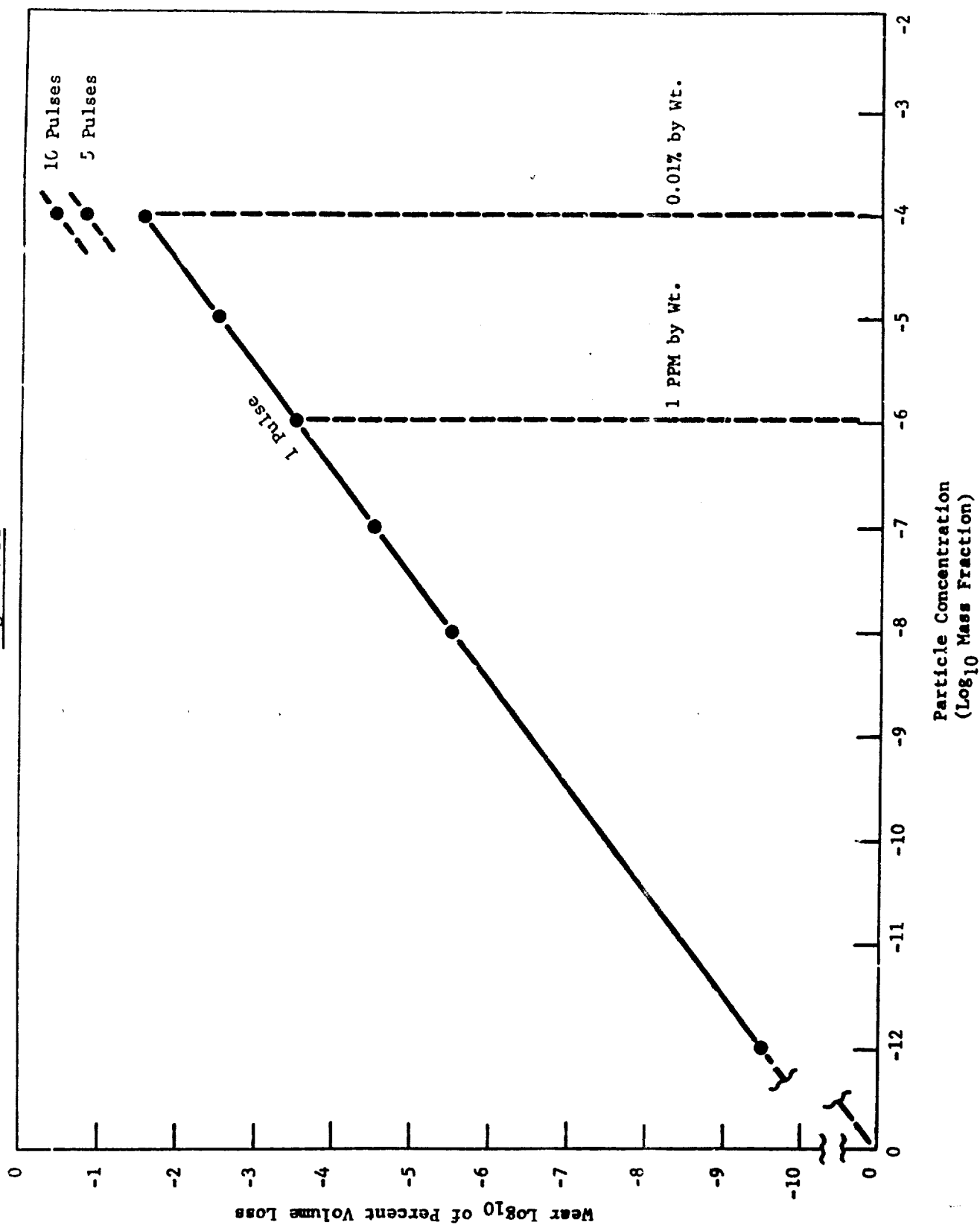
Propellant Flow Rate

A set of 3 runs was conducted to study the effect of propellant flow rate on wear of catalyst pellets. The conditions selected included a particulate concentration of 0.1 percent by weight, and flow rates 14 percent below and above the nominal rate of 34 Kg/sec M^2 (.05 pounds/sec in^2). Since a constant chamber pressure was assumed, the increased propellant flow rate is interpreted as an increased gas velocity.

The results are plotted in Figure 4-52. The flow rate has a significant effect of wear rate. When the rate increases by 33 percent (from 33 to 40 Kg/sec-m^2, .0426 to .0568 pounds/sec-in^2), the wear rate is increased by 2 orders of magnitude.

This effect is not only important in its own right, but also must be considered in the basic wear process by contaminant particles. The program currently accelerates newly generated particles to full gas stream velocity instantaneously. This cannot be strictly correct--the actual velocity of a particle is determined by the diameter of the particle, the velocity of the gas, the relative density of the particle and the gas, and the length of time to which the particle is exposed to the acceleration drag of the gas. In the typical conditions in the catalyst bed, a particle 1 μ in diameter will reach gas velocity (10 m/sec) in about the diameter of a catalyst pellet, but a 10 μ particle will only be moving at about 1 m/sec after traveling the same distance.

In the calculations for particle wear with the propellant contaminated with 1 x 10^{-4} mass fraction of particles, during the period of maximum wear rate the concentration of abraded material was 2 to 3 orders of magnitude greater than the contaminant concentration. Without experimental data on wear-generated particle sizes, it is impossible to determine the exact effect of the negelected acceleration, but the wear rate could be reduced appreciably.

Chamber Pressure

Three runs were conducted with all parameters except the chamber pressure held constant, and at 3 levels of chamber pressure, 3.0, 3.45 and 4.0 x 10^7 N/m^2 (4343., 4989. and 4791. psi). It was found that wear rate is inversely proportional to the square of the pressure, on a parabolic curve. The effect is significant, but not greatly so; an increase of 33 percent in the pressure from 3 to 4 x 10^7 N/m^2 caused the wear rate to decrease by about 50 percent. The results are shown in Figure 4-53. These results must also be interpret as velocity effects, as the program assumes gas velocity to be inversely proportional to gas density.

Bed L/D at Constant Volume

Two runs were made in which the bed radius and length were varied in opposite directions while holding the volume constant. There was an insignificant decrease in wear as the L/D increased. Thus, the L/D ratio is not a significant factor affecting wear.

Figure 4-52

Flow Rate of Liquid
(KG/Sec-M²)

Wear # Log₁₀ of Volume Percent Removed
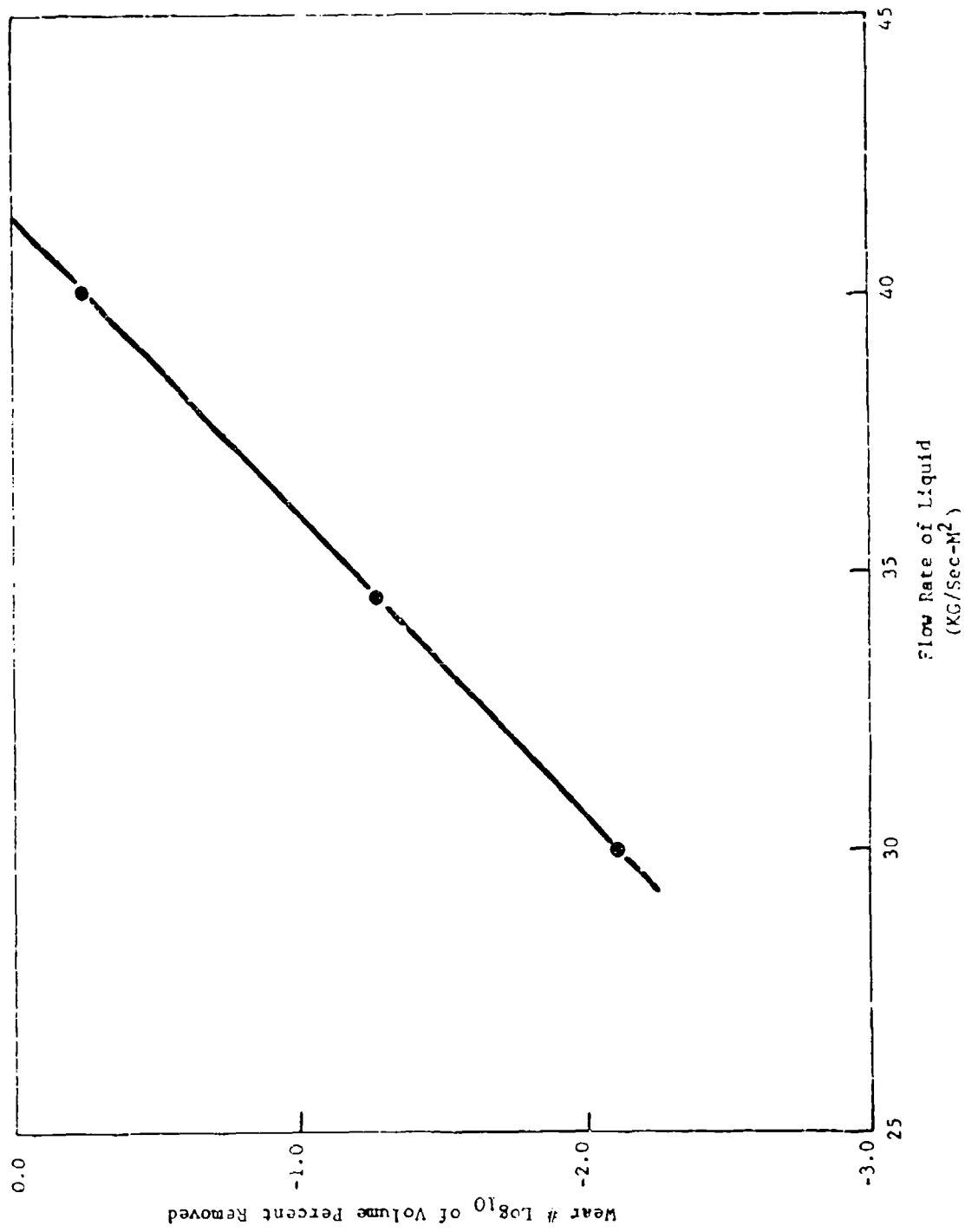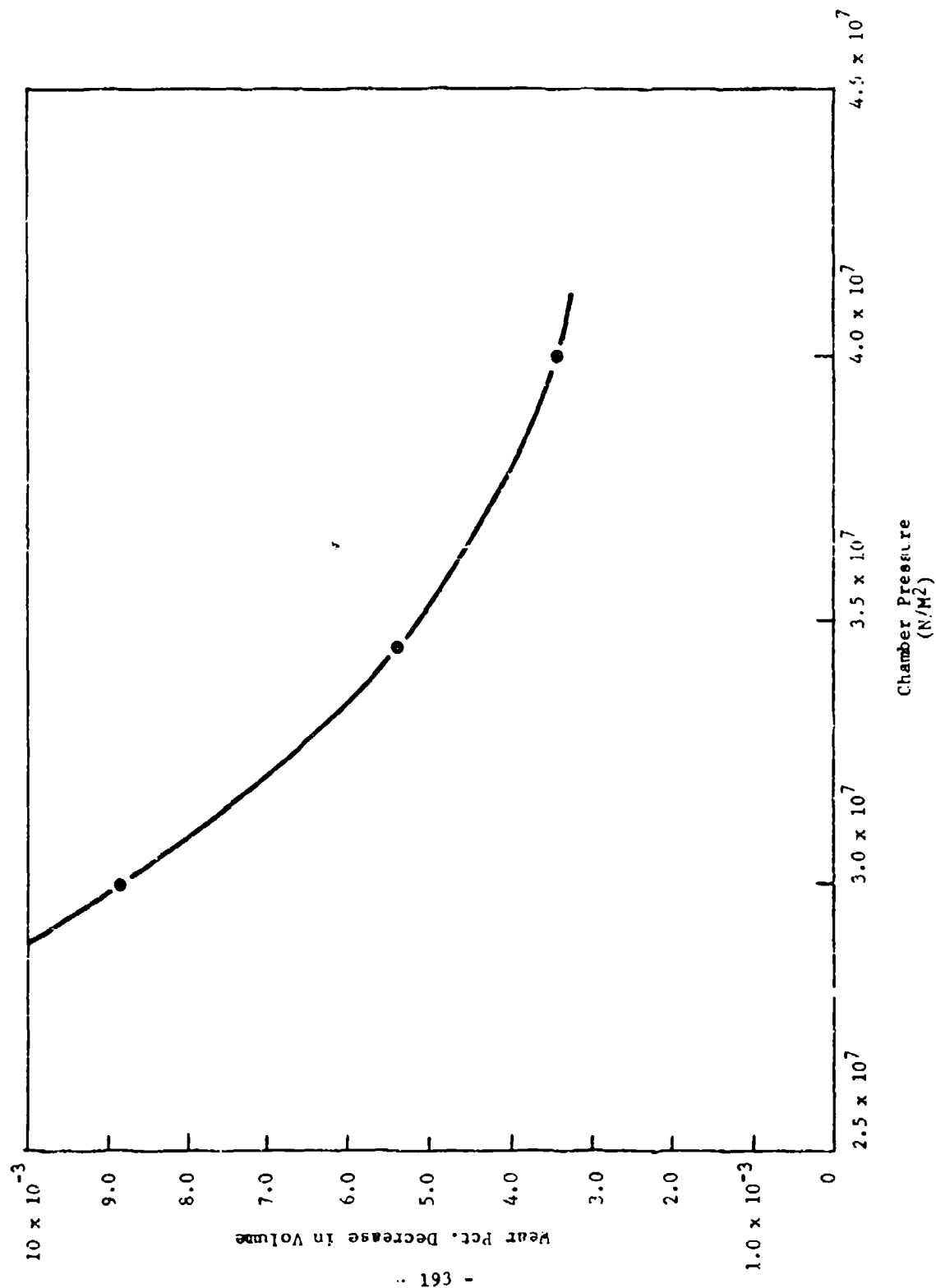
Figure 4-53. Erosion Versus Pressure

| Bed Length | | Bed Radius | | | Percent |
(meter)	(inch)	(meter)	(inch)	L/D	Volume Removed
4.477×10^{-2}	(1.76)	0.12	(4.72)	0.187	6.7×10^{-3}
10.02×10^{-2}	(3.94)	0.08	(3.15)	0.0626	5.6×10^{-3}

4.5.3.2 Discussion and Conclusions

Calculations indicate that the wear of catalyst pellets by abrasion from vapor-suspended particles is affected by a number of parameters which can be selected by system desi ners. The most significant parameters are propellant flow rate and prope lant purity.

The calculations in Section 4.5 were carried out at pressures which are higher than employed in thrusters. Calculations at lower, more typical conditions are planned. However, directionally wear rates should be higher at lower pressures because of increased velocities at lower pressures. Thus, the calculated effects of fluid erosion are expected to be greater at lower pressures.

4.6 Pressure Shock

4.6.1 Catalyst Bed Flow Numerical Model

The compressive force on a catalyst bed associated with a hard start comes from the flow impedance as the gas, explosively produced at the upstream end, attempts to pass through the bed to escape through the nozzle, Figure 4-54. Because of the obvious complexities associated with the non-linear flow relationship in the catalyst bed the sequence of pressure profiles through the bed must be obtained by numerical means. It would be desirable to be able to predict the upstream pressure-time history of an explosive hard start from first principles, however, since this is beyond the present state-of-the-art, our computer model starts with an experimental or hypothesized upstream chamber pressure history, as an imposed upstream boundary condition. The measured (or hypothesized) pressure history is approximated in our computer model by ten straight-line pressure-time segments, each covering one tenth of the total computer time interval. The flow through each axial element of the bed is first calculated based on the assumption of D'arcy Flow (i.e. completely viscous flow). Local Reynolds Number is then calculated, based on mean particle diameter. If the Reynolds Number is higher than 10 a drag coefficient is calculated, a new flow rate, new Reynolds Number, and finally a new drag coefficient. This iteration is continued until the flow rate converges to the correct value. The drag coefficient correlation comes from the work at Fancher, Lewis, and Barnes (Reference 132) and is illustrated in Figure 4-55. The 20-30 mesh ottawa sand used to produce the curve labled "unconsolidated sand" should be very close to 20-30 mesh Shell 405 in grain geometry, and have similar flow characteristics. The conductive and convective heat transport through the bed is calculated simultaneously with the mass flow, using standard explicit numerical techniques quite analogous to those used for the mass flow. The conditions at the downstream boundary of the bed are determined by evaluating the time-varying state in a downstream plenum which has gas and enthalpy flowing into it from the bed, gas efflux through a sonic throat and which can accumulate mass and enthalpy in accordance with the calculated influx and efflux rates to give its time-varying pressure and temperature.

Upstream
Retainer Screen

Downstream
Retainer Screen

Nozzle Throat

Downstream
Plenum

Pressure vs. Time
Imposed as an Upstream
Boundary Condition.

Catalyst Bed Flows and
Accumulates Gas Flow
Rate Follows a Strongly
Non-Linear, Empirical Law.
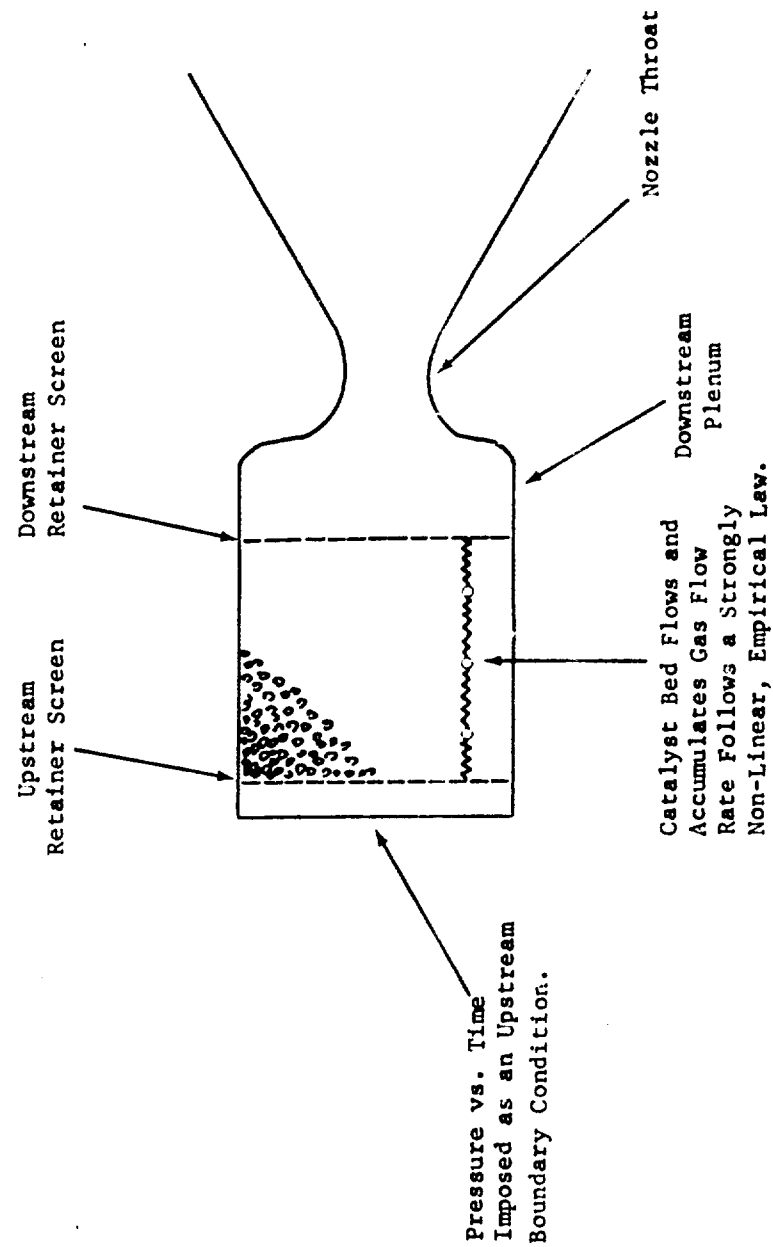
Figure 4-54. Conceptual Model of Hydrazine Rocket.

- 195 -
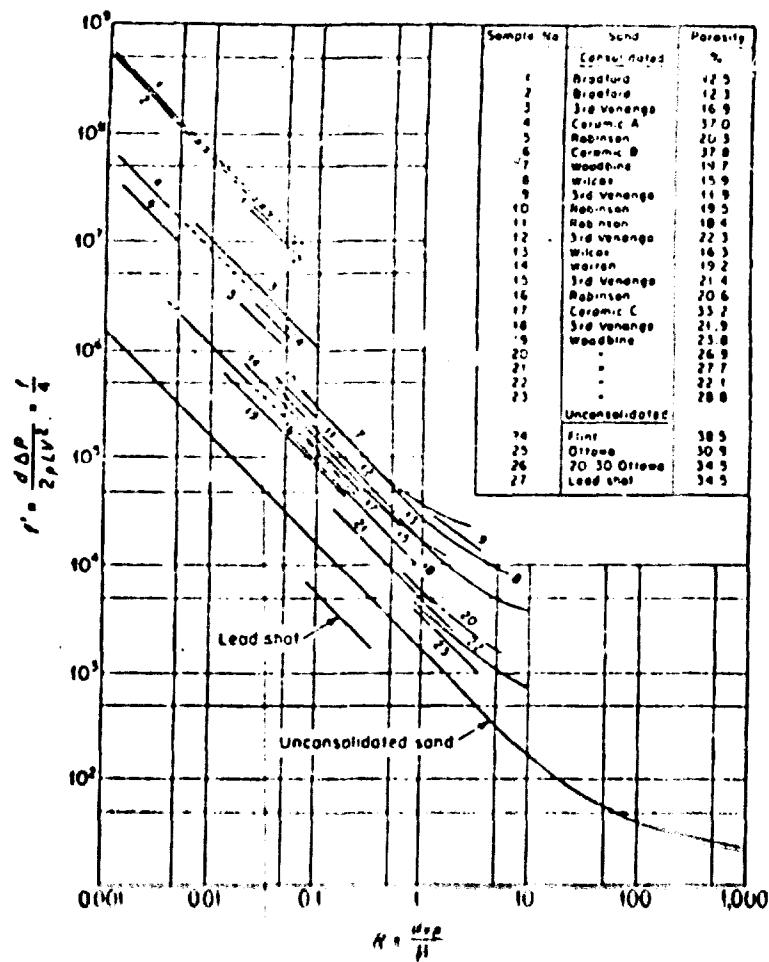
Figure 4-55. Correlation of friction factor with Reynolds number for flow of homogeneous fluids through porous media, where d is defined as the diameter of the average grain and l is the apparent velocity, i.e. volume rate of flow/total cross-sectional area (After Fancher, Lewis, and Barnes).

The output from the program consists of a large number of pressure and temperature profiles corresponding to various times after the start of the calculations. The same information is machine plotted on a Stromberg-Carlson SC-4060 microfilm plotter.

4.6.2 Sample Calculation

The particular hypothetical motor for which the calculations were performed has a cylindrical catalyst bed 1 inch long and with 1 square inch of cross-sectional area. The catalyst load is all 25-30 mesh Shell 405. The downstream plenum has a volume of 0.2 cubic inches and the throat area is 0.4 square inches, corresponding to a contraction area ratio of 25. The upstream gas pressure is applied in a linear ramp in which pressure is raised from an initial value of .001 psia to the final value of 100 psia in 1.6 millisecond. Curve A of Figure 4-59 shows the head-end pressure vs. time. Figure 4-56 illustrates the pressure profile through the bed at a time .35 millisecond after start. It is obtained by numerical calculation of the flow and accumulation of gas in the 25 nodal segments which are used to approximate the bed. Figure 4-57 shows the pressure profile 1.0 millisecond after start and Figure 4-58 shows it 2.0 milliseconds after start.

Curve C of Figure 4-59 shows the calculated pressure downstream of the bed. It is determined in the numerical calculations by simultaneously flowing material out of the downstream end of the bed, accumulating the flow leaving the bed in a small plenum and exhausting from the plenum through a sonic nozzle. Curve B of Figure 4-59 is the compressive and exhausting from the plenum through a sonic nozzle. Curve B of Figure 4-59 is the compressive stress on the catalyst bed from the difference between the upstream and downstream gas pressure forces, which force the bed against the downstream screen or bed restraint. B is the difference between A and C.

Figure 4-60 re-plots curve B of Figure 4-59 along with three other curves of compressive stress versus time for different rates of application of head-end pressure. The curves are for rise-times 0.0, 0.4, 0.8, and 1.6 milliseconds. It can be seen that when the rise times are increased, the peak compressive stress produced tends to decrease.

Figure 4-61 is the locus of peak values from Figure 4-60 and shows how the peak compressive stress produced in a bed decreases as the rise-time of the upstream pressure loading increases.

4.6.3 Mechanical Response of the Bed
to Rapid Loading

If the compressive loading of the bed were rapid compred to the natural period of oscillation of the bed, then the peak compressive stress would be higher for a rapid transient loading than for a slow application of load. As a first cut, the bed may be approximated as a system having a single degree of freedom. In this case the natural period of oscillation of the bed would be:
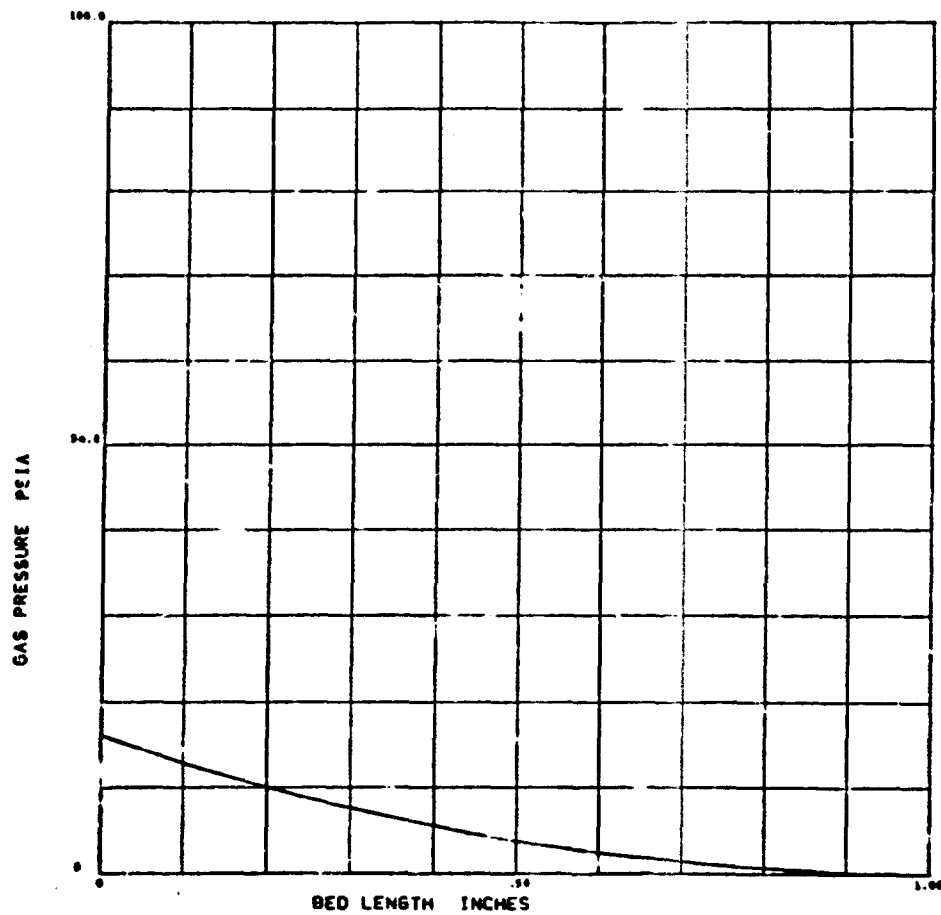
Pressure Profile C.35 Millisecond After Start.

Figure 4-56
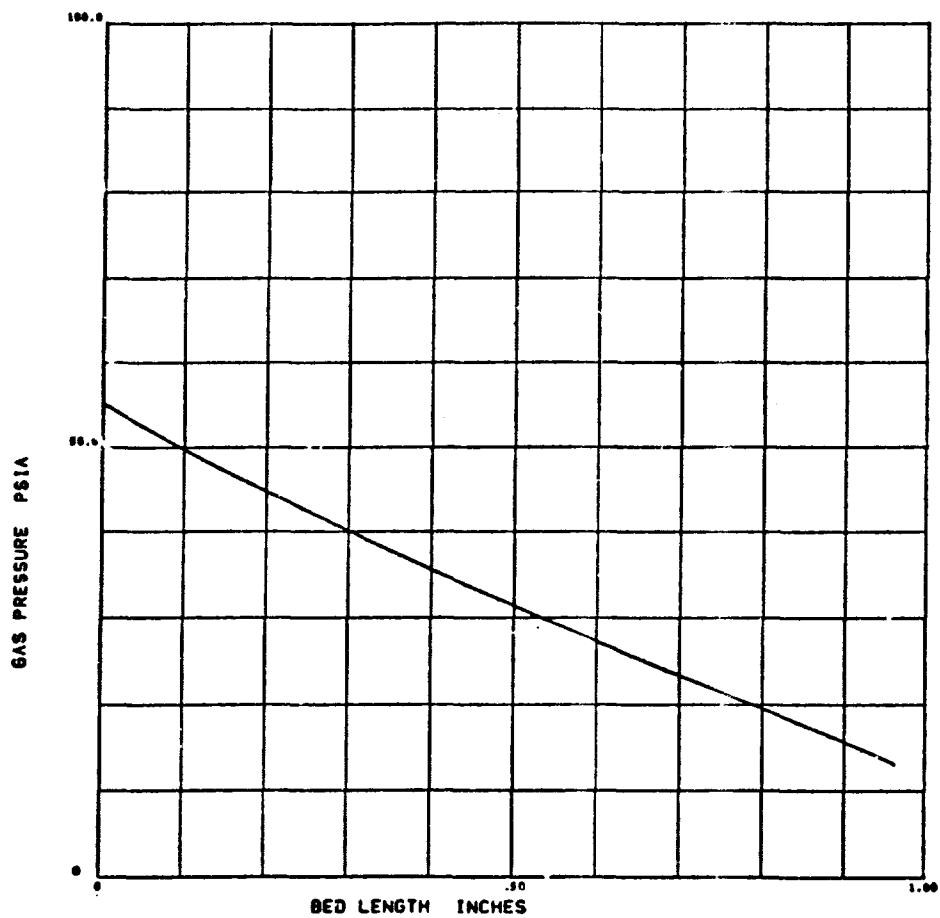
Pressure Profile 1.0 Millisecond After Start

Figure 4-57
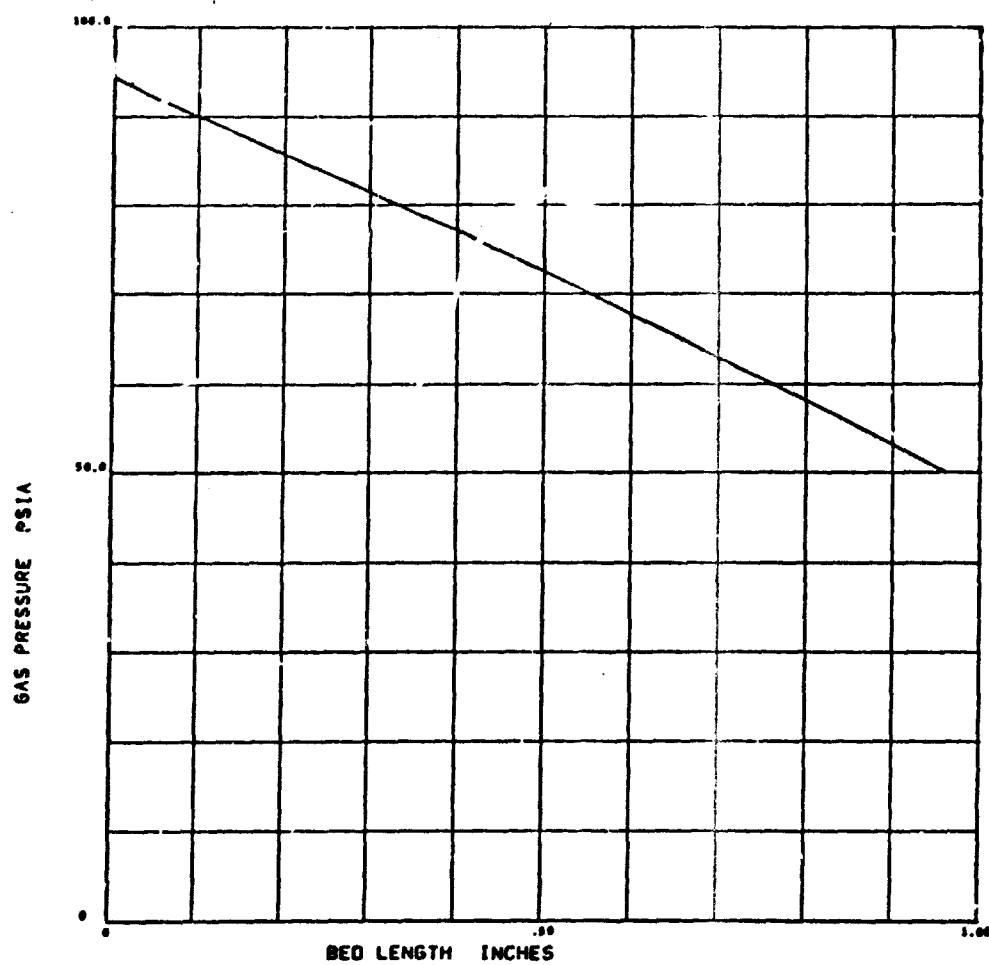
Pressure Profile 2.0 Millisecond After Start

Figure 4-58
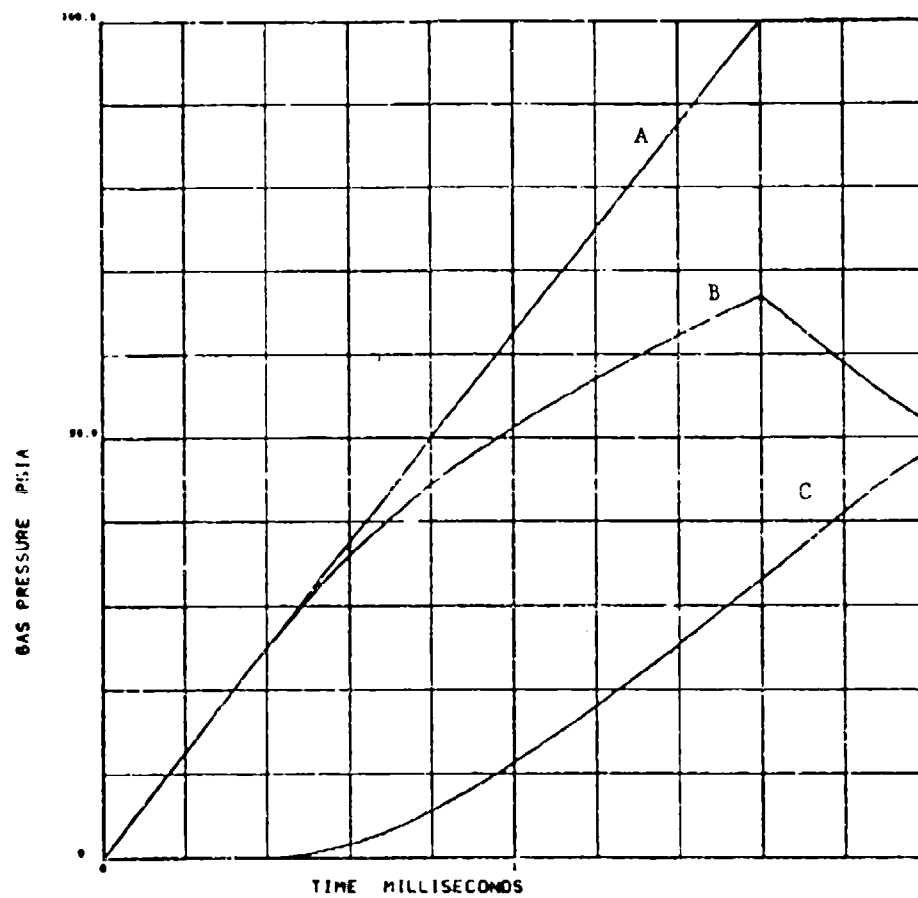
Figure 4-59

Figure 4-60
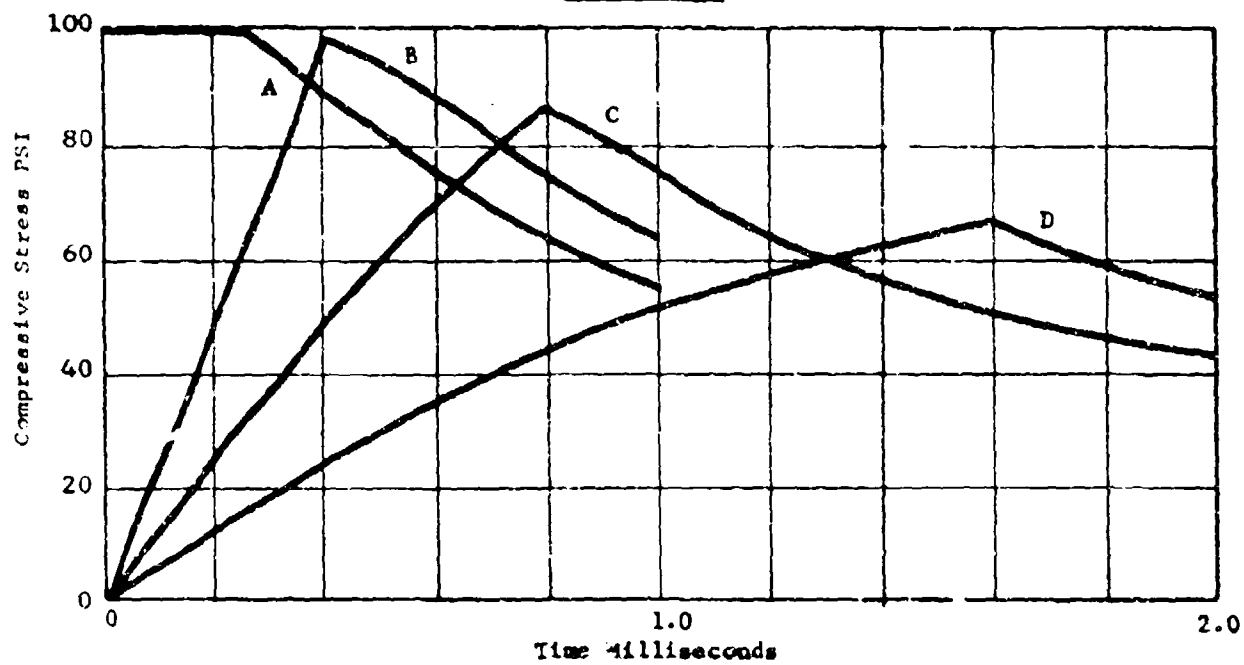
Figure 4-61
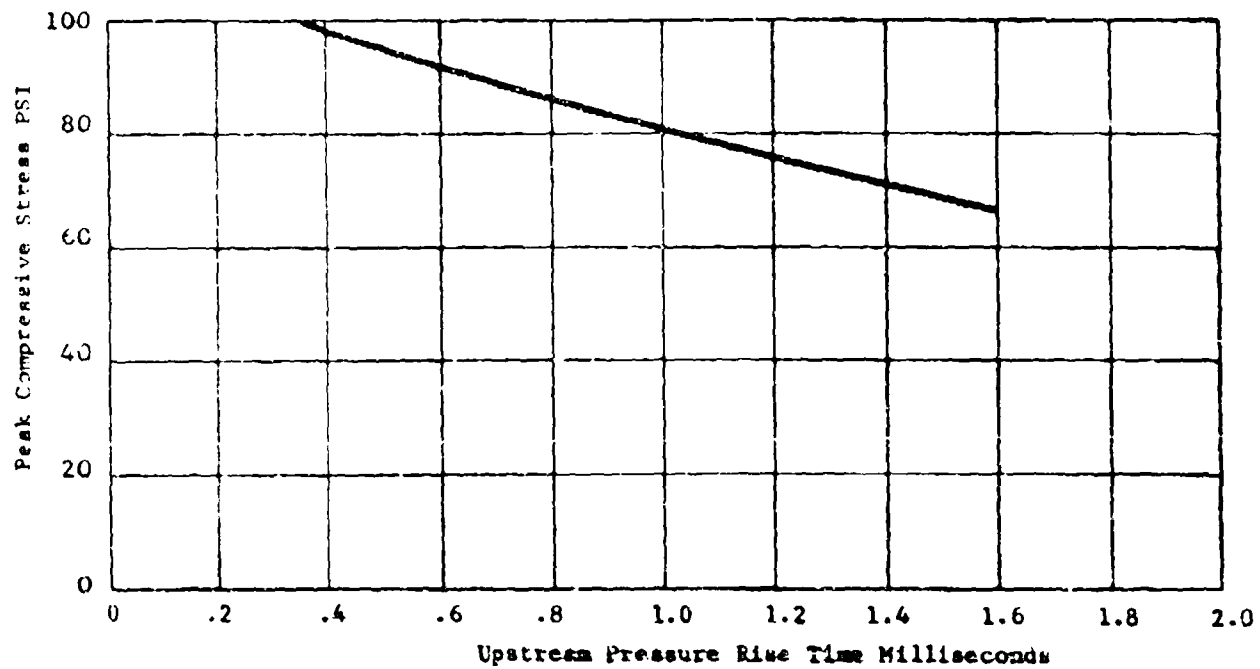
$$\tau = 2\pi \sqrt{\frac{M}{K}} = 2\pi \sqrt{\frac{\rho L A}{E \frac{A}{L}}} = 2\pi \sqrt{\frac{\rho L^2}{E}} \qquad (4.6\text{-}1)$$

where

M is mass of the bed
K is spring constant of the bed
ρ is bulk density of the bed
L is length of the bed
A is cross-sectional area of the bed
E is the compressive modulus of the bed

The compressive modulus of the bed is the only property difficult to estimate. Compression (or compaction) of a granular material may be partly dependent upon the prior history of compaction, and may be irreversible instead of elastic. The stress-strain relationship of a bed of Shell-405 granules has been measured as a part of this study (Section 3.3). A volumetric compaction of 4% was measured at a compressive stress at 1000 psi. This corresponds to an average bed modulus of 25,000 psi over this range of pressure. This number was compared with literature values reported for a bed of flint shot of 28-35 mesh, which should behave similarly to a bed of Shell 405 at low pressures. At a net compressive stress of 100 psi a compressibility of 35×10^{-6} psi^{-1} has been reported, which translates to a compressive modulus of 28,571 psi. The values are obviously in good agreement.

Using the values:

$\rho = 1.60$ gm/cm^3
L = 2.54 cm
E = 1.723×10^9 dynes/cm^2 (25,000 psi)

$$\tau = 2\pi \sqrt{\frac{1.60 \times 2.54^2}{1.723 \times 10^9}} = 5.7 \times 10^{-4} \text{ sec} = 0.48 \text{ millisecond}$$

Hence, the compressive loading of this bed will be "impulsive" only if the time of load application is considerably shorter than 0.5 millisecond.

The literature was consulted to obtain typical pressure rise times in experimental "hard starts" of hydrazine combustors, Reference 124. An oscillograph trace was found for the start of a combustor preconditioned to 35°F at 9×10^{-5} torr. Although the start is delayed and "hard", the most rapid portion of the chamber pressure rise takes approximately 15 milliseconds to be completed. This is a very slow pressure rise in terms of either the time to pressurize the bed, or in terms of the natural period of oscillation of the bed, and would subject the bed only to the normal steady pressure drop associated with the flow of gas through the bed.

4.6.4 Other Conclusions From the Catalyst Bed Mass and Heat Transport Model

For a typical calculation the bed Reynolds number based on particle diameter is approximately 2000. Since the effects of Reynolds number rapidly become important above Reynolds numbers of 10, the flow through the bed is far above flow rates where it could be adequately represented as completely viscous D'arcy flow. The value caclulated by our model for steady-state pressure drop (35-40 psi/inch) appears to be of the correct order of magnitude to agree with reported experimental values.

Although the catalyst bed flow model simultaneously calculates the flow mass andheat, the time scale for the thermal transient is much longer than for the pressure transient, so there is not much dynamic linking between the processes, i.e., the thermal profile through the bed is essentially stationary during the short period of time required for the pressure transient to be completed.

In general, although the transient effects per se in bed pressure buildup are not expected to be important in normal startup, the static effects must nevertheless be considered. The calculations for a typical catalyst which are represented in Figures 4-56 through 4-61 indicate that steady-flow pressure drops through a bed will be on the order of 40 psi. Since the pressure profile through the bed is approximately linear, this indicated that the downstream portions of the bed will be exposed to compaction pressures of 40 psi or more, with the compaction pressure decreasing almost linearly to zero at the upstream portion of the bed. Since both theory and experiment predicts local loss of material at bed compaction pressures considerably lower than this it must be concluded that steady-state pressure drops through the bed can be damaging. The physical weakness of the catalyst particles. combined with their high rigidity and spheroidal shape make them extremely intolerant of bed compression stresses. Corrective measures could be to either shield the catalyst particles from physical stress, or else to modify the shape of the catalyst particles so as to provide larger particle-to-particle bearing areas.

5. CRITICAL ASSESSMENT OF RESULTS TO DATE

Commercial catalytic reactors employing noble metal on alumina catalysts can experience catalyst breakup problems. The general philosophy involved in selecting design parameters for commercial fixed bed reactors is to eliminate the initial catalyst break-up, since the bed after the occurrence of extensive primary degradation generally will be experiencing a major problem requiring a shutdown and catalyst replacement (e.g., channeling of reactants, excessive pressure drop). Many commercial fixed catalyst beds are not mechanically restrained and thus are potentially subject to fluidization. Commercial experience with fixed bed reactors has indicated that inadvertant fluidization in part of the bed often leads to serious problems. Thus factors such as bed inlet design and maximum linear velocities are carefully controlled. Even in a downflow vapor phase reactor fluidization can occur in the inlet area since the vapor jet discharging from the inlet distributor upon striking the surface of the bed will tend to turn and develop a radial velocity component. If the magnitude of this radial gas flow is such that the drag and lift forces generated on the particle overcome gravitational forces than the particle will begin incipient entrainment. In a simple impinging jet designed inlet (located approximately one inlet diameter away from the bed), the maximum surface velocity would occur approximately one diameter away from the axis of the jet. Particles are moved away from the impinging jet in a direction parallel to the bed surface. As erosion proceeds, the particles in the vicinity of the jet are removed also, ultimately leaving a crater in the center of the reactor. The fixed catalyst bed in a hydrazine thruster is mechanically restrained. However, mechanisms or factors leading to void formations in a thruster can similarly expose such a bed to particle movement problems.

Information indicates that the pressure drop across an operating thruster typically ranges from 15 to 40 psi and involves catalyst bed depths of 0.5 to 1 inch. Thus, there is the possibility of static pressure drops of up to 80 psi/inch of bed, not including any effect of bed preloading. Such a pressure drop is very severe when compared to commercial practice in vapor phase fixed bed reactors. As an example, commercial hydroformers used for the production of gasoline generally operate with a pressure drop of 5 to 10 psi per reactor and typically employ catalyst bed depths of 5 to 10 feet, which would be equivalent to static pressure drops ranging from .05 to 0.2 psi/inch of bed. Similarly, it has been estimated that the average gas velocity in a thruster is approximately 110 feet per second. This gas velocity is an order of magnitude greater than that normally experienced in hydroformers. Also design and operating procedures for commercial fixed bed catalytic units normally avoid rapid temperature or pressure transients. Even in catalytic beds used in the treatment of auto exhaust gases the transients experienced when the bed is cycled during the various driving modes are not as rapid as those experienced in a hydrazine thruster, for example, during a cold start. It can be seen that, in general, the environment to which Shell 405 catalyst is exposed in hydrazine thruster use is quite severe compared to the environment experienced by similar alumina based catalysts in use in the petroleum and chemical industries.

A number of potential mechanisms or factors involved in individual catalyst particle degradations have been screened either experimentally or analytically or by means of both techniques. The areas investigated and the interaction between the experimental and analytical studies was summarized in Table 3.3. Experimental work in the areas related to thermal shock such as the effect of repeated hot gas or liquid quick thermal cycling in a bed of catalyst remains to be completed.

An experimental study was made to determine the minimum gas velocity at which particle movement will first occur and expose a voided catalyst bed to particle fluidization, and thus to particle-to-particle abrasion effects. Results from the particle fluidization experiments have shown that the incipient particle movement velocity varies with gas density and particle size as expected. A successful correlation of incipient particle movement velocity as a function of the square root of the ratio of particle diameter to gas density was made. Results indicate that for the range of granular catalyst sizes, gas densities, and gravitational fields expected for hydrazine thrusters, the incipient particle movement velocity will be much lower than an average gas velocity of 110 feet per second. Thus, in general, particle movement will be possible once sufficient void space is present in the catalyst bed. In future work it is planned to investigate the magnitude of particle to particle abrasion effects in a voided bed at velocities above the minimum particle movement velocity. At this time, however, it would be expected that void formation in the catalyst bed would be a major deleterious occurrence in the overall catalyst bed breakup process. Since a Shell 405 catalyst exposed to a pressure load of 100 psi will compact less than 0.5%, actual breakup of catalyst particles will be required for substantial void volume formation.

A number of mechanisms in the fluid dynamic erosion area were investigated either experimentally or analytically. Sensitivity tests in the HSGET apparatus indicate that fresh Shell 405 granular catalysts do not experience any degradation at 1700°F even with exposure to gas velocities up to 250 feet per second. These data indicate that gas fluid dynamic erosion per se is not a mechanism contributing to catalyst degradation. An analytical investigation was made of the effect of the presence of liquid droplets or solid particles in the flowing gas stream on erosion. The calculation indicated in most cases that in the absence of particulates in the gas stream the erosion rates could be expected to be insignificant. On the other hand, the presence of particulates in the 1/2 ppm range or higher suggest wear rates which cannot be ignored. Current specifications for hydrazine used in catalytic thrusters limit solids to a maximum allowable level of 1 mg/liter, which is equivalent to 1 ppm by weight. For this mass loading level the predicted wear rate is 2×10^{-4} per cent for a single 5 second pulse. Extrapolating this on a single linear bases to 5,000 sec of total operation (1000 pulses) indicates an abrasion loss of 0.2%. While this loss level by itself is not catastrophic, it does suggest that prudence would require that particulate contaminants in hydrazine be held as much below the 1 ppm level as possible.

In addition to particulates in the liquid hydrazine entering the thruster, particulates could be generated internally to much higher levels via a rapid decomposition of the catalyst bed as a result of another breakup mechanism. Since the particulate velocity exerts a major effect on the wear rate, a consideration in the latter case is how fast the solids accelerate up to the gas stream velocity. Since the calculations that were made assumed an instantaneous acceleration of catalyst breakup particles, they obviously represent a pessimistic or limiting case. More important the calculations show a need for (1) as low a particulate contaminant level in the fuel as possible, and (2) lower gas velocities to minimize potential particulate abrasion loss by limiting the ultimate velocity the particles can reach in the event another mechanism causes catalyst breakup. Results obtained with the PLPET experiments indicate that a pulsed liquid stream can cause a weight loss with fresh Shell 405 catalyst. This weight loss increases with increasing number of pulses and linear velocity and is higher for 8-12 mesh granules than for 1/8" cylinders. An Analysis of Variance of results from a full factorial statistically designed experiment indicate that the effect of these variables on weight loss is significant but that no interactions exist between the variables. The magnitude of this weight loss, however, will be small at lower liquid velocities. For example, when the linear velocity is held below 50 feet per second, the weight loss experienced by a fresh granular catalyst will be below 1 wt %. The effect of thruster exposure on the ability of Shell 405 catalyst to resist pulsed liquid stream erosion remains to be investigated.

An analytic study was made of the effect of the transients involved when a bed is pressure loaded, i.e. pressure shock effects. Results from this study indicate that a pressure loading occurring in load application times greater than 1/2 millisecond is slow, either in terms of the time to pressurize the bed or in terms of the natural period of oscillation of the bed, subjecting the bed only to the normal steady pressure drop associated with the flow of gas through the bed. Thus, the dynamics per se of a normal pressure shock would not appear to be a major mechanism for catalytic degradation, and the effect of a normal pressure transient can be analyzed in terms of the effect of an equivalent steady state load applied to the bed. The effect of "pop" shock, i.e. the pressure shock effect on a bed interface when hit by a large pressure "cook-off spike" (as could occur from hydrazine detonation), will be investigated experimentally.

An analytical study was made of particle thermal shock. Thermal shock from externally heating a cold particle by hot combustion gases or from externally cooling a hot particle by impingement of cold liquid hydrazine were both analyzed in terms of the temperature profiles obtained, which were taken from dimensionless correlations of temperature ratio with Biot number and Fourier number. The stresses induced in the pellet were obtained from the temperature profiles. These calculations indicate that particle thermal shock is a borderline failure mechanism, in that only occasional

failures of especially weak individual particles are expected. The failures
are particularly to be expected during cooldown from impingement of liquid
hydrazine, rather than heating of a cold particle with hot gas, as cooldown
produces tensile stresses of a greater magnitude compared to mean failure
stress. In general, the calculations suggest merit to the avoidance of
cold liquid impingement upon hot catalyst material. The analytical results
also indicate that (1) liquid impingement will not be damaging if the cata-
lyst temperature is sufficiently high to induce film boiling and thus reduce
liquid to particles heat transfer, (2) reducing the diameter of the parti-
cles will reduce the Biot number, and the stress level produced by cooldown.
The effect of thermal fatigue on a bed of material undergoing repeated hot
gas heat up or liquid quench cycling remains to be experimentally investigated.
The internal particle stresses produced in a particle by rapid gas pres-
surization or depressurization in the absence of liquid hydrazine were also
analytically investigated by calculating the internal pore pressure pro-
files and the stress distribution resulting from these profiles. Particle
depressurization is very fast relative to the rate of thruster chamber de-
pressurization at cutoff so that no significant internal pressure stresses
will occur during a normal cutoff. Internal pressurization is also a very
fast process producing only compressive stresses in the particle. Pressure
loadings of sufficient magnitude and speed to cause significant internal
pore pressure generated stresses are much more likely to cause damage by
simple bed composition pressure stresses. Thus, internal stress failure
caused by internal particle pore pressure changes as a result of rapid
pressurization or depressurization is not an important mechanism. The
results also indicate that pressure equilibration is a very rapid process
compared to thermal equilibration, and thus the processes would not be ex-
pected to be coupled.

An analtyical study was made of the effect of the differential
thermal expansion of the bed and thrust chamber hardware. During startups
the bed heats up more rapidly than the wall. Because of this, the bed
first undergoes compression but then changes to dilation as the effect of
the much higher coefficient of thermal expansion of the metal wall relative
to that of the catalyst bed is manifested. On cooldown two possibilities
are possible. If the bed does not repack itself during the startup di-
lation phase, it remains in dilation during the cooldown period. If, on
the other hand, the bed repacks itself after the startup dilation, it will
experience compression during cooldown. The magnitude of the peak compres-
sion and dilation increases with bed loading. A bed loading of 0.1 lb per
in^2-sec produces a peak startup bed compression of 0.3 vol %, which trans-
lates into a bed pressure of 25 psi. If the bed repacks itself after the
startup dilation, with a similar loading of 0.1 lb per in^2-sec, the bed
will experience a maximum compression of 1.75 vol % during cooldown, which
translates into a 290 psi bed pressure. Catalyst degradation from the
latter case will clearly be serious. The calculations also point out
that higher bed loadings increase the magnitude of the bed compression
forces, both during initial startup and during cooldown with a repacked bed.
Also, higher thruster pressures do not markedly effect the magnitude of the
startup bed volume compression, but they do increase the magnitude of the
bed void volume during the startup dilation period.

Studies carried out by United Technologies Research Center under Contract F04611-74-C-0031 have indicated that the internal pressure generated within a Shell 405 catalyst particle as a result of wetting with liquid hydrazine can cause a catalyst particle to undergo break-up. Analytical modeling studies carried out in this program support this hypothesis. An internal processes computer program was written to investigate the temperatures, pressures, and flow processes which occur when a catalyst particle is wetted with liquid hydrazine. Mass transport within the particles was modeled by D'Arcy flow driven by the pressure gradients resulting from first the capillary imbibitions pressure of the liquid hydrazine and later by the high pressure gases generated from the decomposition of the hydrazine rather than simply by molecular diffusion driven by concentration gradients. Calculations indicate that the flow from D'Arcy processes ranges from 100 to 1000 times larger than that from diffusional processes in a Shell 405 catalyst particle. Heat transport within the particle was modeled considering both convection of heat resulting from flow of gas and liquid plus conduction of heat through the formation rather than just considering heat conduction alone. Calculations indicate that heat transport from convective processes is as least as large as that from conductive processes and could be as great as 10 times larger. Very preliminary operation of this internal processes model has been accomplished. Results indicate that after exposure to liquid hydrazine at 300°K and 1 psia, liquid imbibition proceeds rapidly and liquid hydrazine flows inward countercurrent to the outward flow of gas. Liquid influx at the boundary of the pellet is cut off as the internal gas pressure overcomes the liquid imbibition pressure. The particle is now at its maximum liquid overall saturation level, and liquid hydrazine continues to flow inward toward the center of the particle. The particles temperature increases because of the exothermic decomposition reaction and reaches a maximum of 357°K, a 57°K rise, following which the temperature drops off as the reaction rate declines as the original hydrazine is exhausted. As the last of the liquid hydrazine in the pellet is consumed, a peak pressure of 7390 psi is obtained. The internal pressure rise predicted is clearly of a magnitude to cause concern. It was estimated that a pressure of 7000 psi would result in radial and tangential stresses of 1900 psi, which is above the mean failure stress predicted for fresh Shell 405 for this failure mode. The results strongly suggest the need to prevent such high stresses generated as the result of liquid imbibition by a means such as vaporizing the hydrazine before it reaches the catalyst. In addition, smaller diameter catalyst particles could be used which could allow faster pressure relief. Similarly, the pore size distribution of the substrate could be improved by adding a larger fraction of larger pores which would also allow faster pressure relief. Although these preliminary results clearly point out the deleterious effect of contact with liquid hydrazine, the internal particle processes model has not been checked against experimental data and this is not considered fully developed and may require additional refinement.

Experimental static pressure crushing studies were carried out with both individual particles and aggregate beds. Individual particle measurements were made with fresh and used Shell 405 catalyst and with the catalyst support both before and after the attrition step. The use of the attrition procedure improves the average crush strength of the larger mesh size granules but does not significantly improve the strength of the smaller material. The addition of the iridium metal to the support, in general, does not effect the crush strength. Even with the use of the attriting

procedure, the scatter in the individual crush strengths of both Shell 405 pellets and particles is quite large, which means that an appreciable fraction of aggregate of Shell 405 catalyst such as a bed will have particles with a crush strength significantly lower than the mean crush strength. For example, it is estimated that 10% of fresh Shell 405 particles have a crush strength which is lower than a value equivalent to 68% of the average value for that particle size. Tests of used Shell 405 catalyst indicate that thruster exposure under some conditions may both decrease the average crush strength and increase the standard deviation of the crush strengths. The net result of the combination of such changes is a sharp increase in the percent of very weak particles present in an aggregate such as a bed, which is quite deleterious. Additional work is planned in this area. Initial experimental results of static pressure crushing studies with mini-beds of granular fresh Shell 405 catalyst indicate that significant size reductions can occur at a pressure of 100 psi. For example, with a 20 to 25 mesh materials, 7 wt % of the starting material exhibited a size reduction (passed through 25 mesh) under this pressure. The general shapes of the loss curves as a function of bed pressure were very similar to those normally obtained with petroleum and chemical industry catalysts, i.e. they exhibit a low weight loss at low pressures, followed by a slowly increasing weight loss which ultimately becomes exponentially increasing at much higher pressures. These bed results appear to corroborate individual particle pressure crushing studies which suggest that aggregates contain significant quantities of particles much weaker than the mean strength. Additional experimental work is planned in the static bed pressure crushing area.

Analytical studies were made to predict the particle stresses which result when a bed of catalyst particles is subjected to a compression load. These calculations show that particle to particle contact stresses resulting from external bed compression forces are quite severe, and indicate that some catalyst breakup should occur, even at very low bed pressures. This result appears to corroborate the limited bed pressure crushing experimental work carried out to date. Thus both experimental and analytical studies indicate that the ability of the Shell 405 catalyst to resist pressure crushing from external forces in a thruster bed is an area for genuine concern.

Pressure crushing is thus judged to be a significant mechanism for catalyst breakup. External forces which would result in pressure crushing include pressure drop from steady-state flowing gases, preload forces applied to the bed, compression forces resulting from diferential thermal expansion effects pressure forces occurring during dynamic pressure change periods, and the added effect of factors such as vibration and high G-loads imposed on the bed.

The analytical studies pinpointed a number of strength of material properties which influence the judgements made form calculations and which at present have only been indirectly determined for Shell 405 catalyst. These include tensile failure strength, multiaxis compressive failure strength, the Poisson ration, relative permeability and the Klinkenberg constant.

In summary, the major mechanisms or factors identified to date are (1) particle to particle crushing as a result of various static pressure crushing forces, (2) the build-up of pressure within the pores as a result of imbibed liquid, and (3) the fact that a voided thruster bed has sufficient gas velocity for particle movement and (4) loss of catalyst physical properties such as crush strength with use. Other significant mechanisms or factors identified include fluid dynamic erosion from a pulsed liquid stream, erosion from solid initially present in the hydrazine and thermal shock during liquid quench cooldown. Five mechanisms or factors were judged not be significant. In Table 5-1 and 5-2 are summarized the insignificant factors and significant mechanisms or factors identified in the program to date.

Table 5-1

Summary of Insignificant Factors

Factor	Method Investigated
• Fluid dynamic erosion by pure gas	Experimental and Analytical
• Fluid dynamic erosion by liquid drops in gas	Analytical
• Particle pore pressure gradients during rapid gas pressurization or depressurization (in the absence of liquid)	Analytical
• Transient effects per se in pressure buildup (must consider effect of pressure, however, as static pressure crushing)	Analytical
• Thermal shock from heating a particle with hot combustion gases	Analytical

Table 5-2

Summary of Significant Mechanisms or Factors

I.	Major Factors	Method Investigated
●	Static pressure crushing	Experimental and Analytical
	- High ΔP from steady state gas flow	
	- Differential thermal expansion compression forces particularly during cooldown if bed repacks, but also during starting	
	- Bed preload	
●	Corroboration of the deleterious effect of the build-up of pressures within pores as a result of imbibed liquid hydrazine.	Analytical
●	Voided thruster bed has sufficient gas velocity for particle movement	Experimental
●	Loss of catalyst physical properties such as crush strength in thruster exposure	Experimental
II.	Other Factors	
●	Pulses liquid stream fluid dynamic erosion	Experimental
●	Fluid dynamic erosion from solid particles in gas	Analytical
●	Thermal shock from liquid quench cooldown	Analytical

6: REFERENCES

(1)   Adams, C.R. and Voge, H.H., "Aging of Silica Alumina Cracking Catalyst - Electron Microscope Studies," Journal of Physical Chemistry Vol. 61, p 722, 1957.

(2)   Baddour, R.F., et al., "The Palladium Catalyzed Carbon Monoxide Oxidation Catalyst Break-in Phenomenon," Journal of Physical Chemistry, Vol. 74, No. 8, April 16, 1970.

(3)   Benesi, H.A., et al., "Determination of the Pore Volume of Solid Catalysts," Analytical Chemistry, Vol. 27, p 1963, 1955.

(4)   Bond, G.C., "Absorptive and Catalytic Properties of Small Metal Crystallites," 4th International Congress on Catalysis, Moscow, 6/23-29/68.

(5)   Brooks, C.S., "Characterization of Iridium Catalyst Surfaces by Gas Chemisorption," Journal of Colloid and Interface Science, Vol. Vol. 34, No. 3, November 1970.

(6)   Butt, J.B., "Thermal Conductivity of Porous Catalysts," AIChE Journal, Vol. II, p 106-12 Ja65.

(7)   Caldwell, A.D. and Calderbank, P.H., "Catalyst Dilution - A Means of Temperature Control in Packed Tubulor Reactor," British Chem. Eng. IV, Vol. 14, No. 9, September 1969.

(8)   Carberry, J.J. and Gorring, R.L., "Time-Dependent Pore-Mouth Poisioning of Catalysts," Journal of Catalysis 5, 529-543 (1966).

(9)   Carberry, J.J., "Heat and Mass Diffusional Intrusions in Catalytiac Teactor Behavior," Catalysis Reviews, Vol. 3, p 61-91 (1969).

(10)   Cambell, J.S., "Influence of Catalyst Formulation and Poisoning on the Activity and Die-Off of Low Temperature Shift Catalysts," Ind. and Eng. Chem. Process Designs 9:588-95, 0 1970.

(11)   Chaplin, L.K., "Fundamental Stress-Strain Paths in Granular Materials Sheared with Small or No Volume Change," Proceedings of Sixth Int. Conference on Soil Mechanics, 1965.

(12)   Chu, C., "Effect of Adsorption on the Fouling of Catalyst Pellets," Industrial and Engineering Chemistry Fundamentals 7;p 507. August 1968.

(13) Cusmano, J.A. and Low, J.D., J. Catalysis, p 798, 1970.

(14) Dobkina, E.I., et al., "Determination of Wearability of Catalysts,"
Kinetics and Catalysis, Vol. 11 (3), p 771-4, 1970.

(15) Emelianova, G.I. and Hassan, S.A., "About the Anamolous Character
of Sintering of Supported Catalysts," 4th International Congress on
Catalysis, Moscow, 6/23-29/68.

(16) Ervin, M.A. and Luss, D., "Effect of Fouling of Adiabatic Packed
Bed Reactors," AIChE Journal 16:979-84, November 1970.

(17) Esso Research Report 3GE.72, "Proposed Mechanism for Catalyst
Break-Up in Cyclic Processes." (Unpublished)

(18) Gloria, F.; "Poisoning of Porous Catalyst Particles," Industrial
and Engineering Chemistry (Fundamentals) 10 204-11 Ny 71.

(19) Greer, H., "Vacuum Start Up of Reactors for Catalytic Decomposi-
tion of Hydrazine," J. Spacecraft and Rockets, Vol. 7, 522-8 (1970).

(20) Griffith, R.M., "Silica and Alumina Powders Coherence and
Strength of Composites," Canadian Journal of Chemical Engineer-
ing 44:111-16, April 1966.

(21) Gwyn, J.E., "Particle Size Distribution Function and the Attrition
of Cracking Catalysts," AIChE Journal, 15, 35, Ja 1969.

(22) Harriott, P., "Diffusion Effects in the Preparation of Impregnated
Catalysts," Journal of Catalysis, Vol. 14, 43-48 (1969).

(23) Hasselman, D.P.H., "Relationship Between Macroscopic Shear
Moduli and Micro-Mechanical Shear Stress," Journal of American
Ceramic Society, Vol. 50 (6), p 331-2, 1967.

(24) Hiorns, F.J. and Venables, J., "Controlled Fracture of Brittle
Solids," British Coal Utilization Research Association Monthly
Bulletin, Vol. XXVI, No. 3, March 1962.

(25) Hughs, R. and Shethgar, V.R., "Regeneration of Silica-Alumina
Catalyst Particles," Journal Applied Chem. and Biotech. 21, p 35,
February 1971.

(26) Huxtable, D.D., Capt. USAF, "Hydrazine Catalyst Evaluation,"
Technical Report AFRPL-TR-70-107, November 1970.

(27) Ioffc, I.I., et al., "Fundamentals of the Theory of Chemical Reactor Reliability. III Methods of Calculating the Life of Industrial Catalysts," Chem. Tech., Vol. 23 (6), p 330-1, 1971.

(28) Kehoe, J.P., "The Interactions of Inter- and Intraphase Gradients," In a Diffusion Limited Exothermic Catalytic Reaction, AIChE Journal, Vol. 18, No. 2, p 347-55, March 1972.

(29) Kenney, C.H. and Shah, Y.T., "Effectiveness Factors and Transient Behavior in Gas-Liquid Catalyst Systems," Chemical Engineering Science, Vol. 28, No. 1, p 325-28, January 1973.

(30) Keston, A.S., "A Conceptual Model of Hydrazine Catalytic Reactor Washout Caused by Decomposition Product Poisoning and Pressure Build-Up," Paper in 1972 JANNAF Propulsion Meeting, CPIA No. 228, Vol. IV, December 1972.

(31) Keston, A.S., "Integral Equation Method for Evaluating the Effects of Film and Pore Diffusion of Heat and Mass on Reaction Rates in Porous Catalyst Particles," AIChE Journal, Vol. 15, p 128, January 1969.

(32) Keston, A.S., "Turbulent Diffusion of Heat and Mass in Catalytic Reactors for Hydrazine Decomposition," AIAA Paper 69-421, 1969.

(33) Keston, A.S., "Analytical Study of Catalytic Reactors for Hydrazine Decomposition (V)," Hydrazine Monopropellant Technology Symposium, Johns Hopkins University, 1967.

(34) Lee, J.C.M., "Stability of An Exothermic Reaction Inside a Catalytic Slab with External Transport Limitations," Industrial Engineering Chemistry Fundamentals 11: p 117-22, February 1972.

(35) Levy, R.M., et al., "Effect of Thermal Aging on the Physical Properties of Activated Alumina," Industrial and Engineering Chemistry Product Research and Development, 7:217-20, S 1968.

(36) Levy, R.M. and Bauer, D.S., "The Effect of Foreign Ions on the Stability of Activated Alumina," Journal of Catalysis, Vol. 9, p. 78-86, 1967.

(37) McCullough, F., Jr., Engine Life Considerations Paper at 1972 JANNAF Propulsion Meeting, November 1972, CPIA Pub. No. 228, Vol. IV, December 1972.

(38) Miller, M.R. and Wilhoyte, H.S., "Study of Catalyst Support Systems for Fume Abatement of Hydrocarbons," Air Pollution Control Association J, p 791, December 1967.

(39) Mischke, R.A. and Smith, J.M., "Thermal Conductivity of Alumina Catalyst Pellets," Industrial Engineering Chemistry Fundamentals, Vol. 1, 288-92, 1962.

(40) Morita, N. and Kumazava, "The Effective Diffusion Coefficients in a Porous Catalyst Pellet," 5th Society of Chemical Engineering, Japan Autumn Meeting, Journal of Chemical Engineering, Japan, Vol. 5, No. 4, 375-80, December 1972.

(41) Myers, C. G., et al., "Aging of Platinum Reforming Catalysts," Ind. and Eng. Chemistry, Vol. 53:299, April 1961.

(42) Newkirk, A. E. and Mikie, D. W., "Thermal Decomposition of Rhodium, Iridium and Ruthenium Chlorides," Journal of Catalysis, Vol. 11, p 370-377 (1968).

(43) Omata, H. and Brown, L. F., "The Dusty Gas Diffusion Equation in Catalyst Pores Smaller than 50A. Radius," AIChE Journal, Vol. 18, No. 5, p 967-75, September 1972.

(44) Osteen, S., "Significance of Pressure Gradients in Porous Materials," AIChE Journal, Vol. 11:439-45, May 1965.

(45) Paranski[1], S. A., et al., "Evaluation of the Abrasion Resistance of Catalysts," Kinetics and Catalysis, Vol. 9, p 1072, 1968.

(46) Physical Properties of the Platinum Metals, The Rare Metals Handbook.

(47) Prater, C. D., "The Temperature Produced by Heat of Reaction in the Interior of Porous Particles," Chemical Engineering Science, Vol. 8, p 284-286, 1958.

(48) Ramsen, J. H. and Hill, P. B., Industrial and Engineering Chemistry, Vol. 50, p 117-24, January 1958.

(49) Rebinder, P. D., et al., "Mechanical Density in Porous Dispersion Bodies," Doklady Akad. Nauk, SSSR, Vol. 154 (3), p 695, 1964.

(50) Resen, L., "Catalyst Erosion in Cat-Crackers Case Histories of Its Control," Oil and Gas Journal, Vol. 55, p 101, December 9, 1957; Vol. 61, 3 December 16, December 23, 1957; Vol. 56, p 06, January 6, 1958.

(51) Reuschussel, A. M., et al., "Application of Scanning Electron Microscopy to the Study of the Morphology of Multicomponent Catalyst Systems," Journal of Materials Science, Vol. 4, No. 10, 885-9, 1969.

(52) Roberts, J. E. and Souza, "The Compressibility of Sands," ASTM Proceedings, Vol. 58, p 1269, 1958.

(53) Ruchenstein, E. and Petty, C. A., "On the Aging of Supported Metal Catalyst Due to Hot Spots," Chemical Engineering Science, Vol. 27, p 937, 1972.

(54) Russell, A. S. and Cochran, C. N., "Surface Areas of Heated Alumina Hydrates," Industrial and Engineering Chemistry, Vol. 42 (1950).

(55) Russell, A.S., "Alumina Properties," Technical Paper No. 10, Aluminum Company of America.

(56) Sagara, M., "Effect of Non-isothermal Operation in Catalyst Fouling," AIChE Journal, Vol. 13, 1226-9, N 1961.

(57) Sangiovanni, J.J. and Keston, A.S., "Study of Hydrazine Reactor Vacuum Heat Characteristics," United Aircraft Research Laboratories Report H910758, Contract WAS-7-696, December 1969.

(58) Sangiovanni, J.J. and Keston, A.S., "Motion Picture Studies of the Startup Characteristics of Liquid Hydrazine Catalytic Reactors," Paper No. 71-702, AIAA/SAE 7th Propulsion Joint Specialist Conference, Salt Lake City, Utah, June 14-18, 1971.

(59) Sayer, C.F., "The Decomposition of Hydrazine on Shell 405 Catalyst," AIAA Paper No. 70-606, 1970.

(60) Shackner, H., "Structure and Activity of Platinum-Silica Catalysts Prepared by a Combustion Process," Journal of Applied Chemistry, Vol. 19, p 68-72, March 1969.

(61) Shaw, G.Y. and Parsons, B.I., "Low Density Catalysts and Catalyst Supports II," Canadian Mines Branch of Research and Development Report R230, 1970.

(62) Shchukin, E.D., "Mechanical Strength of Porous Disperse Bodies", Abh. Deut. Akad. Wiss. Berlin Kl. Chem. Geol. Biol., Vol. 5, p 89-91, 1968.

(63) Shirasaki, T., et al., "Preparation of Catalyst and Support by Grinding," Kgzo Kagaku Zasshi, Vol. 9, No. 71, p 1313-8, 1968.

(64) Shean-Liu, Li, "The Influence of Intraparticle Diffusion in Fixed Bed Catalytic Reactors," AIChE Journal, Vol. 16, No. 5, p 747, September 1970.

(65) Sohn, H.Y., "On the Maximum Temperature Rise in Gas-Solid Reactions," AIChE Journal, Vol. 19, No. 1, p 191-3, January 1973.

(66) Stumpf, H.C., et al., "Thermal Transportations of Aluminas and Alumina Hydrates," Industrial and Engineering Chemistry, Vol. 42, No. 7, July 1950.

(67) Voge, H.H., Development of Catalyst for Monopropellant Hydrazine, Final Report, Contract WAS 7-97 Shell Development Company, Report No. S-13889, June 1963.

(68) Wei, J., Chemical Engineering Science, Vol. 21, p 1171, 1966.

(69) Williams, K.F. and Matthews, J.C., "Catalyst Activity and Performance of Stability Limited Fixed Bed Reactors," Industrial and Engineering Chemical Process Design 10, 483-9, October 1971.

- 218 -

(70) Wolfe, S. Cr. "Catalyst Handbook, " Imperial Chemical Industries Limited, 1970, SBN 723401640, London.

(71) Wood, S. E. and Bryant, J. T., "Decomposition of Hydrazine on Shell 405 Catalyst at High Pressure," Ind. Eng. Chemistry (Prod. Res, Dev.), Vol. 12, No. 2, 1973.

(72) Fredrickson F. N."Reaction Engine Module Test Evaluation" Report No. AFRPL-TR-72-44 AFRPL, USAF, Edwards, California July, 1972.

(73) Neuton, N.C., Rice, P.R., Jr. and Huxtable,D. D.,"Shell 405 Catalyst Improvement, Substrate Evaluation, Phase 1", July 1970 to April 1971, Report AFRPL-TR-71-81,AFRPL, USAF, Edwards, California, July 1972.

(74) Fredrickson, F. N., "75-lbf. PBPS Monopropellant Engine Test and Evaluation", Report No. AFRP-TR-72-1, AFRPL, USAF, Edwards, California, June 1972.

('5) Sayer, C.F. and Southern, G. R., "The Comparative Testing of the Shell 405, CNESRO-1 and RJ5 72/1 Hydrazine Decomposition Catalysts" Ministry of Defense, Rocket Propulsion Establishment, Westkott Aylesburn, Buckinghamshire, England.

(76) Ellion, M.F., and Frizell, D.P., and Meese, R.A., "Hydrazine Thrusters-Present Limitations and Possible Solutions" AIAA/SAE 9th Propulsion Conference, Las Vegas, Nevada, November 5-7, 1973.

(77) Russi,M.S., "A Survey of Monopropellant Hydrazine Thruster Technology AIAA/SAE 9th Propulsion Conference Las Vegas, Nevada, November 1973, Paper No. 73-1263.

(78) King. S.M., Max, P.C. and Taylor, D., "The Aerospace Corporation, Shell 405 Catalyst Evaluation Program Vol. I: Physical and Catalytic Properties",Report TR-0066 (5210-4) The Aerospace Corp., El Segundo, August 1969).

(79) Shmitz, B., and Wilson, W. W., "Long-Life Moropropellant Hydrazine Engine Development Program", Final Report AFRPL TR-11-103, September, 1971.

(80) Carlson, R.A., Blumenthal, J. L., Grassi, R. J., "Space Environment Operation of Experimental Hydrazine Reactors" Final Report No. 4715.3.68-27, Contract NAS7-520, July 1968.

(81) Christopher, G. and Russell, S. "Effects of Hydrazine Contaminants on Catalyst Life", AIAA/SAE 9th Propulsion Conference, Las Vegas, November, 1973.

(82) Moynihan, P.I., Bjorklund, R.A., "Performance Characterization Tests on Three Hydrazine Catalytic Thrustors" NASA Technical Report 32-1584.

(83) Barclay, L.P., Capt., USAF "Transtage Catalyst Evaluation" AFRFL-TR-69-140, June, 1969.

(84) Greer, H.G., "An Investigation of the First Pulse Characteristics of Monopropellant Hydrazine Reactors" Technical Report TR-0066 (5305)-1, July, 1961.

(85) Traina, F. and Pernicone, N., 20th Int. Ind. Catal. Congr. (Milan 5/19-21/69) Chim Ind. (milan) 52 #1:1-12, Jan., 1970.

(86) Papmahl, F. and Rose, H.F., Ind. Eng. Chem., Prod. Res. Development 8 #4:352-58, December, 1969.

(87) Basmadjian, D., "Venting of High Pressure Fixed-Bed Catalytic Reactors", Canadian Journal of Chemical Engineering 42 #3:104-6, June, (1964).

(88) Paranskii, S.A., Mechiedeva, et al., "The Evaluation of Catalyst Strength Under Condition of Attrition" Kinet. Katal 12 #2:473-79 (June 1971).

(89) Smith, O.I. and Solomon, W.C., "Kinetics of Hydrazine Decomposition and Iridium and Alumina Supported Indium Catalysts" AFRPL-TR-73-59.

(90) Petty, W. L., "Variation in Shell 405 Catalyst Physical Characteristics, Test Catalyst Preparation" AFRPL-TR-73-56 Final Report, May 72-May 73.

(91) Beaver, L.R., Collier, C.L. and Murrell, C.R., ACS Pet. Div. Preprints 18, #4, 726 (1973).

(92) Adams, A.R., Sartor, A.F. and Welch, J.G., Chemical Engineering Progress 71, 35 (1975).

(93) Davies, O.L., "Statistical Methods in Research and Production," Chapter 6, Hafner Publishing Company, N.Y., 1958.

(94) Cordfunke, E.H.P. and Meyer, G., Recueil Trav. Chim. 81, 495 (1962).

(95) Cordfunke, E.H.P. and Meyer, G., Recueil Trav. Chim. 81, 670 (1962).

(96) Alcoch, C.B., Platinum Metals Review, 5, (1961).

(97) Alcoch, C.B. and Hooper, G.W., Proc. Royal Society, A254, 551 (1960).

(99) J. Jortner, MDAC. Private Communication.

(101) S. Timoshenko and J. N. Goodier. Theory of Elasticity. Second Edition. McGrawy-Hill Book Company, New York. 1951.

(102) H.W. Babel and G. Sines. A Biaxial Failure Criterion for Porous Brittle Materials. Transactions of the ASME, Journal of Basic Engineering. Pg. 285-291. June 1968.

(103) P. J. Schneider. Temperature Response Charts. John Wiley & Sons. New York, 1963.

(104) M.A. Biot. Theory of Elasticity and Consolidation of a Porous Aniso-tropic Solid. Journal of Applied Physics, Volume 25, No. 2. February 1955.

(105) R.R. Scott. Principles of Soil Mechanics. Addiston Wesley Publishing Company. Reading, Massachusetts. 1963.

(106) C.D. Babcock. California Institute of Technology. Private Communication.

(107) G.H. Love, Stress Produced in a Semi-Infinite Solid by Pressure on Part of the Boundary, Phil. Tran. A228, 1929.

(108) R.J. Miller. Mechanics of Erosion Phase I. Defense Nuclear Agency. Washington, D.C. DNA 3446F-1. November 1974.

(109) W. F. Taylor. Progress Report No. 7. January 1975.

(110) W. F. Taylor. Exxon Research Laboratories. Private Communication.

(111) H. Brandt. A Study of the Speed of Sound in Porous Granular Media. Journal of Applied Mechanics. Vol. 22, No. 4, pp. 479-486. December 1955.

(112) I. Fatt. Compressibility of a Sphere Pack Comparison of Theory and Experiment. Journal of Applied Mechanics. Vol. 24, No. 1, . 140-149. March 1957.

(113) Hom-Yim Ko and R. R. Scott. Deformation of Sand in Hydrostatic Compression. Journal of Soil Mechanics and Foundation Division Proceedings of the American Society of Civil Engineers. pp. 137-156. May 1967.

(114)   Scheidegger, A. E., The Physics of Flow Through Porous Media, University of Toronto Press, 1959.

(115)   Muscat, M., Physical Principles of Oil Production, McGraw-Hill Book Co., New York, 1949.

(116)   Amyx, J. W., D. M. Bass, and R. L. Whiting, Petroleum Reservoir Engineering - Physical Properties, McGraw-Hill Book Co., New York, 1960.

(117)   Rapoport, L. A. and W. J. Leas, Relative Permeability to Liquid in Gas-Liquid Systems, Trans. AIME, Vol. 192, 1951.

(118)   Leverett, M. C., Flow of Oil-Water Mixtures Through Unconsolidated Sands, Trans. AIME, 1939, p. 149.

(119)   Klinkenberg, L. J., The permeability of Porous Media to Liquids and Gases, Drilling and Production Practices, p. 200, American Petroleum Institute, 1941.

(120)   Recommended Practice for Determining Permeability of Porous Media, American Petroleum Institute, Division of Production, September 1952.

(121)   Brown, H. W., Capillary Pressure Investigations, Trans. AIME, 1951.

(122)   Leverett, M. C., Capillary Behavior in Porous Solids, Trans. AIME, Vol. 142, p. 152, 1941.

(123)   Rose, Walter, and Bruce, Evaluation of Capillary Characters in Petroleum Reservoir Rock, Trans. AIME, 1949.

(124)   Sangiovanni, J. J. and A. S. Kesten, Study of Hydrazine Reactor Vacuum Start Characteristics, United Aircraft Research Laboratories, Report H910758, December 1969.

(125)   Hoffman, R. J., W. T. Webber, et al., Plume Contamination Effects Prediction - The CONTAM Computer Program - Version II, AFRPL-TR-73-46, August 1973.

(126)   Tamura, Z. and Y. Tanasawa, Evaporation and Combustion of a Drop Contacting with a Hot Surface, Seventh Symposium (International) on Combustion, Butterworths, London, 1959.

(127)   Bernath, L., A Theory of Local-Boiling Burnout and its Application to Existing Data, Chem. Eng. Prog. Symposium Series 56, No. 30, 95-110, 1960.

(128)   Tong, L. S. , Boiling Heat Transfer and Two-Phase Flow, John Wiley and Sons, 1965.

(129) J. H. Nielson and A. Gilchrist, "Erosion by a Stream of Solid Particles,"
       Wear, 11 (1969), 111-122.

(130) W. D. English and H. D. Samuel, Jr., "Failure Mechanism of Attitude
       Control System Value in Chlorine Pentafluoride Service," AFML-TR-71-94,
       McDonnell Douglas Corp., July 1971.

(131) E. Rabinowicz, "Friction and Wear of Materials," John Wiley and Sons,
       New York, 1965.

(132) G. H. Fancher, J. A. Lewis, and K. B. Barnes, "Some Physical
       Characteristics of Oil Sands," Penn. State Coll. Bull. 12, 1933.

APPENDIX A

HSGET DATA ON THE EFFECT OF GAS EROSION
AT 250 FEET PER SECOND(a)

Fresh Shell 405 1/8" x 1/8" Cylinders

Pellet	Initial Weight, grams	Final Weight, grams	Weight Change grams
1	.04937	.04795	-.00142
2	.05055	.04857	-.00198
3	.04723	.04559	-.00164
4	.05288	.05116	-.00172
5	.04900	.04774	-.00126

Fresh Shell 405, 8-12 Mesh Particles

Particle	Initial Weight, grams	Final Weight, grams	Weight Change grams
1	.01295	.01337	+.00042
2	.02177	.02160	-.00017
3	.01253	.01234	-.00019
4	.01345	.01321	-.00024
5	.01761	.01684	-.00077

Fresh Shell 405, 14-18 Mesh Particles

Particle	Initial Weight, grams	Final Weight, grams	Weight Change grams
1	.00200	.00210	+.00010
2	.00363	.00360	-.00003
3	.00331	.00335	+.00004
4	.00241	.00233	-.00008
5	.00284	.00277	-.00007

Fresh Shell 405, 20-25 Mesh Particles

Particle	Initial Weight, grams	Final Weight, grams	Weight Change grams
1	.00104	.00107	+.00003
2	.00087	.00091	+.00004
3	.00079	.00091	+.00012
4	.00080	.00089	+.00009
5	.00108	.00112	+.00004

Fresh Shell 405, 25-30 Mesh Particles

Particle	Initial Weight, grams	Final Weight, grams	Weight Change grams
1	.00068	.00093	+.00025
2	.00080	.00085	+.00005
3	.00083	.00074	-.00009
4	.00099	.00090	-.00009
5	.00068	.00072	+.00004

Fresh Shell 405, 20-30 Mesh Particles

Particle	Initial Weight, grams	Final Weight, grams	Weight Change grams
1	.00058	.00079	+.00021
2	.00062	.00055	-.00007
3	.00098	.00101	+.00003
4	.00095	.00078	-.00017
5	.00048	.00050	+.00002

(a) Nitrogen flowing at 250 feet per second, 1700°F, specimens in preheated tube for 1 hour total. All catalyst specimens dried overnight in a vacuum oven at 110°C and 120 mm Hg total pressure before weighing.

HSGET DATA ON THE EFFECT OF GAS EROSION
AT 110 FEET PER SECOND(a)

Fresh Shell 405   1/8" x 1/8" Cylinders

Pellet	Initial weight, grams	Final weight, grams	Weight change, grams
1	.05311	.05220	-.00091
2	.05103	.04975	-.00128
3	.05178	.05041	-.00137
4	.04986	.04810	-.00176
5	.05041	.04889	-.00151

Fresh Shell 405   14-18 Mesh Particles

Particle	Initial weight, grams	Final weight, grams	Weight change, grams
1	.00400	.00424	+.00024
2	.00652	.00675	+.00023
3	.00214	.00220	+.00006
4	.00491	.00503	+.00012
5	.00434	.00439	+.00005

Fresh Shell 405   25-30 Mesh Particles

Particle	Initial weight, grams	Final weight, grams	Weight change, grams
1	NA	NA	NA
2	.00058	.00066	+.00008
3	.00065	.00067	+.00002
4	.00055	.00070	+.00015
5	.00056	.00059	+.00003

(a) Nitrogen flowing at a superficial velocity of 110 feet per
second, 1700°F, specimens in preheated tube for 1 hour total.
All catalyst specimens dried overnight in a vacuum oven at
110°C and 120 mm Hg total pressure before weighing.

HSGET DATA ON THE EFFECT OF GAS EROSION
AT 50 FEET PER SECOND (a)

Fresh Shell 405 1/8" x 1/8" Cylinders

Pellet	Initial weight, grams	Final weight, grams	Weight change, grams
1	.04949	.04844	-.00105
2	.05002	.04826	-.00174
3	.04952	.04755	-.00197
4	.05015	.04824	-.00191
5	.05382	.05220	-.00162

Fresh Shell 405 25-30 Mesh Particles

Particle	Initial weight, grams	Final weight, grams	Weight change, grams
1	.00079	.00074	-.00005
2	.00067	.00075	+.00008
3	.00076	.00074	-.00002
4	.00105	.00102	-.00003
5	.00038	.00055	+.00017

(a) Nitrogen flowing at a superficial velocity of 50 feet per second, 1700°F, specimens in preheated tube for 1 hour total. All catalyst specimens dried overnight in a vacuum oven at 110°C and 120 mm Hg total pressure before weighing.

ANALYSIS OF PERCENTAGE WEIGHT CHANGE RESULTS
FROM GAS EROSION DATA IN HSGET

Gas Velocity	Fresh Shell 405 Catalyst	Percentage Change in Weight			
		Individual Rate	Mean	Standard Deviation	Standard Error
110 feet per second	1/8" x 1/8" Pellets	− 1.71 − 2.51 − 2.64 − 3.53 − 3.02	− 2.68	0.67	0.30
"	14-18 Mesh	+ 6.00 + 3.53 + 2.80 + 2.44 + 1.15	+ 3.18	1.79	0.80
"	25-30 Mesh	+13.80 + 3.80 +27.30 + 5.36	+12.38	10.96	5.84
50 feet per second	1/8" x 1/8" Pellets	− 2.12 − 3.48 − 3.98 − 3.81 − 3.01	− 3.28	0.75	0.33
"	25-30 Mesh	− 6.33 +11.94 − 2.63 − 2.86 +44.70	+ 8.96	21.18	9.47
250 feet per second	1/8" x 1/8" Cylinders	− 2.88 − 3.94 − 3.40 − 3.26 − 2.57	− 3.22	0.529	0.237
	8-12 Mesh	+ 3.24 − 0.78 − 1.52 − 1.78 − 4.38	− 1.04	2.75	1.23
	14-18 Mesh	+ 5.00 − 0.83 + 1.23 − 3.32 − 2.46	C.07	3.30	1.47

Gas Velocity	Fresh Shell 405 Catalyst	Percentage Change in Weight			
		Individual Rate	Mean	Standard Deviation	Standard Error
	20-25 Mesh	+ 2.88 + 4.59 +15.19 +11.25 + 3.70	7.52	5.42	2.42
	25-30 Mesh	+36.76 + 6.25 -10.82 - 9.10 + 5.88	5.79	19.08	8.53
	20-30 Mesh	+36.20 -11.28 + 3.07 -17.89 + 4.17	2.85	20.88	9.34

ANALYSIS OF VARIANCE(a) OF GAS FLUID
DYNAMIC EROSION TEST RESULTS

A. Data:

Weight Change in 10^{-5} Grams

	Superficial Gas Velocity, ft/sec		
	50	110	250
1/8" x 1/8" Cylinders	-105 -174 -197 -191 -162	- 91 -128 -137 -176 -152	-142 -198 -164 -172 -126
25-30 Mesh Granules	- 5 + 8 - 2 - 3 + 17	+ 8 + 2 + 15 + 3 (+7)	+ 25 + 5 - 9 - 9 + 4

B. ANOVA Results

Variance Component	Sum of Squares	Degrees of Freedom	Mean Square
Columns	1,559.267	2	779.633
Replicates	5,634.797	4	1,408.699
Columns x Replicates	1,722.400	8	215.300
Rows	188,972.000	1	188,972.000
Columns x Rows	870.066	2	435.033
Replicates x Rows	2,879.467	4	719.866
Columns x Replicates x Rows	3,404.933	8	425.616
TOTAL	205,042.800	29	

(a)See O. L. Davis, "Statistical Methods in Research and Production", Chapter 6, Hafner Publishing Company, New York, 1958.

APPENDIX F

EFFECT OF WATER CONTENT ON
PARTICLE CRUSHING STRENGTH

ITI Crush Strength Data on As-Is-Specimens

Fresh Shell 405 1/8" x 1/8" Cylinders	Fresh Shell 405, 14-18 Mesh Granules	Harshaw Al 1602 1/8" x 1/8" Cylinders
32.75 lbs	2.80 lbs	25.20 lbs
30.75	2.97	24.10
39.70	1.00	23.50
25.90	1.60	29.10
27.95	1.62	25.00
39.07		21.90
43.12		31.60
38.20		24.80
27.85		21.90
38.62		39.20

ITI Crush Strength Data on Vacuum Oven Dried Specimens[a]

Fresh Shell 405 1/8" x 1/8" Cylinders[b]	Fresh Shell 405, 14-18 Mesh Granules[c]	Harshaw Al 1602 1/8" x 1/8" Cylinders[d]
30.05 lbs	1.43 lbs	29.00 lbs
30.05	2.40	16.15
25.20	2.45	23.26
38.30	1.06	33.20
21.85	0.77	24.10
43.35	0.76	25.80
37.00	1.43	40.50
38.30	0.59	20.00
26.00	1.25	42.40
37.55	3.72	
45.10		
31.20		
46.85		
40.90		
33.00		

(a) Dried in a vacuum oven overnight at 110°C and 120 mm Hg total pressure.
(b) Average weight loss was 6.04% from as is basis.
(c) Sample showed no average weight loss from as is basis.
(d) Average weight loss was 4.93% from as is basis.

ITI Crush Strength Data on Water Saturated Specimens[a]

Fresh Shell 405 1/8" x 1/8" Cylinders[b]	Fresh Shell 405, 14-18 Mesh Granules[c]	Harshaw Al 1602 1/8" x 1/8" Cylinders[d]
30.00 lbs	2.17 lbs	24.00 lbs
39.10	1.74	27.85
41.35	1.53	16.50
42.35	1.61	30.50
28.60	0.89	27.60
38.00	0.85	21.50
34.35	0.44	15.50
20.10	0.69	24.10
35.00	0.35	25.50
39.60	1.46	33.10
36.60		
45.50		
30.60		
32.60		
31.60		

(a) Saturated with water vapor at 80°F and 1 atm total pressure.
(b) Average weight gain was 1.39% from as is basis.
(c) Average weight gain was 12.6% from as is basis.
(d) Average weight gain was 2.59% from as is basis.

APPENDIX B

ITI CRUSH STRENGTH DATA ON FRESH SHELL 405 CATALYST

8-12 Mesh	20-25 Mesh	25-30 Mesh	20-30 Mesh
4.46 lbs	1.340 lbs	0.360 lbs	0.500 lbs
3.05	0.525	1.050	0.865
4.60	0.930	1.060	0.435
1.50	0.300	0.760	0.650
3.84	0.185	0.510	0.780
6.82	2.030	0.650	1.235
6.40	0.950	0.770	0.490
7.08	1.000	0.655	0.400
2.66	0.415	0.715	0.695
2.90	0.615	0.750	0.300
2.42	1.350	0.910	0.660
7.34	0.800	0.520	0.130
2.64	0.905	0.600	0.465
6.76	0.640	0.040	0.430
2.48	0.150	0.410	0.165
7.12	0.600	0.350	0.960
5.00	0.825	0.290	2.000
4.68	0.520	0.210	0.500
3.00	1.080	0.700	0.930
4.24	0.160	0.890	0.840
2.88	0.900	0.580	0.350
2.71	0.400	0.320	0.200
5.40	0.110	0.405	0.430
4.20	0.615	0.250	0.610
4.80	1.075	0.250	0.100

ITI CRUSH STRENGTH DATA ON ALUMINA
SUPPORT BEFORE ATTRITION

8-12 Mesh	14-18 Mesh	20-25 Mesh	25-30 Mesh	20-30 Mesh
1.100 lbs	0.950 lbs	0.100 lbs	0.250 lbs	0.115 lbs
1.020	2.020	0.310	0.695	0.260
3.970	0.080	0.380	0.275	0.335
2.020	0.590	0.012	0.705	0.375
5.190	0.640	0.270	0.220	0.650
0.900	1.585	0.310	0.410	0.215
2.390	0.720	0.640	0.315	0.845
3.800	0.235	0.655	0.320	0.610
2.940	0.710	0.510	0.260	0.285
0.620	1.225	0.050	0.335	0.585
1.730	0.350	0.175	0.415	0.450
1.180	1.250	0.200	0.340	0.645
0.630	0.825	0.495	0.305	0.310
1.100	2.465	0.190	0.190	0.345
2.490	1.550	0.195	0.590	0.450
4.400	0.465	0.195	0.390	0.510
3.330	1.300	0.563	0.180	0.340
1.120	2.530	0.890	0.230	0.350
3.400	1.340	1.075	0.665	0.700
0.620	1.655	0.620	0.365	0.350
2.830	1.235	0.275	0.640	0.750
1.440	0.320	0.330	0.530	0.685
1.200	0.225	0.150	0.395	0.560
2.600	1.610	0.605	0.385	0.340
4.380	1.500	0.475	0.690	0.110

APPENDIX J

ITI CRUSH STRENGTH DATA ON ALUMINA
SUPPORT AFTER 50% ATTRITION STEP

8-12 Mesh	14-18 Mesh	20-25 Mesh	25-30 Mesh	20-30 Mesh
3.680 lbs	1.915 lbs	0.410 lbs	0.415 lbs	0.485 lbs
2.220	3.345	0.565	0.335	0.260
2.190	2.240	0.600	0.450	0.515
5.050	2.735	0.390	0.950	0.430
4.560	0.730	0.575	0.610	0.625
0.900	0.170	0.085	0.615	0.195
4.425	1.580	0.615	0.485	0.500
3.660	2.310	1.315	0.445	0.345
3.375	1.740	0.300	0.190	0.250
3.410	1.970	1.240	0.300	0.610
4.910	1.150	0.420	0.550	0.150
2.950	3.100	1.410	0.170	0.110
4.875	1.110	1.195	1.020	0.550
3.565	2.830	0.615	1.155	0.260
2.630	2.550	0.360	0.160	0.200
2.715	1.035	1.650	0.275	1.015
2.560	2.580	0.440	0.560	0.625
2.665	1.360	0.290	0.690	0.325
1.680	2.510	0.775	0.345	1.660
3.015	0.775	0.800	0.340	0.290
3.900	2.325	0.720	0.565	0.555
4.500	2.310	0.825	0.270	0.800
0.850	1.230	0.930	0.810	1.005
2.400	0.460	0.550	0.315	0.020
2.170	2.400	0.815	0.560	0.360

APPENDIX K

ITI CRUSH STRENGTH DATA ON USED SHELL 405
CATALYST SAMPLES RECEIVED FROM TRW

1/8" x 1/8" Cylinders[a]	14-18 Mesh[b]	18-20 Mesh[c]	18-20 Mesh[d]
20.60 lbs	0.750 lbs	0.660 lbs	0.740 lbs
15.30	0.385	0.450	0.845
9.50	2.220	0.165	1.210
11.20	3.665	0.850	1.065
40.80	2.145	0.590	1.360
27.80	1.813	0.170	0.410
20.25	0.945	0.805	0.210
21.50	0.915	0.735	0.875
40.80	2.570	0.550	1.830
11.00	1.765		1.630

(a) Detailed history not available, however, estimated at a few thousand seconds steady state operation.
(b) Approximately 250 seconds of steady state firing over 51 cold starts.
(c) Sample saw 84,000 pulses in 5 lbf thruster in November 1972. Sample from downstream end of bed.
(d) Sample saw 210,000 pulses in 5 lbf thruster in August 1973. Sample from upper portion of bed near the injector.

APPENDIX L

SEQUENTIAL COMPRESSIVE MINI-BED CRUSHING
OF 20-25 MESH FRESH SHELL 405

Series:		1				2	
Pressure lb/in^2:	21.9	91.8	200	322	27.4	50	99
Weight in Grams:							
Starting	.9050	.8662	8414	.8132	.9226	.9080	.8949
On 25 Mesh	.8662	.8414	.8132	.5148	.9080	.8949	.8619
Through 25 Mesh	.0390	.0243	.0245	.2775	.0157	.0115	.0337
On 30 Mesh	.0366	.0232	.0165	.0815	.0145	.0091	.0333
Through 30 Mesh	.0024	.0010	.0080	.1825	.0008	.0021	.0004

APPENDIX N

SEQUENTIAL COMPRESSIVE MINI-BED CRUSHING
OF 25-30 MESH FRESH SHELL 405

Pressure lb/in^2:	25	44.9	97.9	204	324
Weight in Grams:					
Starting	.9257	.9218	.9227	.9193	.9122
On 30 Mesh	.9218	.9227	.9193	.9122	.8964
Through 30 Mesh	.0043	.0006	.0023	.0064	.0118
On 35 Mesh	--	--	--	--	.0076
Through 35 Mesh	--	--	--	--	.0059

FRESH SHELL 405 PARTICLE FLUIDIZATION EXPERIMENTAL DATA

Minimum Inlet Distributor Superficial Velocity
For Particle Movement[a] Meters per Second

	Pure Nitrogen			Pure Helium	
8-12 Mesh	14-18 Mesh	20-30 Mesh	8-12 Mesh	14-18 Mesh	20-30 Mesh
5.33	3.55	2.88	13.0	11.1	6.51
3.98	4.40	2.62	12.3	11.1	7.27
6.42	4.23	2.11	13.8	9.40	6.76
3.64	4.99	2.62	11.5	7.73	7.45
5.92	3.55	1.69	9.90	8.96	6.18
7.35	3.98	2.45	11.1	8.45	6.43
7.02	3.46	1.77	11.3	6.18	8.03
6.94	3.81	1.52	13.3	9.90	4.82
4.72	4.32	2.62	13.3	10.5	4.82
8.11	3.98	2.54	12.3	11.0	8.95

8-12 Mesh		14-18 Mesh		20-30 Mesh	
Fresh Shell 405		Fresh Shell 405		Fresh Shell 405	
Gas Comp. $\%N_2$[b]	Velocity Meters/Sec	Gas Comp. $\%N_2$[b]	Velocity Meters/Sec	Gas Comp. $\%N_2$[b]	Velocity Meters/Sec
86.9	5.59	78.8	4.40	55.2	2.45
88.2	6.43	75.6	3.46	66.7	2.54
87.5	6.09	60.4	4.05	76.0	2.21
81.1	7.61	55.8	3.46	50.0	4.06
92.3	5.50	61.4	3.72	46.7	2.54
85.3	6.34	59.6	3.97	55.8	3.64
87.7	6.17	44.3	5.92	68.6	2.96
85.5	6.42	58.3	4.06	92.0	2.12
74.4	6.93			58.7	3.89
81.4	7.26			63.2	3.22
26.0	11.8	37.9	5.56	16.7	2.02
18.1	7.01	30.3	6.42	45.4	1.52
25.6	3.63	30.2	3.63	26.7	1.27
16.4	10.3	19.2	2.79	14.7	4.31
18.0	7.52	13.1	5.15	36.4	1.86
27.5	5.82	23.1	3.30	32.1	2.37
17.6	8.61	30.2	3.63	21.7	3.89
29.0	3.21	21.4	3.55	34.8	3.89
24.5	3.80	31.0	2.45	32.1	2.37
20.3	5.82	25.7	2.96	41.2	2.88

(a) Minimum inlet distributor superficial velocity which results in any particle movement.

(b) Volume $\%N_2$ in a N_2-He blend.

PLPET DATA ON THE EFFECT OF LIQUID EROSION

- Fresh Shell 405 1/8" x 1/8" Cylinders at
  100 Feet per Second and 8,200 Pulses

Pellet	Initial Weight grams	Final Weight grams	Weight Change grams
1	.05159	.05150	-.00009
2	.05122	.05105	-.00017
3	.05225	.05194	-.00031
4	.05025	.05012	-.00013
5	.05416	.05407	-.00009

- Fresh Shell 405 1/8" x 1/8" Cylinders at
  100 Feet per Second and 100,000 Pulses

Pellet	Initial Weight grams	Final Weight grams	Weight Change grams
1	.04819	.04775	-.00044
2	.04930	.04891	-.00039
3	.04796	.04748	-.00048
4	.04899	.04854	-.00045
5	.05134	.05090	-.00044

- Fresh Shell 405 1/8" x 1/8" Cylinders at
  100 Feet per Second and 500,000 Pulses

Pellet	Initial Weight grams	Final Weight grams	Weight Change grams
1	.05143	.05016	-.00127
2	.04995	.04989	-.00006
3	.04885	.04855	-.00030
4	.04947	.04940	-.00007
5	.05034	.04935	-.00099

- **Fresh Shell 405 1/8" x 1/8" Cylinders at 55 Feet per Second and 8,200 Pulses**

Pellet	Initial Weight grams	Final Weight grams	Weight Change grams
1	.05204	.05201	-.00003
2	.04963	.04955	-.00008
3	.04684	.04675	-.00009
4	.04982	.04976	-.00006
5	.04998	.04995	-.00003

- **Fresh Shell 405 1/8" x 1/8" Cylinders at 55 Feet per Second and 100,000 Pulses**

Pellet	Initial Weight grams	Final Weight grams	Weight Change grams
1	.05111	.05126	+.00015
2	.04953	.04946	-.00007
3	.04996	.04976	-.00020
4	.05158	.05046	-.00112

- **Fresh Shell 405 8 to 12 Mesh Granules at 100 Feet per Second and 8,200 Pulses**

Particle	Initial Weight grams	Final Weight grams	Weight Change grams
1	.01383	.01378	-.00005
2	.01538	.01527	-.00011
3	.01418	.01409	-.00009
4	.02309	.02205	-.00024

- **Fresh Shell 405 8 to 12 Mesh Granules at 100 Feet per Second and 100,000 Pulses**

Particle	Initial Weight grams	Final Weight grams	Weight Change grams
1	.02226	.02194	-.00032
2	.01696	.01674	-.00022
3	.01334	.01993	-.00034
4	.01334	.01318	-.00016
5	.01601	.01583	-.00018

- **Fresh Shell 405 8 to 12 Mesh Granules at 55 Feet per Second and 8,200 Pulses**

Particle	Initial Weight grams	Final Weight grams	Weight Change grams
1	.00865	.00864	-.00001
3	.01571	.01564	-.00007
4	.00816	.00818	+.00002
5	.01191	.01183	-.00008

- **Fresh Shell 405 8 to 12 Mesh Granules at 55 Feet per Second and 100,000 Pulses**

Particle	Initial Weight grams	Final Weight grams	Weight Change grams
1	.01448	.01438	-.00010
2	.02615	.02608	-.00007
3	.01959	.01940	-.00019
4	.01822	.01803	-.00019
5	.01211	.01199	-.00012

ANALYSIS OF PERCENTAGE WEIGHT CHANGE RESULTS
FROM PULSED LIQUID EROSION DATA IN PIPE

Liquid Velocity feet per second	Number of Pulses	Fresh Shell 405 Catalyst	Percentage Change In Weight		
			Individual Change	Mean	Standard Deviation
100	8,200	1/8" X 1/8" Cylinders	-0.17 -0.33 -0.59 -0.26 -0.17	-0.30	0.17
100	8,200	8-12 Mesh Particles	-0.36 -0.72 -0.63 -1.04	-0.69	0.28
100	100,000	1/8" X 1/8" Cylinders	-0.91 -0.79 -1.00 -0.92 -0.86	-0.90	0.08
100	100,000	8-12 Mesh	-1.44 -1.30 -1.68 -1.20 -1.12	-1.35	0.22

Liquid Velocity feet per second	Number of Pulses	Fresh Shell 405 Catalyst	Individual Change	Mean	Standard Deviation
55	8,200	8 to 12 Mesh Granules	-0.12 -0.44 +0.24 -0.67	-0.25	0.40
55	8,200	1/8" x 1/8" Cylinders	-0.06 -0.16 -0.19 -0.12 -0.06	-0.12	0.06
55	100,000	1/8" x 1/8" Cylinders	+0.29 -0.14 -0.40 -2.17	-0.61	1.08
55	100,000	8 to 12 Mesh Granules	-0.69 -0.27 -0.97 -1.04 -0.99	-0.79	0.32
100	500,000	1/8" x 1/8" Cylinders	-2.47 -0.12 -0.61 -0.14 -1.97	-1.06	1.09

PLPET INDIVIDUAL DATA USED IN THE ANOVA

VELOCITY OF LIQUID RELATIVE TO PARTICAL

Number of Pulses	55 Feet per Second		100 Feet per Second		Row Means (Number of Pulse Effect)
	1/8" x 1/8" Cylinders	8-12 Mesh Granules	1/8" x 1/8" Cylinders	8-12 Mesh Granules	
8,200	.06 .16 .19 .12 .06	0.12 0.44 -0.24 0.67 (.25)	0.17 0.33 0.59 0.26 0.17	0.36 0.72 0.63 1.04 (.69)	.339
100,000	-.29 .14 .40 2.17 (.61)	0.69 0.27 0.97 1.04 0.99	.91 .79 1.00 .92 .86	1.44 1.30 1.68 1.20 1.12	.910
Column Means (Velocity Effect)	.461		.809		
Group Means (Catalyst Type Effect)	.481		0.769		

APPENDIX R

REPORTS OF DR. D. P. H. HASSELMAN

October 27, 1974

Dr. W. P. Taylor
Government Research Laboratory
EXXON Research and Engineering Company
P. O. Box 8
Linden, N. J. 07036

Dear Dr. Taylor:

As we discussed during my last visit, it may be diffi-
cult to get the necessary property values for the Shell 405
catalyst, in view of the irregular shape of the individual
particles. I recommended at the time that good approximations
for the catalyst properties can be obtained from composite
theory in terms of the properties of the alumina and iridium
and their volume fractions in the composite.

Enclosed are the results of my estimates for a number
of properties of single particles of Shell 405 catalyst. The
property values are summarized in the attached Table I. A
summary of the calculations and a list of appropriate litera-
ture references are also included. I have been deliberately
brief in writing down the calculations in order not to spend
a lot of time writing a lengthy report. Please contact me
if I can give any clarification.

With regard to the actual expressions I chose to compute
the composite properties, from the many that are available,
it turns out that in view of the small volume fraction of Ir,
the choice of the equation is not critical. The relatively
large pore content introduces a far greater uncertainty. For
the latter effect I chose a semi-empirical expression, which
I believe gives us the proper range of values. Since at this
time I was unaware of the distribution of the pores in the
composite, in the calculations I first calculated the proper-
ties for a theoretically dense composite, which were then cor-
rected for porosity. The particular property data chosen are
from the literature. For the Al_2O_3, the property values are
those close to α-Al_2O_3. For the Ir I have taken data from
the list you sent me plus a few data points from the litera-
ture. If it turns out that property data better than the

ones I have chosen become available, the values for the composite properties can easily be recalculated. Clearly, I have assumed the particles to be isotropic.

In estimating these property values a mechanism for catalyst degradation occurred to me, in addition to all those we discussed during my last visit. I prefer to call this mechanism "internal fatigue". This arises from the slight mismatch of the coefficients of thermal expansion of the Al_2O_3 and the Ir. This causes internal stresses within a single particle whenever the particle is at a temperature different from the one at which the Ir was deposited into the Al_2O_3. For a small volume fraction, the internal stresses in a second phase to a first approximation are:

$$\sigma_{int} \sim \Delta\alpha \, E\Delta T/(1-\nu) \qquad (1)$$

where $\Delta\alpha$ is the difference in coefficients of thermal expansion, E is Young's modulus of the second phase, ΔT is the difference between the temperature of the particle and the temperature at which the composite was formed, and ν is Poisson's ratio.

For $\Delta\alpha = 0.5 \times 10^{-6} \, C^{-1}$, $E \sim 74 \times 10^6$ psi and say $\Delta T = 500 \, C$ and $\nu = 0.25$, the value of internal stress becomes some 20,000 psi. If the particle is above its forming temperature this stress is compressive; if below, the stress is tensile. Cycling the temperature of the particles up and down, as occurs in practice, subjects the Ir to cyclic fatigue. In my view, the above value of stress is sufficient to fatigue a brittle material even if the stresses from mechanical loading and the continuum thermal stresses were negligible, which I doubt. To check on these internal stresses I suggest that an X-ray analysis be performed on the particles and the patterns compared with those of the single-phase Al_2O_3 and Ir. Peak broadening and shifting will be indicative of internal stress content.

If this mechanism indeed is responsible for the catalyst degradation, we could solve the problem by selecting a substrate material with a coefficient of thermal expansion which more closely matches the expansion of the Ir than Al_2O_3. If this is difficult, one might possibly first coat the Al_2O_3 with a ductile material such as Au or Pt prior to Ir deposition. The ductile material will reduce the internal stress level. As an alternative solution, perhaps a method may be found of replacing the catalyst in the rocket-motor.

Dr. W. F. Taylor - 3

Please give me your comments.

Sincerely,

D. P.-H. Hasselman, Director
Ceramics Research Laboratory

Dr. W. F. Taylor -4

Table I.   Estimated property values for single particles
            of Shell 405 catalyst with 56% porosity.

1. Volume fraction Al_2O_3 0.932

2. Volume fraction Ir   0.068

3. Theoretical density ($gm.cc^{-1}$)   5.06

4. Porosity %   56

5. Shear modulus (10^6 psi)   3.7-4.7

6. Bulk modulus (10^6 psi)   6.2-7.8

7. Young's modulus (10^6 psi)   9.1-11.5

8. Poisson's ratio (ν for Al_2O_3)   0.25

9. Coefficient of th. exp. ($^\circ C^{-1}$) 0-100 $^\circ$C 6.05×10^{-6}

10. Thermal conductivity ($cal.cm^{-1}.s^{-1}.^\circ C^{-1}$)
                        Room temp.   0.013-0.011
                        800 $^\circ$C   0.007-0.003

11. Specific heat ($cal.gr^{-1} C^{-1}$)(R.T.)   0.19

12. Thermal diffusivity ($cm.^2 s^{-1}$)(R.T.)   0.028

PROPERTY ESTIMATER FOR SHELL 405 CATALYST

A. Volume fractions, theoretical density and porosity

Volumes assumed	Ir	Al_2O_3
Wt. fraction (W)	0.3	0.7
Density (ρ). gms.cc^{-1}	22.4	3.8

1. Volume fractions

$$V_i = W_i \rho_i / \sum_{i=1}^{i=2} W_i \rho_i$$

Yields Al_2O_3 V = 0.932
         Ir   V = 0.068

2. Theoretical density, ρ_{th}

$$\rho_{th} = \sum V_i \rho_i$$

Yields $\rho_{th} \approx 5.06$ gms.cc^{-1}

3. Porosity (P)

$$P = \rho_{actual} / \rho_{th} \qquad P \approx 56\% \qquad \rho_{actual} \approx 2.24 \text{ gm.cc}$$

B. Elastic Properties

Values assumed for fully dense Ir and Al_2O_3

	Ir	Al_2O_3
Young's modulus, E (10^6 psi)	74	55
Poisson's ratio, ν	0.25	0.25
Shear modulus, G (10^6 psi)	29.6	22.0
Bulk modulus, B (10^6 psi)	49.	36.7

1. Shear modulus of dense Al_2O_3 - Ir

After Hashin & Shtrikman:

$$G_c = G_m \left[1 + \frac{15(1-V_m)(G_p/G_m - 1) c}{7 - 5 V_m + 2 (4-5 V_m)(G_p/G_m - (G_p/G_m - 1)c)} \right]$$

Where G_c, G_m, and G_p are the shear moduli of the composite, matrix phase and second phase, resp. V_m is Poisson's ratio of second phase and C is volume fraction 2nd phase.

Taking Al_2O_3 as the reaction phase, substitution of values yields

$$G_c = 22.5 \times 10^6 \text{ psi}$$

This is only slightly higher than G for Al_2O_3 as expected from small value of volume fraction of Ir.

2. Bulk Modulus of dense Al_2O_3 - Ir

   After Haskin & Shtrikman:

   $$B_c = B_m \left[1 + \frac{3 \ (1-V_m)(B_p/B_m - 1) \ C}{2 \ (1-2 \ V_m) + (1+V_m) \left[B_p/B_m - (B_p/B_m - 1) \ C \right]} \right]$$

   Where B_c, B_m, and D are the bulk moduli of the composite, matrix and 2nd phase resp.

   Substitution of appropriate values yields

   $B = 37.4 \times 10^6$ psi

3. Young's modulus of dense Al_2O_3-Ir

   $E = g \ B/(3B + C)$

   Substitution of appropriate values for $\mathcal{G}_c$ and B_c yields:

   $E = 55.2 \times 10^6$ psi

   As expected the value is only slightly higher than for Al_2O_3.

4. Young's modulus of porous composite

   Semi-empirically:

   $$E = E_o \left[1 - AP/\left(1 + (A - 1) \ P \right) \right]$$

   When E and E are Young's moduli of the porous and non-porous material, resp. P is the fraction porosity, and A is a constant which from experiments $3 < A < 4$.

   This yields:

   $E \approx 9.1$ to 11.5×10^6 psi

C. Thermal Conductivity

Values assumed: K (Cal C^{-1} cm^{-1} sec^{-1})	Al_2O_3	Ir
Room Temp	0.06	0.35
800°C	0.02	0.35

   From Haskin (same as Kerner)

   $$K_c = K_m \left[1 + \frac{V_2 \ (K_p - K_m)}{K_m + 1_3 \ (K_p - K_m)Vi} \right]$$

Where K_c, K_m, and K_p are the thermal conductivities of the composite, matrix and 2nd phase, resp. V_2 is the fraction 2nd phase, $V_1 = 1 - V_2$.

Substitution of appropriate values yields:

$K \approx 0.068$ at RT

$K \approx 0.024$ at 800°C

D. Thermal conductivity for porous composite

Same general expression as for porosity effect on Young's modulus with $A \approx 4$

Yields: $K_c \approx 0.011$ cal. $°C.^{-1}cm^{-1}s^{-1}$ at RT

         $K_c^c \approx 0.004$ "   "   "   " 800°C

Thermal conductivity estimates from upper (K^+/and lower (K^-) bonds in the cond. of composite.

$$K_+ = K_1 V_1 + K_2 V_2$$

$$^1/K_- = V_1/K_1 + V_2/K_2$$

	dense comp.	porous comp.	
K_+	0.0797	0.0132	RT
	0.040	0.0066	800°C
K_-	0.064	0.0106	RT
	0.020	0.0033	800°C
Avg. K_+ and K_-	0.012		RT
	0.005		800°C

About the same as values on top of page.

E. Coefficient of Thermal Expansion After Turner

$$\alpha = (\alpha_1 B_1 V_1 + \alpha_2 B_2 V_2)/(B_1 V_1 + B_2 V_2)$$

For Al_2O_3 $\alpha = 6.0 \times 10^{-6} °C^{-1}$ at RT

For Zr $\alpha = 6.5 \times 10^{-6} °C^{-1}$ at RT

Yields: $\alpha_c = 6.05 \times 10^{-6} °C^{-1}$.

F. Specific Heat

$$c_c = c_1 \rho_1 + c_2 \rho_2$$

At room temp.

Al_2O_3 $C \approx 0.26$ cal. $°C^{-1} \, g_2^{-1}$

 Ir $C \approx 0.033$ "   "   "

Yields:

$C_c \approx 0.19$ cal. $°C^{-1} \rho_r^{-1}$.

G. Thermal Deffusivity (K)

     $K = k/\rho c$

     Where K = thermal conductivity
         ρ = density
         C = specific heat

     Yields $K \approx 0.028$ $cm^2 S^{-1}$. at RT

List of literature references (by no means exhaustive):

1. P. S. Turner, "Thermal-Expansion Stresses in Reinforced Plastics," J. NBS. 37 239 (1946).

2. R. A. Schapery, "Thermal Expansion of Composite Materials Based on Energy Principles", J. Comp. Mat., 2, 388 (1968).

3. G. W. Brassel and K. B. Wischmann, "Mechanical and Thermal Expansion Properties of a Particulate Filled Polymer", J. Mat. Sc., 9, 307-14 (1974).

4. F. H. Kerner, "The Elastic and Thermus-Elastic Properties of Composite Media", Proc. Phys. Soc., Vol. 69 B, 808 (1956).

5. A. A. Fahmy and A. N. Rajai, "Thermal Expansion Behavior of Two-Phase Solids", J. Appl. Phys. 41, 5108 (1970).

6. W. D. Kinpery, "Note on Thermal Expansion and Microstresses in Two-Phase Compositions", J. Am. Ceram. Soc., 40 (10) 351 (1957).

7. Z. Haskin, "The Elastic Moduli of Heterogeneous Materials", J. Appl. Mech. (1960).

8. Z. Haskin and S. Shtrikman, "A Variational Approach to the Theory of the Elastic Behavior of Multiphase Materials", J. Mech. Phys. Solids 11, 127-140 (1963).

9. D. P. H. Hasselman, "On the Porosity Dependence of the Elastic Moduli of Polycrystalline Refractory Materials", J. Am. Ceram. Soc. 45, 452 (1962).

10. E. H. Kerner, "The Electrical Conductivity of Composite Media", Proc. Phys. Soc. (B), 69, 802 (1956).

11. A. E. Powers, "Conductivity of Aggregates", AEC Report KAPL-2145 (Kuells Atomic Power Laboratory) (1961).

12. Z. Haskin, "Assessment of the Self-Consistant Scheme Approximation: Conductivity of Particulate Composition", J. Comp. Mat., 2, 284 (1968).

13. S. C. Chery and R. I. Vachan, "The Prediction of the Thermal Conductivity of Two- and Three-Phase Solid Heterogeneous Mixtures", Int. J. Heat Mass Transfer 12, 249 (1969).

LEHIGH UNIVERSITY
Bethlehem, Pennsylvania 18015

March 3, 1975

Dr. W. F. Taylor
Government Research Laboratory
EXXON Research and Engineering Laboratory
P. O. Box 8
Linden, N. J. 07036

Dear Bill:

This letter serves to provide you with a summary of the comments I gave at the Advisory Committee Meeting held in Princeton on Feb. 25. A few thoughts which occurred to me since the meeting are included as well.

This was the first meeting of the Advisory Committee I attended. I found it very helpful as it filled me in on many more of the observations and details of the research program.

My comments, which are not presented in order of relative importance, are as follows:

1.   It is my view that in the test for compressive strength, actual failure of the catalyst particles occurs in a tensile mode, due to the presence of a tensile stress state in the particle interior. The direction of this tensile stress is perpendicular to the direction of the compressive load.

The tensile strength (σ_t) is related to the failure load (P) by $\sigma_t = 1.37 \ P/a^2$ where a is the particle diameter. This equation is used at Carnegie-Mellon University to calculate the tensile strength of abrasive grain, subjected to failure in compression. It may well be interesting to see what values of tensile strength you may be able to get from the experimental data. It may also be of benefit to take into account the size of each individual particle. This could very well reduce the scatter in the data, which should reduce the total number of tests required in order to obtain results with a given degree of statistical significance.

It was of interest to note that, in the list of property data you presented, the tensile strength was about 1/3 of the compressive strength. I understand the tensile strength was

estimated, and please fill me in on how this was done. It
may be fortuitous, but it is of interest to note that for a
cylindrical pore with circular cross-section, the stress con-
centration factors are 3 and -1 for the stress at the pore
equator and poles, resp. In compression this gives a tensile
stress equal to the compressive stress applied externally.
A tensile load, however, gives a tensile stress at the pore
three times the applied stress. The ratio of the compressive
to tensile strength then is expected to equal three. The
existence of a tensile stress at a pore even during compression
should facilitate tensile failure under these conditions, as
I mentioned earlier.

2.   During thermal shock on heating, a brittle material can
fail in tension or in shear depending on geometry. Protrud-
ing corners on irregularly shaped particles will shear off on
heating, which tends to spheroidize the particle. A near-
spherical particle will fail in tension because of the tensile
stress state in the particle interior. In this case, the
fragments tend to be of conical shape. I mention this for two
reasons. On thermal shock by heating we should keep track of
both the tensile and the compressive thermal stresses (i. e. ,
320 and 500 psi as given in the next-to-last report.) On
cooling these stress values are reversed. This tends to make
thermal shock by cooling more severe than thermal shock by
heating, for the same Biot number. Cooling is expected to
be more severe also for the reason that at the higher temper-
atures from which cooling takes place, the thermal conductiv-
ity tends to be lower. This increases the Biot number and the
corresponding tensile thermal stress. This is why it is vital
to firmly establish values for the Biot number in order to
render the thermal stress calculations most meaningful quanti-
tatively.

The other reason why I bring this up is that an examin-
ation of the shape of the fragments may tell us something of
the failure mode. Generally, on heating a brittle material
will fail catastrophically into a relatively small number of
fragments, which for a spherical particle tend to be cone-
shaped, as I mentioned. If the fragments are cone-shaped,
you may possibly conclude that failure occurred on heating.
On cooling, generally failure occurs non-catastrophically,
by the formation of numerous small cracks on the surface, giv-
ing rise to loosely attached fragments. Such fragments can
be removed gradually by the aerodynamic forces, leading to
gradual breakdown of the catalyst particles. In other words,
such degradation would be a two-stage process.

3.   The following thought occurred to me after the meeting.
Although I have not read the specific work-statement and have
not talked to Dr. Webber as yet, I understand that the aim of
his analysis is to superpose thermal stresses resulting from
thermal shock and internal stresses arising from gas pressures
within the pore. This approach is quite proper in order to
analyze failure mechanisms. I wish to suggest a further com-
plicating factor which should be taken into account in such
an analysis as follows: As the result of the flow of heat
during the transient heating or cooling, the disturbing effect
of the pore on the temperature gives rise to micro-mechanical
thermal stresses around the pore perimeter. These stresses
exist in addition to the continuum thermal stresses (as con-
centrated by the pore) and the stresses which arise from the
internal pressure. All three stress systems need to be con-
sidered. Appropriate literature references for these micro-
mechanical thermal stresses are:
    Tauchert, T. R.   J. Comp. Matls. $\underline{2}$ (4) 478-86 (1968);
    $\underline{3}$ (1) 192-95 (1969).
I hope that sometime in the future I may be able to get together
with Dr. Webber to discuss these aspects in greater detail.

4. I wish to make a minor comment on the data for particle
breakdown in the simulated crushing test. Please give me
some more detail on the particular screening operation used,
but generally, screening itself can result in particle break-
down. This is a common problem in carrying out and interpret-
ing screening tests. In my opinion (subject to correction)
the data for particle breakdown for pressure less than 100 psi
are the result of the screening subsequent to the compression
testing. If so, we can conclude that for pressures less than
some 100 psi the resistance to compressive breakdown is even
more than suggested by the experimental data.

5.   I was intrigued by the observations reported by United
Aircraft, which at least to me seem to suggest that at least
one of the contributing mechanisms of failure can be attribut-
ed to particle rupture due to internal pressure build-up.
If so, it may be worthwhile, as I suggested at the meeting,
to carry out a simulated test which would involve a rapid
decompression of the catalyst particles impregnated with an
appropriate liquid. I realize that the contract already
specifies the tasks and their rates of effort (generally I
am accustomed to some greater flexibility). Nevertheless,
it may be wise to carry out such a test at some later time,

perhaps as part of a program extension. Since particles can
be fatigued by this mechanism, such tests if deemed worth-
while, should include single as well as multiple decompressions.

6.   I was very pleased to learn more about the actual struc-
ture of the catalyst particle. Nevertheless, I would like
to see some SEM's of the internal structure of a fresh alumina
and impregnated particle as well as a used particle and of
fragments resulting from actual service. Nevertheless, I
understood that the Ir is located on the pore surface in rela-
tively isolated particles. This helps a great deal in pre-
dicting property values, because for a number of properties
the Ir cannot contribute much, such as for strength, thermal
conductivity and elastic behavior. Density and specific heat,
of course, are expected to depend on Ir content. As a result
some of the values I estimated earlier should be re-assessed.
These estimates depended in part on theoretical solutions for
materials containing near-spherical inclusions. Pending examin-
ations of some SEM's, the latter structure does not appear
appropriate to the catalyst. Nevertheless, we can make a num-
ber of educated guesses.

From the rather low value of Young's modulus, I conclude
that the alumina consists of a mass of particles which are
only lightly bonded together. Indirectly, this value of Young's
modulus is confirmed by Dr. Webber's thermal stress analysis,
since for the Biot number of unity, my original value of Young's
modulus would result in unrealistically high thermal stresses
in comparison to the strength values. We can use the value
of Young's modulus as a guide in estimating other property
values, since to a very first approximation those properties
affected by porosity follow similar relative dependence on
pore content. This gives us a handle on thermal conductivity,
for instance. As a result I attach a new list of estimated
property values, which again is open to further revision when
more information becomes available as the program progresses.

As far as property measurements are concerned, it may be
of interest to point out that in our ceramics laboratory we
have recently installed equipment which measures thermal dif-
fusivity by the laser flash technique. This requires a circu-
lar disc specimen 0.5 inch in diameter by about 0.1 to 0.2
inch thick. If a specimen of those dimensions could be acquired
(such as the alumina with or without the Ir) we will be most
happy to run it through our apparatus to measure thermal dif-
fusivity and calculate thermal conductivity. It should also
be possible to determine the diffusivity of a catalyst if a

suitable specimen holder can be devised. Incidentally, a value of thermal conductivity can be very useful in verifying the Biot number used for the thermal stress analysis.

7. A further mechanism of particle degradation which has occurred to me may be attributed to the attrition procedure. The damage to the particles during attrition may result in fairly loosely bonded fragments which detach themselves during operation. I suggest that an ultra-sonic cleaning operation following attrition can be of benefit in removing these loosely bonded fragments. Clearly, during such ultra-sonic cleaning additional particle impact should be avoided by using dilute suspensions.

8. I suggested earlier that possibly an internal fatigue mechanism may be operating which on heating and cooling results from the cyclic stressing due to the slight differences in coefficients of thermal expansion of the alumina and Ir. It may well be that as the result of this internal fatigue the Ir becomes detached from the pore surface and finds its way out. If so, we would expect that the dust clogging the bed should be richer in Ir than the original catalyst composition. Were compositions ever determined? If not, one might do this.

9. Clearly at this time, we cannot say anything about the actual fatigue mechanism with any degree of confidence. Nevertheless, we might give some thought to a pre-sorting or prooftesting operation which would rapidly eliminate those particles which cause the difficulty.

For instance, if it turns out that the compressive strength test of the single or bed of particles correlates well with the fatigue behavior, we might proof-test by passing the particles through a set of rollers or use the impeller impact test used by the abrasive industry for testing friability or toughness of abrasive grain.

On the other hand, if we find that breakup occurs because of internal pressure, a batch process involving decompression could be designed. In this respect, it is my thought at this time that it may well be that the denser, stronger particles with the smaller pore sizes are more likely to break up because of internal pressure. It could be of interest to examine the

fracture surface microstructure of those particles which
failed in the testing done at P. and W.

If we find that thermal shock is the culprit, a quenching
of the particles may be in order. Or, in this case, thermal
shock resistance can be improved by decreasing the particle
size, which lowers the Biot number.

Since it is my feeling at this time that the mechanical
behavior of the particle primarily is controlled by the proper-
ties of the alumina, it may well be profitable to carry out
these proof-tests on the attrited alumina particles prior to
Ir impregnation.

These are my thoughts and recommendations at this time.
Please call me if I can give any further clarification.

Best wishes.

Sincerely,

D. P. H. Hasselman, Director
Ceramics Research Laboratory
Professor, Metallurgy and
Materials Science

Table I. Estimated property values for single particles
of Shell 405 catalyst. (3/1/75)

1. Volume fraction Al_2O_3	0.932
2. Volume fraction Ir	0.068
3. Theoretical density (gm/cc)	5.06
4. Porosity (%)	56
5. Young's modulus (10^5 psi)	3.0
6. Poisson's ratio	0.25
7. Shear modulus (10^5 psi)	1.2
8. Bulk modulus (10^5 psi)	2.0
9. Coef. th. exp. ($^{\circ}C^{-1}$) 0-100°C	6.0×10^{-6}
10. Th. cond. (cal.cm^{-1}.s^{-1}.°C^{-1})	
R. T.	2×10^{-4}
800 °C	0.67×10^{-4}
11. Specific heat (cal.gr^{-1}. C^{-1})	0.19
12. Th. diffusivity (cm^2.s^{-1})	
R. T.	4.7×10^{-4}
800°C	1.6×10^{-4}

LEHIGH UNIVERSITY
Bethlehem, Pennsylvania 18015

March 21, 1975

Dr. W. F. Taylor
EXXON Research and Engineering Company
Government Research Laboratory
P. O. Box 8
Linden, N. J. 07036

Dear Bill:

Vic Moseley of Bell Aerospace sent me a section of their proposal, which contained a great deal of information on the Shell 405 catalyst. I still have to absorb most of it but here are a couple of preliminary comments:

1. The Bell proposal lists a value of thermal conductivity of approx. 0.75×10^{-6} BTU/in sec °F. If my conversion is correct this value corresponds to approx. 1.4×10^{-4} cal/cm sec °C. For the single particle I estimated a value of thermal conductivity of 2.0×10^{-4} cal/cm sec °C at the same temperature. Since the bed is expected to have a somewhat lower thermal conductivity than the individual particle, my estimate appears to be fairly well on target. This justifies the assumption I used for my estimate, namely that the relative effect of porosity on properties such as thermal conductivity and Young's modulus is the same to a first approximation.

For the higher temperature, my estimate was based on the temperature dependence of the thermal conductivity of the solid alumina, which decreases with increasing temperature. The experimental data shown in the Bell report show an increase of thermal conductivity with temperature. Although this increase is somewhat greater than I would expect, nevertheless it indicates that radiation heat transfer can make a significant contribution to the overall thermal conductivity.

This positive temperature dependence for the catalyst pellets in contrast to dense ceramics may well make thermal shock on heating (cold specimen) more severe than on cooling when the specimen is hot.

2. In regard to thermal shock, the Bell proposal lists a value of heat transfer coefficient of 2000 BTU/ft^{2}hr $^\circ$F. Taking the value of thermal conductivity of K- 0.75 x 10^{-6} BTU/in sec $^\circ$F and a particle radius of 0.01 inch, yields a value of the Biot number of the order of 600 (of course, assuming again that my conversions are correct). Such a value is far higher than the value of unity used by Bill Webber. Even taking a value of K - 10 BTU in/ft^{2}hr $^\circ$F (as quoted by Bell for a single particle) still yields a value of the Biot number, m = 20, for the same particle size and heat transfer coefficients.

A very crude calculation (open to corrections) showed that for a tensile strength of 10^3 psi, the particle can undergo a total temperature change of 1040 and 1200 °C for m = 20 and 600, resp. Since, in practice, these values are somewhat less, the particle is not expected to fail, at least not during the first cycle.

Another way of looking at this is that for a final surface temperature of 1110 $^\circ$F ($\sim$600 $^\circ$C), the thermal stresses for the same sized particle originally at 0 $^\circ$C, will be 500 and 550 psi for m - 20 and 600 resp. (Again, crude estimates). These stress values are sufficiently high in comparison to the tensile strength of around 10^3 psi, that weakening and eventual breakup can occur by thermal fatigue. Thermal fatigue predictions can be carried out for homogeneous ceramic bodies, as we are doing now in our laboratory. But I doubt that such predictions for the catalyst with its highly complex structure can be quantitatively meaningful, unless these were performed at a rate of effort far greater than is available or even justified at this time.

3. A further question occurs to me. Was the Shell 405 catalyst developed to give maximum reactivity by making as porous a structure as possible at the expense of long-term structural integrity? And if so, could a trade-off be made such that a stronger catalyst be developed at the expense of a slight decrease in reactivity?

Your comments are invited.

Sincerely,

D. P. H. Hasselman, Director
Ceramics Research Laboratory
Professor, Metallurgy and
Materials Science

P. S. I just received your report and will look at it as soon as I can.

"This technical report has been reviewed and is approved for publication"

EDWARD J. BERGHORN
Branch Chief

PAUL A. KOSSEY
Deputy Division Director